

**STUDIES ON ELECTROCHROMIC THIN
FILM DEVICES AND SENSORS**

A Thesis Submitted to

The Maharaja Sayajirao University of Baroda

For the Degree of

Doctor of Philosophy

In

Applied Physics

By

Patel Keyurkumar Jaysukhlal

Under the Supervision of

Dr. C. J. Panchal

**Applied Physics Department
Faculty of Technology and Engineering
The M. S. University of Baroda
Vadodara-390001**

May 2012

STUDIES ON ELECTROCHROMIC THIN FILM DEVICES AND SENSORS

A Thesis Submitted to

The Maharaja Sayajirao University of Baroda

For the Degree of

Doctor of Philosophy

In

Applied Physics

By

Mr. Patel Keyurkumar Jaysukhlal

Under the Supervision of

Dr. C. J. Panchal

**Applied Physics Department
Faculty of Technology and Engineering
The M. S. University of Baroda
Vadodara-390001**

May 2012

APPLIED PHYSICS DEPARTMENT

Telephone No.: (0265) 2434188

Fax No.: (0265) 2423898



Faculty of Technology & Engineering

M S University of Baroda,
Kalabhavan

VADODARA-390 001

GUJARAT STATE, INDIA

CERTIFICATE

This is to certify that the thesis entitled “**Studies on Electrochromic Thin Film Devices and Sensors**” submitted by **Patel Keyurkumar Jaysukhlal** to **The Maharaja Sayajirao University of Baroda, Vadodara** for the award of degree of **Ph.D. in Applied Physics** is bona fide and the work has been carried out by him in this department.

C. J. Panchal
19/5/12

Dr. C. J. Panchal

Research Guide,

Applied Physics Department

Date: 19th May, 2012

C. J. Panchal

I/c Head,

Applied Physics Department

PK

I/Dean
Faculty of Tech. & Engg.
M. S. University of Baroda,
Dean, Baroda.

Faculty of Technology and Engineering

Head
Applied Physics Department
Faculty of Technology & Engineering
The Maharaja Sayajirao University of Baroda.
Vadodara - 390 001.

DEDICATED TO
MY PARENTS
AND
MY DEAREST WIFE PALAK

CONTENTS

Acknowledgement	IV
Abstract	V
1 Introduction	
1.1 What is electrochromism?	1
1.2 A brief history of electrochromism	2
1.3 Electrochromic materials	3
1.4 Electrochromic device structures	4
1.5 Criteria for electrochromic devices	8
1.6 Applications of electrochromic devices	10
1.7 Gas sensor	12
1.8 Aim of this work	12
1.9 Organization of the thesis	13
2 Thin Films Preparation and Characterization Techniques	
2.1 Thin film preparation	15
2.1.1 Physical vapor deposition (PVD)	16
2.1.2 Experimental	20
2.2 Thin film characterizations	22
2.2.1 Structural and compositional characterizations	23
2.2.2 Optical characterization	27
2.2.3 Electrical characterizations	28
2.2.4 Impedance spectroscopy	31
2.2.5 Electrochromic characterizations	31
3 Transparent Conducting Indium-Tin Oxide (ITO) Thin Film Layer	
3.1 Introduction	37
3.2 Film preparation	40
3.3 Film characterizations	40

3.3.1	Effect of RF power	41
3.3.2	Effect of working pressure	46
3.4	Conclusions	51
4	Electrochromic Tungsten Trioxide (WO₃) Thin Film Layer	
4.1	Introduction	52
4.2	Film preparation	55
4.3	Film characterizations	56
4.3.1	Structural and compositional characterizations	56
4.3.2	Electrical characterization	62
4.3.3	Optical characterization	63
4.3.4	Electrochromic characterizations	66
4.4	Conclusions	79
5	Electrolyte Zirconium Oxide (ZrO₂) Thin Film Layer	
5.1	Introduction	81
5.2	Film preparation	83
5.3	Film characterizations	84
5.3.1	Structural and compositional characterization	84
5.3.2	Optical characterization	90
5.3.3	Impedance spectroscopy	92
5.4	Conclusions	95
6	Ion-Storage Nickel Oxide (NiO) Thin Film Layer	
6.1	Introduction	96
6.2	Film preparation	99
6.3	Film characterizations	99
6.3.1	Structural and compositional characterizations	100
6.3.2	Optical characterization	107
6.3.3	Electrochromic characterizations	109
6.4	Conclusions	117

7	Electrochromic Device Fabrication and Characterizations	
7.1	Introduction	118
7.2	Electrochromic device fabrication	120
7.3	Electrochromic device characterizations	124
7.3.1	Transmittance modulation	122
7.3.2	Memory effect	125
7.3.3	Switching time	128
7.3.4	Cycle-life	129
7.4	Conclusions	130
8	WO₃ Based Thin Film Gas Sensor	
8.1	Introduction	131
8.2	Gas sensing mechanism	133
8.3	Gas sensor fabrication and characterization	134
8.3.1	Sensor fabrication	134
8.3.2	Sensor characterization	134
8.4	Results and discussions	137
8.4.1	EDX and SEM analyses	137
8.4.2	Gas sensing properties	139
8.5	Conclusions	143
9	Summary and Future Outline	
9.1	Summary	144
9.2	Future outline	145
	References	146
	List of Symbols	154
	Abbreviations	156
	List of Publications	157

ACKNOWLEDGEMENT

It is a pleasure to thank several individuals who in one or another way contributed towards the completion of this study.

Firstly, I would like to thank my guide, Dr. C. J. Panchal, for his continuous support and assistance during my research. Without his guidance, this study would not have seen the light of the day. His care and patience motivated me to go ahead in my research work. I am indebted to him not only for introducing me to this work but also for his encouragements and trust in me, which enabled me to solve the problems encountered during the various stages of my work.

I must express my personal and particular gratitude to Dr. M. S. Desai, Applied Physics Department, for his deep interest, concern, and advices. I have also benefited enormously and learned a lot from his writing skills and I am very grateful to him for revising my manuscripts and thesis. In addition, special thanks are due to Dr. Bharti Rehani and Dr. P. K. Mehta for providing me educational aid during my research.

I would like to express thanks to teachers who had taught me during my school, graduation, and post-graduation study. I also like to thank the non-teaching staff members of Applied Physics Department for their support during this work. I take this opportunity to thank Mr. Y. Pawar for keeping our lab clean.

I am especially thankful to The M. S. University of Baroda for providing me financial support under the university research fellowship. Also, thanks are due to the UGC-DAE Consortium for Scientific Research, Indore, for characterization of my thin film samples.

I am indebted to my colleagues, Dr. Vipul Kheraj, Dr. Nitin Shah, Pravin Patel, Pranav Vakil, and especially Jaymin Ray, and Gopal Bhatt, for their support without which this work would be next to impossible. In addition, I would like to express my thanks to all my friends for their support during my research work.

Last, but not the least, my deepest gratitude goes to my family for their unflagging love and support throughout my life; this thesis would simply be impossible without them.

Finally, great thanks to God for always being with me during crucial times and thereby increasing my potential and self-confidence during my journey.

May 2012

Keyur J. Patel

ABSTRACT

The present thesis deals with the studies of solid-state electrochromic (EC) thin film device. In addition to this, a brief study related to the gas-sensing properties of the transition metal oxide (WO_3) thin films was also undertaken. The Electrochromic device (ECD) controls the optical properties such as optical transmission, absorption, reflectance, and/or emittance in a continual but reversible manner on application of a voltage. This property enables the ECD to be used for numerous applications like smart-window, EC mirror, and EC display.

The solid-state ECD consists of a multilayered structure of several thin film layers of EC materials. The basic structure of solid-state thin film EC device consists of glass substrate / transparent conducting electrode (TCO) / ion-storage layer (IS) / solid-electrolyte / EC layer / TCO. Depending upon the applications, one of the TCO layers in the above structure is replaced by a reflecting metal electrode. The EC layer is the most active layer of ECD, in which coloration occurs when any charge is inserted in it or extracted out of it. Tungsten trioxide (WO_3) thin film has acquired considerable interest as an EC material for the fabrication of an ECD. An electrolyte is a substance containing free ions, which behaves as an electrically conductive medium for the ions to be injected into or ejected from the EC layers. ZrO_2 acts as a solid electrolyte in the form of thin film. The ECD requires a counter electrode or an ion-storage layer, which can supply ions, but remain colorless or have a complementary color in the process. NiO thin film is a typical example of an ion-storage layer used with WO_3 EC layer. The ECD works on the application of an external voltage for conducting electrodes were used. Indium tin oxide (ITO, $\text{In}_2\text{O}_3:\text{Sn}$), which is conductive and transparent for wavelengths near UV-Visible region, acts as a transparent conducting electrode in ECD.

The overall performance of the ECD depends on the properties of the individual thin film layers. Thus, it is necessary to optimize each individual thin film layer for best possible performance of ECD. This thesis discusses certain physical vapor deposition (PVD) techniques used for the preparation of thin films. The EC properties strongly depend on the structural and compositional characteristics, which, in turn, depend directly on the deposition conditions. In addition, various thin film characterization techniques are briefly discussed. The following are some of the parameters required for quantifying the ECD: transmittance modulation, switching time, open-circuit memory effect, and cycle-life. Transmittance modulation is defined as the change in transmittance in colored and bleached states during the

device operation while, the switching time is the time required for the coloring ↔ bleaching process. Depending on the polarity of the applied voltage, the ECD can exist either in colored or bleached state, which will be retained by the ECD after removal of the voltage; this effect is called “open-circuit memory effect.” Lastly, the cycle-life parameter is the number of color-bleach cycles that can be performed by the ECD before any significant extent of degradation in optical modulation has occurred.

The ITO thin film is prepared using radio frequency (RF) magnetron sputtering on glass substrate at room temperature (RT) by varying the RF power and the working pressure. The ITO thin films deposited with 75 W RF power and 0.5 mTorr working pressure shows a high transparency of above average 80 % and the low sheet resistance of $4.7 \Omega/\square$.

Thin films of WO_3 are deposited by the thermal evaporation method. The insertion of the cations H^+ , Na^+ , K^+ on the EC properties of WO_3 thin films grown at different substrate temperatures are investigated. The EC measurements are done using two-electrode electrochemical-setup with WO_3 thin film deposited on the ITO coated glass substrate acting as the working electrode. A stainless steel plate is used as an auxiliary electrode and solutions of 0.1M H_2SO_4 , 0.1M Na_2SO_4 , and 0.1M KCl are used for inserting H^+ , Na^+ , and K^+ , respectively, as an electrolyte. The thin film deposited at RT and intercalated with H^+ ions are found to possess adequate transmittance modulation and switching time.

Solid electrolyte layer of ZrO_2 thin film is prepared by the e-beam evaporation method. The effect of substrate temperature on the optical and ion-conducting properties is investigated, which shows that the film shows high transmittance up to 80 % and the film deposited at RT shows higher ionic conductivity. Ion-storage (IS) layer of NiO thin films are prepared by the e-beam evaporation technique at different substrate temperatures. The EC properties of NiO thin films were investigated in an aqueous alkaline electrolyte (1M KOH) with the help of two-electrode electrochemical cell. The NiO thin film prepared at RT gives better transmittance modulation compared to film grown at higher substrate temperatures.

The solid-state thin film of multilayered structure ITO / NiO / ZrO_2 / WO_3 / ITO is grown one by one on a single glass substrate. The NiO and ZrO_2 thin film is deposited on the ITO coated glass substrate. For the operation of the ECD the H^+ ions are required, which are injected into the NiO film via ZrO_2 / NiO / ITO film structure is electrochemically cycled it

in 0.1 M KOH electrolyte. Subsequently, the remaining thin film layers of WO₃ and the top ITO is deposited on above structure. Suitable shadow mask is used in order to avoid short-circuiting in-between the layers. The performance of solid-state thin film ECD is studied by electrochemical measurements. When a positive potential is applied to the bottom ITO thin film electrode, H⁺ ions are intercalated electrochemically into the WO₃ film from NiO film via ZrO₂ electrolyte and the ECD change to colored state from transparent. When the polarity of the applied potential is reversed, the H⁺ ions are de-intercalated from the WO₃ thin film and the color changes to transparent reversibly. For the optimization of the ECD performance the thickness of the ZrO₂ electrolyte thin film was varied. A constant voltage (± 5 V) was applied for color and bleach state of the device, which showed the transmittance modulation of 56 % in visible-near infrared range. The device showed good open-circuit memory effect in which the states lasted for about 170 minutes. The switching time and cycle-life of the EC device are measured by applying a square-wave voltage to the device and the device shows the coloration and bleaching time of 120 s and 2 s, respectively, with a desirable cycle-life.

As a spin-off, we are also fabricating the WO₃ thin film based gas sensor for NH₃ gas-sensing applications operated at RT. Nowadays thin film based gas sensors are extensively used due to its high sensitivity towards the various hazardous or non-hazardous gases and its compactness. The basic mechanism of thin film based gas sensor is change in resistance by chemisorption and catalysis reaction at the film surface when it is exposed to gas. The WO₃ thin film also shows good sensing properties towards a number of gases viz. NH₃, LPG, NO₂, H₂, CO. Tin (Sn) modified WO₃ thin film gas sensor was prepared on Al interdigitated electrodes by thermal evaporation for detecting Ammonia (NH₃) gas. The resistance of the film was measured by the direct current two-point probe method. The important parameters of the gas sensor are the response and response time. The response can be calculated as R_a/R_g for reducing gases where R_a is the resistance of gas sensor in the air and R_g is the resistance in the gas atmosphere. The response time is defined as the time for the sensor's resistance to reach 90 % of its steady state value after exposure to or removal of the target gas. At RT, a good response of 19 towards NH₃ and a response time of the order of 1 s was obtained for the sensor having 125 Å Sn film thickness deposited on the 2000 Å WO₃ thin film sensor annealed at 300 °C temperature in air.

Chapter - 1

Introduction

1. INTRODUCTION

An electrochromic (EC) thin film device consists of a multilayered structure of several thin film layers of EC materials, which are capable of changing the optical properties of EC device (ECD) on application of a voltage and reverts to its original state when the polarity of the voltage is reversed. This property enables the ECD to be used for applications like smart-window, mirror, and display devices. This theses deals with the fabrication of EC thin film devices using all solid thin film layers. The present chapter gives an introduction and a brief history of electrochromism. The EC materials, ECD structures, and criteria for ECD are also described herein. Some of the applications related to ECD are also presented in this chapter. As a spin-off, EC materials, like WO_3 , also give good sensitivity towards the different gases, which is also discussed in the penultimate section of this chapter. The organization of the thesis is given in the last section of this chapter.

1.1 WHAT IS ELECTROCHROMISM?

The phenomenon of color change by chromic materials under particular environmental conditions is called chromism. Chromic materials change their optical properties such as optical transmission, absorption, reflectance, and/or emittance in response to change in their ambient conditions, in a persistent but reversible manner. Chromism is due to the change in electronic state of molecules. Hence, this phenomenon is induced by various external stimuli such as electric field, temperature, pressure, light, solvent, etc., which can alter the electron density of materials. Chromism is classified on the basis of the type of stimuli used. Electrochromism is defined as a reversible color change of a material caused by an application of an electric potential. The changes in the optical properties of Electrochromic (EC) materials are due to an oxidation-reduction (redox) process [1]. Thermochromism is the phenomenon in which the color change is caused by the absorption of heat leading to the thermally induced chemical reaction or phase transformation [2]. Photochromism is induced by light irradiation; the photochromic materials absorb electromagnetic energy and absorption band in the visible part of the spectrum changes [3]. Piezochromism is defined as the color change caused by mechanical pressure [4] and solvatochromism depends on the polarity of the solvent [5]. However, the most promising chromic effect is electrochromism induced by electric field. One of the prime advantages of electrochromism is that an electric

field is needed only during the color or bleach process which can be controlled at any intermediate stage. Moreover, a low-switching voltage (1 to 5 V) is required for electrochromic phenomenon, and varied range of colors viz., blue, grey, brown, etc. are its other advantages.

1.2 A BRIEF HISTORY OF ELECTROCHROMISM

The history of coloration goes back to 1704 when Diesbach discovered Prussian blue (hexacyanoferrate), which changes the color from transparent to blue under oxidation of iron [6]. However, in 1815 Berzelius reported that pure tungsten trioxide changed its color when it is heated in hydrogen (H_2) gas atmosphere [7]. Ion intercalation/de-intercalation is responsible for the change in coloration between deep blue to transparent states. electrochromic device (ECD) based on electrochemical reaction involving color formation was presented as a patent in London by F. H. Smith in 1929 [8]. In the 1930s, Kobosew and Nekrassow first noted electrochemical coloration in bulk tungsten oxide [9]. They found that tungsten oxide powder could be colored blue by electrochemical reduction in an acidic solution. In 1951, Brimm et al. observed reversible color change during electrochemical treatment of sodium tungsten bronze [10]. While working at Balzers in Lichtenstein, T. Kraus provided a detailed description of electrochemical coloration in thin film of tungsten trioxide (WO_3) on 30th July 1953 [11]. A theoretical explanation of the phenomenon of electrochromism was given by J. Platt in 1961. He explained that with the application of an external electric field the absorption and emission spectra of certain dyes may be shifted and the sharp change in color can be observed due to the Stark Effect in dyes [12].

In 1969, S. K. Deb demonstrated electrochromic coloration in WO_3 thin films. Deb observed electrochromic color by applying electric field of the order of 10^4 Vcm^{-1} across WO_3 thin film [13]. In fact, the real birth of the EC technology is usually attributed to S. K. Deb's seminal paper of 1973, wherein he described the coloration mechanism in WO_3 [14]. Since then WO_3 is one of the most studied EC materials. In the mid-1970s, electrochromic devices were being developed for small digital information displays. The area of electrochromics was started again in the mid-1980's for large area applications such as for automotive mirrors and windows for cars and buildings.

1.3 ELECTROCHROMIC MATERIALS

The phenomenon of electrochromism occurs in numerous inorganic and organic materials. These materials are currently of considerable interest for newer technological aspects and for the construction of ECD. Today, a large group of materials are available which show a reversible coloration change on application of an electric field. EC materials are grouped into two main categories: organic materials viz. viologen, pyrazoline, and some conductive organic polymers and inorganic materials viz. alkali halide and transition metal oxide [15,16]. The coloration in organic material(s) is observed due to an electro-redox reaction while in inorganic materials the coloration is due to a double injection of ions and electrons. Most of the organic EC materials suffer from two major problems: one, because of the use of aqueous solution, which introduces water electrolysis, and second, due to soluble colored products that causes color diffusion and, hence, gives rise to fuzziness of the image so we have concentrated on the inorganic materials, which show better stability and 'cyclability'. In inorganic EC materials, almost all of the materials are oxides of transition series that are in the form of thin films [1,17]. Electrochromic materials could be divided into two types: cathodic EC materials, which become colored under charge insertion (reduction process), and anodic EC materials, which are colored under charge extraction (oxidation process). Table 1.1 shows the periodic table of elements in which the cathodic and anodic coloring materials are highlighted differently. Cathodic coloration is found in WO_3 , TiO_2 , Nb_2O_5 , MoO_3 , and Ta_2O_5 , in which WO_3 is the most extensively studied one, which is transparent in oxidation state and deep blue in the reduction state [1]. Anodic coloration is found in NiO , IrO_2 , Cr_2O_5 , MnO_2 , FeO_2 , and CoO_2 with NiO and IrO_2 being the ones investigated widely [1]. V_2O_5 is found to exhibit both anodic and cathodic electrochromism depending on its oxidation state. In transition metal oxides only some of the oxides viz. WO_3 , TiO_2 , Nb_2O_5 , NiO , IrO_2 can be fully transparent to visible light while the other oxides show some absorption in the visible range of the spectrum. Table 1.2 gives an overview of the color change in the electrochromic materials with fully transparent or not in visible range. Apart from the materials discussed above many binary and tertiary mixed oxides [$\text{TiO}_2\text{-V}_2\text{O}_5$, $\text{WO}_3\text{-Li}_2\text{O-FeO}$, $\text{WO}_3\text{-MoO}_3$, $\text{WO}_3\text{-CeO}_2$] also show electrochromism [18,19].

Table 1.1: The periodic table of elements wherein cathodic and anodic electrochromic materials are highlighted [1].

Electrochromic Oxide																		
H																	He	
Li	Be			Cathodic coloration									B	C	N	O	F	Ne
Na	Mg			Anodic coloration									Al	Si	P	S	Cl	Ar
K	Ca	Sc	Ti	V	Cr	Mn	Fe	Co	Ni	Cu	Zn	Ga	Ge	As	Se	Br	Kr	
Rb	Sr	Y	Zr	Nb	Mo	Tc	Ru	Rh	Pd	Ag	Cd	In	Sn	Sb	Te	I	Xe	
Cs	Ba	La	Hf	Ta	W	Re	Os	Ir	Pt	Au	Hg	Tl	Pb	Bi	Po	At	Rn	
Fr	Ra	Ac	Rf	Db	Sg	Bh	Hs	Mt	Ds	Rg	Cp							

Table 1.2: Examples of some electrochromic materials with their color change properties [20].

	Material	Color change	Full transparent
Cathodic	WO ₃	Transparent ↔ Blue	Yes
	MoO ₃	Transparent ↔ Blue	Yes
	Nb ₂ O ₅	Transparent ↔ Pale blue	Yes
	TiO ₂	Transparent ↔ Pale blue	Yes
Anodic	NiO	Transparent ↔ Dark brown	No
	IrO ₂	Transparent ↔ Blue	Yes
	CoO ₂	Red ↔ Blue	No
	MnO ₂	Yellow ↔ Brown	No
	PB	Transparent ↔ Blue	Yes
Cathodic & Anodic	V ₂ O ₅	Pale blue ↔ Brown / Yellow	No

1.4 ELECTROCHROMIC DEVICE STRUCTURES

Electrochromic devices are one kind of electrochromic cells. The basic structure of ECD consists of two-EC layers separated by an electrolytic layer. The ECD works on an external voltage, for which the conducting electrodes are used on the either side of both EC layers. Electrochromic devices can be categorized in two types depending upon the kind of electrolyte used viz. laminated ECD are the one in which liquid gel is used while in solid electrolyte EC devices solid inorganic or organic material is used. The laminated ECD is

easy to construct but rarely used owing to their tendency to dissolve EC thin film layers and its leakage of liquid electrolytes [21]. Finally, as shown in Fig. 1.1 the basic structure of electrochromic device embodies five superimposed layers on one substrate or positioned between two substrates in a laminated configuration. Normally, the substrates are made of glass or flexible polyester foil.

The basic structure of solid-state thin film EC devices is: glass / transparent conducting oxide (TCO) layer / ion-storage layer (IS) / ion-conducting layer (electrolyte) / EC layer / TCO layer / glass.

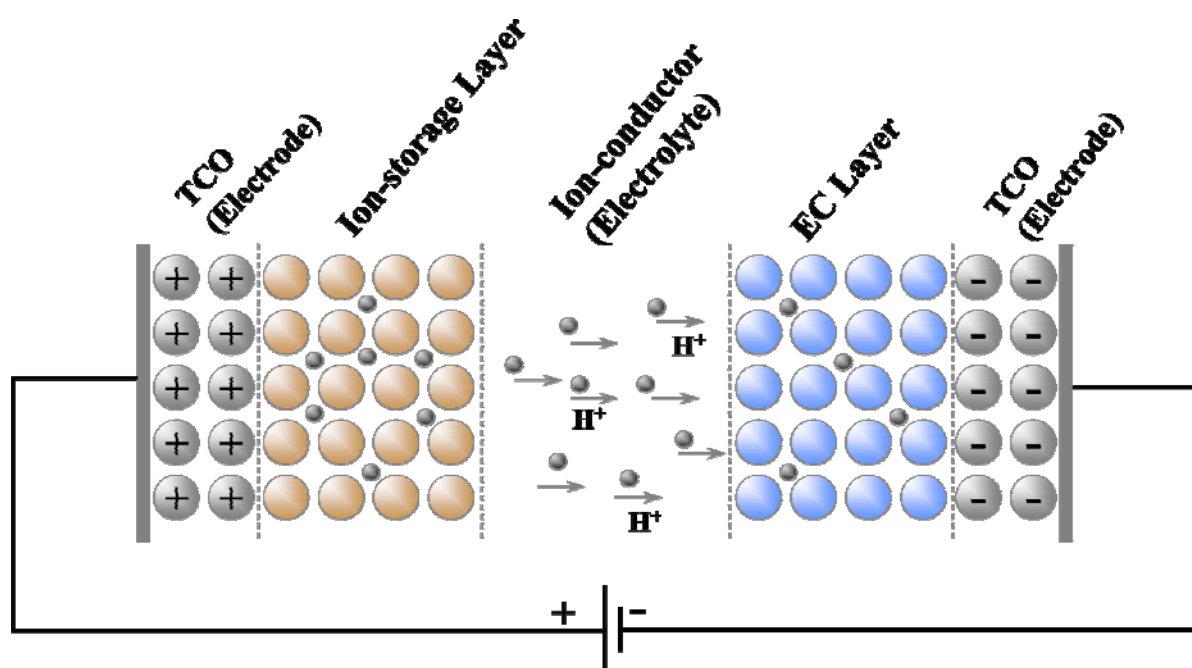


Figure 1.1: The bare bones of an electrochromic device.

Transparent Conducting Oxide (TCO) Layer: For the electrochromic devices to be used in a particular application, electrodes on both the sides need to be transparent in the visible region and should be electrically conducting. Prior to this requirement, the TCO such as Indium-doped tin oxide (ITO), Fluorine-doped tin dioxide (FTO), and/or Aluminum doped Zinc oxide (Al-ZnO) deposited on glass or flexible substrate are used [22,23]. The electrical conductivity of TCO is high but a surface resistivity of $10 \Omega/\square$ is needed with more than 75% transmission in visible region of spectrum. Among all above TCO materials, ITO is conductive and transparent for wavelengths near UV-Visible region and acts as a transparent conducting electrode in ECD [24].

Electrochromic (EC) Layer: It is the most active layer of ECD in which coloration occurs when any charge is inserted in it or extracted out of it. The electrochromic layer was deposited on the top of the transparent conductor. The crucial criteria for EC material's selection are: high-coloration efficiency, low-switching time, large number of coloration bleaching cycles, and good-memory effects under open circuit conditions. We have already discussed about the large range of EC materials and among these WO_3 (a cathodically coloring material) is most widely used because it satisfies all of the above criteria.

Ion-Conducting Layer (Electrolyte): An electrolyte is a substance containing free ions, which behaves as an electrically conductive medium. It should be a good conductor for small voltages, and a good insulator for open-circuit condition. It should have a high ionic conductivity ($10^{-3} < \sigma_i < 10^{-8}$ S/cm), low electron conductivity ($\sigma_e < 10^{-12}$ S/cm), and it must be optically transparent. The electrolyte gives electrical contact and pathway for the ions to be injected into or ejected from the EC layers. The ions should be 'small' enough so as to pass easily through the electrolyte. Generally, protons (H^+), lithium (Li^+), sodium (Na^+), and potassium (K^+) are used for this purpose. ZrO_2 acts as a solid electrolyte in the form of thin film.

Ion-Storage Layer: The ECD require a counter electrode or an ion-storage layer which can supply ions, but remain colorless or have a complementary color in the process. The ion-storage film is also electrochromic, but it is complementary to the electrochromic layer. Thus, when the primary electrochromic film becomes dark due to the ion-intercalation, the ion-storage film should darken upon de-intercalation of ions. NiO is a typical example of an ion-storage layer with WO_3 thin film as an electrochromic layer.

Typically, EC devices are of two types depending on the modes of electrochromic device operation viz. transmission mode and reflectance mode, as shown schematically in Fig. 1.2. In transmission mode, the conducting electrodes are transparent and they control the light intensity passing through them; this mode is used in smart-windows application. In reflectance mode, one of the transparent-conducting electrodes is replaced with a reflective surface like aluminum (Al), gold (Au), or silver (Ag), which controls the reflective light intensity; this mode is useful in rearview mirrors of cars and EC display devices.

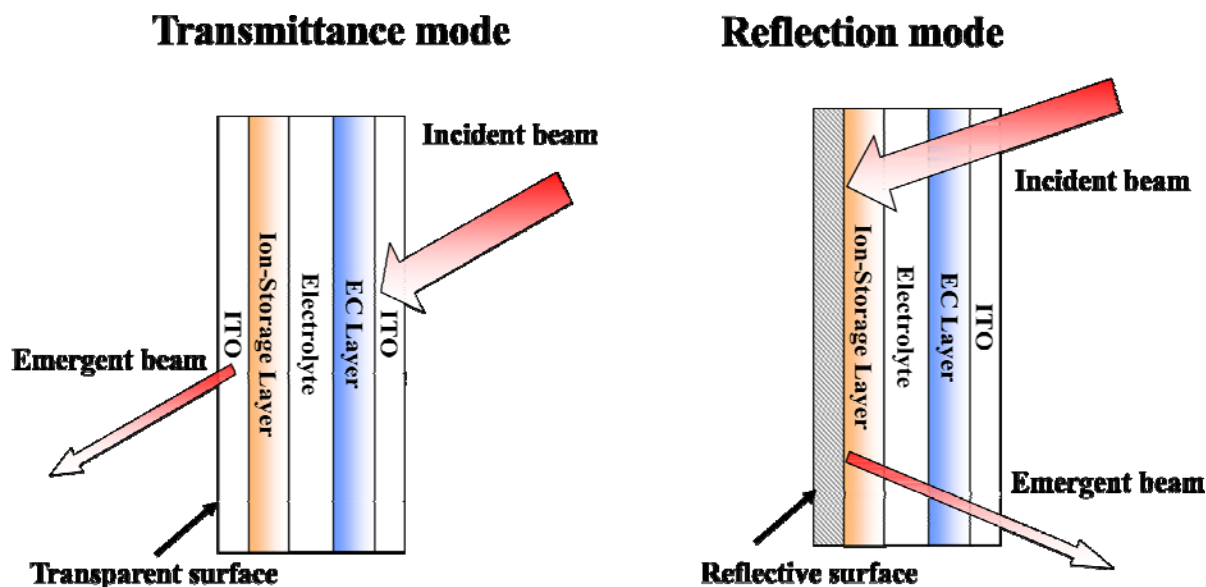


Figure 1.2: A schematic diagram of two basic modes of operation of electrochromic devices.

In both types of ECDs the working principles are same. As shown in Fig. 1.1, when a small dc voltage is applied across the TCO films, the external and internal movements of the ions in EC film via electrolyte is observed. Charge balances current flow from the external circuit, which results in the change of the optical properties. If the device is initially transparent (open-circuit situation) and if on sufficient application of a voltage the transparency of the whole device changes to a darken-state then on reversing the polarity the device will return to its original transparent state. If the ion-conductor has negligible electronic conductivity, the device has open-circuit memory, that is, the device retains its properties until another voltage is applied.

In the proposed ECD all layers used are of thin film form in multilayered structure. We have selected thin film of ITO deposited on organically cleaned glass substrate as the TCO electrode. The anodically coloring, NiO, thin film acts as an ion-storage layer deposited on the ITO substrate. The ZrO_2 thin film acts as an ion conducting solid electrolyte and the cathodically coloring WO_3 thin film acts as an electrochromic layer. So finally, the electrochromic device structure is ITO / NiO / ZrO_2 / WO_3 / ITO on a single glass substrate. Figure 1.3 shows a schematic diagram of the proposed ECD in which shadow mask is used for different layer deposition on the glass substrate to avoid short circuit between the two-electrochromic electrodes. The whole system should be electrochemically compatible is an important criterion for the material's selection. In addition, the different layers should be adherent, and good contact between the different interfaces should exist.

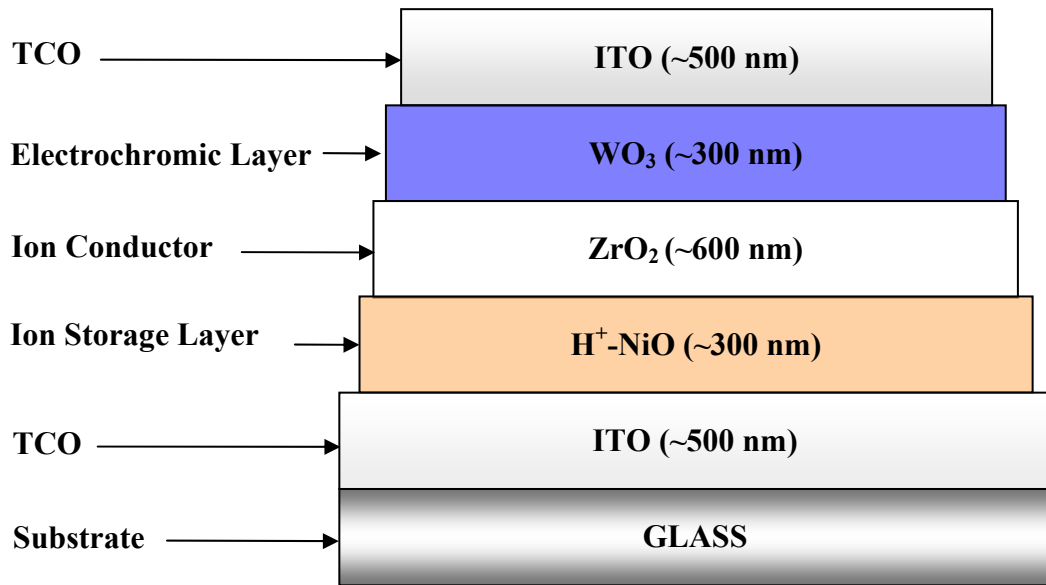


Figure 1.3: Proposed solid-state electrochromic device structure.

1.5 CRITERIA FOR ELECTROCHROMIC DEVICES

The following are some of the parameters required for quantifying the ECD: high transmittance modulation, high-coloration efficiency, low-switching time, good-memory effect, and long cyclic life. Here we have briefly defined and explained the ECD criteria.

Transmittance Modulation (ΔT): Transmittance modulation is one of the most important electrochromic parameter for electrochromic device operations. It is defined as the transmittance change in colored and bleached state. Since the transmittance modulation depends on the wavelength, the change in the transmittance is measured by the optical transmittance spectra of the bleached (T_b) and the colored (T_c) state of the sample as a function of wavelength (λ):

$$\Delta T = T_b - T_c \quad (1.1)$$

Generally, ΔT , lying between 70 – 80 %, is particularly used for device applications.

Coloration Efficiency (CE): Another key parameter for the electrochromic devices application is the coloration efficiency (CE) also known as electrochromic efficiency. The CE is described as how large is the magnitude of optical modulation formed by per injected/extracted charge i.e., the change in the optical density (ΔOD) per unit of injected/extracted charge density (Q) per unit electrode area:

$$CE(\lambda) = \frac{\Delta OD(\lambda)}{Q} \quad (1.2)$$

The ΔOD depends on the light absorption ability of electrochromic materials. The change in the optical density is measured from the optical transmittance spectra of the bleached (T_b) and the colored (T_c) state of the sample:

$$\Delta OD(\lambda) = \log \frac{T_b}{T_c} \quad (1.3)$$

The charge density i.e. the charge injected per unit electrode area of the film is obtained from integration of the corresponding current for total time:

$$Q = \frac{I \times t}{A} \quad (1.4)$$

where, I is the current (A), t is the total time (s) for which the current is passed and A is the area of the electrode (cm^2). CE is positive if coloration is generated cathodically and negative if coloration is generated anodically.

Switching Time: Switching time (t) is the time required for the coloring \leftrightarrow bleaching process of an ECD. Coloration time (t_c) is defined as the time required to switch from the bleached state to the colored state (90 % to 10 %) and the bleaching time (t_b) is the time taken to switch from the colored state to the bleached state (10 % to 90 %). Some applications do not require a rapid color change such as the electrochromic office windows, which requires a very slow response; however, applications such as display devices, require a more rapid response. The switching time is influenced by certain factors viz. ionic conductivity of the electrolyte, the applied electric field, device area, and film structure.

Memory Effect: Depending on the polarity of the applied voltage, the ECD can exist either in colored or bleached state, which will be retained by the ECD after removal of the voltage; this effect is called “open-circuit memory effect.” This is one of the excellent benefits of electrochromic devices. In open-circuit condition, when the inserted charge is self-removed from the electrochromic film, due to an electrical leakage current or ion diffusion it loses memory, this phenomenon is called self-bleaching. Therefore, the ion conductor plays crucial role for the optical memory effect. The electrochromic memory can be for several days or weeks even without any current. However, some EC devices may require small refreshing charges to maintain the charged state because, side reactions or short circuits may change the desired color.

Cycle-Life: It represents the number of color-bleach cycles that can be performed by the ECD before any significant extent of degradation has occurred. The cycle-life is therefore a measure of the electrochromic durability testing. The maximizing of the cycle life is an obvious aim of device fabrication and a minimum 10,000 cycles are acceptable. ECD are generally used in window and display applications, deterioration is best gauged by eye vision, and the same illumination that would be employed for normal device operation. However, 50 % degradation is often tolerable for display application.

The three common reasons for the low cycle life or device failures are: The TCO layer failure, electrolyte failure, or one or both of electrochromic layers failure. Most common cause of TCO degradation is decomposition of TCO, which increases the resistance and decreases the transparency [25]. The reason for electrolyte failure is due to solar irradiation and generation of hydrogen gas, when electrolytes use proton for conduction. In electrochromic layers failure, the layers gets dissolved when they come in contact with electrolyte and, in other cases, layer changes volume during redox process [26].

1.6 APPLICATIONS OF ELECTROCHROMIC DEVICES

Electrochromism has remained an active area for basic [27] and applied research with large possibilities for applications in emerging technologies since many years. Some of the applications are already developed at the technological level and are commercialized successfully whereas some are still in the developmental stage. Few of them are already available in market such as electrochromic windows, which are used in office windows, architectural and automobiles, rear-view mirror for car and vehicles, and large area EC display devices. Some other application's viz. eyewear, visors of helmets, electrochromic paper will be available in near future. However, due to lack of manufacturing techniques and durability of the available devices the ECD are not so common in markets.

Electrochromic Window: One of the most important applications of ECD, which are available in market, is the EC window. The electrochromic windows, also known as smart windows, are new technological arrangement for achieve energy efficiency in buildings, with variable transmittance of light and solar energy [28]. The “smart windows” can automatically control the amount of light and solar energy passing through the windows and provides indoor comfort [29]. It is also used in architectural glazing or skylights to control the solar heat entrance and to save energy for air-conditioning in summer and heating in

winter [30,31]. Furthermore, it is also used in automobiles, airplane, and trains in order to avoid dazzling. Such a device needs a high transmittance modulation and lifetime of at least 20 years with switching time of few seconds to few minutes.

Electrochromic Mirror: The electrochromic mirrors are (operated in a reflectance mode) one of the important applications of ECD. Reflecting intensity is reduced as an optically absorbing color is induced over the reflecting surface [32]. Here total opacity is to be avoided, to persist a slow reflection in the darkened state. The self-darkening EC rear-view mirror generally available for cars and other vehicles is one of its important applications. During daytime, the rear view mirror is adjusted in such a way that the electrochromic component is in the bleached state resulting in a reflection from the back-reflecting part of the mirror. At night, the mirror is adjusted in such a way that the headlights behind the car only hit a photosensitive sensor on the front glass surface of the mirror. Therefore, it resists the light from following vehicles and thereby improves driver's comfort. The device need to be able to switch at least 10^4 - 10^5 cycles without visible degradation, with a switching time of less than 5 s.

Electrochromic Display Devices: Researchers have been working on information displays since the discovery of electrochromic device [33]. The electrochromic display can act in either reflectance or transmissive modes; the majority of devices work in the reflectance mode. The EC display can be easily viewed from any angle so it is particularly useful where people are walking (on railway station, airport, traffic direction boards, etc). People have also put efforts to use it in television and digital watch display. Switching time and high color reproducibility over a large number of switching cycles are the major shortcomings in using such devices.

However, there are various other display applications where ECD can be used viz. electrochromic paper [34], electrochromic goggles [35], motorcycle helmet-visors [36]. Electrochromic paper, which on touching it with a stylus electrode can create an image, has been prepared by incorporating ECs in paper [37]. Furthermore, visors of helmets and goggles can be colored to a chosen degree at day times and bleached during the night or when entering tunnels.

1.7 GAS SENSOR

There are several types of solid-state gas sensors, which can be used for detection of various gases [38]. However, at present we will focus only on the transition metal oxide base conductometric WO_3 thin film gas sensors. Generally, the conductance or the resistance of the sensor is measured as a function of concentration of the target gases. In 1962, T. Seiyama et al. [39] first reported ZnO thin film layer for detecting inflammable gases. As soon as the target gas reacts with the surface of the metal oxide thin film, it causes change in the concentration of charge carriers, which results in the change of material conductivity. Since in an n-type semiconductor, the majority charge carriers are electrons an increase in conductivity is observed when it interacts with a reducing gas. Moreover, an oxidising gas interaction reduces the number of charge carrying electrons thereby resulting in a decrease in conductivity. In a p-type semiconductor positive holes are the majority charge carriers and the opposite effect is observed. In the presence of oxidising gas, an increase in conductivity is observed and the conductivity decreases in a reducing gas [38]. A gas sensor element normally contains a sensitive layer deposited over a substrate with electrodes for the measurement of the electrical characteristics.

Metal oxide semiconductor (MOS) gas sensor is quite sensitive, chemically selective, reversible, durable, small, easy to fabricate and eco-friendly. Apart from these, one of the important parameters of the gas sensor is its response. Usually, the response can be defined as R_a/R_g for oxidizing gases or R_g/R_a for oxidizing gases, in n-type semiconductor and R_a/R_g for oxidizing gases or R_g/R_a for oxidizing gases, in p-type semiconductor, where R_a is the resistance of gas sensors in the air and R_g is the resistance in the gas atmosphere. WO_3 is an n-type semiconductor, which has been extensively used for detection of various gases [40]. In order to improve the performance of a device, it should be doped with the metal or metal oxide [41,42]. The doping of such a metal will increases the response, selectivity towards the particular gas and reduces the operating temperature.

1.8 AIM OF THIS WORK

The aim of this work is to fabricate ECD of multilayered solid thin film structure grown one by one on a glass substrate. The proposed solid-state electrochromic device structure is already shown in Fig. 1.3. The overall performance of the ECD depends on the properties of the individual thin film layers. Thus, our primary aim is to optimize each individual thin film

layer of material as it plays an important role in ECD and make an attempt to fabricate the EC devices using PVD techniques. The performance of solid-state thin film ECD is studied by electrochemical measurement. The transmittance modulation, coloration efficacy, switching time, and memory effect of the EC device are measured. For the optimization of the EC device performance, the growth conditions of the individual thin film layers are varied. In addition to this, in this work the WO_3 based thin film gas sensor is also fabricated by thermal evaporation techniques and its sensing properties towards the NH_3 vapor was studied at room temperature. The effect of different Tin (Sn) doping concentration on the sensing properties of Sn- WO_3 thin film sensor is also investigated.

1.9 ORGANIZATION OF THE THESIS

CHAPTER 2: The experimental procedure of growing thin films and the techniques required for its characterization are discussed in this chapter. The physical vapor deposition (PVD) technique is used for the fabrication of thin films. Various thin film characterization techniques used for the study of the structural, compositional, electrical, and optical properties of the films are discussed. This chapter also includes the experimental facility indigenously developed and automated at our lab to study the electrochemical properties viz. transmittance modulation, coloration efficiency, switching time.

CHAPTER 3: This chapter deals with the transparent conducting oxide (TCO) thin films. The preparation and characterization of indium tin oxide (ITO) thin films by RF magnetron sputtering under different growth conditions are discussed. The effect of various growth conditions like the sputtering power and the working pressure, on the electrical and optical properties of the thin films is studied in present chapter. The lower resistive ($\sim 10^{-4} \Omega \text{ cm}$) and excellent transparency ($\sim 80 \%$) in the visible region of the light spectrum are optimized for its use as a transparent conducting electrode in an ECD.

CHAPTER 4: This chapter contains optimization of cathodically coloring WO_3 thin films as an active EC layer in ECD applications. The details of sample preparation using thermal evaporation and characterizations are discussed. The growth, structural, electrical, and optical properties of the WO_3 thin film is discussed. Furthermore, we have discussed the effect of different growth

conditions and insertion of different cations viz. H^+ , Na^+ , and K^+ on the EC properties of the WO_3 thin films.

CHAPTER 5: ZrO_2 thin films are grown by the e-beam evaporation technique on sapphire and glass substrates. The effect of substrate temperature on the structural and optical properties of ZrO_2 thin films is investigated. The ion-conducting property of ZrO_2 thin films, as a solid electrolyte, is also optimized.

CHAPTER 6: In this chapter, the optimization of anodically coloring NiO thin films as a counter electrode or an ion-storage layer is discussed. The preparation of NiO thin films using the e-beam evaporation techniques and various deposition conditions are also discussed. The characterization of NiO thin films related to its role as a counter electrode is also discussed over here.

CHAPTER 7: This chapter deals with the fabrication of the overall solid-state thin film ECD. The thickness of the ion conducting layers is varied to optimize for ECD performance. The devices' performance viz. transmittance modulation, open-circuit memory, switching time, and cycle-life are measured using electrochemical measurement.

CHAPTER 8: This chapter gives an introduction to thin film transition metal oxide based gas sensor and its sensing mechanism. The characterization setup for gas sensing and fabrication of sensing devices are also explained. Finally, we present the gas sensing properties viz. response and response time, towards the NH_3 gas.

Chapter - 2

Thin Films Preparation and Characterization Techniques

2. THIN FILM PREPARATION AND CHARACTERIZATION TECHNIQUES

In thin film based electrochromic devices the first step for device fabrication is the film preparation and characterization. This chapter discusses some of the thin film Physical Vapor Deposition (PVD) techniques like thermal evaporation, e-beam evaporation and RF magnetron sputtering, to be used for the fabrication of required quality thin film. Various thin film characterization techniques used as, X-ray diffraction for structural properties, atomic force microscopy for surface morphology, X-ray photoelectron spectroscopy for surface composition, and four-point probe and Hall-Effect measurement for electrical properties measurement are briefly discussed here. Transmittance measurement setup and electrochemical measurement setup were established in our laboratory for investigating various optical and electrochemical properties.

2.1 THIN FILM PREPARATION

Thin films, having high surface to volume ratio, are widely used due to very attractive optical, electrical, and electrochemical properties. There are various techniques to grow thin films viz. physical vapor deposition (PVD) [43], chemical vapor deposition (CVD), and electrochemical deposition methods. A thin film deposition process can be done in vacuum, plasma, gaseous, or electrolytic environment. In general, any film or device is grown on the substrate, which provides the mechanical support. Therefore, the cleaning of the surface of the substrate prior to deposition of thin films is a very crucial issue to ensure that the adhesion of the thin film on the substrate is adequate.

Substrate Cleaning: In general, glasses are used for the deposition of thin films. Prior to the deposition, the substrate must be cleansed from various contaminants. The substrates are ultrasonically cleaned using liquid detergent and by de-ionized water in ultrasonic bath for half an hour. Then the substrate is first degreased in warm trichloroethylene (TCE) and then treated with acetone. Methanol is then used to remove acetone and finally, de-ionized (DI) water is used to clean the substrates and, subsequently, they are dried in a nitrogen atmosphere. This cleaning process effectively removes the dust particles and grease (oil impurities) from the surface.

2.1.1 Physical Vapor Deposition (PVD)

In the Physical Vapor Deposition (PVD) technique, there are three main steps:

- (1) Emission of the appropriate atoms and molecules from the source material;
- (2) The atoms and molecules are transported to the substrate through the medium;
- (3) Condensation/Sticking of atoms and molecules on the substrate.

PVD, basically is a vacuum or low pressure gaseous environment deposition process in which the material to be coated is vaporized from a solid or liquid source in the form of atoms or molecules and the vapor phase is transported through a vacuum or low pressure gaseous environment to the substrate, where it condenses and forms a thin film. The deposition occurs in a vacuum of such a magnitude that the mean free path of the ambient gas molecules is greater than both the dimension of the deposition chamber and the distance from source to substrate.

When atoms or molecules land on the substrate surfaces, they can be physically adsorbed on the surface. Adatoms are initially not in thermal equilibrium with the substrate. Once if they have high mobility, they can move around on the substrate surface where as if the adatoms are not mobile enough they can stick where they land. The nucleation and the average nucleation size will depend on the temperature, the arrival rates of species, the energy of the impinging species, desorption, thermal diffusion, nature of substrate, etc. Depending on the deposition parameters, the nucleation and growth stages can be modeled as Volmer-Weber type (island growth), Frank Van Der Merwe type (layer-by-layer growth), or Stranski-Krastanov type (mixture of island and layer-by-layer growth) [44]. Figure 2.1 is a schematic representation of three basic modes of thin film growth.

In island growth, atoms are more strongly bound to each other than to the substrate and form three-dimensional islands. While in layer-by-layer growth atoms are more strongly bound to the substrate than to one another and the two-dimensional film forms by completed films prior to the growth of subsequent layers. In this case crystalline quality is 'good'. In the case of the mixed growth, initially layer-by-layer is formed and then three-dimensional island forms on it.

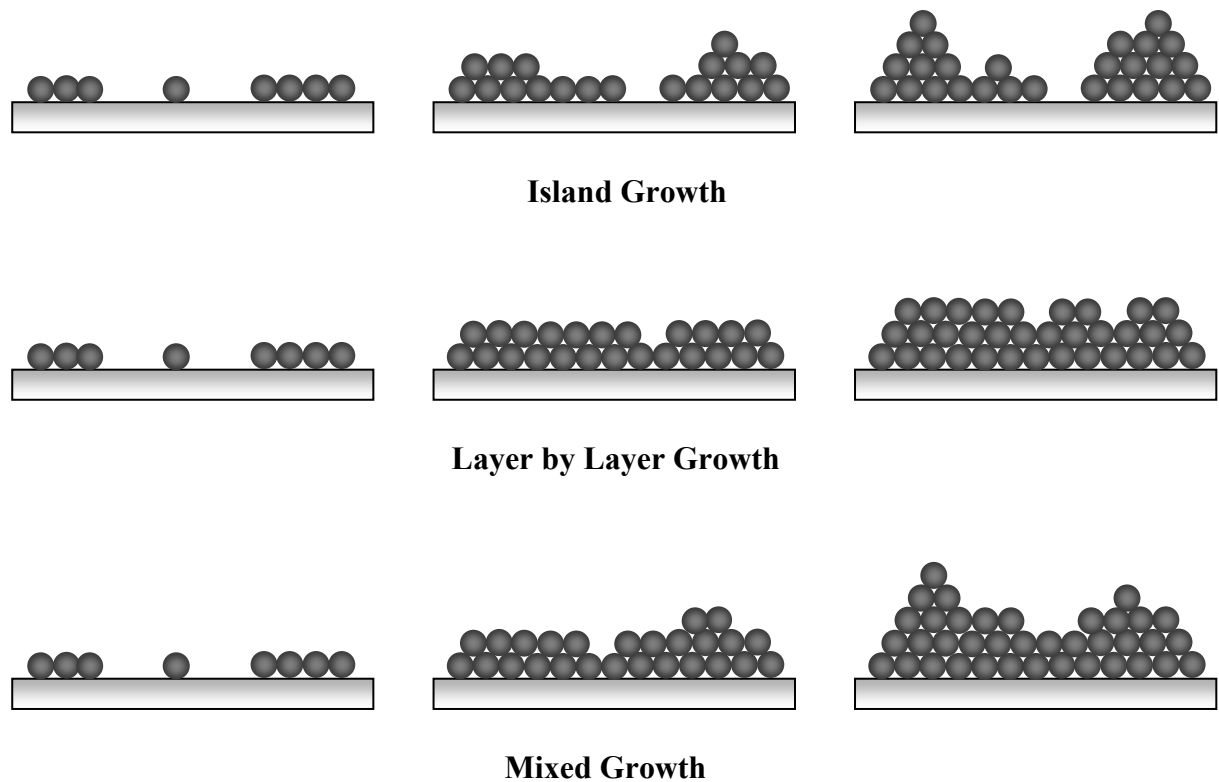


Figure 2.1 Schematic of the three basic modes of thin film growth including island, layer-by-layer, and mixed growth.

In PVD processes atoms or molecules from the original source can be ejected by thermal heating of the source or energetic particle bombardment by electrons, atoms, ions, molecules, or photons. PVD is a line-of-sight process in which atoms travel from a metallic source to the substrate on a straight path. Once the atoms or small atom clusters are removed from the original source material surface, they travel within an evacuated chamber until they impinge on a solid surface, and hence a probability for condensation arises. Depending on the method of applying heat to the source material, the PVD is classified into various techniques such as thermal evaporation, electron-beam (e-beam) evaporation, sputtering.

Thermal Evaporation Technique: Thermal evaporation is one of the well-known and simplest PVD techniques. In this technique, materials are evaporated by resistive type joule (I^2R) heating effect. The material that is to be evaporated is placed into a container, known as boat, which is thermally heated to vaporize. The simplest vapor sources are resistance-heated wire and metal foils of W, Mo, Ta, or Pt. Figure 2.2 shows a schematic representation of the thermal evaporation technique. The power supply is connected to the vapor sources using electrode and current flowing through the boat, which supplies the heat for vaporization.

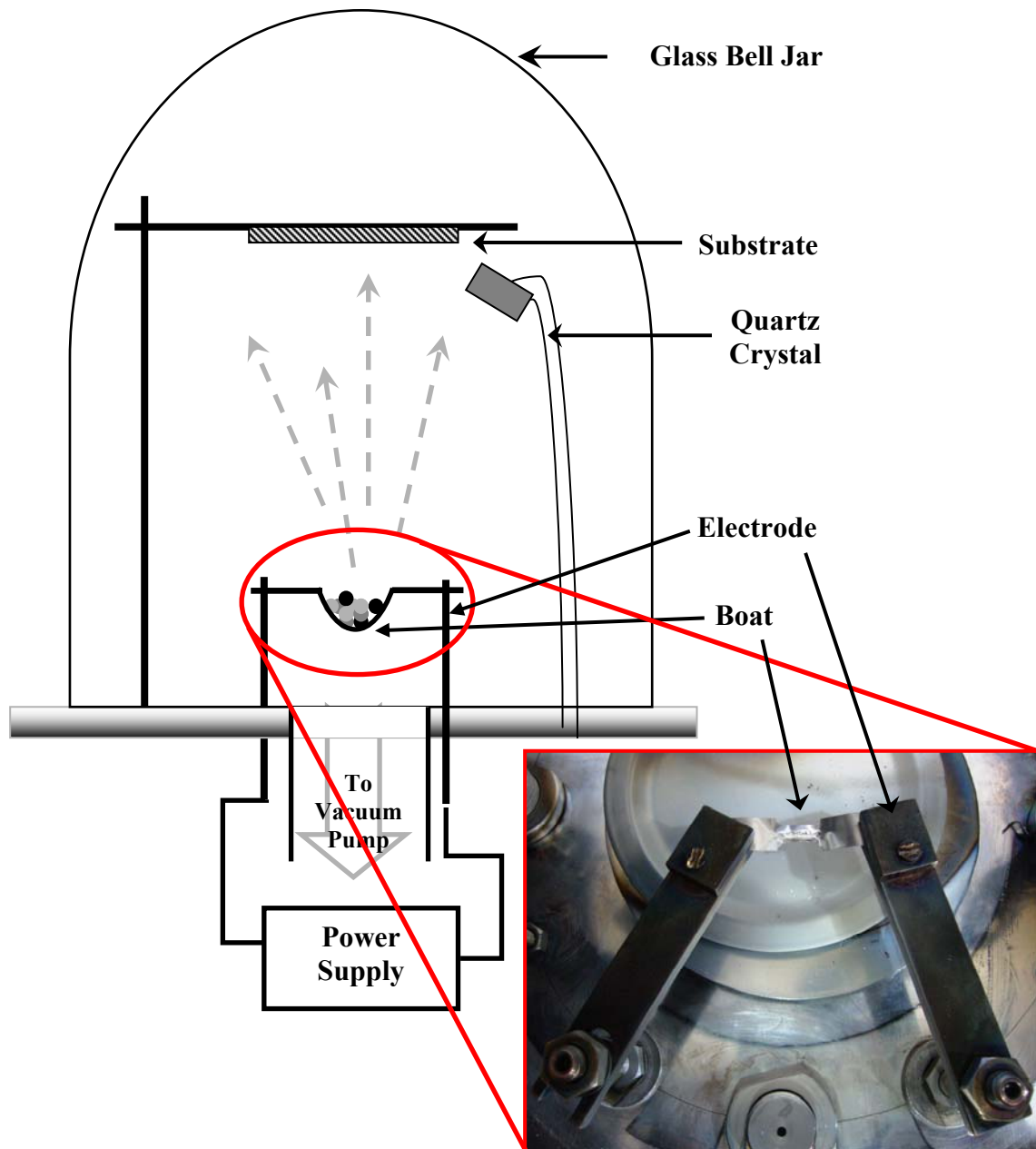


Figure 2.2: Schematic representation of thermal evaporation technique.

E-beam Evaporation Technique: The e-beam evaporation technique is similar to that of the thermal evaporation method but in this technique, the material is evaporated by high energetic e-beam. In this technique, the material to be evaporated is placed into a graphite crucible in an open metal cup, called hearth, which is water-cooled. The energetic e-beam, emitted by e-gun through thermoionic emission from a tungsten filament, is accelerated, directed, and focused, onto the source material by means of permanent and/or electro-magnet. The energetic e-beam imparts energy to the source material, melts it, and evaporates it. The advantage of the e-beam evaporation is that the temperature at the focused spot is as high as 3000 °C so, the high melting point materials can easily evaporate. Figure 2.3 shows a schematic representation of the e-beam evaporation technique.

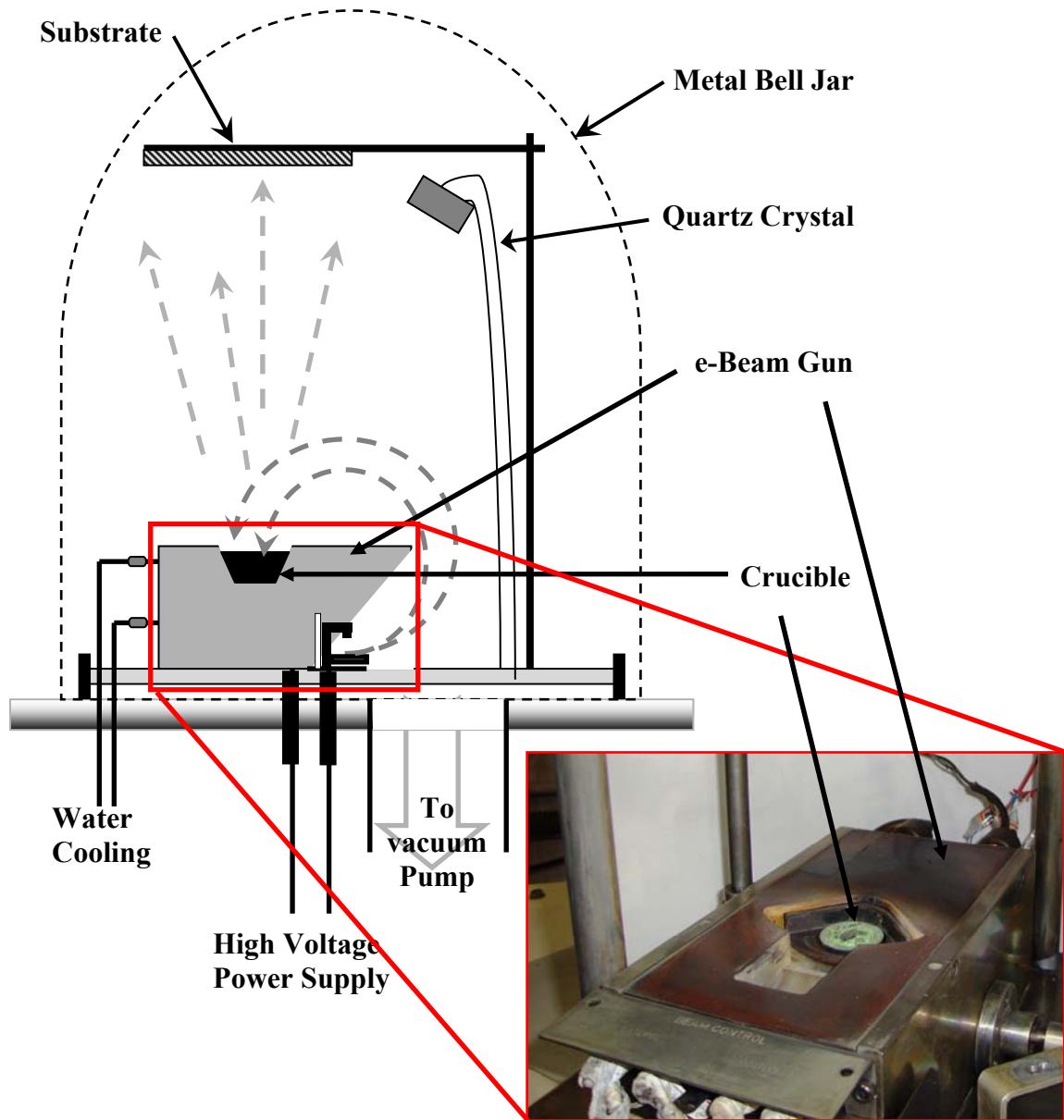


Figure 2.3: Schematic representation of e-beam deposition technique.

In thermal and e-beam deposition technique, the deposition occurs simply by placing a sample in the direct line-of-sight of the source. Generally, the substrates are mounted at an appreciable distance from the source to reduce radiant heating of the substrate by the vaporization source and to cover larger deposition area. The flux emitted from the source has cosine distribution. Most evaporative deposition systems require high vacuum to operate efficiently. Apart from the issue of impurity incorporation, it is necessary for the mean free path of evaporated-flux to be more than the distance of source to sample. The mean free path is related to the density and pressure of atoms and molecules in the gas phase. From the kinetic theory of gas, the mean free path ℓ , is calculated as:

$$\ell = \frac{k_B T_a}{\sqrt{2} Pr^2 \pi} \quad (2.1)$$

Here, k_B is Boltzmann constant, T_a is absolute temperature, r is molecular diameter, and P is pressure in Pascal.

Typically, vacuum deposition takes place in the vacuum range of 10^{-5} to 10^{-9} Torr depending upon the tolerance level of gaseous contamination in deposition system. In vacuum evaporation method, the rate of deposition is very high compare to the other PVD method.

RF Magnetron Sputtering: In sputter deposition, particles are vaporized by the physical interaction among gaseous ions accelerated to form plasma and hence impacts on the source material (target). There are a number of sputtering techniques that are currently used to deposit thin films viz. direct current (DC) sputtering and radio frequency (RF) sputtering with or without magnetron, ion beam sputtering and reactive sputtering. Among these techniques, RF magnetron sputtering is the most commonly used technique as materials having high melting point and electrically non-conductive ceramics can be evaporated easily. A schematic picture of the RF magnetron sputtering system is shown in Fig. 2.4.

In RF magnetron sputtering, the RF generator and impedance matching networks are used for supplying the power and a strong magnetic field is applied near target to confine the plasma which results in the increase of the rate of deposition. The sputtering is done in low vacuum or gaseous atmosphere such as argon (Ar). The gas plasma is created by RF power source, which ionizes the gas ions. These ions impacts on the target vaporize the atom of source materials and condense on the substrate. In sputtering process generally source-to-substrate distance is short compared to other vacuum deposition methods.

2.1.2 Experimental

PVD is a vacuum or low pressure gaseous environment deposition process so prior to the deposition certain level of vacuum is required. The high vacuum is created in coating chamber using an oil diffusion pump backed by a rotary pump in a vacuum coating unit in our lab (Hind High Vacuum Co. (P) Ltd.). For the e-beam evaporation, the 6 KW electron beam evaporator equipped with 270° bend e-beam gun facility is used. For the RF magnetron sputter deposition, the 2-inch magnetron (Angstrom science) is placed inside chamber and 600 W RF generator and impedance matching network (PFG 600 RF, Huttinger elektronik) are used for power supply. Figure 2.5 shows the actual picture of the vacuum coating unit with thermal evaporation, RF magnetron sputtering, and e-beam evaporation facility.

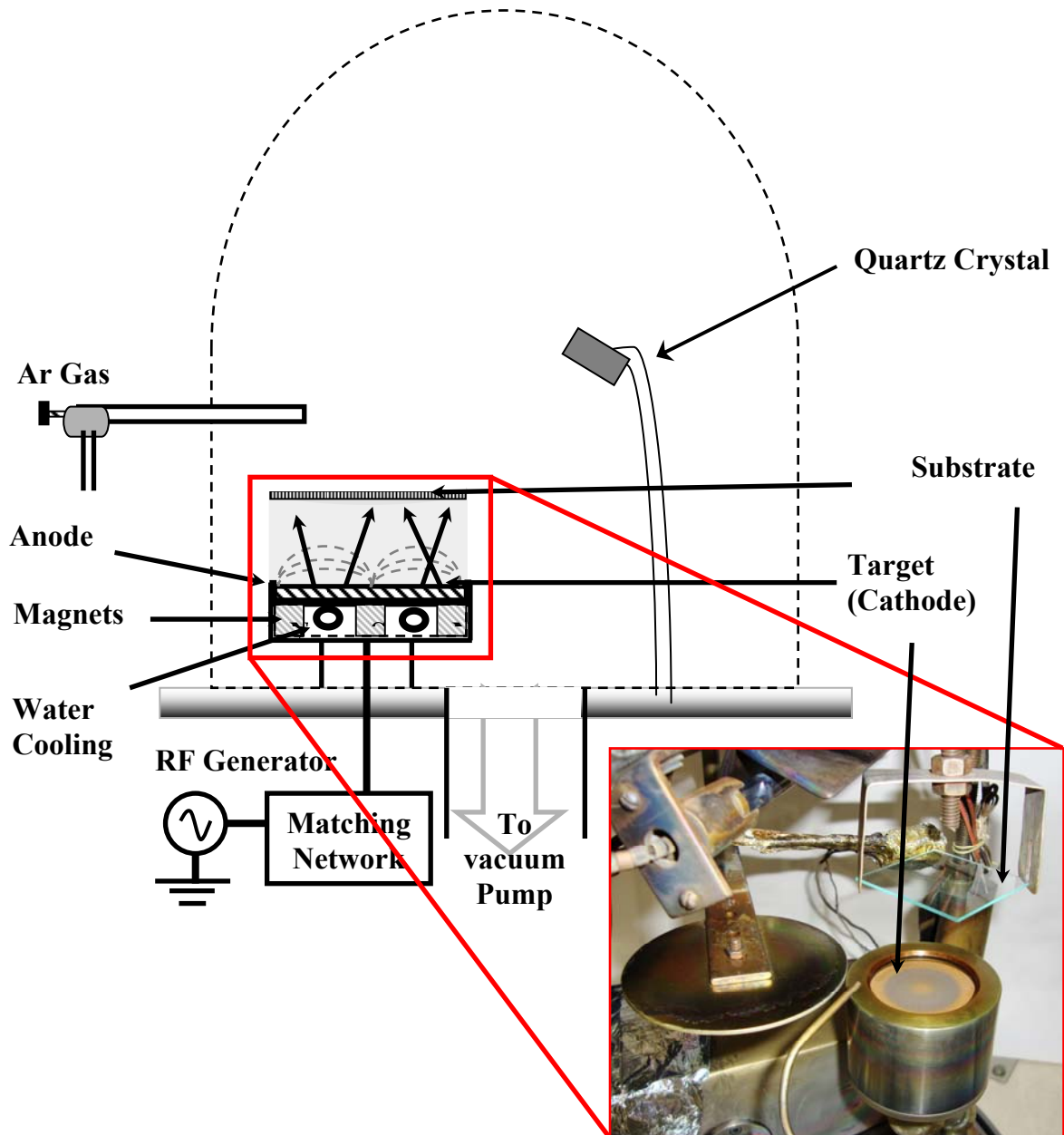


Figure 2.4: A schematic picture of the RF magnetron sputtering system.

The in-situ thickness measurement is carried out using piezoelectric quartz crystal placed inside the vacuum chamber. The oscillating frequency of the quartz crystal is varied from its original frequency (6 MHz) in order to deposit the coating materials on the crystal. The rate of change of the crystal frequency depends on the mass of the material deposited. Consequently, the thickness of the coating on the crystal can be calculated by measuring the fall of the crystal oscillation frequency, area of the crystal exposed to vapor and the density data of the material. The e-beam evaporation system is also interfaced with thin film deposition controller (SQC-122c SIGMA) to precisely monitor and control the thickness and deposition rate of the thin film.



Figure 2.5: Photograph of the High vacuum coating unit with Thermal evaporation, 2-inch diameter RF magnetron sputtering and 270 ° bend e-beam gun facility.

2.2 THIN FILM CHARACTERIZATIONS

Thin film characterization can determine many material parameters required for electrochromic device (ECD) point of view. There are wide varieties of characterization techniques available for thin films. The structural properties crystallinity and surface morphology are investigated using X-ray diffraction (XRD) analysis and atomic force microscopy (AFM) technique, respectively. The surface composition of the thin films was investigated using X-ray photoelectron spectroscopy (XPS) measurement. Impedance spectroscopy (IS) was used for the characterization of solid electrolyte. Optical properties are measured using the transmittance measurement setup. The electrical properties viz. resistivity and mobility are measured using four point probe and Hall-Effect measurements,

respectively. The electrochemical characterizations are done using electrochemical technique with the help of an electrochemical cell.

2.2.1 Structural and Compositional Characterizations

Structural and compositional characterizations of thin films by XRD, AFM, and XPS techniques are discussed below.

X-ray Diffraction (XRD): XRD is a versatile, non-destructive technique, which reveals detailed information about the crystallographic structure and chemical composition of materials and thin films. When X-rays interact with a crystalline substance's parallel and equally spaced atomic planes, one gets a diffraction pattern. The diffraction pattern is like a fingerprint of the substance, i.e. the same substance always gives the same pattern under identical conditions. So, it is used for the identification and determination of unknown substances present in materials by comparing diffraction data with standard JCPDS database maintained by international center for diffraction data (ICDD). The basic phenomenon involved is the diffraction of X-ray by an ordered crystal structure. The interaction of the incident rays with the sample produces constructive interference (and a diffracted ray) when the Bragg's condition is satisfied. $n\lambda = 2b \sin\theta$, where b is the spacing between diffracting planes, θ is the incident angle, n is any integer, and λ is the wavelength of the beam [45]. Symmetric representation of Bragg's constructive interference is shown in Fig. 2.6.

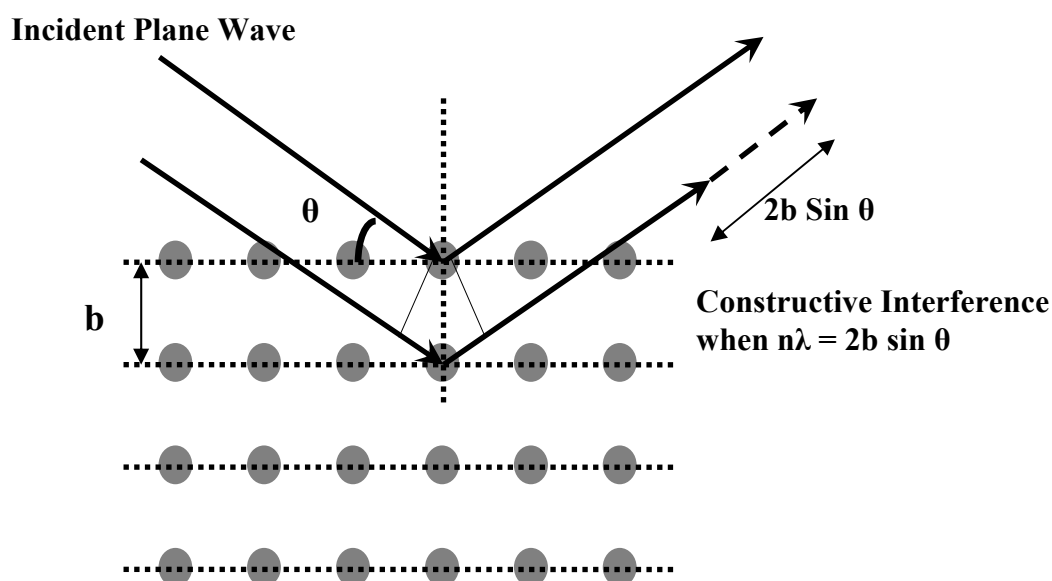


Figure 2.6: A schematic representation of Bragg's constructive interference.

The mechanical assembly consists of X-ray source ($\text{CuK}\alpha_1 - 1.5406 \text{ \AA}$) and detector. X-ray from the tube is incident on the sample, which may be placed at a desired angle θ with respect to the incident beam. The diffracted intensity of the X-rays from the sample is measured using detector positioned at a desired angle. The angle between the diffracted beam and transmitted beam is always 2θ , which is known as diffraction angle. In 2θ -geometry measurement the X-ray source is stationary, the sample moves by the angle θ and the detector simultaneously moves by the angle 2θ . In the ω scan (rocking curve scan) method, value of 2θ (i.e. position of detector) is kept fixed and ω is varied. Symmetric representation of 2θ geometry is shown in Fig. 2.7.

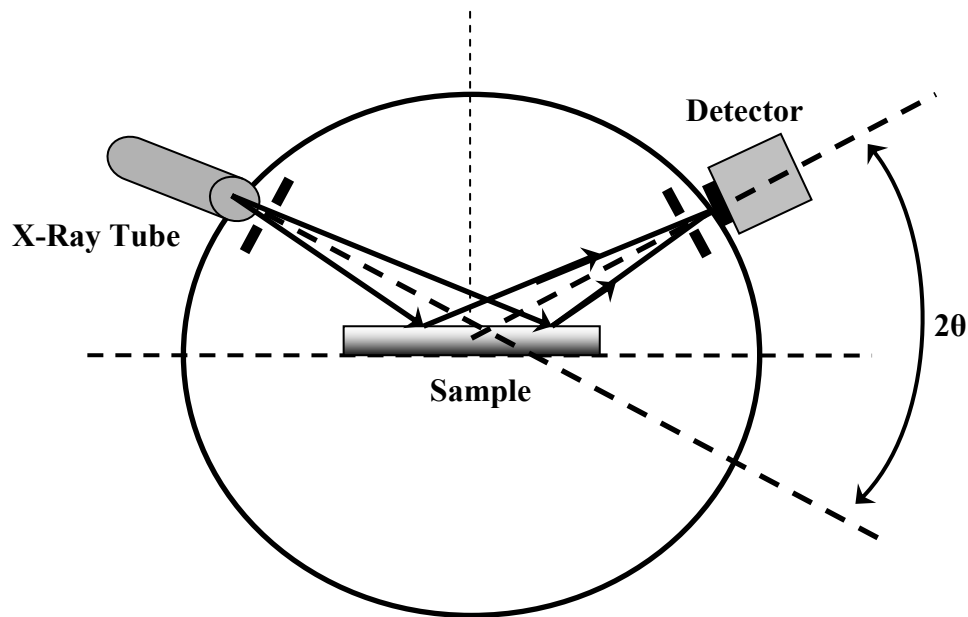


Figure 2.7: A schematic representation of 2θ geometry in XRD measurement.

From the XRD pattern, we can find the crystallographic structure, crystalline size and preferred orientation of plans. The crystallite size (L) was determined from the full width half maxima (FWHM) of specific XRD peaks using the Scherrer's equation [46],

$$L = \frac{k\lambda}{\text{FWHM} \cdot (\cos\theta)} \quad (2.2)$$

where, k is the shape factor (0.9), λ is the X-ray wavelength, and θ is the Bragg's angle.

Atomic Force Microscopy (AFM): AFM, a scanning probe microscopy, is a mechanical imaging instrument that measures the three dimensional (3D) topography as well as physical properties of a surface with a sharpened tip. The AFM consists of a cantilever with a sharp tip at end made-up from silicon (Si) or silicon nitride (Si_3N_4), with a typically tip radius of few tens of nanometers. The tip is positioned closed to the sample such that it can interact

with the Van der Waals forces associated with the surface and the tip. Then the probe is slowly scanned across the surface and the force due to deflection of the cantilever is measured according to Hooke's law. The deflection of the cantilever is measured using laser light reflected from the top surface of cantilever and is detected by the position-sensitive-detector which is shown in the Fig. 2.8. Monitoring the X-Y and/or Z position of the tip 2-D or 3-D image of the surface is constructed [47].

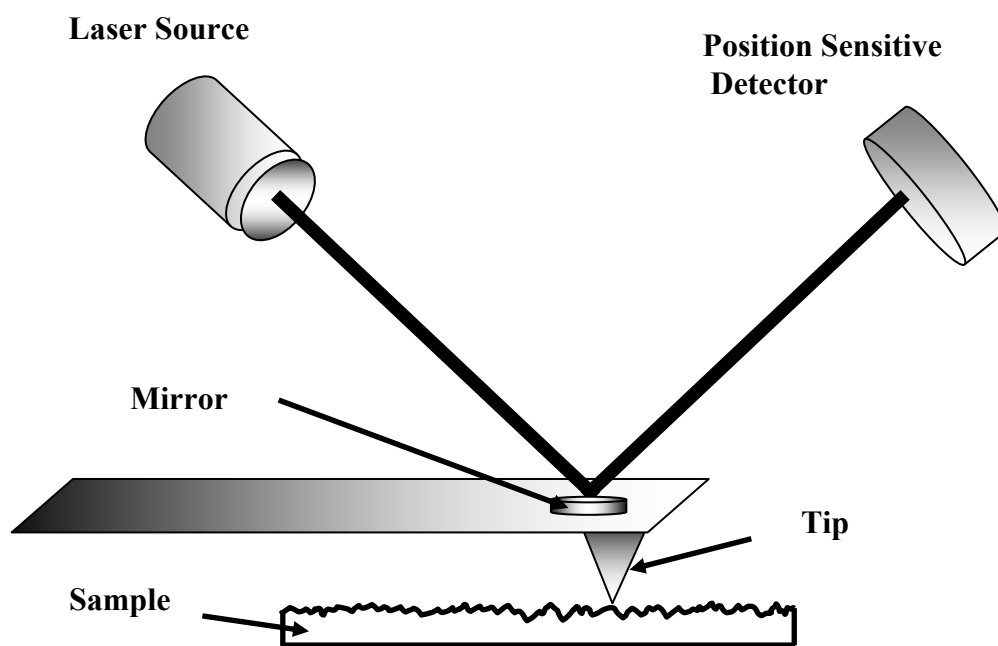


Figure 2.8: A schematic representation of AFM measurement.

The main advantage of the AFM is its capability of measuring images with nanometer resolution of conducting and non-conducting surfaces. With the image analyses, we can measure the surface roughness and the average grain size of film surface. Depending upon the application, in AFM the image can be obtained by three main modes viz., contact mode, tapping mode and non-contact mode.

X-ray Photoelectron Spectroscopy (XPS): XPS, also known as electron spectroscopy for chemical analysis (ESCA), is a spectroscopic technique to investigate the chemical composition of surface based on the photoelectric effect. It is used for the elemental identification (except H and He), chemical state information, and quantitative analysis on the sample surface with the sensitive to as low as 0.1 atomic percent. It is non-destructive method and it can be applied to all solid materials, including insulators such as polymers and glasses. The XPS spectra are obtained by the core level electron escape from a surface when the sample is illuminated with X-ray source generally Al-K α (1486.6 eV) [48]. The schematic representation of the XPS measurement system is shown in Fig. 2.9.

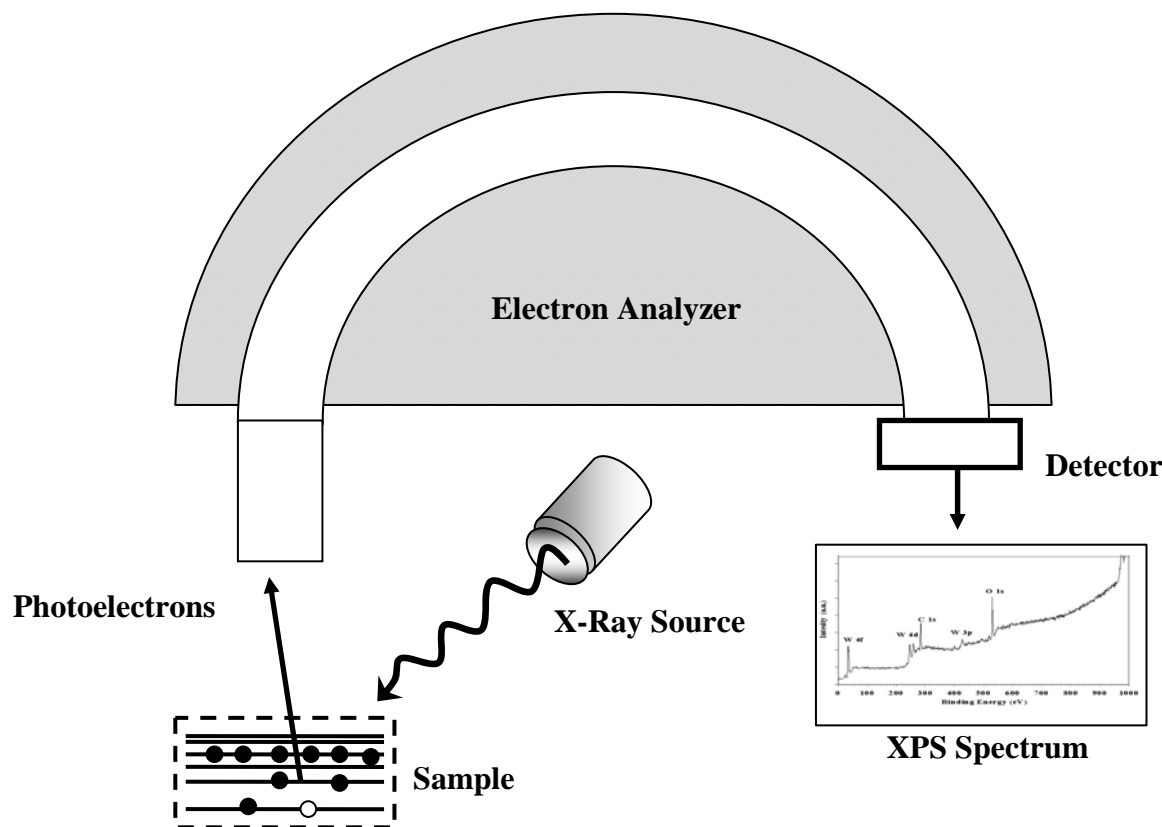


Figure 2.9: Schematic representation of the XPS measurement system

When the photons of energy ($h\nu$) are bombarded on the sample surface, and if it is large enough, than the core level electron escape from the atom and ejected out from the surface with kinetic energy (E_k) also referred as photoelectron. The binding energy (E_b) of core level electron is calculated by,

$$E_b = h\nu - E_k \quad (2.3)$$

where, h is Planck's constant and ν the X-ray frequency. Binding energy for the core level electron is a unique identity of each element so we can identify any element. For the quantitative analysis, XPS spectrum that is the kinetic energy distribution of ejected photoelectrons with the respective binding energies is recorded. All spectra were first analyzed using software, i.e. peak shifts due to any apparent charging effect were normalized with the help of C_{1s} peak set to 284.8 eV. The background from each spectrum was subtracted using a Shirley-type background to remove most of the extrinsic loss structure. To determine the stoichiometry of the compound the peak areas are converted to atomic concentrations with the use of elemental sensitivity factors. Furthermore, the binding energy of core electron is very sensitive to the chemical environment of element, so small shifts in the binding energy provide the information about the chemical state present on the surface.

2.2.2 Optical Characterization

To study the optical properties, viz. the transmittance (T) and optical energy band-gap (E_g), of thin films, the main characterization necessary is the transmittance measurement. Figure 2.10 shows the transmittance measurement setup established in our laboratory for measuring the wavelength range from visible-near infrared (400 - 1200 nm) region. Here, a Tungsten-Halogen lamp is used as a polychromatic light source. The light from the lamp is focused on the monochromator input slit using a convex lens. We have used 1/8m monochromator (CVI-CM110). The output beam from the monochromator is chopped using a mechanical chopper. This chopped beam is focused using a convex lens, and is then incident on the photo-detector, after passing through the sample. The detector measures the intensity of the beam with the help of a lock-in amplifier (SR-530) and the transmittivity of the sample is measured with reference to the direct beam intensity, without the sample. The monochromator and the lock-in amplifier have been interfaced with the computer using communication (COM) port and general-purpose interface bus (GPIB), respectively. The experiment is automated using the LabVIEW (Ver. 8.2) program.

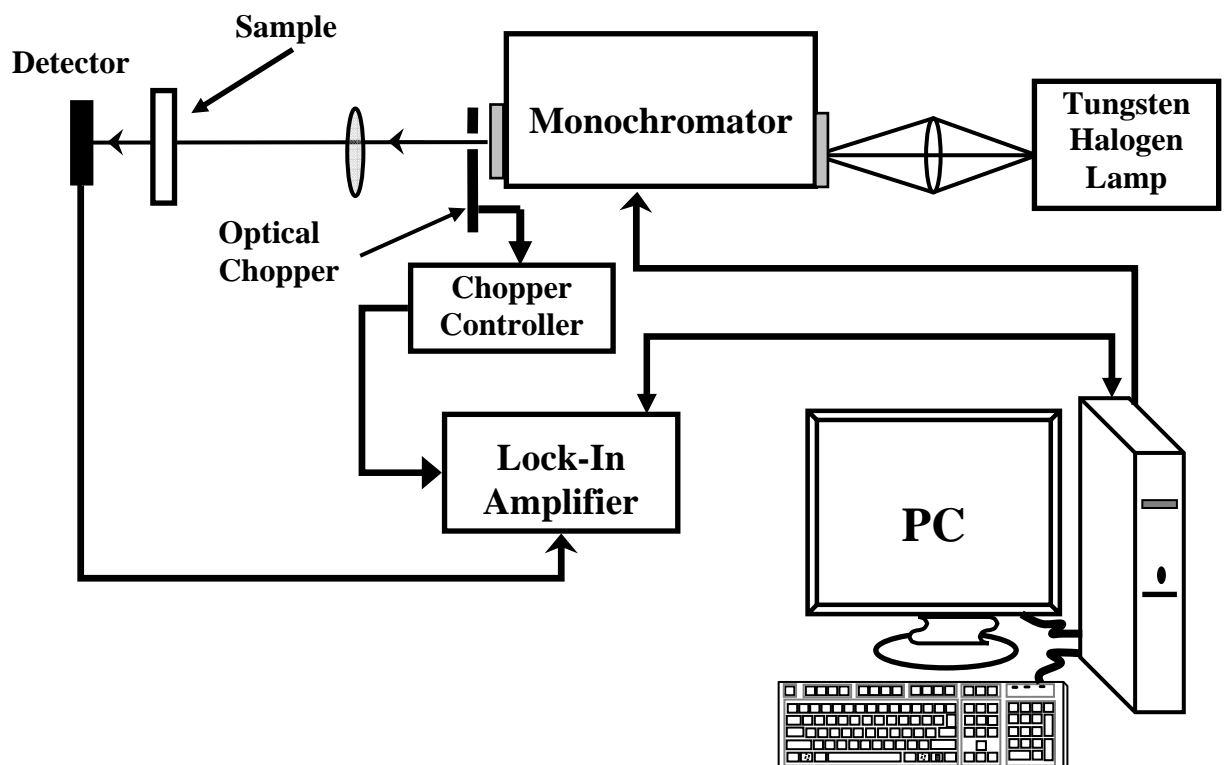


Figure 2.10: Block diagram of the experimental setup for transmission measurement.

For the energy band-gap calculation, the transmission spectra were measured using UV-Visible spectrometer (Thermo Scientific), in the wavelength range 200 – 900 nm. The optical band-gap is the minimum energy required to excite an electron from the valance band to the conduction band by an allowed optical transition. Quantitative values of E_g can be derived using the Tauc's relation [49] in the spectral range where the absorption is strong, which is given as

$$(\alpha hv) = B(hv - E_g)^\eta \quad (2.4)$$

where, B is a constant, hv is the incident photon energy, E_g is the optical energy band-gap, and α is the absorption coefficient, which is obtained near the absorption edge from the transmittance, using the equation

$$\alpha = -\frac{\ln(T)}{d} \quad (2.5)$$

where, d is the thickness of the film. The exponent η depends on the kind of optical transitions occurring in the material; when the transitions are direct allowed, direct forbidden, indirect-allowed, and indirect-forbidden, the values of η are 0.5, 1.5, 2, and 3, respectively. Thus, the optical energy band-gap of thin film is determined by plotting $(\alpha hv)^\eta$ versus the incident photon energy (hv) and linearly extrapolating to intercept the hv axis, which gives the value of energy band-gap.

2.2.3 Electrical Characterizations

In electrical properties of thin films viz. sheet resistance (R_s), resistivity (ρ), Hall mobility (μ), and carrier concentration (n) are measured using various electrical characterization method. The resistivity of the thin film is measured using four-point probe method while the other properties viz. hall mobility and carrier concentration are measured using the Hall-Effect measurement setup.

Four-point Probe Method: Four-point probe method is the standard method for the measurement of sheet resistance (R_s) of thin films and solid materials. The Four-Point Probe arrangement has four needle-like electrodes in a linear arrangement with a current (I) applied via the outer two electrodes and the resultant voltage (V) is measured via the two inner electrodes [50]. The schematic representation of the Four-Point Probe is shown in Fig. 2.11.

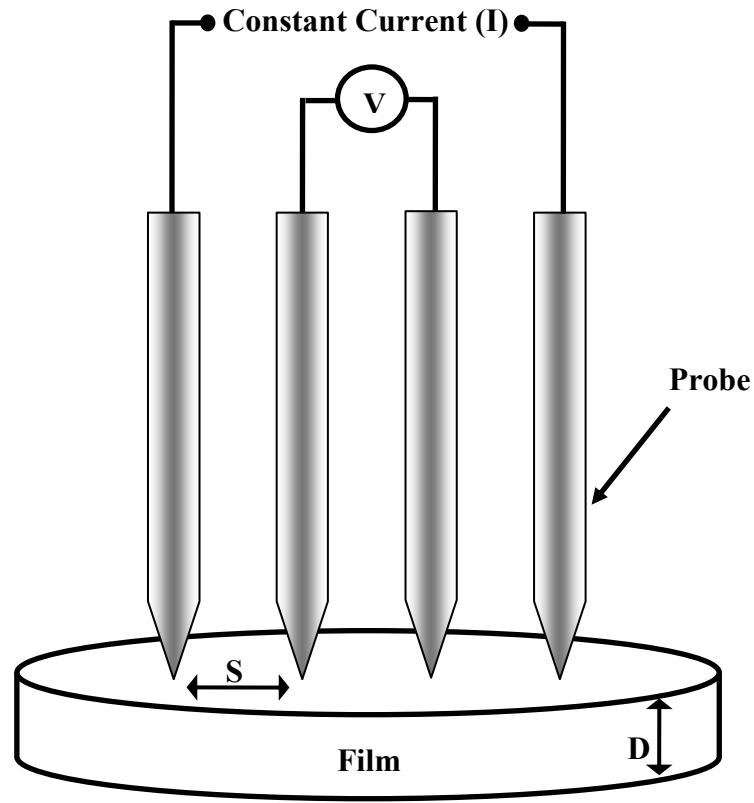


Figure 2.11: Schematic representation of the Four-Point Probe method.

In Four-point probe method, the separate current and voltage electrodes are used for eliminate the contact resistance between the electrodes and the material. In particular, in the case of thin films, the distance between the two probe(s) is very high compared to the film thickness (d), and hence the sheet resistance (Ω/\square) can be given as,

$$R_s = k \frac{V}{I} \quad (2.6)$$

where, k is a constant dependent on the configuration and spacing of the contacts. If the film is large in extent compared with the probe assembly and the probe spacing is large compared with the film thickness, $k = \pi/\ln 2 = 4.53$, then

$$R_s = (4.53) \frac{V}{I} \quad (2.7)$$

The sheet resistance of film is independent of the film dimensions. The resistivity ($\Omega \text{ cm}$) of thin film can be calculated by multiplying the sheet resistance with the film thickness (d);

$$\rho = R_s \times d \quad (2.8)$$

Hall-Effect Measurement: For the measurement of the hall mobility and the carrier concentration the Hall-Effect experiment is performed. In the Hall-Effect experiment the current carrying conductor is placed in a transverse magnetic field, Lorentz force on the

moving charges push them towards one side of the conductor producing a charge separation and, as a result, a small voltage is developed in the direction perpendicular of both, the field and the current [50]. The schematic representation of the Hall-Effect measurement is shown in the Fig. 2.12.

If the sample with resistivity (ρ), thickness (d), and the width (w) are placed in the magnetic field (B) then the Hall voltage (V_H) is developed perpendicular to both the magnetic field and the current, and the hall coefficient (R_H) can be calculated using

$$R_H = \left(\frac{V_H}{I} \right) \times \frac{d}{B} \quad (2.9)$$

The mobility (cm^2/Vs), a measure of how easily a carrier moves in a particular material, is given by

$$\mu = \frac{R_H}{\rho} \quad (2.10)$$

where, R_H is the hall coefficient. The carrier concentration (cm^{-3}) as a function of the mobility and resistivity can be derived using

$$n = \frac{1}{\mu \times \rho \times q} \quad (2.11)$$

where, q is the charge in coulomb.

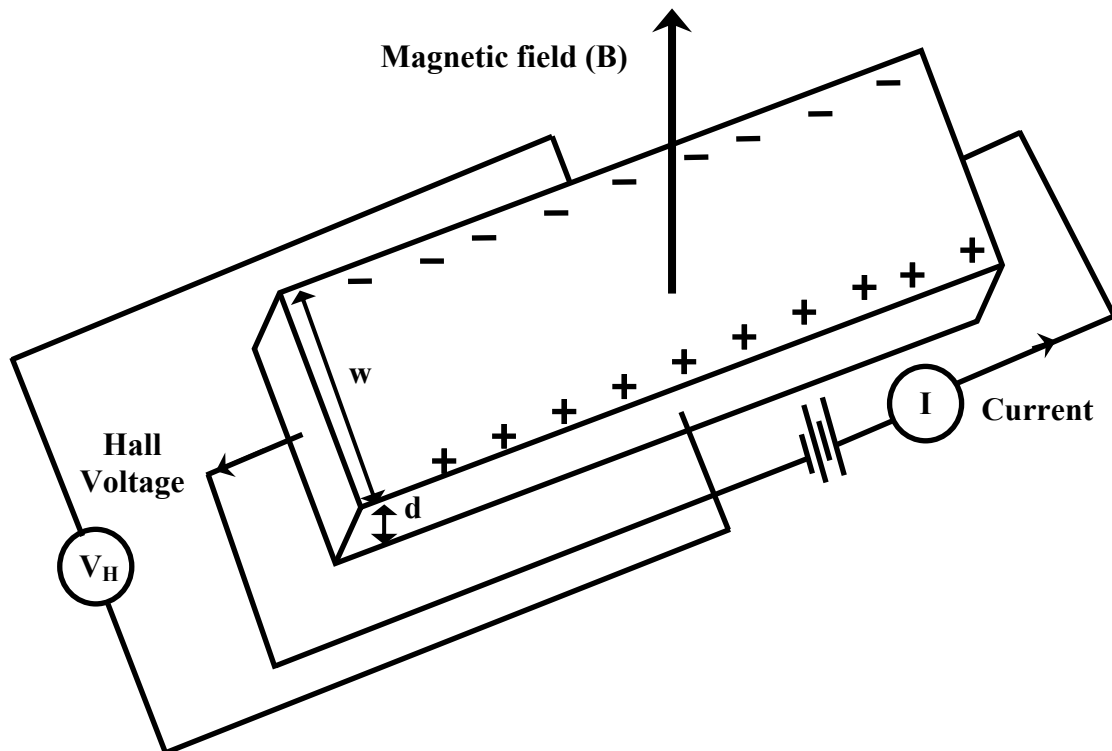


Figure 2.12: Schematic representation of the Hall-Effect measurement.

2.2.4 Impedance Spectroscopy

Impedance Spectroscopy (IS) is a very versatile electrochemical technique to characterize intrinsic electrical properties of any material and its interface. Electrical measurements are used to evaluate the electrochemical behavior of electrode and/or electrolyte materials. The measurement is usually carried out with electrochemical cell structure having two identical electrodes applied to the surfaces of a sample. In IS technique, an alternating current (AC) signal of low amplitude at varying frequency is applied to the solid electrolyte cell and comparison of the input and output signals is carried out to get information about phase shift and amplitude. The impedance (Z) of the structure is the ratio of the voltage to current as ohms law holds in the time domain.

$$V(t) = V_0 \exp(j\omega t) \quad (2.12)$$

$$I(t) = I_0 \exp(j\omega t) \quad (2.13)$$

The impedance is a complex quantity, having both magnitude $|Z|$ and phase angle (ϕ), which is expressed as,

$$Z(\omega) = |Z| \exp(-j\phi) \quad (2.14)$$

$$Z(\omega) = |Z| \cos\phi - j|Z| \sin\phi \quad (2.15)$$

$$Z^* = Z' + jZ'' \quad (2.16)$$

The resultant response of solid electrolyte can be displayed in the complex plane either in the more commonly used impedance formulation i.e. as the imaginary (Z'') vs. the real part (Z'), with frequency as a varying parameter. Equivalent, series, and parallel circuits of resistors and capacitors can be fitted to these kinds of plots. This plot contains a wealth of information regarding charge transport both at interfaces and inside the material [51]. The intersection of the semicircle with the real axis gives the best bulk resistance (R_b) of the material.

2.2.5 Electrochromic Characterizations

Electrochromic characterization were carried out using electrochemical method with the help of two-electrode electrochemical cell. The WO_3 and NiO thin films, deposited on ITO coated glass substrate, act as the working electrode, and a stainless steel (SS 304) plate is used as a counter electrode. The different electrolyte solutions are used for the intercalation of different ions viz. H_2SO_4 , Na_2SO_4 , KCl, for WO_3 and KOH for NiO. In electrochemical

measurement the chemical reactions, which take place in a solution at the interface of an electrode and an ionic-conductor (electrolyte), and which involve electron transfer between the electrode and the electrolyte, the chemical reaction is driven by either current or voltage between the working and counter electrode. The oxidation and reduction take place, which transfer electron and ions to or from atoms or molecules and change its oxidation state as measured by the current or voltage during an electrochemical reaction. The different electrochemical techniques are used to determine the different electrochromic parameters viz. the cyclic-voltammety (C-V) for the diffusion coefficient, constant current measurement for transmittance modulation (ΔT) and coloration efficiency (CE) and the chronoamperometry (CA) with concurrent change in transmittance for the switching time measurement. The block diagram of basic experimental setup for electrochemical measurement is shown in Fig. 2.13. The experimental setups have been interfaced with the computer using data acquisition (NI USB DAQ-6251) system. The dedicated virtual instrument made in LabVIEW (Ver. 8.2) computes and displays the results simultaneously with data acquisition and storage.

Cyclic-Voltammety Measurement: A cyclic-voltammety, an electrochemical method, shows the redox nature of the material that is used to determine the diffusion coefficients of mobile ions in the material.

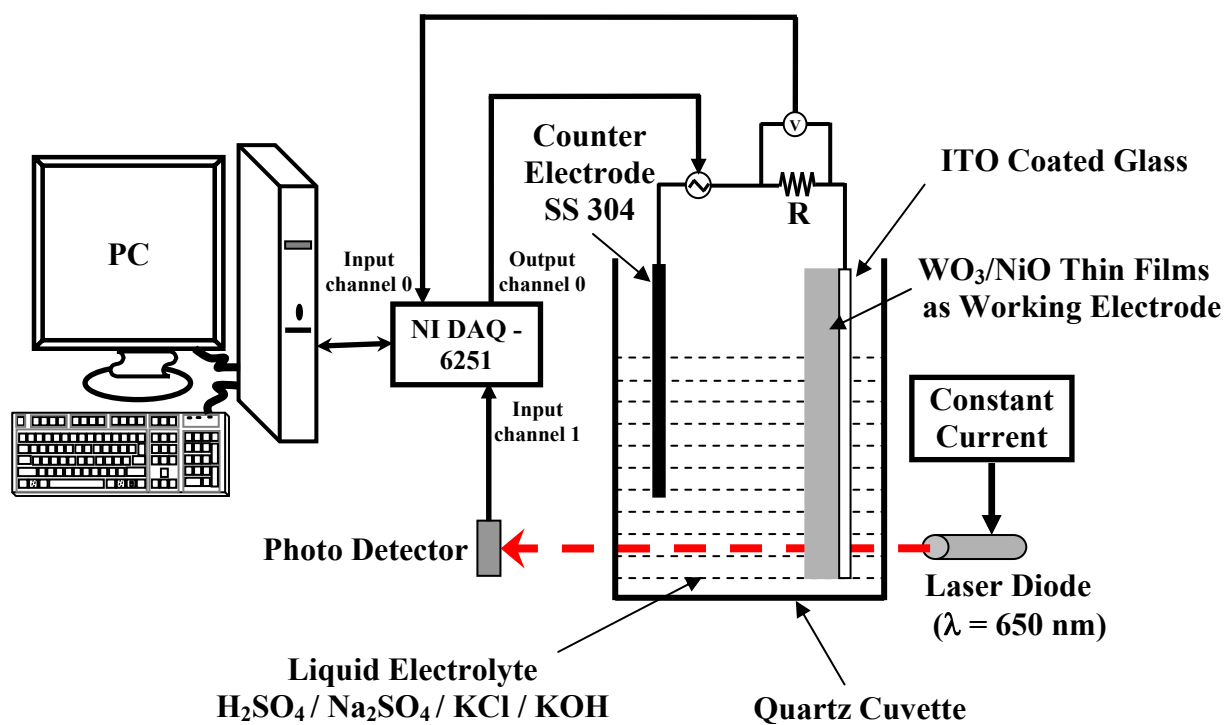


Figure 2.13: Block diagram of basic experimental setup for electrochemical measurement.

In C-V experiment, the potential across two electrodes varies linearly between two fixed values with time at a certain scan rate and the cyclic voltammogram i.e. the current versus voltage graph is plotted. Since redox reactions involve ion-intercalation and de-intercalation from the EC thin films, there is a drastic increase in the current and hence the current peak is obtained as soon as the applied voltage reaches to a certain level. During the negative potential cycle cathodic peak is observed and for the positive potential cycle an anodic peak is observed, which is further used to calculate the diffusion coefficient (D). Diffusion coefficient of the ion in the thin film is calculated using Randles–Servcik equation [52],

$$i_p = 2.72 \times 10^5 \times n^{\frac{3}{2}} \times D^{\frac{1}{2}} \times C_0 \times v^{\frac{1}{2}} \quad (2.17)$$

where, D is the diffusion coefficient in cm^2s^{-1} , C_0 is the concentration of active ions in the electrolyte solution in molcm^{-3} , v is the potential scan-rate mV/s , i_p is the peak current density in Acm^{-2} from cyclic voltammogram, and n is the number of electrons, which is assumed to be unity.

The LabVIEW virtual instrument (VI) is used to automate and control the C-V experiment. Figure 2.14 (a) shows the front panel controls and displays of the VI. The corresponding programming code, called block diagram, is shown in Fig. 2.14 (b).

Constant Current Measurement: Constant current measurement technique is particularly used for the comparative study of the transmittance modulation and CE. In all the cases, the same constant current density (i) is applied for a certain time interval (t) for coloring or bleaching the films, which ensures the same concentration of the intercalated and de-intercalated species in the films. The CE is calculated using the equation (Eq. 1.2) explained in chapter 1. The transmittance of the sample is measured in both bleached (T_b) and colored (T_c) states using the optical transmittance measurement setup in wavelength range from 400 - 1200 nm. The total inserted charge density (Q) can be calculated by multiplying the total time by the applied current density, $Q = i \times t$, where i is current density and t is time.

Chronoamperometry Measurement: Finally, the chronoamperometry (CA) is performed for intercalation/de-intercalation of ions in the films for switching time measurement. CA is an electrochemical technique, in which the square wave potential is applied to the working electrode, and the resulting current from faradic processes occurring at the electrode is monitored as a function of time and concurrently optical data is recorded between colored and bleached state. The optical measurement is carried out with the help of a laser diode ($\lambda = 650$ nm) and Si photo-detector. The constant current supply is used to drive the laser diode and the photo-detector is used in photo conducting mode. Figure 2.15 shows the photograph of CA measurement setup used for switching time.

Switching time is estimated from the current and optical transmittance data variation as explained in chapter 1. The entire experiment is interfaced and automated using Lab VIEW program. Figure 2.16 (a) and (b) shows the front panel (controls and displays) and block diagram (programming codes) of the virtual instrument (VI) of the CA setup.

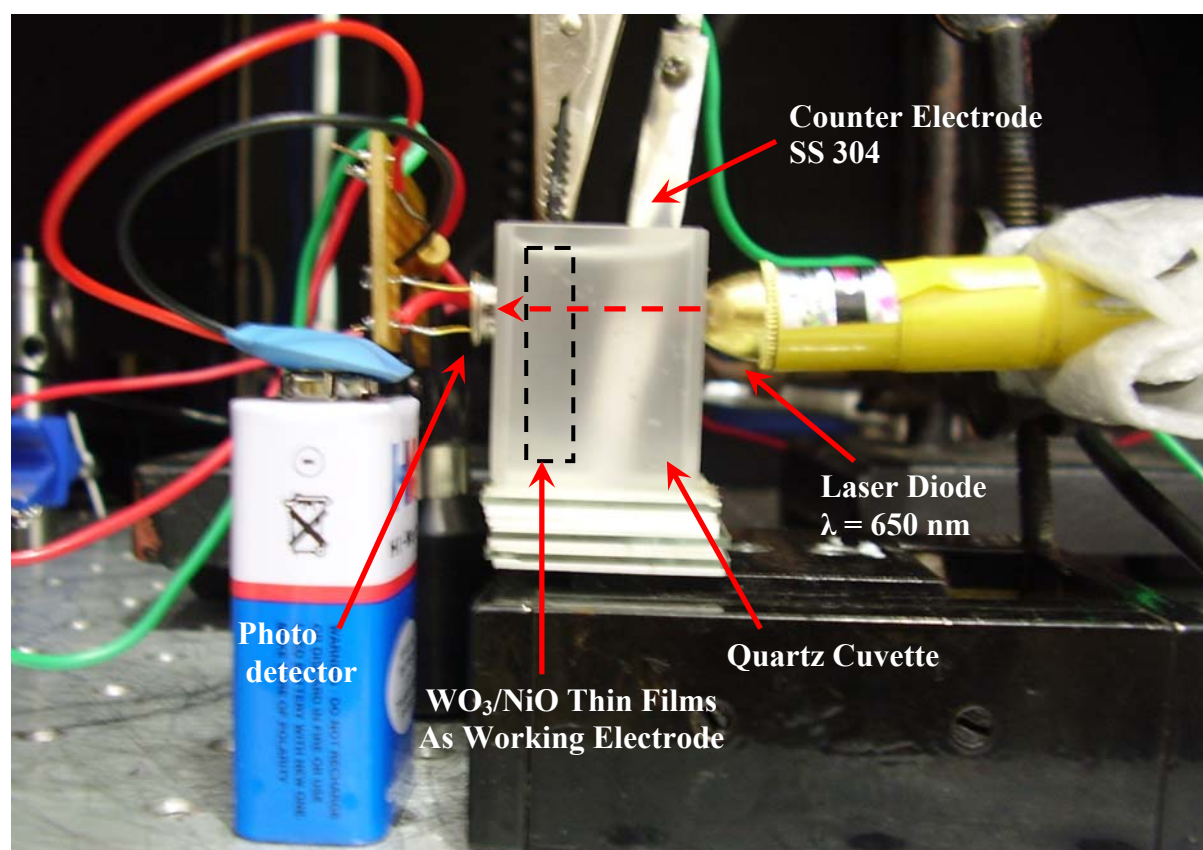
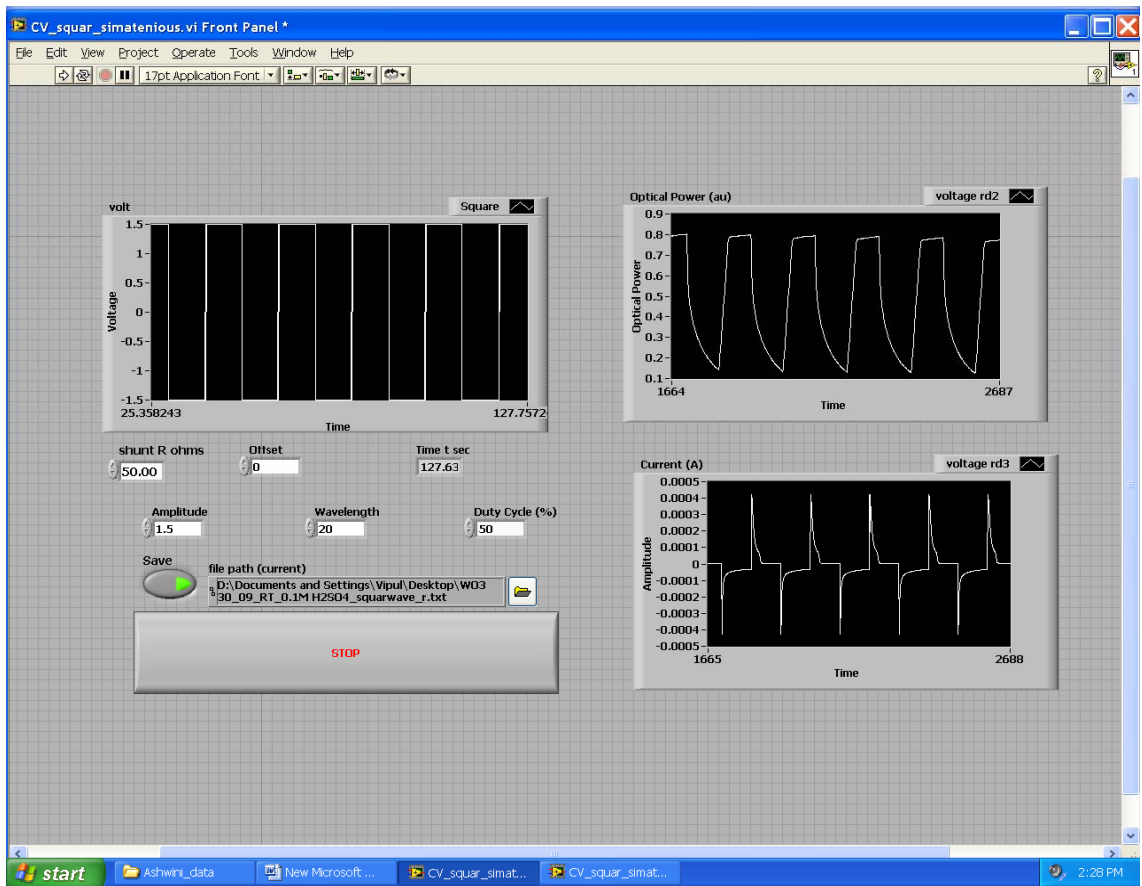
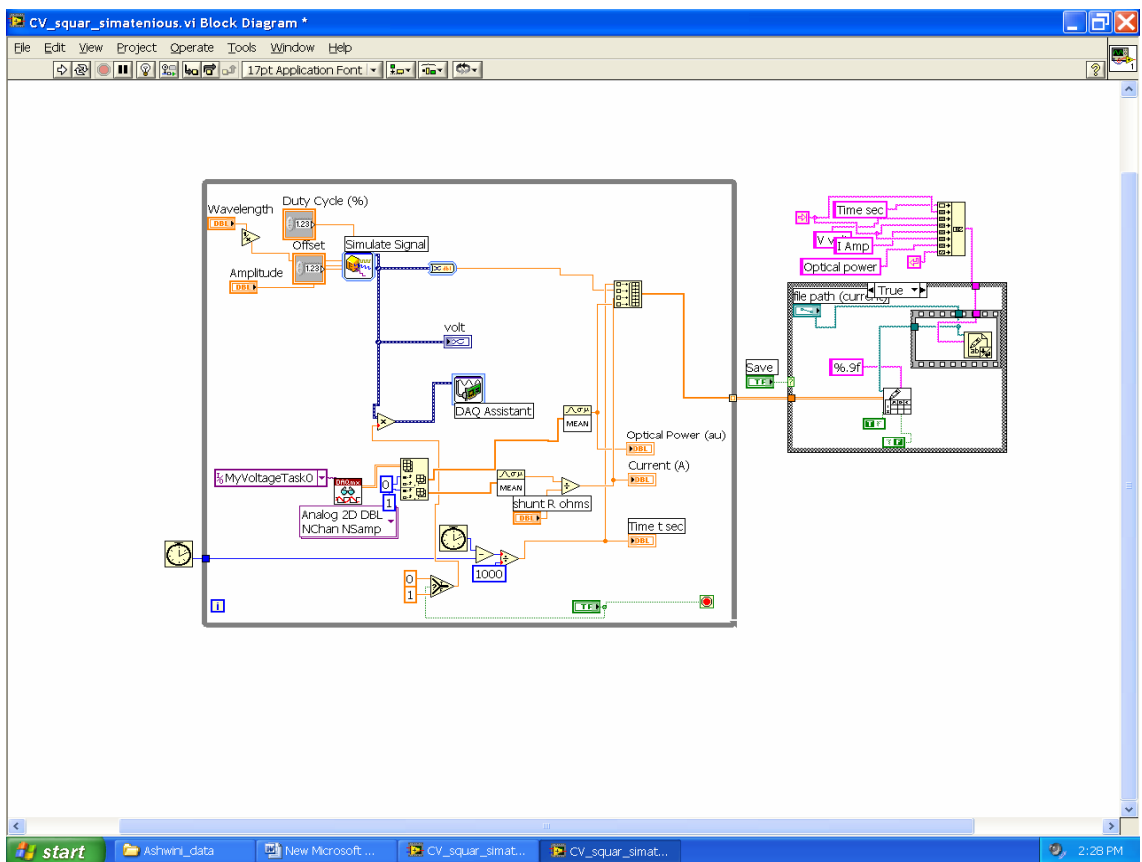


Figure 2.15: Photograph of CA measurement setup.



(a)



(b)

Figure 2.16: (a) Front panel and (b) Block diagram of the VI for switching time measurement using CA technique.

Chapter - 3

Transparent Conducting Indium-Tin Oxide (ITO) Thin Film Layer

3. TRANSPARENT CONDUCTING INDIUM-TIN OXIDE (ITO) THIN FILM LAYER

Transparent conducting oxides (TCO) are the materials that exhibit nearly metallic electrical conductivity with “good” optical transmittance and act as the transparent electrode in optoelectronic devices. The indium-tin-oxide (ITO) thin film is the most widely used TCO for electrochromic device (ECD) applications. The present chapter gives a brief introduction about ITO and its fundamental material physics. Here the preparation of ITO thin films using RF magnetron sputtering is discussed in detail. In particular, the deposition parameters such as working pressure and RF power are varied to optimize the thin film.

3.1 INTRODUCTION

The transparent conducting oxide (TCO) materials have low electrical resistivity and excellent transparency in the visible range. These are widely used in optoelectronic device applications such as, solar cell, electrochromic devices, light emitting diode (LEDs), flat panel displays (FPD). A good combination of transparency and conductance in the film can be achieved in two ways. The first one is in thin metallic films (Ag, Au, or Cu), with typical film thicknesses of a few times $0.01 \mu\text{m}$. In the second category a number of heavily doped metal oxide semiconductor thin films are made, which are widely used nowadays compared to the previous one.

The German scientist K. Badeker first reported the Cadmium oxide film prepared by thermal oxidation of sputtered Cadmium (Cd) metal films as TCO in 1907 [53]. Similar behavior in Indium oxide (as TCO) was reported by A. Thelen in 1956 [54]. Then, approximately a decade later, doped SnO_2 and $\text{In}_2\text{O}_3:\text{Sn}$ (indium tin oxide or ITO) with excellent electrical and optical properties was reported in 1965 [55,56]. The intrinsic, stoichiometric, oxide can not show the high transparency and simultaneously high conductivity, which is only obtained by creating electron degeneracy in a wide band-gap oxide by introducing non-stoichiometry and/or appropriate dopants [57]. Nowadays, various materials are developed which are used as TCO viz. tin-doped indium oxide (ITO), fluorine-doped tin oxide (FTO), and aluminum doped Zinc oxide (Al-ZnO) [23]. Different materials behave differently, some have sharp transparency, some have metallic conductivity, and hence, depending on the requirements, the materials are selected. While selecting the TCO its cost should also be taken into consideration. Al-ZnO is a common choice of TCO because

of its reasonable cost and good optical transmittance in solar spectrum. However, ITO consistently overcomes Al-ZnO in almost every performance category, including chemical stability and moisture, i.e., ITO degrades less compared to Al-ZnO. The ITO is formed by substitution-doping of In_2O_3 with Tin (Sn). The structure and physical properties of bulk ITO is discussed below.

Indium oxide has a cubic bixbyite structure. The bixbyite structure is similar to the fluorite structure, but one-fourth of the anions are vacant, allowing for small shifts of the cations. The two non-equivalent indium sites present in In_2O_3 cubic bixbyite crystal structure [58] are shown in Fig. 3.1. In In-1 site, In atom has six equidistant oxygen anion neighbors and the oxygen atoms are at the corner of the cubes with two oxygen vacancies along one body diagonally. While in In-2 site, In atom are separated from six oxygen anions at three different distances, the oxygen anions are at the corners of the cube, with two oxygen vacancies along one face diagonally.

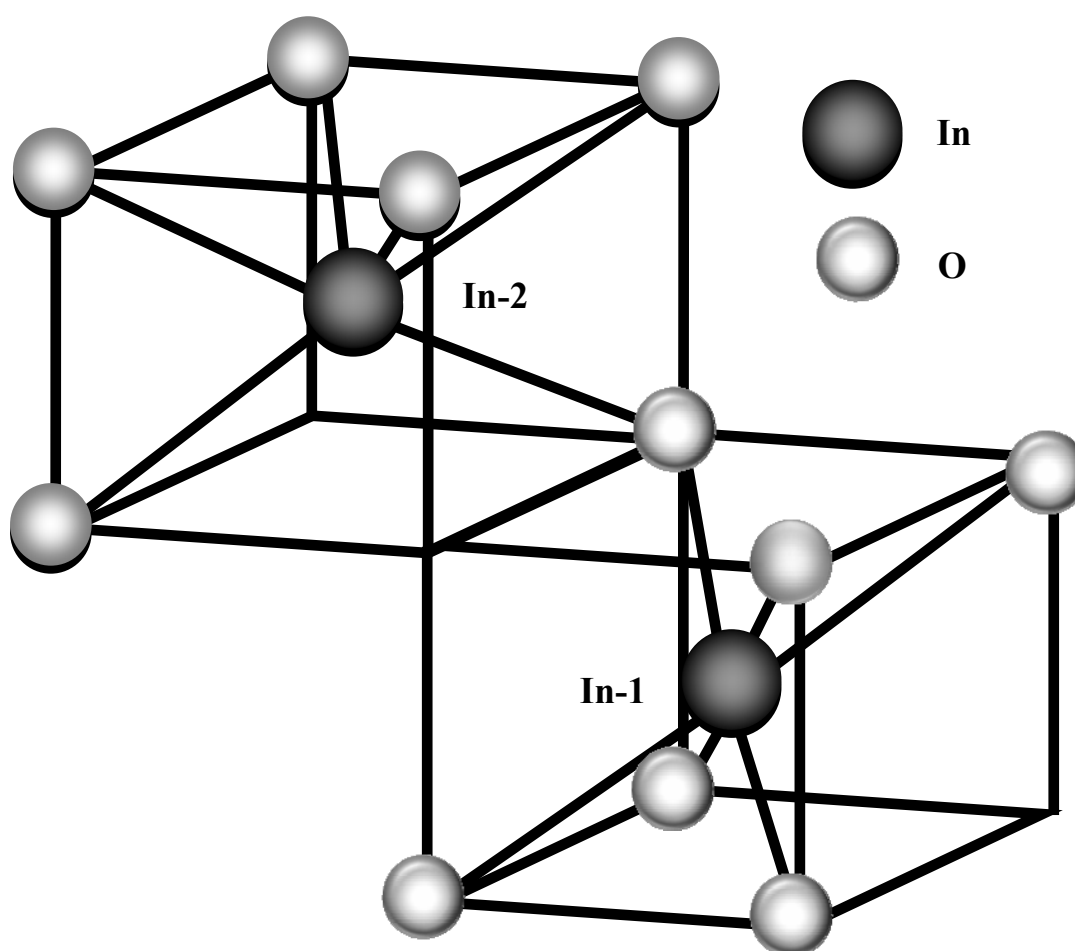


Figure 3.1: Non-equivalent indium sites in cubic bixbyite crystal structure In_2O_3 .

ITO is formed by substitutional doping of In_2O_3 with Sn, which replaces the In^{3+} atoms from the cubic bixbyite structure of indium oxide. The material retains its bixbyite structure and has a lattice parameter close to that of In_2O_3 . The doped Sn forms an interstitial bond with oxygen either as SnO or SnO_2 and accordingly it has a valency of +2 or +4. This valence state plays an important role in the conductivity of ITO. At lower valence state i.e., SnO state, a hole is created, which acts as a trap and as a result a reduction in carrier concentration is observed. On the other hand, prevalence of the higher valence state i.e. SnO_2 state acts as an n-type donor, releasing electrons to the conduction band and increasing the carrier concentration. Nevertheless, in ITO, both substituted tin and oxygen vacancies contribute to the high conductivity. However, too many oxygen vacancies and high Sn concentration may lead to reduction in transmission [59]. In order to optimize the properties, the control of the Sn doping and non-stoichiometric is necessary. In solid form ITO is typically pale yellow to greenish yellow colored material which depends on SnO_2 concentration. The density of ITO is 7.14 g/cm^3 and the melting point is $\sim 1900 \text{ }^\circ\text{C}$. Nowadays ITO having low electrical resistivity ($\sim 10^{-4} \Omega \text{ cm}$) and excellent transparency ($\sim 80 \%$) in the visible range, are being widely used in optoelectronic devices such as, solar cells [60], light emitting diodes (LED) [61], electrochromic devices [24] and transparent p-n junction diode [62].

The electrical, as well as the optical properties of ITO thin film can be modified by controlling the deposition parameters. The variety of techniques viz. sputtering [63], thermal evaporation [64], e-beam evaporation [65], spray pyrolysis, pulsed laser deposition (PLD) [66] and screen printing techniques are used for depositing ITO films. The substrate temperature as well as post-heat treatment also influences properties of the ITO thin film [64,67]. Among these techniques, the radio frequency (RF) magnetron sputtering technique is widely used because of its reproducibility and larger size sample using large area sputtering systems [68,69]. In the case of RF magnetron sputtering, electrical, and optical properties of ITO thin films are affected by the deposition conditions such as deposition temperature [70], working pressure [63], RF power [59], target to substrate (T-S) distance [71], oxygen pressure [72] etc. Although much work has been reported on ITO thin film deposition at higher substrate temperatures ($>200 \text{ }^\circ\text{C}$) and/or with annealing above $200 \text{ }^\circ\text{C}$ [70,73], to improve its transparency and conductivity, nevertheless this confines its use in some areas of applications [74]. For example, multilayered device structure like a solar cell and ECD or devices on plastic substrate, requires a low deposition temperature. At higher temperature, the device structure or plastic substrate gets damaged. For instance, in the case of RF

magnetron sputtering, the high RF power used to optimize ITO thin films may damage the previously deposited layer or the substrate itself, which limits its use in multilayered structures. J. B. Chu et al. reported the ITO thin film prepared without external heating for solar cell application showing transparency between 80 to 90 % in the visible spectrum and 14 - 120 Ω/\square sheet resistance under different Ar pressures [60]. Our attempt is to deposit ITO thin films having lower sheet resistance with high transparency at low deposition temperature and low RF power without post-heat treatment. We have deposited ITO thin film with high transparency of above 80 % and a low-sheet resistance of 4.7 Ω/\square at 75 W RF power and 0.5 mTorr working pressure without externally unheated glass substrate [75]. The film preparation condition and the characterization for optimization of ITO thin film are discussed in next section.

3.2 FILM PREPARATION

The ITO thin films are deposited by RF magnetron sputtering (PFG 600 RF, Huttinger elektronik) onto externally unheated soda lime glass substrates from a ceramic ITO target ($\text{In}_2\text{O}_3 : \text{SnO}_2$, 90:10 wt.%, 99.99 %). The glass substrates employed are of dimensions $5 \times 5 \text{ cm}^2$ and they were organically cleaned. Prior to deposition, the chamber is evacuated down to 10^{-5} Torr by a rotary and diffusion pump and then the Argon (Ar) gas is introduced into the chamber as the sputtering plasma gas. The working pressure of the chamber was varied from 0.5 to 10 mTorr and the RF power is kept at 50 and 75 W. The substrate is continuously rotated at 40 revolutions per minute (rpm) during the sputtering to improve the film's uniformity and, prior to the actual deposition, a 10-minute pre-sputtering period is required to clean the ITO target surface. The sputtering time was adjusted in such a manner that all the films studied had the same thickness viz. 5000 Å. A quartz crystal-based thin film deposition controller monitored the thickness and the rate of deposition. The deposition parameters used in this study are shown in Table 3.1.

3.3 FILM CHARACTERIZATIONS

The crystallinity of the ITO thin films is ascertained using the Grazing Incidence X-ray Diffraction (GIXRD, Bruker-AXS D8 Advance) analysis with $\text{Cu-K}\alpha$ radiation in 2θ range from 20° to 70° . The incident angle is fixed at 0.5° at a scan speed $0.05^\circ/3 \text{ s}$. The surface morphology of the ITO thin films is examined using an atomic force microscope (AFM) in non contact mode with the scan area $1 \mu\text{m}$. The optical transmission spectra of the ITO thin

films are measured at room temperature (RT) using a UV-Visible spectrophotometer (Shimadzu UV-2450) in the wavelength range 300 – 900 nm at RT. The sheet resistance (R_s) of the prepared ITO thin films is measured by Keithley 2420C source meter using the standard four-point probe method.

Table 3.1: The deposition parameters and their typical values used in the present study.

Deposition parameters	Values
Target composition	In ₂ O ₃ : SnO ₂ , 90:10 wt.%
Target size (cm)	5
Target-substrate distance (cm)	7
Film thickness (Å)	5000
Sputtering power (W)	50 and 75
Working pressure (mTorr)	0.5 – 10

3.3.1 Effect of RF Power

Structural Characterization: In RF magnetron sputtering the rate of deposition of the films and its properties depends on the RF power. On increasing the RF power at a given pressure, an ionized Ar atom are bombard on the target (cathode) with higher energy which leads to the ejection of more target atoms and thus an increase in the deposition rate of the film is observed. The rate of deposition, at 1 mTorr working pressure, is found to be 1.3 Å/s at 50 W RF power and it increased up to 2.6 Å/s at 75 W.

Figure 3.2 shows the XRD spectra of the ITO thin films grown at 1 mTorr working pressure and 50 and 75 W RF power on externally unheated glass substrates. From the Fig. 3.2, the XRD measurements show that the ITO thin films deposited at 50 and 75 W power for 1 mTorr working pressure gave strong (222) preferred orientations with small peaks observed in (211), (400), (431), (440), and (622) planes, which indicates the cubic bixbyite structure of the thin films [JCPDS 06-0416]. The bump under (222) peak is due to a two-phase structure. In RF sputtering, the kinetic energy of sputtered particles arriving at the substrate surface is, on the average, higher than those of the thermally evaporated atoms, and thus leads to a crystallization of films even though the substrate is not externally heated. Furthermore, at 50

W RF power the deposition rate is low, and for the same thickness longer deposition time is required, which will lead to increase in the average substrate temperature during deposition, this in turn will lead to an improvement in the crystallization of film.

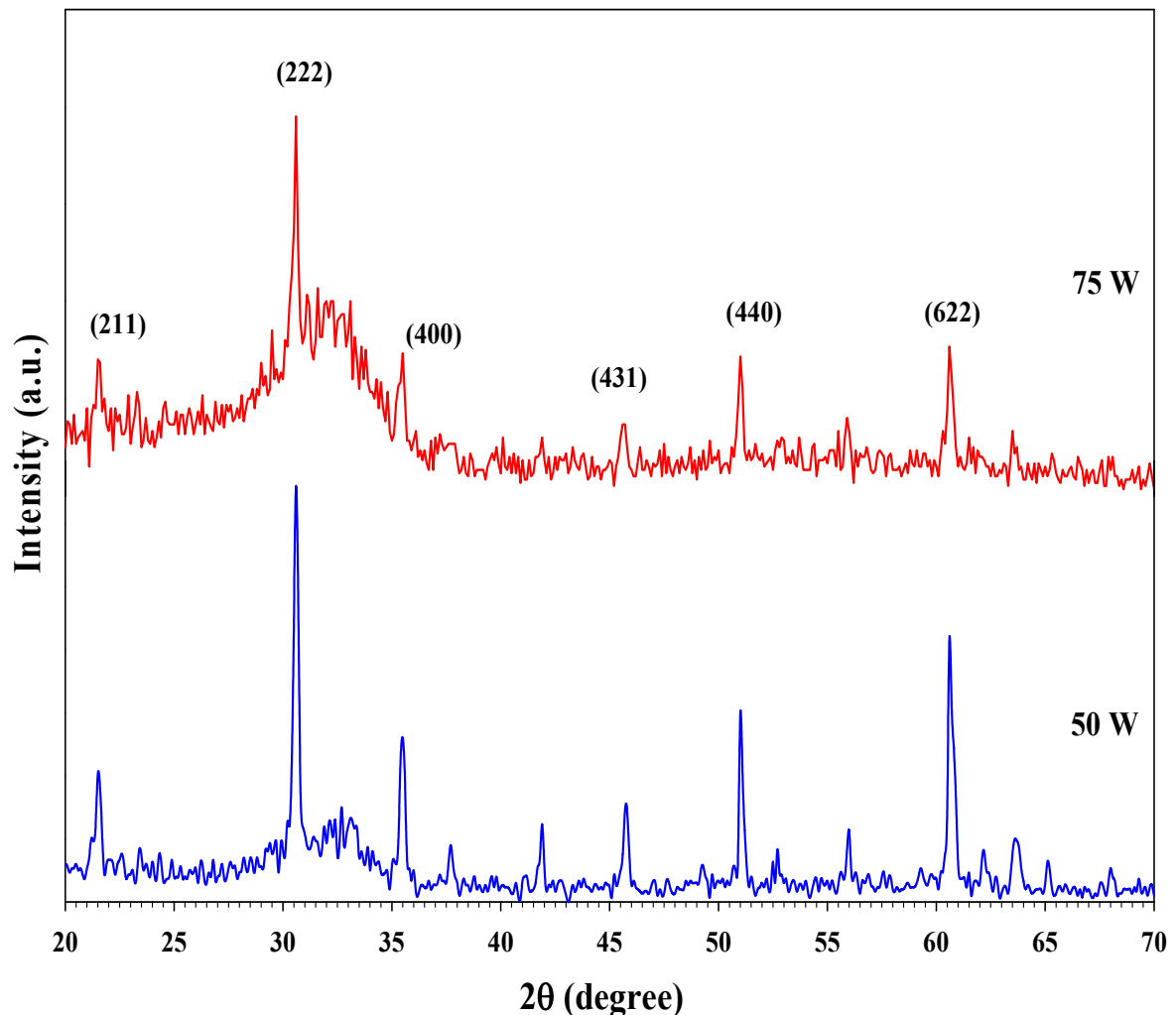


Figure 3.2: The XRD spectra of ITO thin films grown at 50 and 75 W RF power at 1 mTorr working pressure.

The root mean square (rms) surface roughness of the thin films, as estimated from the AFM images shown in Fig. 3.3, decreases from 13.27 to 4.02 nm as RF power increases from 50 to 75 W. The thin films grown at 50 W RF power have relatively low kinetic energy of sputtered particles compared to 75 W RF power, which leads to relatively more random orientation and different size of grain growth is observed which results in the rough surface. With increase in RF power, the sputtered particles have enough energy for uniform distribution of grain growth and thus lead to a smoother surface.

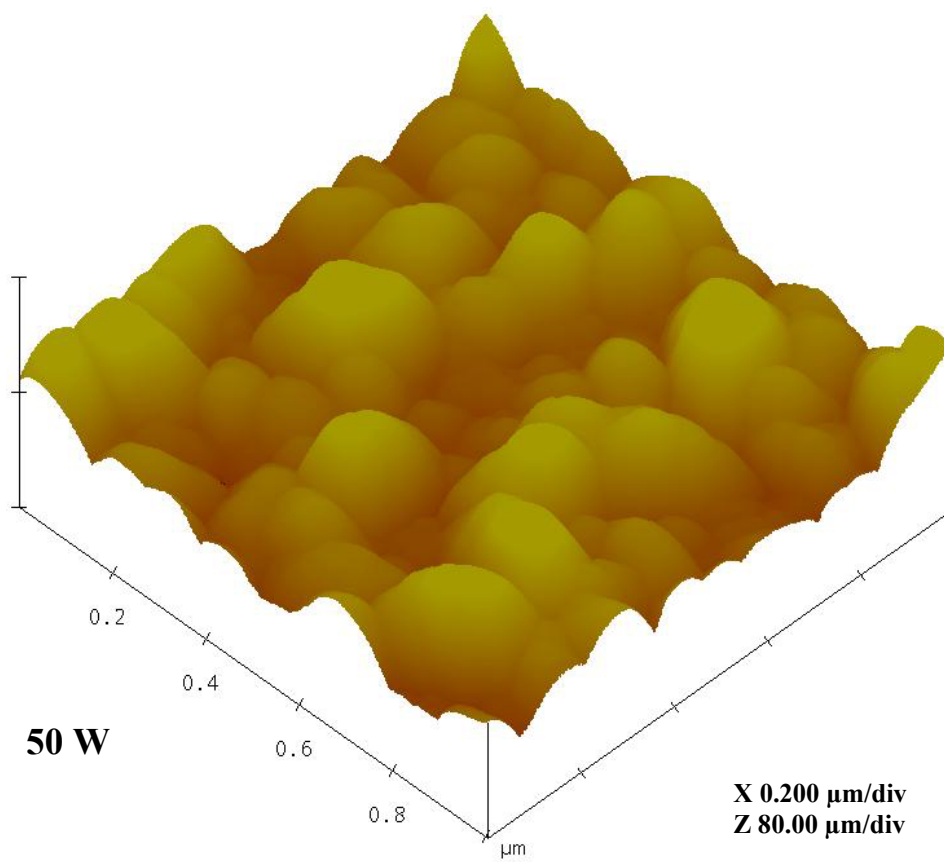
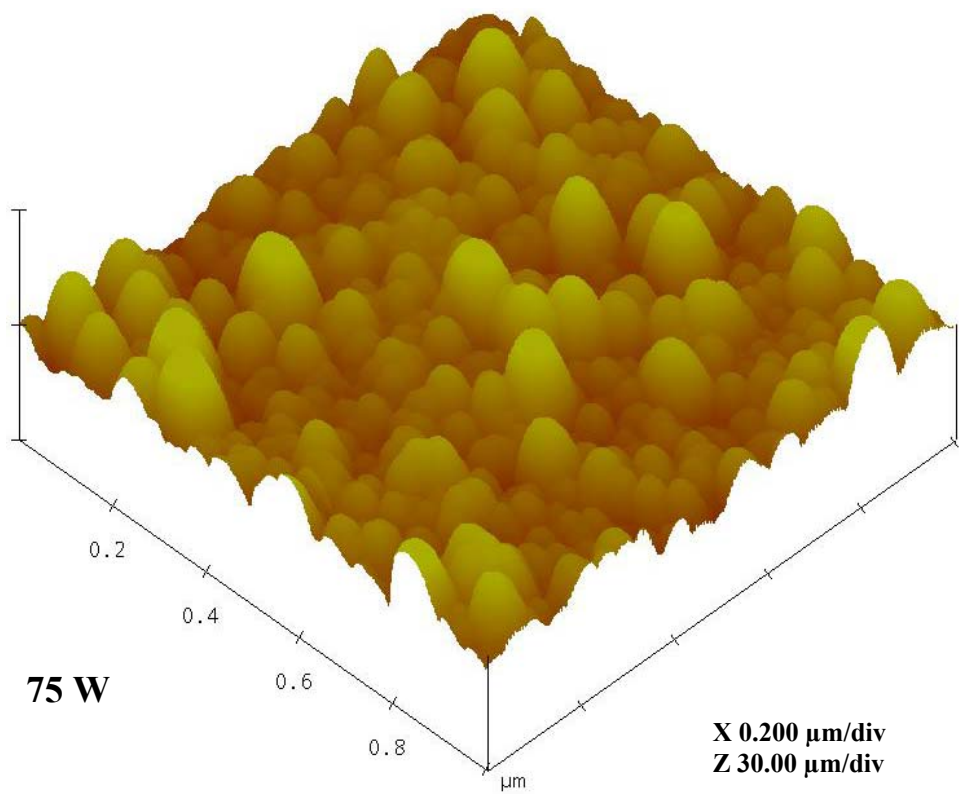


Figure 3.3: The AFM images of the different RF power and 1 mTorr working pressure grown ITO films.

Optical Characterization: The optical transmittance of ITO thin films grown at 50 and 75 W, at 1 mTorr working pressure, are shown in Fig. 3.4 (a), which is further used to calculate the optical energy band-gap. The optical energy band-gap of the ITO thin film is calculated using the Tauc's relation in which η is equal to 1/2, for direct allowed transitions [76]. Thus, the optical energy band-gap of ITO is determined by plotting $(\alpha hv)^2$ versus the incident photon energy (hv), and by extrapolating the curve to $\alpha hv = 0$ as shown in Figure 3.4 (b). Fig. 3.4 (a) shows the small variations in the transmittance, decreasing from 89 to 85 %, with increase in RF power from 50 to 75 W. The decrease in transmittance with increase in power is due to decrease in the oxygen content in the film [59]. With the sputtering power increasing from 50 to 75 W, as shown in Fig. 3.4 (a), the absorption edge shifts towards the shorter wavelength and the band gap value increases from 3.34 to 3.42 eV. As the RF power increases the oxygen vacancies are created in the film that leads to increase in carrier concentration. The carriers are partially filling the conduction band of the tin oxide, thus the band-gap shifts to a higher value. The shifting of the band-gap (ΔE_g) in this type of degenerate semiconductor, due to carrier concentration is explained by the Burstein–Moss (B-M) effect [77,78] using the equation, $\Delta E_g = \frac{h^2}{8m^*} \left(\frac{3}{\pi}\right)^{2/3} n^{2/3}$ where, h is Planck's constant, m^* is the electron effective mass in the conduction band and n is the carrier concentration. Thus, according to the B-M effect the widening of the band-gap is directly proportional to the increase in the carrier concentration.

Sheet Resistance Measurement: The electrical measurements show that the sheet resistance and resistivity are influenced by the RF power. The values of the sheet resistance and the resistivity, 117.23 Ω/\square and 2.3×10^{-2} Ωcm , respectively, for 50 W RF power grown thin films reduces to 14.59 Ω/\square and 2.9×10^{-3} Ωcm , respectively, for the thin films grown at 75 W power. This decrease in resistance with increasing RF power is attributed to the generation of oxygen vacancies. The sputtering deposition of an oxide material from an oxide target results in dissociation of some of the more volatile material viz. oxygen, which creates the oxygen vacancy and it increases with increase in RF power. It is known that the conductivity of ITO is related to the substitution of tin in place of indium and oxygen vacancies in the films. The former generates one electron in the conduction band whereas the latter effectively leads to two electrons in the conduction band and thereby increase in the carrier concentration is observed [79].

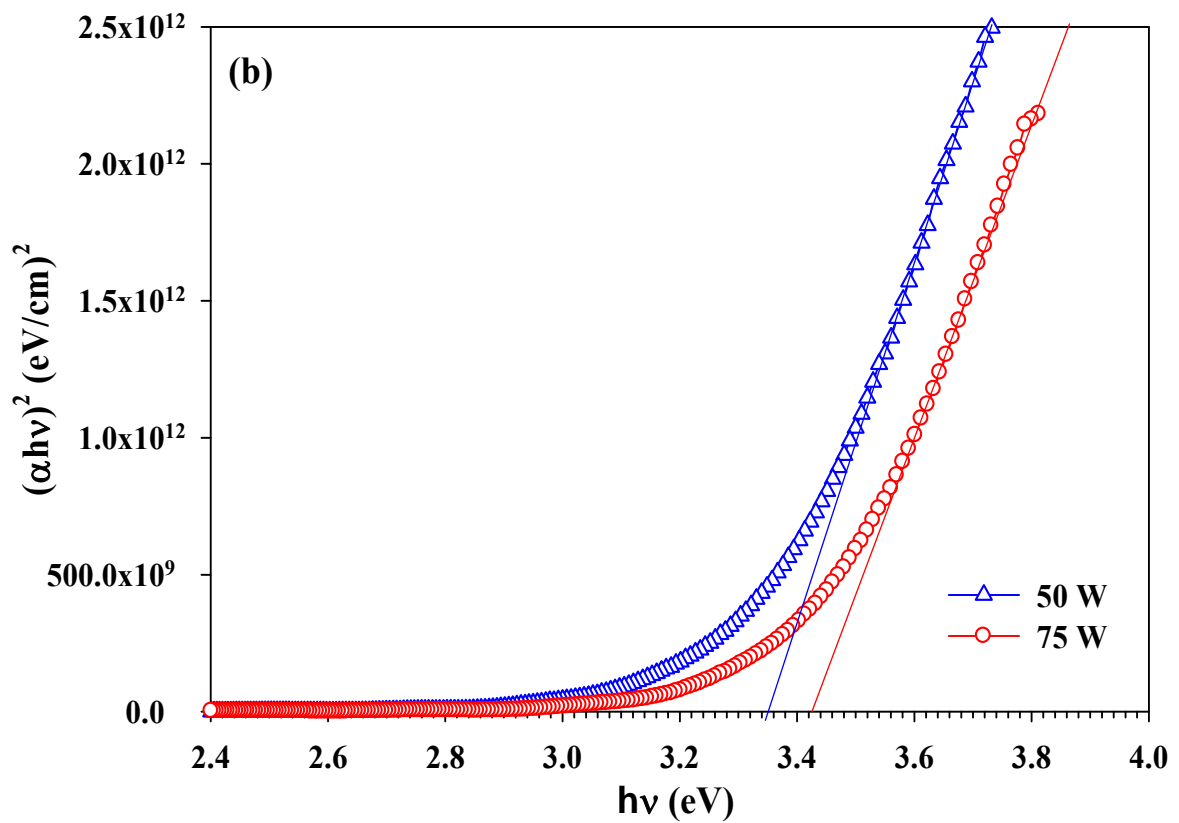
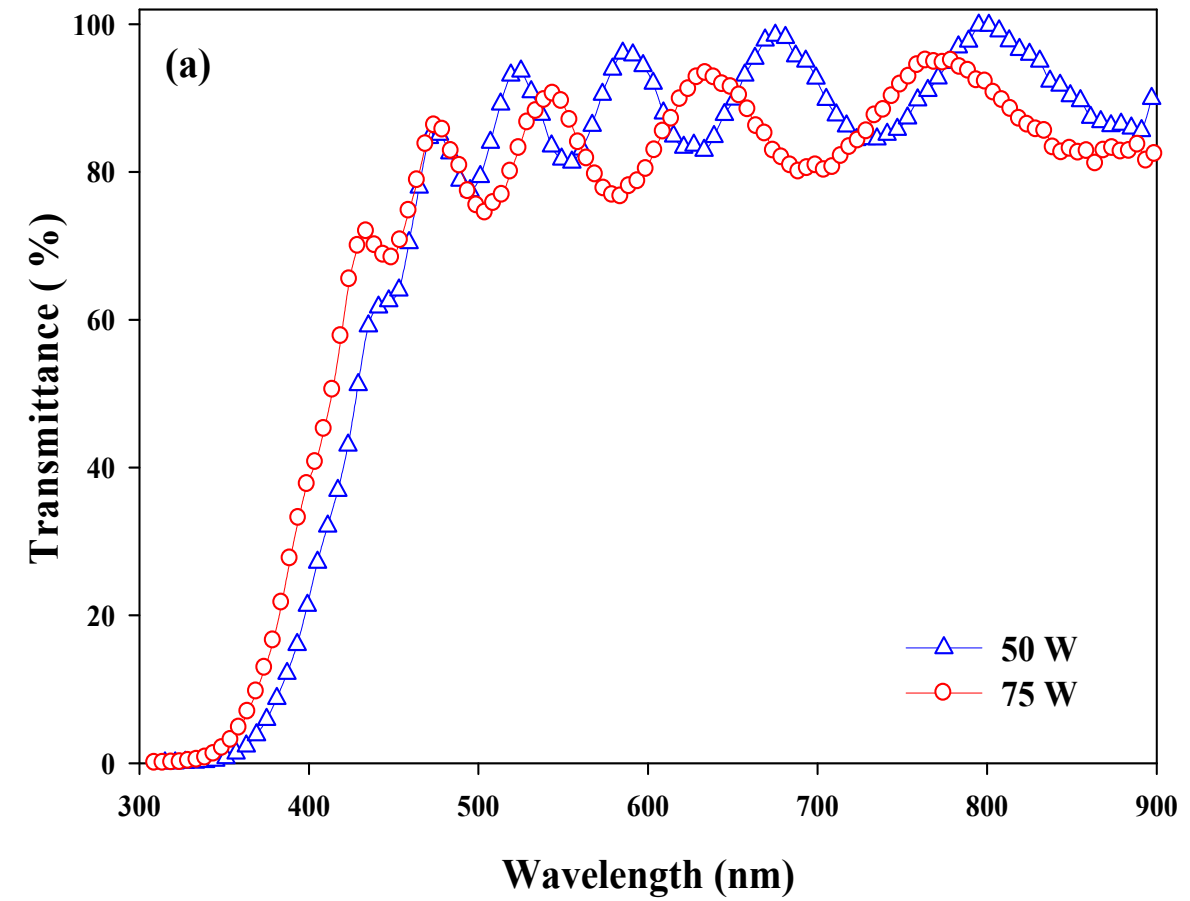


Figure 3.4: (a) The transmittance spectra and (b) the plot of $(\alpha h\nu)^2$ versus $(h\nu)$ of the ITO thin films grown at 50 and 75 W RF power at 1 mTorr working pressure.

For transparent conducting electrode, ideally, both parameters, electrical conductivity and optical transmittance, should be large but actually, both are inversely correlated. Higher conductivity usually causes low transmittance due to increase in carrier concentration. So the performance of transparent conducting films is judged by a figure of merit, (ϕ_{TC}), as proposed by Haacke [80], $\phi_{TC} = T_{avg}^{10}/R_s$ where, T_{avg} is the average transmittance in visible region of light and R_s is the sheet resistance. At 1 mTorr working pressure, the figure of merit increases from $2.66 \times 10^{-3} \Omega^{-1}$ to $13.5 \times 10^{-3} \Omega^{-1}$ as the RF power increases from 50 to 75 W, respectively.

3.3.2 Effect of Working Pressure

Furthermore, to study the effect of the working pressure on the properties of the ITO thin films, we have characterized the films grown in the working pressure range of 0.5 to 10 mTorr at 75 W RF power on externally unheated glass substrates. One of the main factors, which affect the deposition rate is the working pressure. Figure 3.5 shows the variation of the deposition rate with the working pressure. As shown in Fig. 3.5, the rate of deposition of ITO thin films significantly decreases from 2.7 to 0.8 Å/s with increase in the working pressure from 0.5 to 10 mTorr. The decrease in the rate of deposition with increase in the working pressure is attributed to the increased number of collisions of the sputtered particles with the gas molecules, which results in a partial loss of energy and randomizes the direction of the sputtered particles during their transport to the substrate, and thus the decrease in the deposition rate is resulted.

Structural Characterization: Typical XRD spectra of ITO thin films deposited at different working pressure and 75 W RF power are represented in Fig. 3.6. ITO thin films prepared at lower working pressure 0.5 mTorr has preferred orientation along (222) direction with other dominant (400), (440) and (622) orientations. This indicates the cubic structure of the films [JCPDS 06-0416]. As the working pressure increases the intensity of (222) peak decreases and the films show preferred orientation along (622) at 5 mTorr. The variation in orientation from (222) to (622) with other orientation is due to the presence of more oxygen in thin films and lower energy of adatoms on the substrate at higher working pressure. For the higher working pressure at 75 W RF power the deposition rate is low and for fixed thickness the longer deposition time is required. Local heating will lead to increase in the substrate temperature during deposition, which in turn, will have an effect on the crystallization of films.

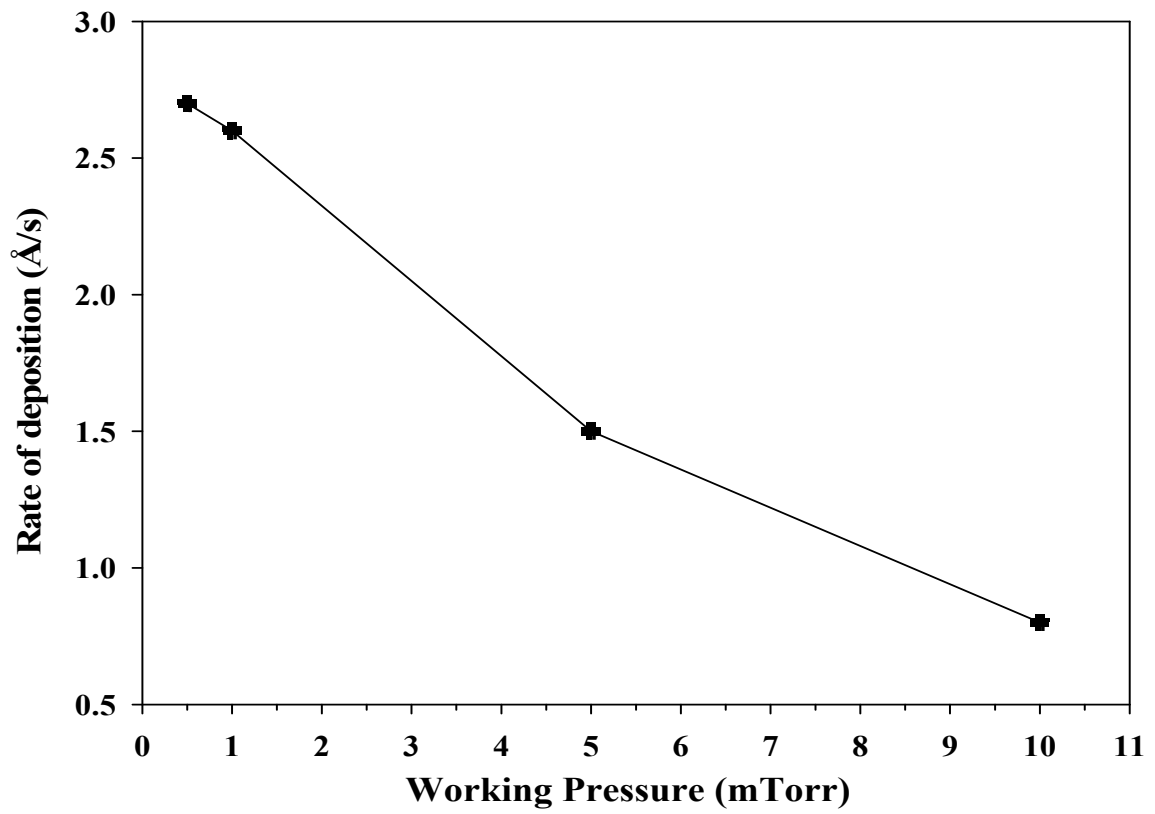


Figure 3.5: The rate of deposition versus the working pressure at 75 W RF power

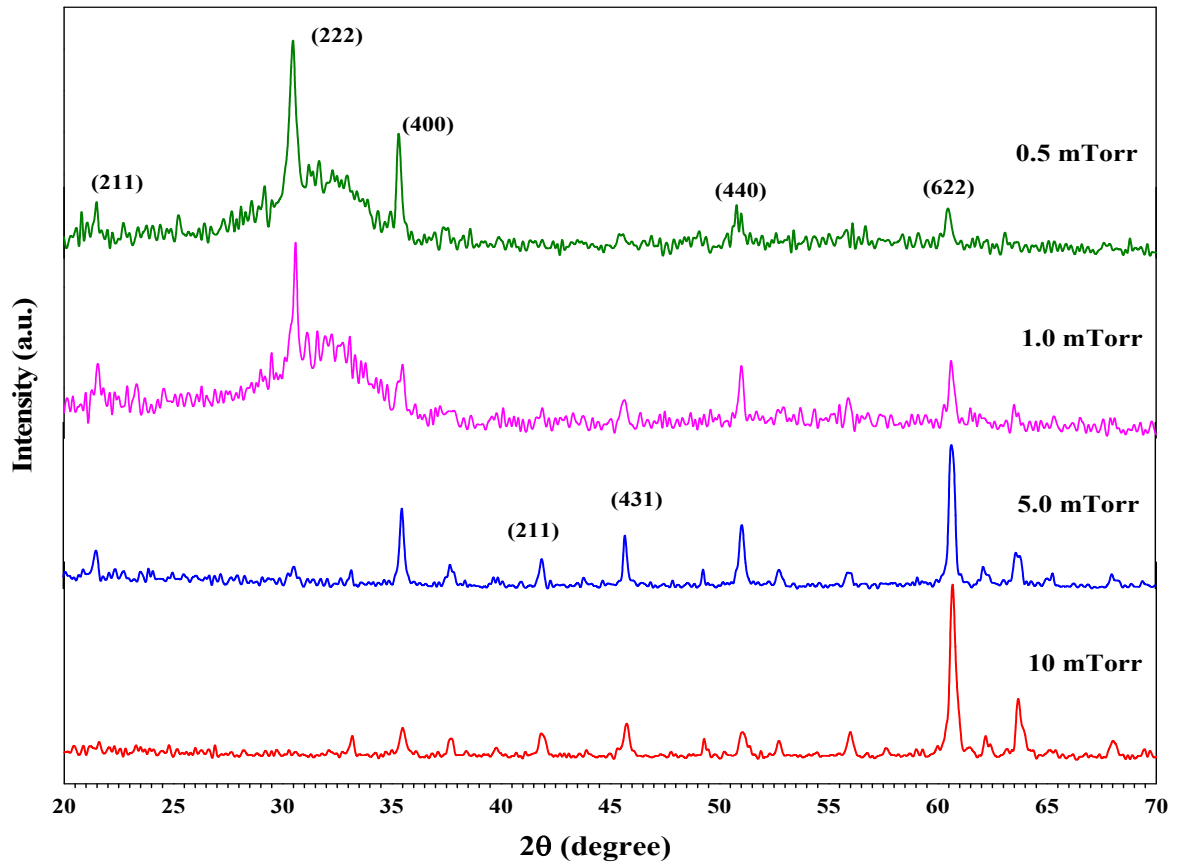


Figure 3.6: The XRD spectra of thin films grown at different working pressures at 75 W RF power.

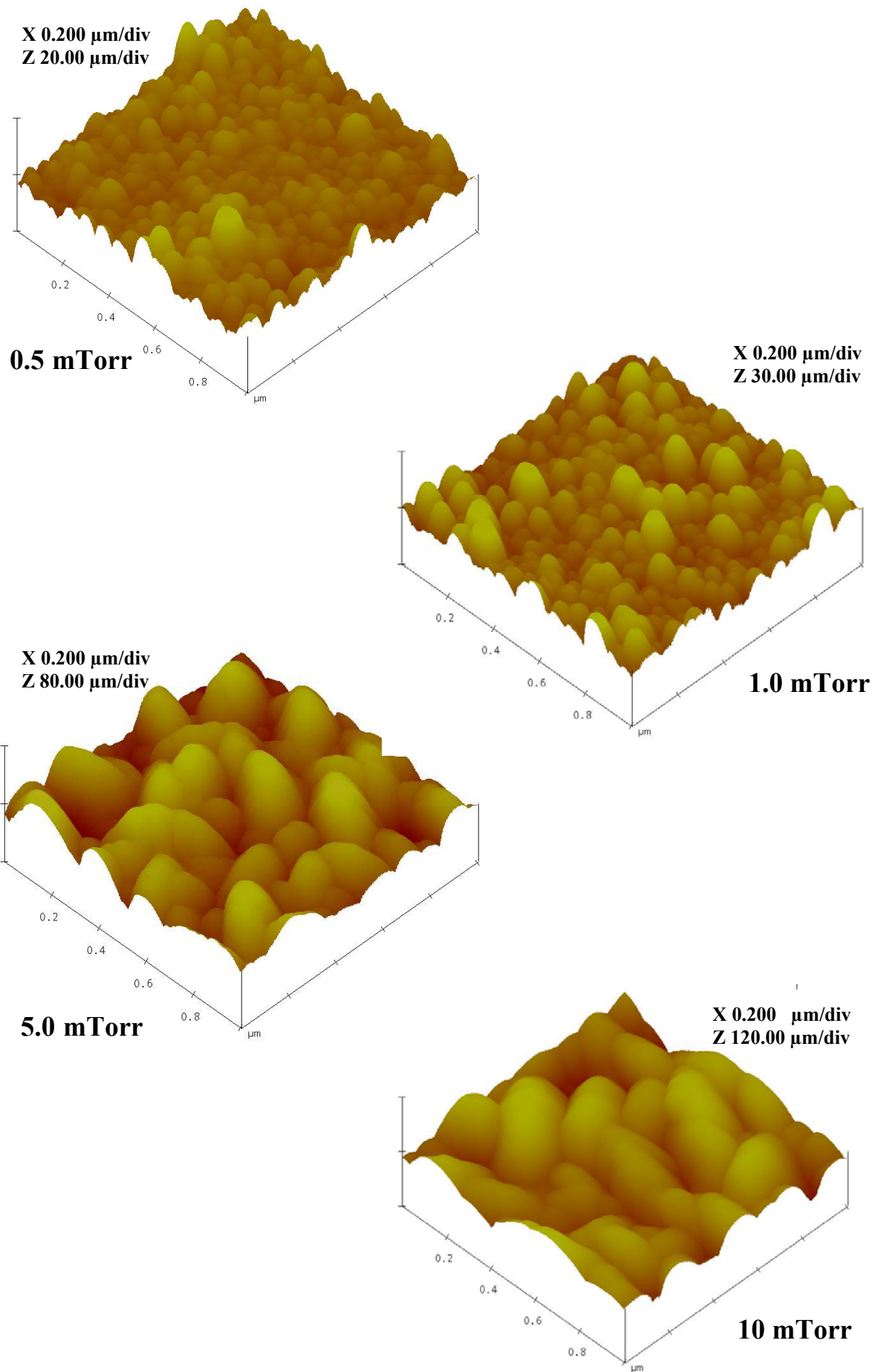


Figure 3.7: The AFM image of the ITO thin films grown at different working pressure at 75 W RF power.

Figure 3.7 shows the AFM image of the ITO thin films grown at different working pressures at 75 W RF power. The values of the rms surface roughness are listed in Table 3.2. At 0.5 and 1 mTorr working pressure, thin films show a uniform grain distribution with the rms surface roughness 2.52 nm and 4.10 nm, respectively; however, at higher working pressure random orientation of big grains results in the rough surface [63]. At higher working pressure, an increase in the number of collisions of the sputtered particles with the gas molecules results in the reduction of energy of the sputtered particles, which leads to random orientation of grain growth as observed and also an increase in the surface roughness.

Optical Characterization: The optical transmittance spectra in the visible region and the $(\alpha hv)^2$ versus (hv) plots are shown in Fig. 3.8 (a) and (b), respectively. The ITO thin films grown at lower working pressure have little less transmittance due to the high oxygen vacancy. Oxygen vacancy leads to generate free electrons, so, the more oxygen vacancy, higher the carrier concentration [79]. Transmittance and carrier concentration are inversely proportional and thus the absorption of light by the free carriers reduce the transmittance. The absorption edge shifts towards lower wavelength and the widening of the band gap at lower pressure is caused by the increase in the carrier concentrations as explained by the B-M effect. This is due to the filling of the lowest levels of the conduction band by the charge carrier. The average transmittance in the visible range and the energy band gap values as a function of the working pressure are shown in Table 3.2.

Sheet Resistance Measurement: The sheet resistance and the resistivity value as a function of working pressure are presented in Table 3.2. The ITO resistivity is found to decrease with decrease in the working pressure and reach at $9.47 \times 10^{-4} \Omega\text{cm}$ for the films deposited at 0.5 mTorr working pressure. It is expected that the sputter deposition performed at low working pressure results in the creation of more oxygen vacancy due to the dissociation of oxygen. The oxygen vacancies increase the carrier concentration, and thus the decrease in the electrical resistance takes place. The figure of merit calculated for ITO thin films grown at different working pressures are shown in Table 3.2. The ITO films deposited with 75 W RF power and 0.5 mTorr working pressure show good electrical and optical properties with high figure of merit viz. $37.2 \times 10^{-3} \Omega^{-1}$.

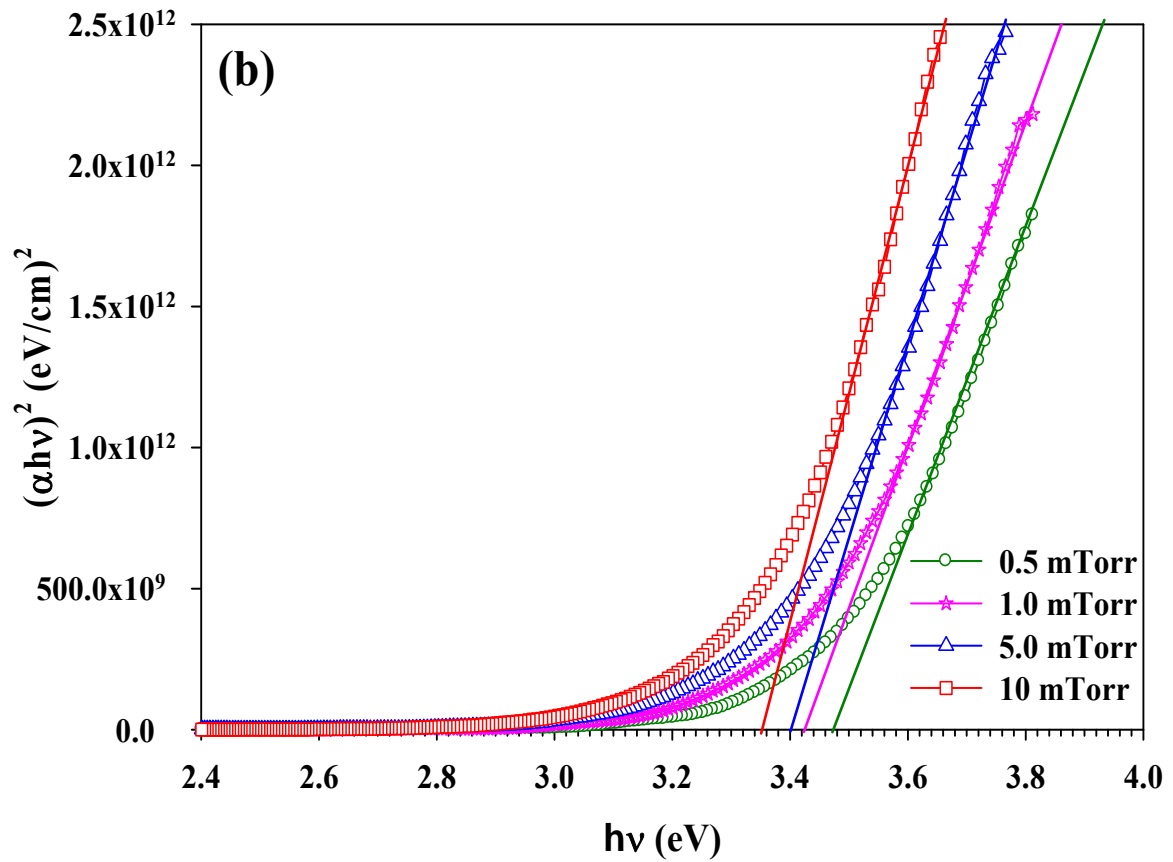
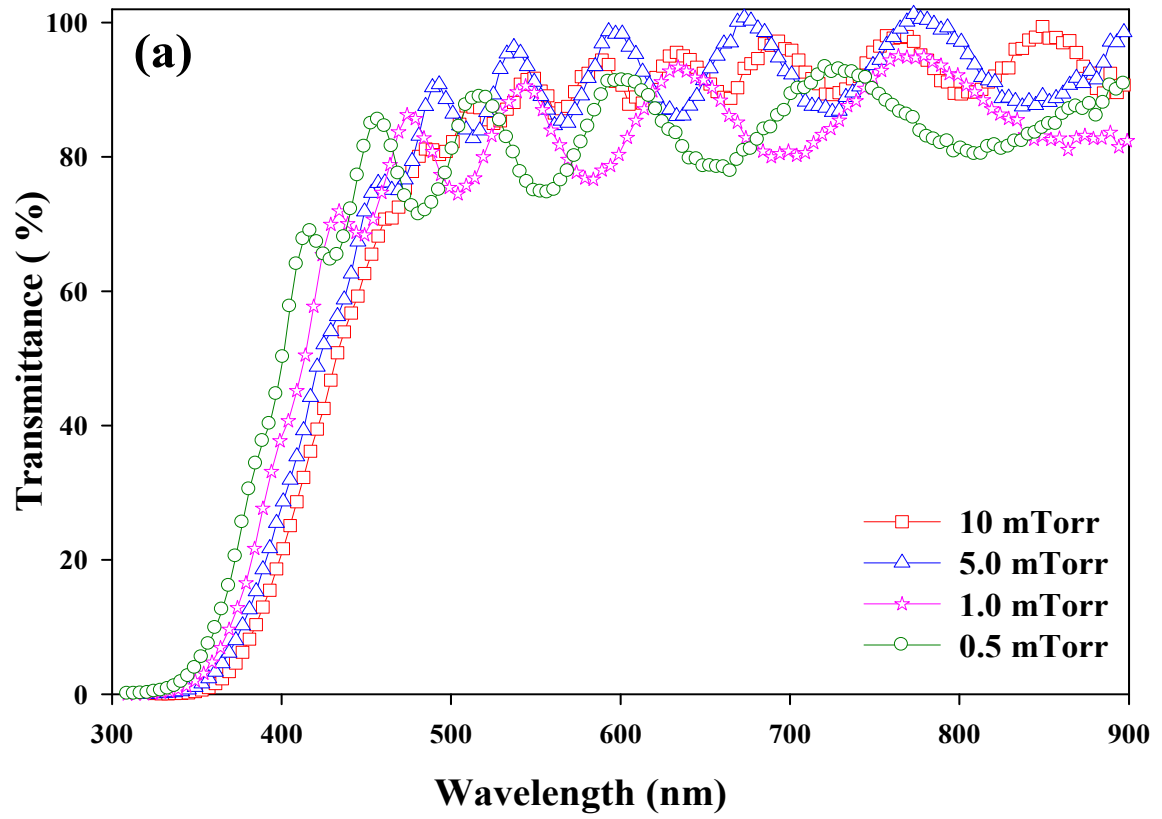


Figure 3.8: (a) The transmittance spectra and (b) the plot of $(\alpha h\nu)^2$ versus $(h\nu)$ of the ITO thin films grown at different working pressure at 75 W RF power.

Table 3.2: The rms surface roughness, average transmittance, Energy band-gap, sheet resistance, and resistivity as a function of the working pressure of ITO thin films grown at 75 W RF power.

Working pressure (mTorr)	0.5	1.0	5.0	10
rms surface roughness (nm)	2.52	4.10	14.05	17.16
Average transmittance, T_{avg} (%)	84	85	89	91
Energy band gap, E_g (eV)	3.47	3.42	3.40	3.35
Sheet resistance, R_s (Ω / \square)	4.7	14.6	277.3	330.6
Resistivity, ρ (Ωcm)	9.47×10^{-4}	2.92×10^{-3}	5.6×10^{-2}	6.6×10^{-2}
Figure of merit, ϕ_{TC} (Ω^{-1})	37.2×10^{-3}	13.5×10^{-3}	1.12×10^{-3}	1.18×10^{-3}

3.4 CONCLUSIONS

The RF magnetron sputtering is used for the deposition of the ITO thin films with low resistivity and high optical transmittance without any post deposition heat treatment. The RF power and the working pressure significantly influence the deposition rate, structural, optical, and electrical properties. It is observed that with increase in RF power and decrease in the working pressure the conductivity improves with band gap widening due to the formation of oxygen vacancy. The ITO thin films deposited with 75 W RF power and 0.5 mTorr working pressure shows a high transparency of above average 80 % and the low sheet resistance of 4.7 Ω/\square . These types of conducting oxide thin films satisfied technical requirements of a variety of applications, including TCO, optical coatings, and transparent electronics.

Chapter - 4

Electrochromic

Tungsten Trioxide (WO_3)

Thin Film Layer

4. ELECTROCHROMIC TUNGSTEN TRIOXIDE (WO₃) THIN FILM LAYER

Electrochromic (EC) layer is the most active layer of solid-state electrochromic devices (ECD). The overall performance of ECD is predominantly affected by the properties of the EC layers. In the present chapter, we discuss the preparation of tungsten trioxide (WO₃) thin films by the thermal evaporation method. We study the effect of different growth conditions on the structural, optical, and electrical properties of the WO₃ thin films. Finally, the EC properties viz. transmittance modulation, coloration efficiency, and switching time, which are affected by the insertion of ions and substrate temperature, are also discussed.

4.1 INTRODUCTION

Transition metal oxides represent a large family of materials possessing various interesting properties in the field of electrochromic devices (ECD) [81], memory devices, and sensors [82,17]. Among them, tungsten trioxide (WO₃), an n-type semiconductor, is the most extensively studied material due to its appreciable electrochromic (EC) properties in the visible and infrared region, high-coloration efficiency, and relatively low price [83]. It is used for construction of smart-windows [81], mirrors, optical shutters, and display devices [84], etc.

Peter Woulfe was the first to recognize a new element in the naturally occurring mineral, Wolframite (W, tungsten) during the 18th century. In 1841, Robert Oxland first gave the procedure of preparing WO₃ compound. The WO₃ powder appears yellow in color having density of 7.16 g/cm³. The melting temperature of WO₃ is ~ 1473 °C but its sublimation starts at nearly 900 °C. WO₃ shows different crystal structures at different temperatures. The most common monoclinic crystal structure of WO₃ is represented in Fig. 4.1. There is another stable tungsten oxide compound, also existing in the tungsten-oxygen system, in which the oxidation state of W varies from 2 to 6. WO₃ is the highest oxidation state compound in tungsten-oxygen system.

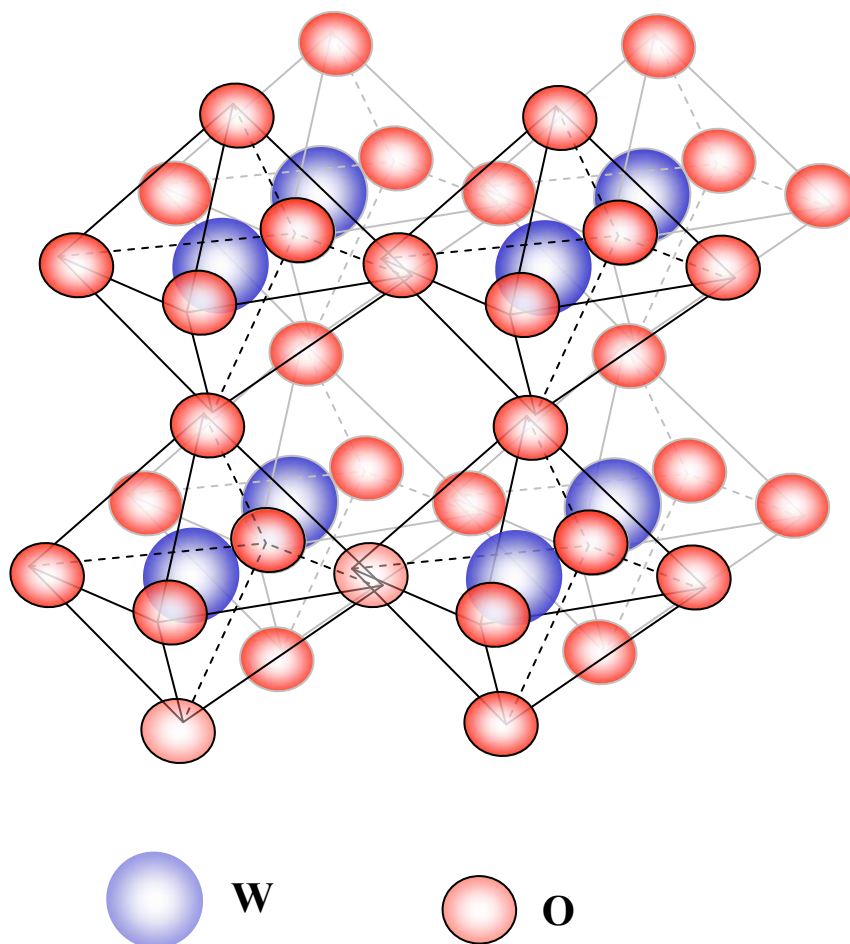


Figure 4.1: Monoclinic crystal structure of WO_3 .

Nowadays, WO_3 has been investigated extensively for its EC properties for the fabrication of ECD. Electrochromic device employ both amorphous as well as crystalline WO_3 film owing to their highly catalytic behavior both in oxidation and reduction processes [85,86]. The amorphous films have their applications in transmittance modulation devices in the visible region, whereas the crystalline WO_3 film, due to its better reflection modulation in near-infrared region of the spectrum, is used for thermal modulation [85,87]. The coloration in WO_3 thin film occurs due to ionic insertion but the coloration mechanism in crystalline WO_3 films is different from that of the amorphous thin films. Many investigations have been carried out to understand the mechanism of electrochromism in WO_3 and different authors have suggested various models. S. K. Deb was the first to suggest that the formations of F-like centers are responsible for the coloration in WO_3 thin films [14]. The coloration in highly disordered amorphous structure is due to the injection of electrons at cathode. The electrons are localized on tungsten sites instead of oxygen vacancies, and hence positively charged structural defects are responsible for the color center. It is believed that the

formation of tungsten bronze is by double injection/extraction of an electron and a cation in the film, which is given by,



where M^+ denotes H^+ , Li^+ , Na^+ or other alkali metal ions. In this process, the number of the color centers is increased due to the increase in W^{5+} ions. It has been assumed that the inserted electrons are trapped at W sites and are then transferred to the neighboring sites by absorption of photons i.e., the coloration is formed due to inter-valency transition between $\text{W}^{5+} \leftrightarrow \text{W}^{6+}$ adjacent states [88].



Schirmer et al. gave a new model for electrochromism in the WO_3 thin film which is closely related to the above model with detailed interpretation in terms of the “small” polaron theory [89]. According to this model, the inserted electrons are localized in W^{5+} sites and polarize their surrounding lattice by short-range interactions. The concept of optical absorption by polaron formation was introduced by L. Landau in 1933 [90]. Physically, when an electron is inserted into a crystal structure, it can distort the surrounding lattice and create a potential well that will be self-trapping the charge carrier. All the above models had certain shortcomings and hence were not able to explain some of the experimental results like the oxygen deficient WO_3 thin film which appears transparent [91] and the increases in coloration with the increase in oxygen deficiency [92,93]. In 1997, J. Zhang et al. proposed a model for the electrochromic mechanism in amorphous tungsten oxide films [94]. In this model amorphous WO_3 thin films are supposed to be oxygen deficient and a certain amount of water is available in the film. The molecular formula should be expressed as $\text{WO}_{3-y}\text{nH}_2\text{O}$, where n is the amount of water bound in the film. The as-deposited film has mainly W^{6+} and W^{4+} state and can be expressed as $\text{W}^{6+}_{1-y}\text{W}^{4+}_y \text{nH}_2\text{O}$. In these model coloration is based on the inter-valence charge transition (IVCT) between the W^{5+} and W^{4+} state in place of W^{5+} and W^{6+} states. This process can be expressed as;



The above model is generally accepted [94] for the coloration between a bleached and a colored state in amorphous WO_3 thin films, which is based on IVCT and double injection/extraction of electrons and ions.

However, in crystalline WO_3 it is believed that the coloration mechanism is due to Drude-like free electron absorption [95]. Svensson and Granqvist have developed a more

detailed theory based on the band structure of WO_3 for optical properties of crystalline electrochromic WO_3 films [96]. In crystalline materials, according to the double injection model, when the same density of electrons and ions are introduced, the free electrons occupy the lowest level of conduction band and ions are to a significant extent delocalized near the surrounding lattice and act as a scattering center for the free electron. (This mechanism is similar to heavily doped semiconductors with ionized impurities [97].) Free electron like behavior in semiconducting film show the reflective optical modulation i.e., ion intercalation into crystalline WO_3 films can lead to a high reflectance in the infrared region of wavelength.

The EC properties of WO_3 , like the transmittance modulation (ΔT), coloration efficiency (CE), switching time, and cyclic durability, strongly depends on its structural, morphological, and compositional characteristics [98], which, in turn, depends directly on the deposition method and deposition conditions. Electrochromic WO_3 thin films have been produced by a large number of techniques, such as thermal evaporation [99], flash evaporation [100], e-beam evaporation [101], pulsed laser deposition [102], RF magnetron sputtering [103], and sol-gel coating [104]. Among them, the physical vapor deposition (PVD) techniques such as the thermal evaporation and the sputtering are the most commonly employed techniques. In the present chapter we discuss the EC properties viz. transmittance modulation, and CE, of the WO_3 thin films, grown by thermal evaporation, for three different inserted ions H^+ , Na^+ , and K^+ . We also discuss the effect of substrate temperatures on the CE and switching time of the WO_3 thin films. However, our aim is to fabricate ECD, so the low temperature process is optimized in order to fabricate smart ECD. The WO_3 thin film preparation method and different characterization techniques for optimization are discussed below.

4.2 FILM PREPARATION

Thin films of WO_3 are deposited on organically cleaned glass substrates and ITO coated glass substrates by thermal evaporation of high-purity WO_3 powder (Sigma Aldrich, 99.9 %). A tungsten boat is used for the evaporation of WO_3 powder using a vacuum coating unit (Hindhivac, Model-15F6). The films are grown at a base pressure of 10^{-5} Torr and substrate temperatures ranging from room temperature (RT) to 510°C , which is measured using a Chromel-Alumel thermocouple. WO_3 thin films of thickness 2500 \AA are deposited at a constant rate of 4 \AA s^{-1} . The thickness of the film and the rate of deposition are monitored and controlled using the automatic thin film deposition controller (Sigma Instruments, SQC-122c).

4.3 FILM CHARACTERIZATIONS

The structural properties and crystallinity of the film are investigated by X-ray diffraction (XRD) using CuK α radiation (Rigaku D-Max-III) whereas the surface roughness of the film is determined by atomic force microscopy (AFM) (Nanosurf easyScan 2). The surface composition of these thin films is determined using X-ray photo-emission spectroscopy (XPS). The XPS measurement is carried out using VSW ESCA instrument, with Al-K α (1486.6 eV) X-ray source at base vacuum of 8.0×10^{-10} Torr. The electrical properties like the resistivity (ρ), carrier concentration (n), and mobility (μ), are obtained at RT by the four-point-probe method using a Keithley source meter (2400C). The optical transmission spectra are measured using UV-Visible spectrometer (Shimadzu UV-2450) in the wavelength range 300 - 800 nm. The electrochromic measurements are done using two-electrode electrochemical-setup at RT, with WO₃ thin film deposited on the ITO coated glass substrate acting as the working electrode, a stainless steel plate is used as an auxiliary electrode, and 0.1M H₂SO₄, 0.1M Na₂SO₄, and 0.1M KCl for H⁺, Na⁺, and K⁺ respectively, as an electrolyte. The various electrochemical parameters viz. diffusion coefficients (D), transmittance modulation, CE are determined for the WO₃ thin films. The switching time (t) is measured by concurrently measuring the transmittance spectra.

4.3.1 Structural and Compositional Characterizations

XRD Measurement: Figure 4.2 shows the XRD patterns of WO₃ thin films deposited at different substrate temperatures. As shown in the Fig. 4.2, films grown at the substrate temperature up to 400 °C shows a broad hump near $2\theta = 23^\circ$, which indicates its amorphous nature. On increasing the substrate temperature, small overlapping peaks appear near $2\theta = 23.6^\circ$, as observed in the case of the film grown at 450 °C. This indicates the formation of small crystalline grains in the films. Furthermore, at 500 °C substrate temperature the high intensity peak at $2\theta = 23.6^\circ$, which corresponds to the d-value of 3.7605 Å, becomes sharper, indicating the crystalline nature of the film with (020) as the preferred plane of orientation [105]. For thin films deposited at high temperature, adatom mobility at the surface is high enough, which leads to induce crystallization with preferred orientation in the films.

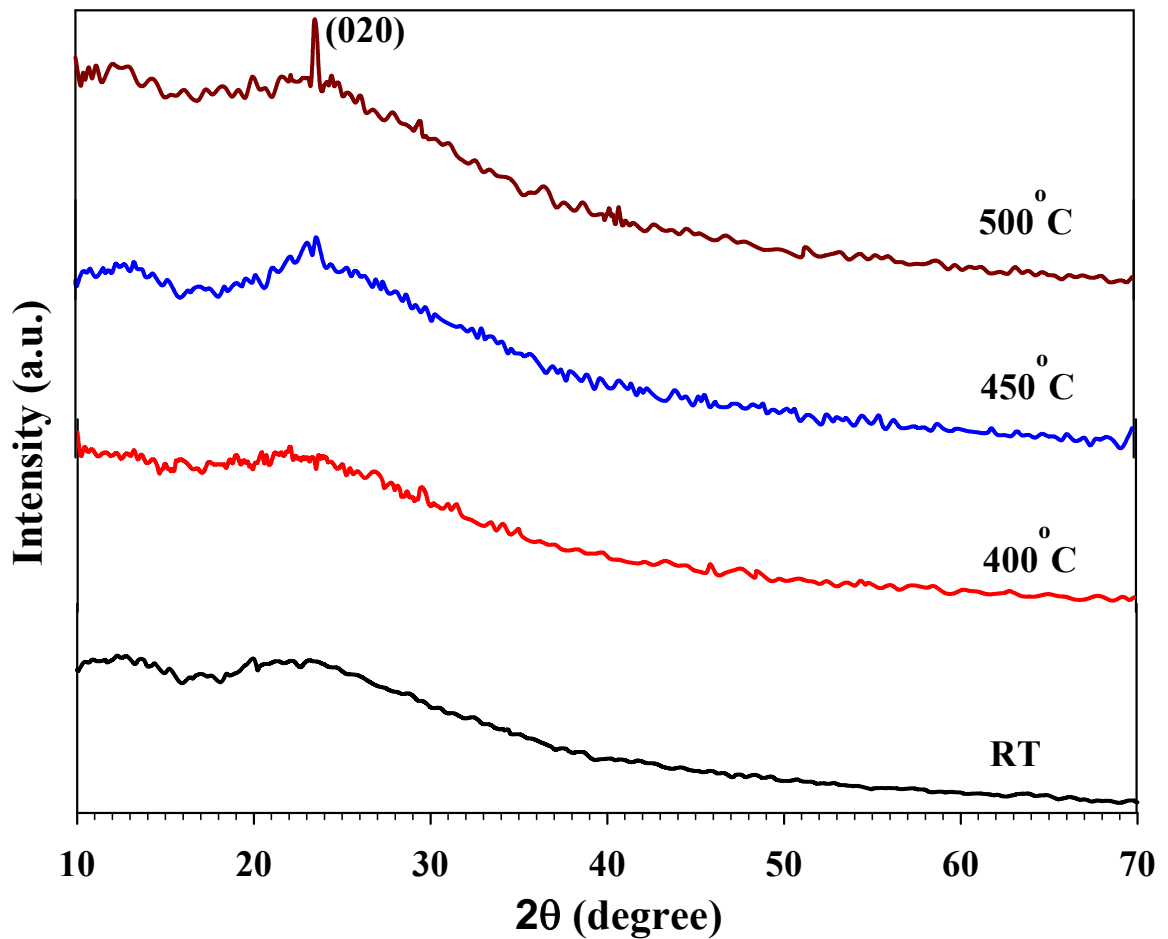


Figure 4.2: The XRD pattern of WO₃ thin films grown at different substrate temperatures.

AFM Measurement: The effect of the substrate temperature (T_s) on the surface morphology of the WO₃ films is studied using an AFM. Figure 4.3 shows the three-dimension (3D) AFM images of the WO₃ film deposited at different substrate temperatures. As shown in Fig. 4.3, the films show grain like morphology with well-defined grain boundaries. The deposited films at RT have comparatively smoother surface. The surface roughness and the grain size of the films get increased on increasing the substrate temperature as measured using Nanosurf easyScan-2 software. At RT, the root mean square surface roughness is found to be 0.92 nm. As the substrate temperature is increased from 200 °C to 400 °C, the surface roughness increases from 1.56 nm to 2.78 nm, respectively. The increment in the grain size with the substrate temperature is attributed to an atomic rearrangement that takes place due to the increased mobility of an atom on the surface of the substrate at higher temperatures, which leads to the formation of larger grains [44].

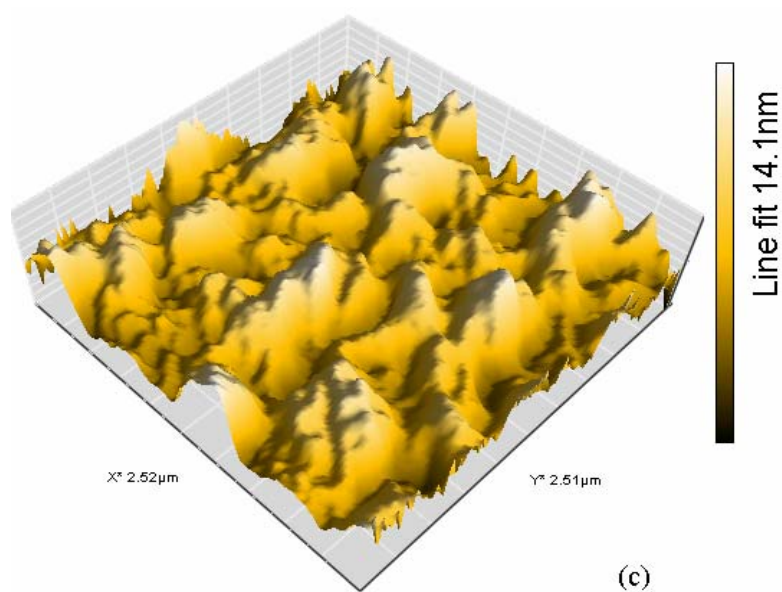
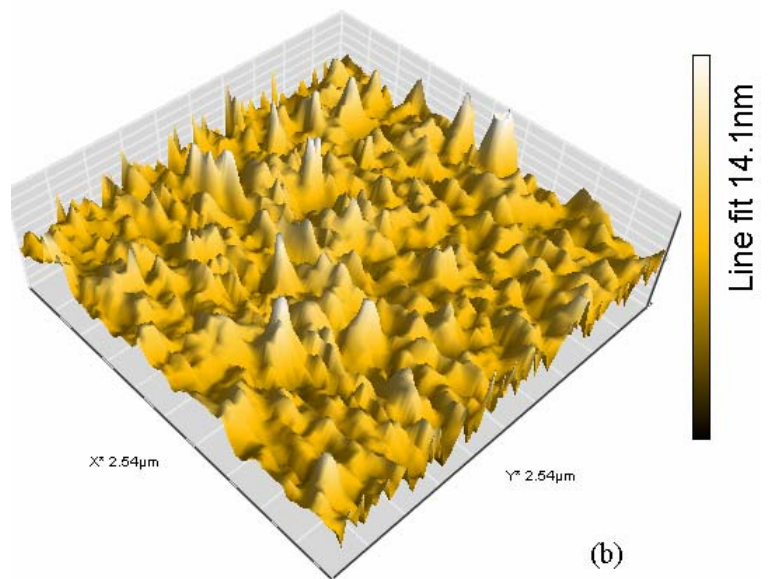
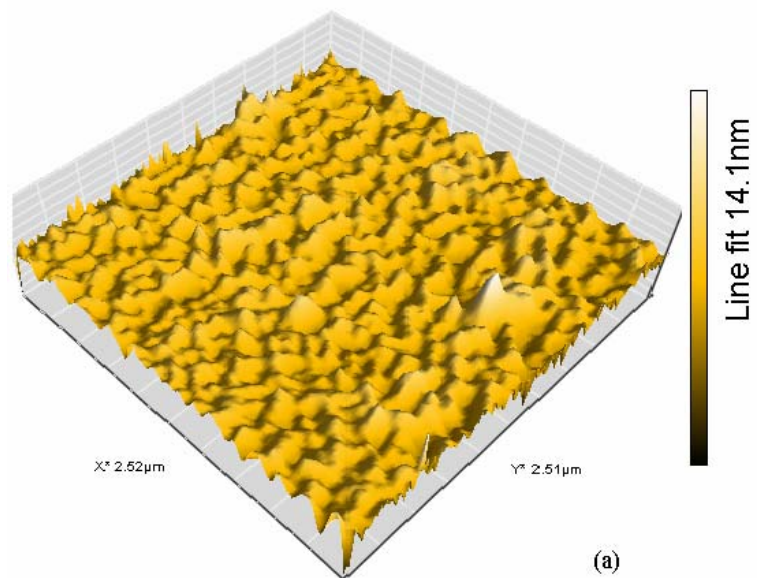


Figure 4.3: 3D AFM images of WO_3 thin films grown at substrate temperature (a) RT, (b) 200 °C, and (c) 400 °C.

XPS Measurement: The compositional characterization of WO_3 thin films deposited on the glass substrates is determined using the XPS spectra measurements. Figure 4.4 shows the XPS survey scan spectra, in the 0 – 1000 eV binding energy range, of WO_3 thin films deposited at different substrate temperatures. The survey scan spectra are particularly useful for the identification of the elements present at the film's surface. From the XPS spectra of Fig. 4.4, we can infer that the WO_3 thin films prepared in the present work shows only the characteristic peaks of W and O with C as a reference peak; hence, the compositional purity of WO_3 thin films is borne out.

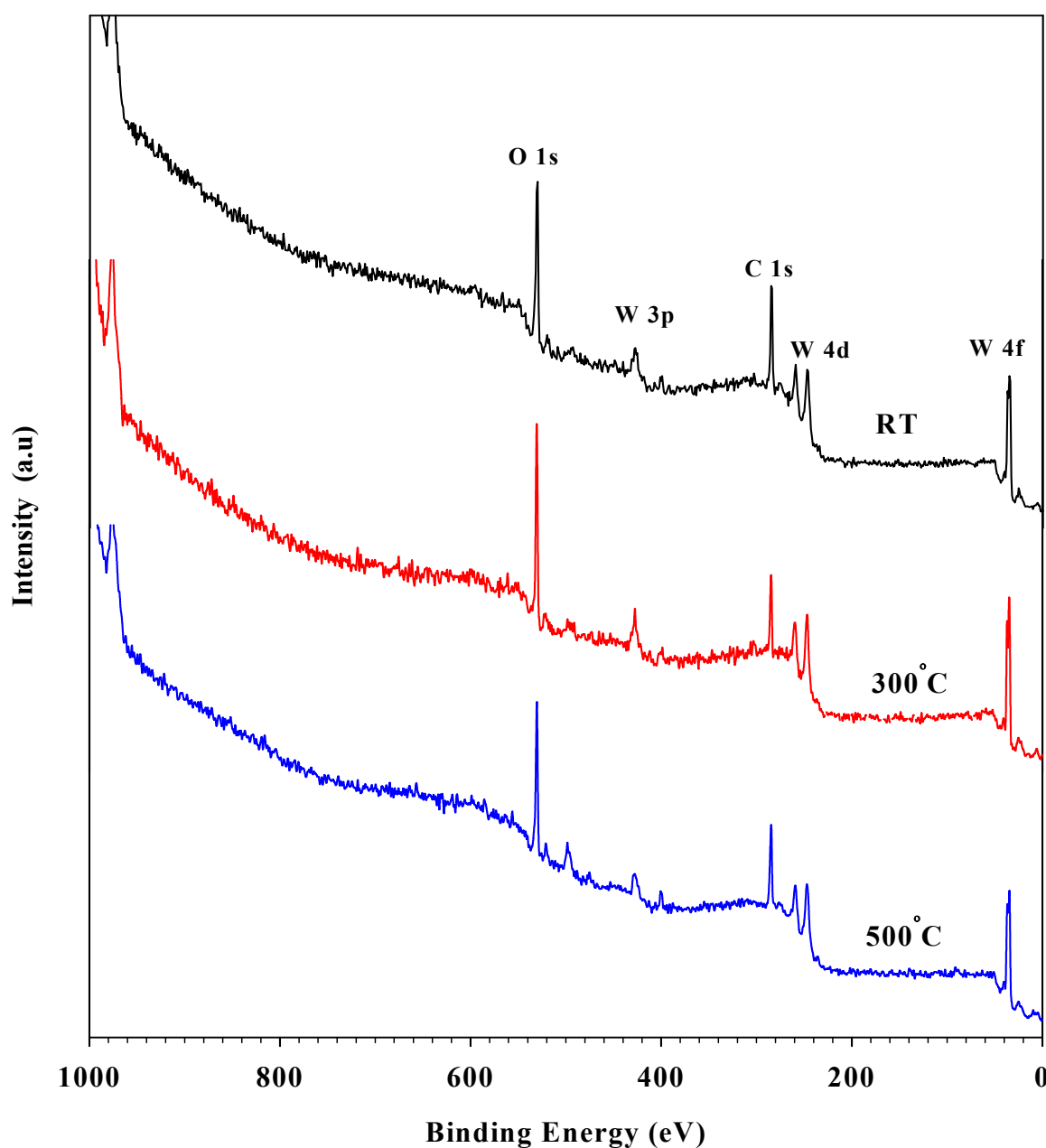


Figure 4.4: The XPS survey scan spectra of the WO_3 thin films for different substrate temperatures.

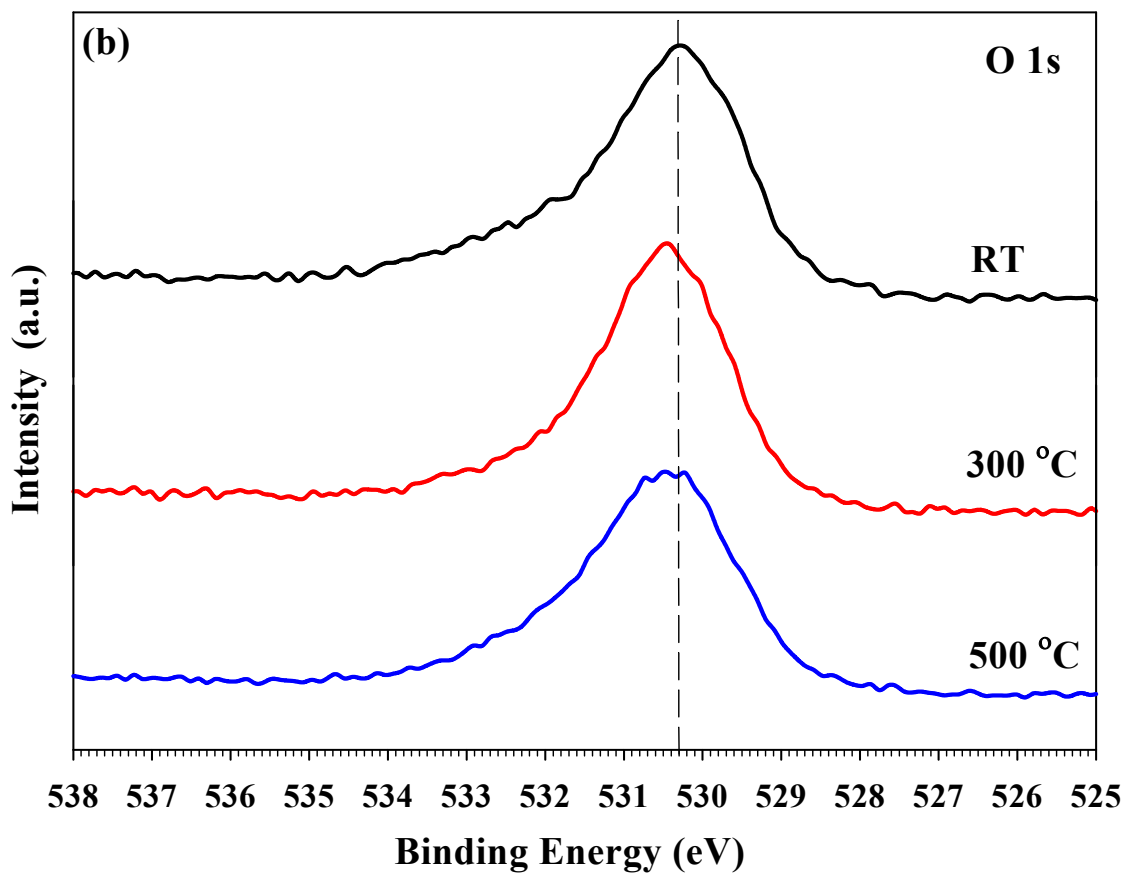
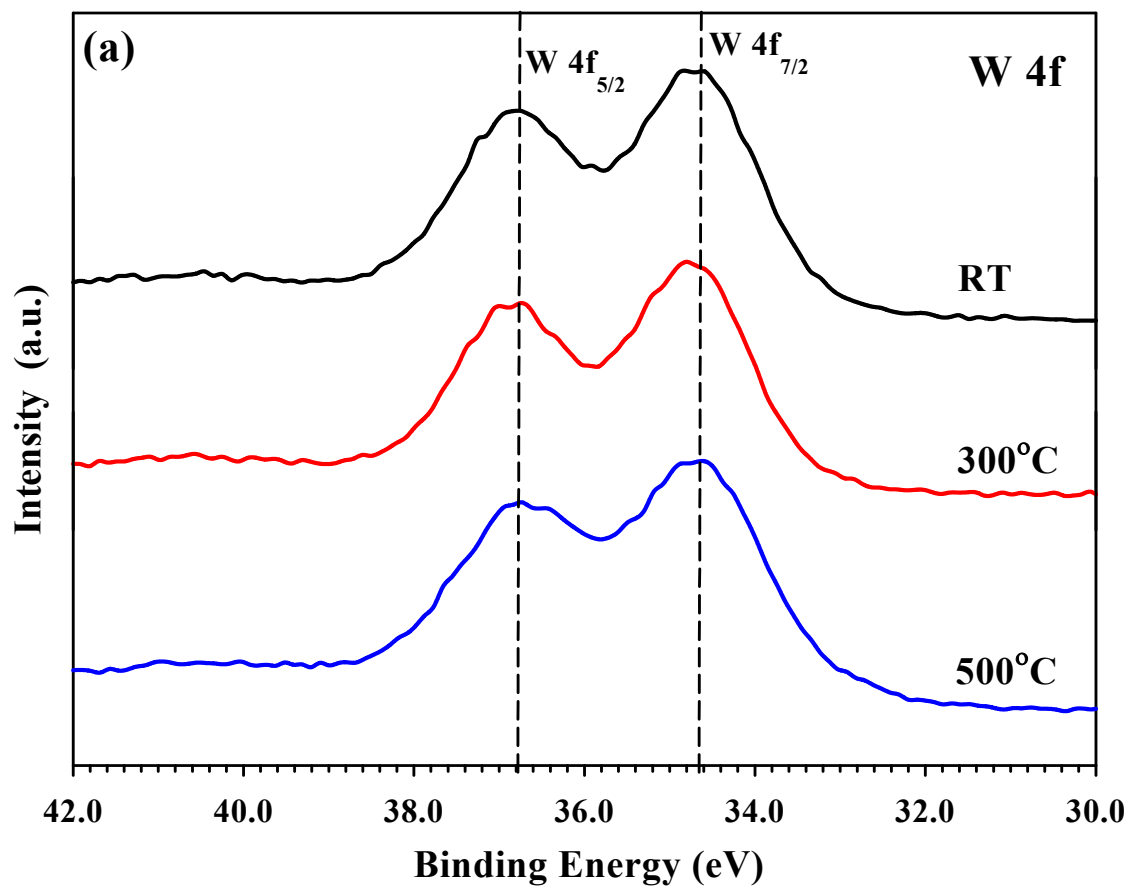


Figure 4.5: The XPS spectra of the (a) W4f and (b) O1s for different substrate temperatures.

Furthermore, to reveal the ratio of O to W, a detail scan spectra of W4f and O1s, of the as-deposited WO₃ thin films at three different substrate temperatures viz. RT, 300 °C, and 500 °C, are shown in Figure 4.5. The core level spectra of W4f, Fig. 4.5 (a), show the doublet observed at the binding energies of 34.6 and 36.8 eV, corresponding to W4f_{7/2} and W4f_{5/2}, respectively. Figure 4.5 (b), which shows the core level spectra of O1s, is unsymmetrical; this can be resolved on further examination of the XPS spectra as shown in Fig. 4.6.

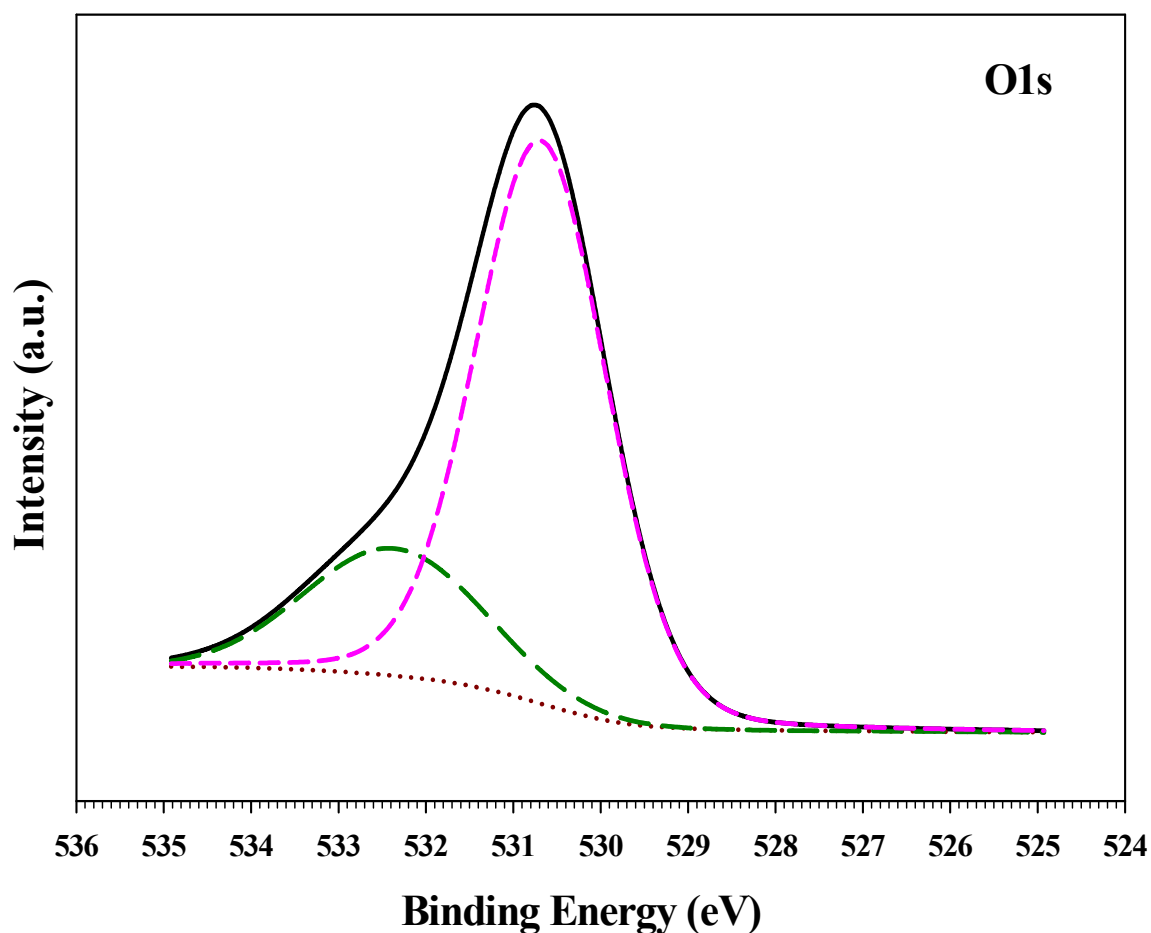


Figure 4.6: The XPS spectra of the O1s for RT grown WO₃ thin films.

It may be noted that typically there are two peaks in Fig. 4.5 (b) as depicted in Fig. 4.6: one due to the inherent O associated with W (tungsten) and another due to the contaminated O on the surface of the thin film [106]. The latter contribution gives the unsymmetrical nature of the plot of Fig. 4.5 (b). The major peak position of O1s level of WO₃ films is at binding energy 530.4 eV while the minor peak is at 532.5 eV. The binding energy (eV) and atomic ratios of oxygen to tungsten (O/W), estimated from the intensity ratio of XPS, O1s and W4f peaks, are shown in Table 4.1.

Table 4.1 The binding energy and O/W ratio of WO₃ thin films deposited at RT, 300 °C, and 500 °C.

Substrate temperature (°C)	Binding energy (eV)			Atomic concentration (%)		O/W ratio
	W4f _{7/2}	W4f _{5/2}	O1s	W	O	
RT	34.65	36.78	530.67	25.18	74.82	2.97
300	34.73	36.84	530.47	26.70	73.30	2.74
500	34.71	36.83	530.40	27.18	72.82	2.67

The O/W atomic ratio decreases as the substrate temperature increases for the WO₃ thin films grown by the thermal evaporation method. The concentration of oxygen decreases with increase in substrate temperature, which spells out the formation of oxygen ion vacancy and generation of W⁵⁺ in WO₃ thin films. This arises because at higher substrate temperature in vacuum, the oxygen atoms have a lower sticking coefficient on the substrate than the tungsten atoms [107].

4.3.2 Electrical Characterization

Electrical characterization shows that a WO₃ thin film behavior changes from high resistivity type to a highly conductive one, when the substrate temperature increases from RT to nearly 500 °C. Since the thin film grown below 400 °C are highly resistive, hence we have studied the electrical properties of the WO₃ thin films (like the resistivity (ρ), mobility (μ), and carrier concentration (n)) for the different samples grown at substrate temperatures 425 °C to 510 °C [108]. Figure 4.7 shows the variation in resistivity, mobility, and carrier concentration, as a function of substrate temperature for WO₃ thin film prepared by thermal evaporation on a glass substrate.

The resistivity of the WO₃ thin films decreases significantly while the carrier concentration and mobility increases with increase in the substrate temperature as shown in Fig. 4.7. The reduction in the resistivity can be attributed to the oxygen deficiency in the WO₃ films due to its reduced sticking coefficient at higher substrate temperature. Moreover, the oxygen deficiencies at higher substrate temperatures act as shallow donors that lead to the higher carrier concentration. The increment in the carrier concentration with the substrate temperature is also supported by the increased grain size. As observed in the AFM, the films exhibit grain-like structure. The grain size, in such films, increases due to the growth and agglomeration of grains at higher substrate temperature.

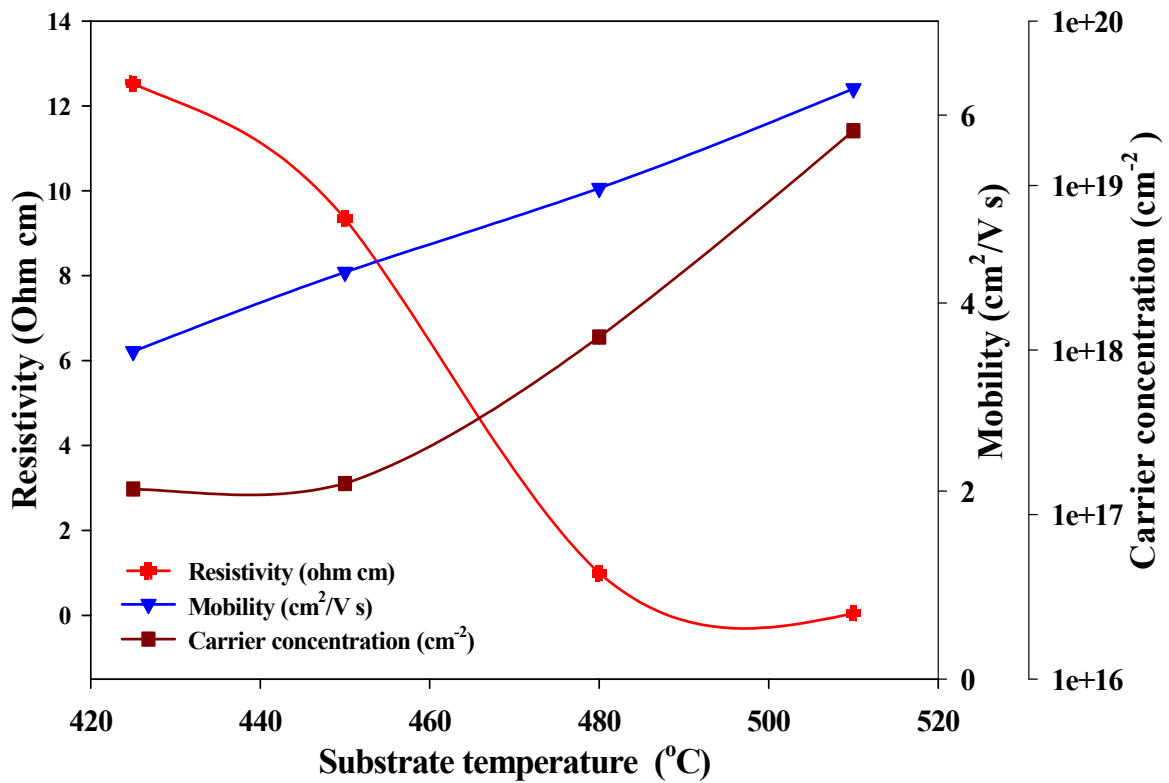


Figure 4.7: The resistivity (ρ), mobility (μ), and carrier concentration (n) of WO_3 films grown at different substrate temperatures.

In the grain-like structure, the small crystallites are joined together by grain boundaries, i.e., layers of disordered atoms, which produce a density of traps. Thus, the grain boundaries contribute to the trapping centers for free charge carriers. Moreover, the charged grain boundaries, due to trapping of free carriers, get surrounded by the space charge region of opposite polarity, which act as scattering centers for the free charge carriers and reduce the carrier mobility. A large grain means less grain boundaries existing in the film, which results in the reduced density of trapped free charge carriers [109]. Thus, the free carrier concentration increases with the substrate temperature. The less grain boundaries also result in the less carrier scattering and, consequently, the increased carrier mobility at higher substrate temperatures. Furthermore, the WO_3 films were found to be of n-type in nature, as observed from the Hall-effect experiment. This was also confirmed by the simple hot-probe method.

4.3.3 Optical Characterization

Figure 4.8 shows the transmission spectra of WO_3 thin films prepared at different substrate temperatures. The transmittance of the films, in each case, decreases sharply at the wavelength ~ 350 nm due to the fundamental absorption edge. The films prepared at substrate temperatures ranging from RT to 300°C are transparent in the visible region with more than

80 % transmittance. The films deposited at and above 400 °C are semi-transparent blue colored and the spectral transmittance decreases with increase in the substrate temperature. The decrease in the film transmission with the increase in the substrate temperature is related to the changes in the thin film stoichiometric as oxygen is released, i.e., reduction of W^{+6} to W^{+5} and W^{+4} and the formation of color centers [106]. This agrees with the XPS analysis, which showed, albeit at the surface, the presence of oxygen vacancies at higher substrate temperatures in WO_3 thin films.

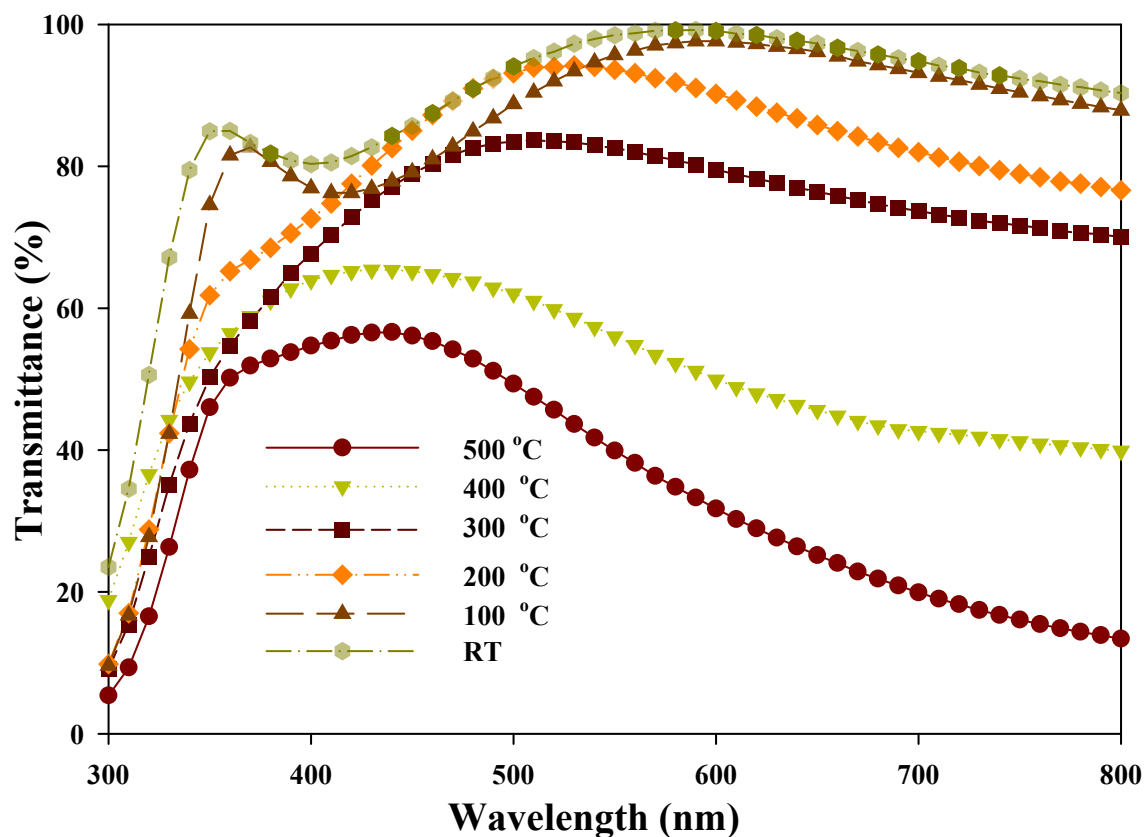


Figure 4.8: Transmission spectra of WO_3 thin films deposited at different substrate temperatures.

The optical energy band-gap of these films is determined from the transmission spectra using Tauc's relation [49]. For indirect transitions, which is the case for WO_3 film, the exponent takes the value, $\eta = 2$. Thus, the optical energy band-gap of WO_3 films deposited at different substrate temperatures was determined by plotting $(\alpha h\nu)^{1/2}$ versus the incident photon energy ($h\nu$), as shown in Fig. 4.9 (a).

The variation of optical energy band-gap with the substrate temperature is shown in Fig. 4.9 (b). As seen from the figure, the optical energy band-gap was determined to be 3.38 eV for the amorphous film deposited at the RT, whereas the optical energy band-gap for the crystalline film deposited at 500 °C comes out to be 3.05 eV.

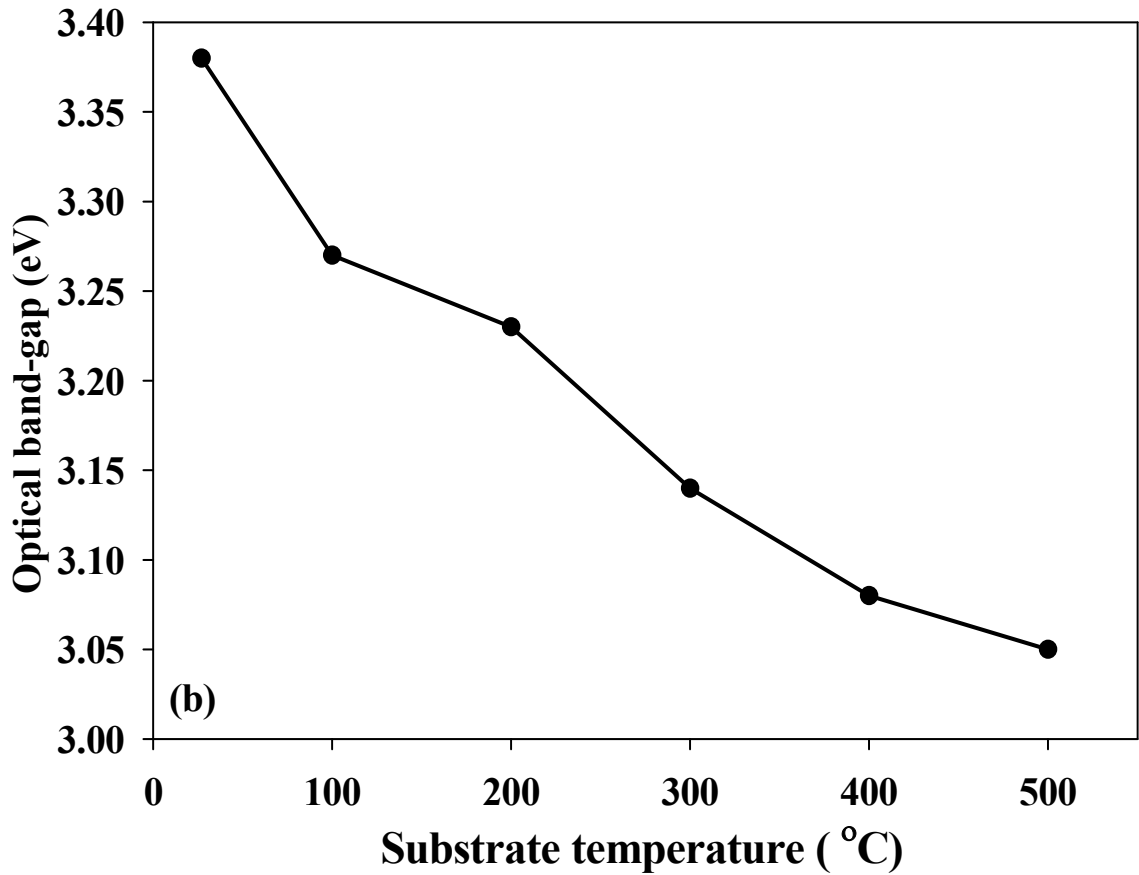
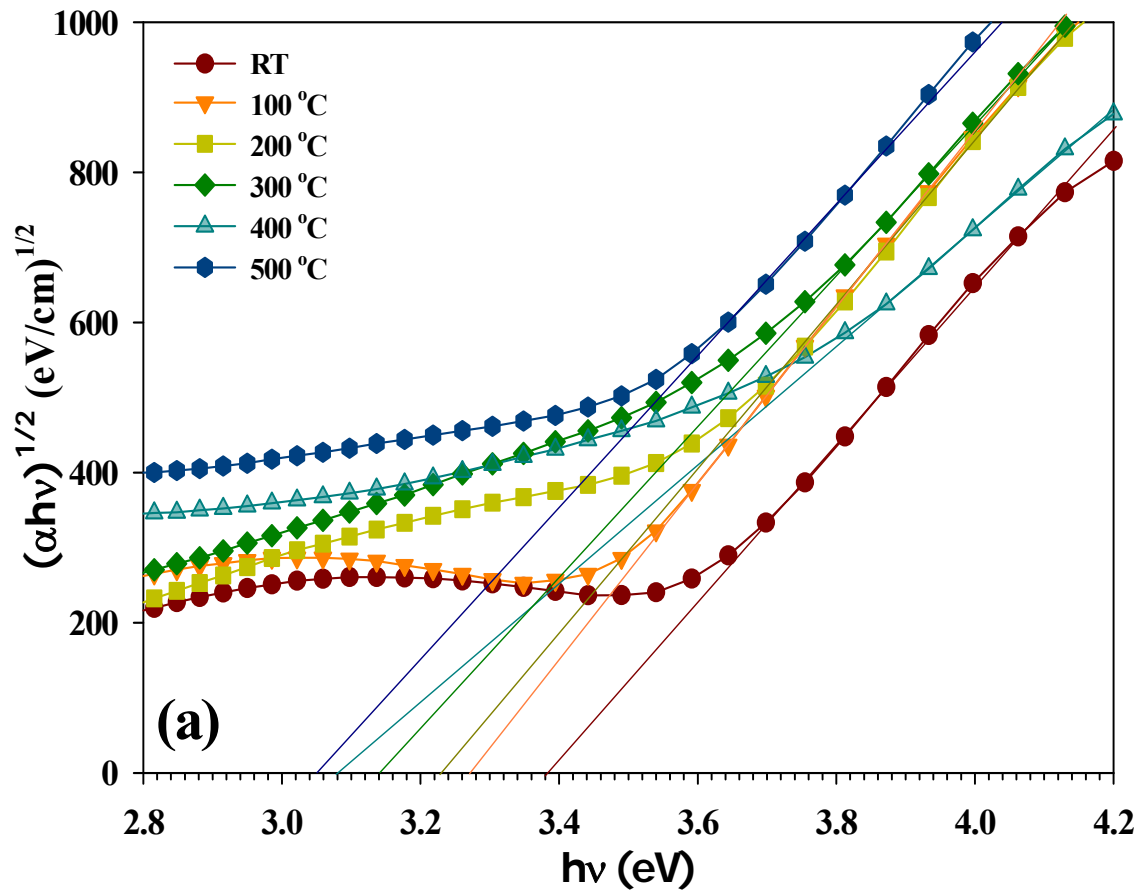


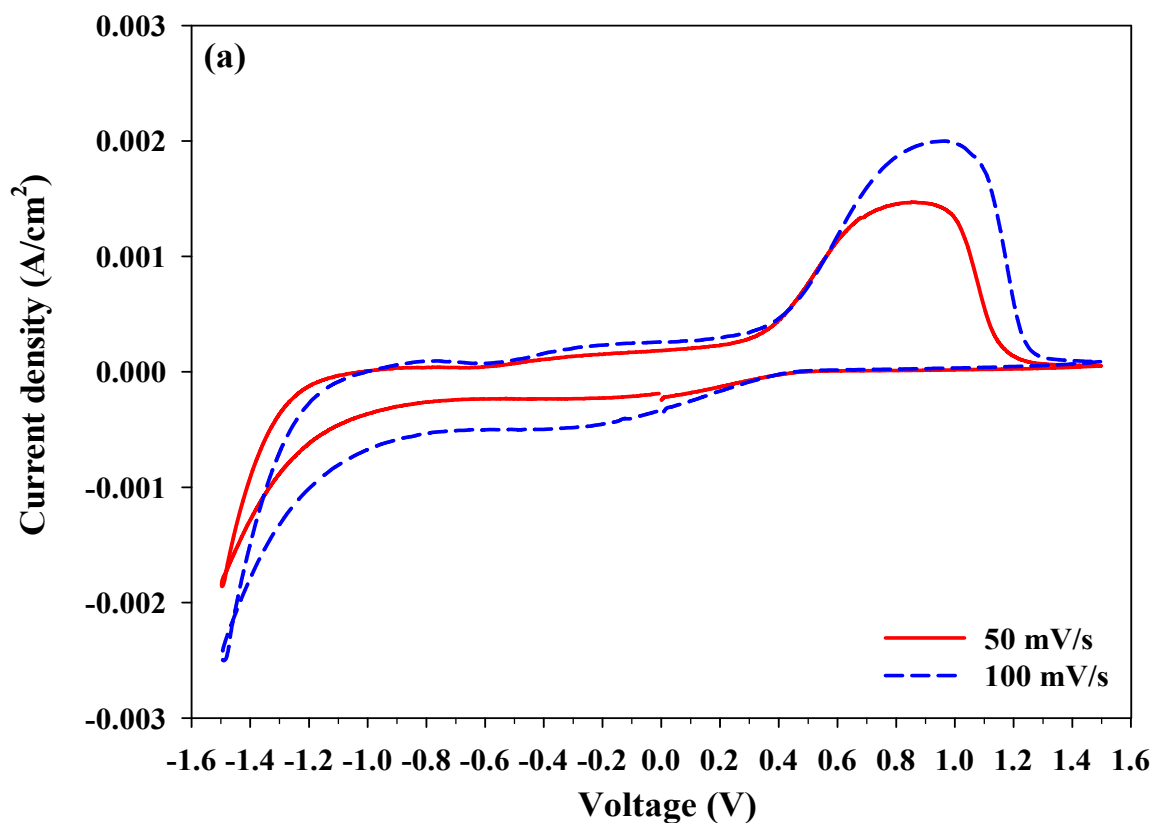
Figure 4.9: (a) $(\alpha hv)^{1/2}$ versus $h\nu$ plots for WO_3 thin films deposited at different substrate temperatures and (b) variation in optical energy band-gap (E_g) with substrate temperature.

These values of optical energy band-gap are in good agreement with the reported values of optical energy band-gap, i.e. 3.27 eV and 3.05 eV for amorphous and crystalline WO₃ film, respectively, deposited by thermal evaporation [110]. Optical energy band-gap decreases monotonically as the substrate temperature is increased. The decrement in the optical energy band-gap with the substrate temperature is due to the crystallization of films.

4.3.4 Electrochromic Characterizations

The electrochromic behavior of WO₃ thin films grown at different substrate temperatures and different ions is tested by the standard two-electrode electrochemical technique viz. cyclic voltammetry, constant current measurement, and chronoamperometry techniques. The effect of different ions H⁺, Na⁺, and K⁺ and substrate temperature are discussed here.

Effect of Different Ions: The electrochromic behavior of WO₃ thin films grown at 300 °C substrate temperature is tested for different ions. EC properties of the thin films can be related to the diffusion properties of the intercalated ions in oxides, in particular, to the ionic radius of the ions. The ionic radius of H⁺ (0.029 nm) is less compared to Na⁺ (0.095 nm) and K⁺ (0.133 nm) [111]. The diffusion coefficient of the ions in the thin film was calculated using cyclic-voltammetry (C-V) measurement in the range of -1.5 to +1.5 V. Figure 4.10 shows the cyclic-voltammogram recorded for WO₃ thin films for intercalated H⁺, Na⁺, and K⁺ ions at two different scan rates viz. 50 mV/s and 100 mV/s.



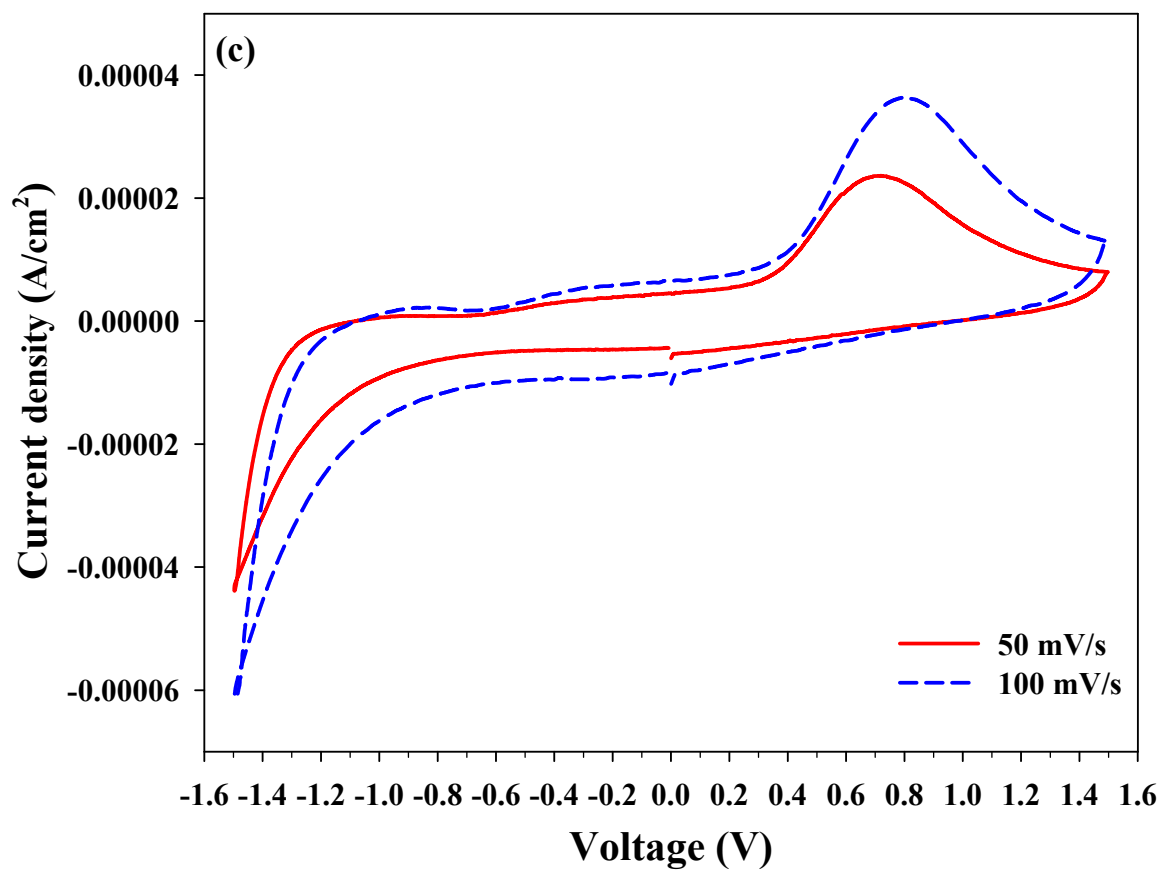
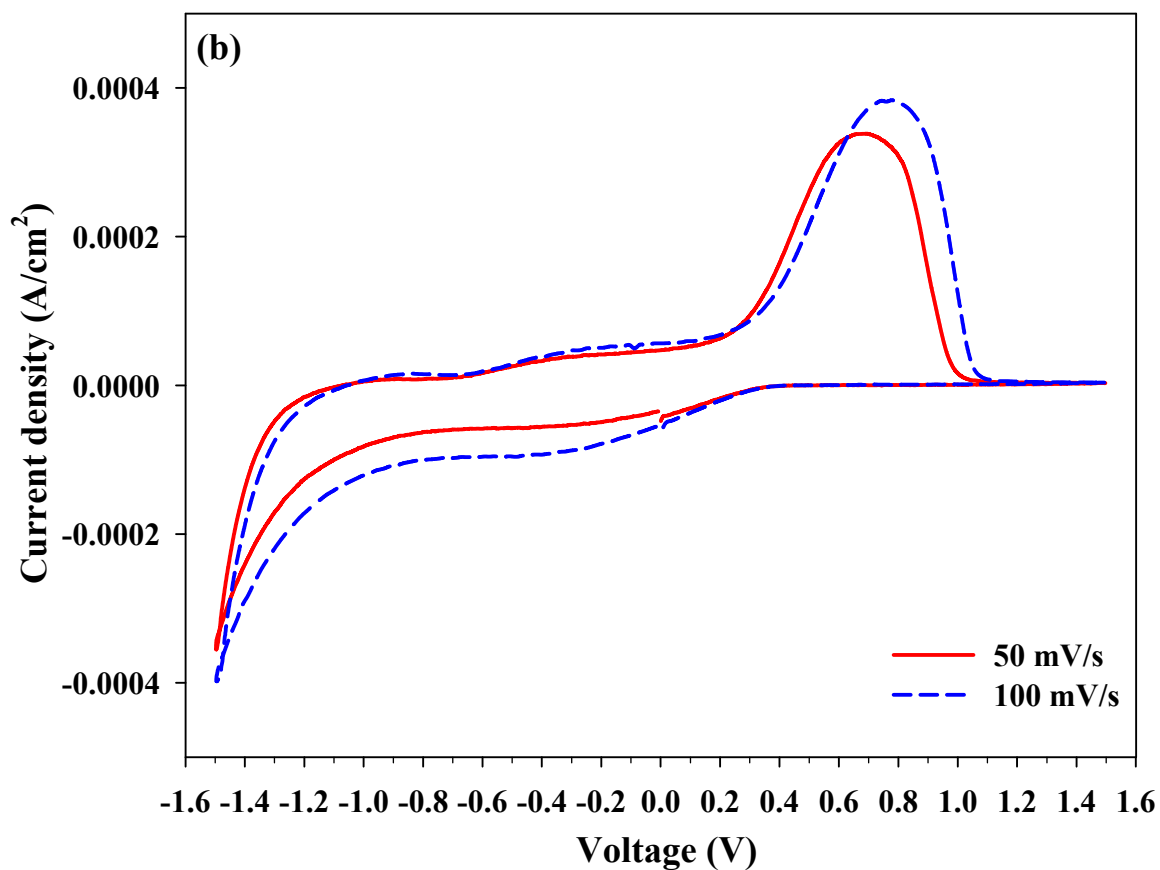


Figure 4.10: The cyclic-voltammogram of WO_3 thin films grown at substrate temperature $300\text{ }^\circ\text{C}$ for the intercalated (a) H^+ , (b) Na^+ , and (c) K^+ ions at two different scan rates 50 mV/s and 100 mV/s .

The cyclic-voltammogram shows the cathodic spike current density (i_{pc}) during negative potential scans and anodic peak current density (i_{pa}) during positive potential scans of the working electrode. The values of both the i_{pc} , and i_{pa} , for Na^+ , K^+ , and H^+ ions are used to calculate the diffusion coefficient of the ions in WO_3 thin films using Randle-Servcik equation. The electrochemical parameters i_{pc} , i_{pa} , and diffusion coefficient (D) are shown in Table 4.2.

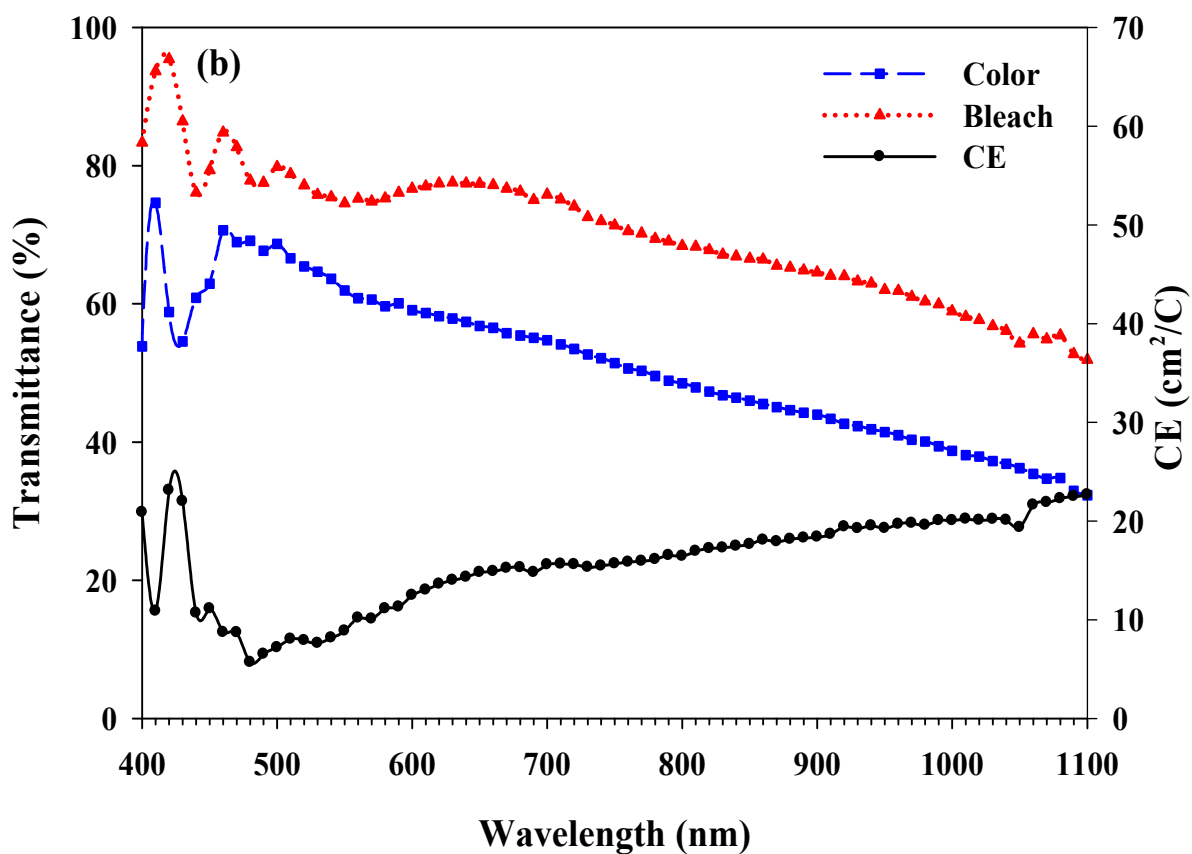
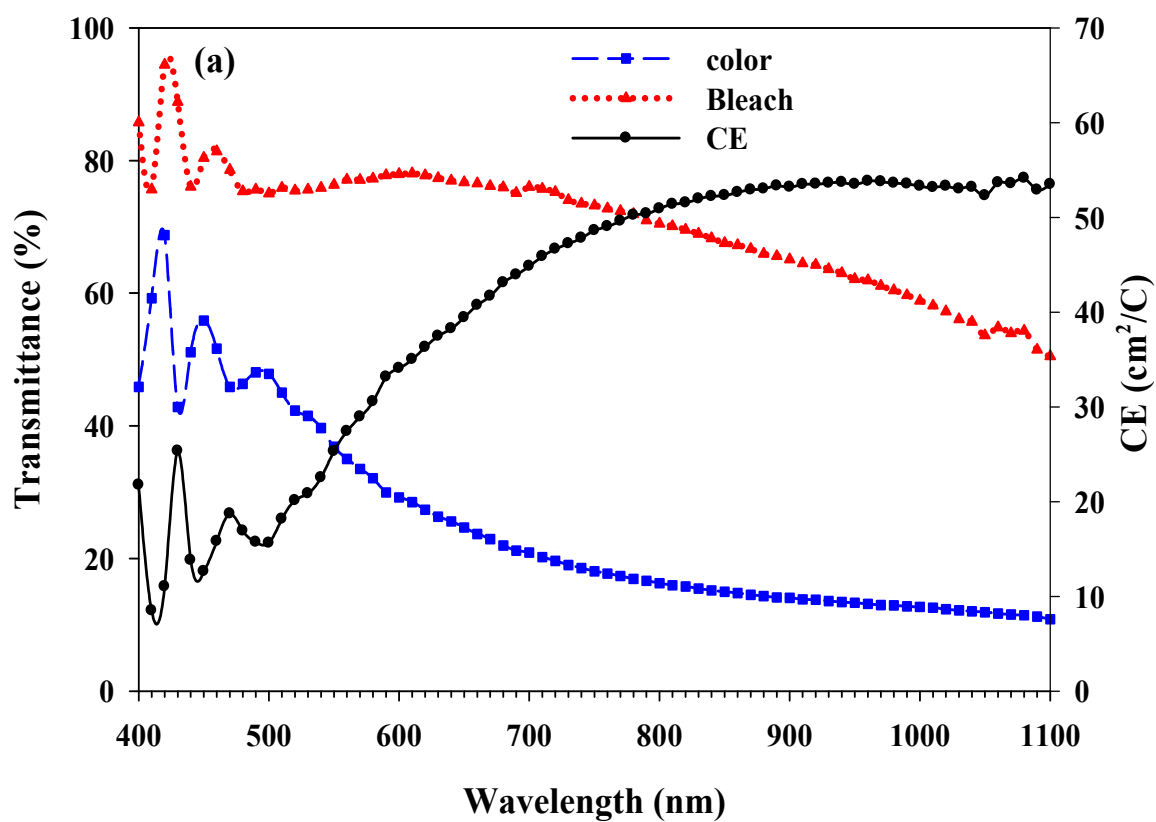
Table 4.2: Electrochemical parameters i_{pc} , i_{pa} , and D of WO_3 thin films grown at substrate temperature 300 °C for intercalated H^+ , Na^+ , and K^+ ions at 50 mV/s and 100 mV/s scan rates.

Ions	Scan Rate v (mV/s)	Current Density i (A/cm ²)		Diffusion Coefficient D (cm ² /s)	
		Cathodic spike i_{pc}	Anodic peak i_{pa}	for i_{pc}	for i_{pa}
H^+	50	1.86×10^{-3}	1.47×10^{-3}	2.40×10^{-8}	1.50×10^{-8}
	100	2.48×10^{-3}	2.00×10^{-3}	2.13×10^{-8}	1.38×10^{-8}
Na^+	50	3.55×10^{-4}	3.39×10^{-4}	8.73×10^{-10}	7.94×10^{-10}
	100	3.98×10^{-4}	3.84×10^{-4}	5.48×10^{-10}	5.09×10^{-10}
K^+	50	4.38×10^{-5}	2.36×10^{-5}	5.32×10^{-11}	1.55×10^{-11}
	100	6.12×10^{-5}	3.63×10^{-5}	5.19×10^{-11}	1.83×10^{-11}

It can be seen that the diffusion coefficient of the H^+ ions in WO_3 thin films is an order of magnitude or two more than that of Na^+ and K^+ ions, which is in agreement with the fact that as the size of the ions increases, the diffusion coefficient, and hence, the rate of diffusion decreases.

For a comparative study of transmittance modulation and CE for three different ions H^+ , Na^+ , and K^+ , the WO_3 thin films deposited on the ITO coated glass substrates at $T_s = 300$ °C are used. The variation of the optical density of the WO_3 thin films was measured by applying a constant current density of 0.4 mAcm^{-2} for 25 s both to color and bleach the thin film and concomitantly measuring the transmission spectra for both the color and the bleach states; this leads to the evaluation of the CE. Figure 4.11 shows both the wavelength dependence in the visible and near infrared region of the transmittance spectra in the colored and the bleached state and CE of WO_3 thin films for the intercalated H^+ , Na^+ , and K^+ ions. The transmittance modulation and the CE at 650 nm and 1000 nm of WO_3 thin films colored using H^+ , Na^+ , and K^+ are shown in Table 4.3. The results show that the maximum transmittance modulation and CE is for H^+ ions intercalation compared to Na^+ and K^+ ; the

decrease in the transmittance modulation and CE is caused by the decrease in diffusion coefficient due to the increase in the size of the ions [112]. Similar results were also reported for H^+ , Li^+ , and K^+ ions by K. D. Lee [113].



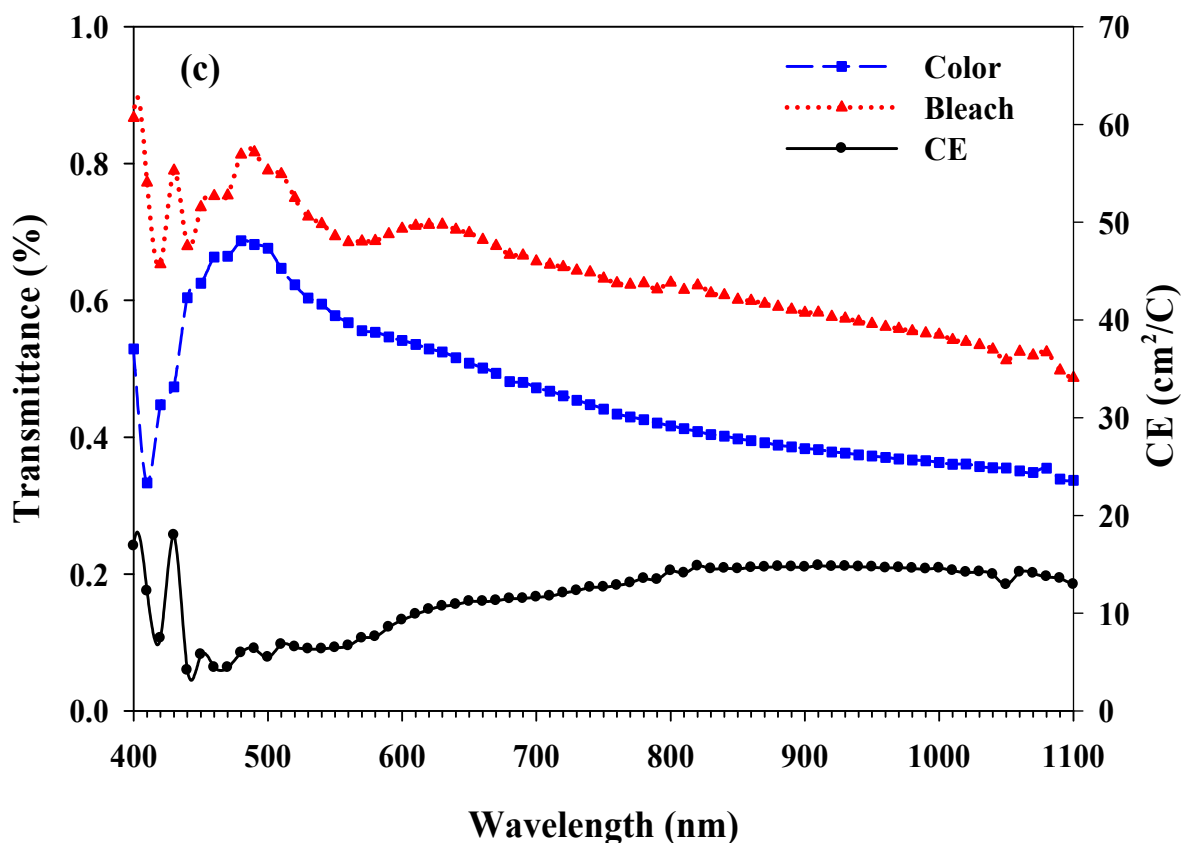


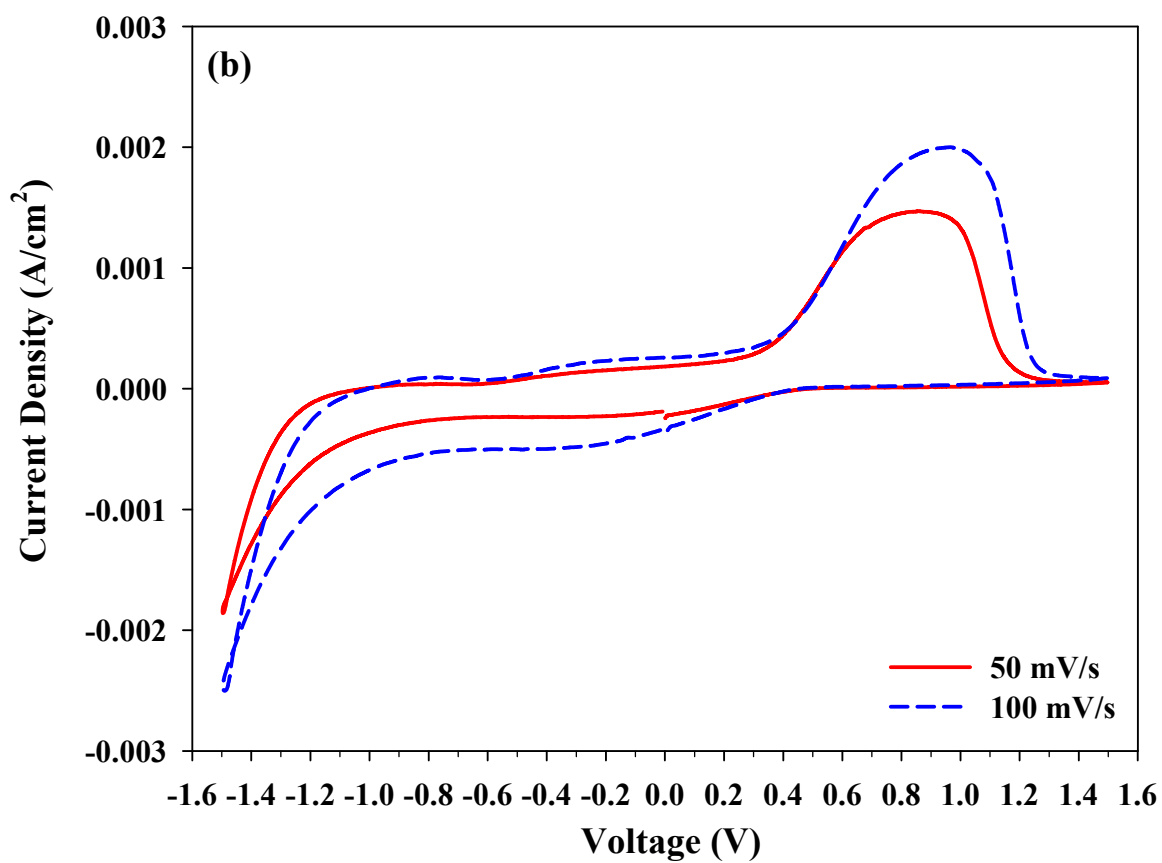
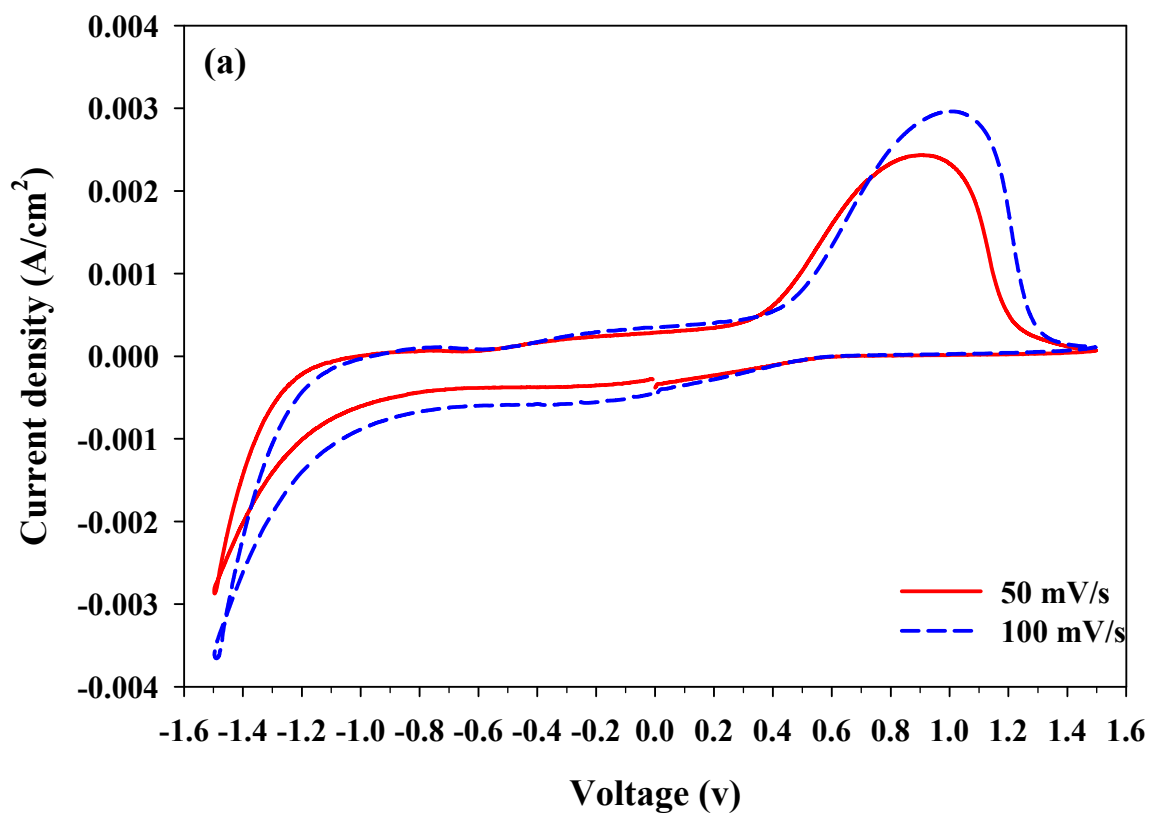
Figure 4.11: The transmittance spectra in the colored and bleached states and the CE of WO₃ films grown at T_s = 300 °C for the intercalated (a) H⁺ (b) Na⁺ and (c) K⁺ ions.

Table 4.3: The transmittance modulation and CE for different intercalated H⁺, Na⁺ and K⁺ ions for the WO₃ thin films grown at T_s = 300 °C.

Ions	Transmittance Modulation ΔT (%)		Coloration Efficiency CE (cm ² /C)	
	$\lambda = 650$ nm	$\lambda = 1000$ nm	$\lambda = 650$ nm	$\lambda = 1000$ nm
H ⁺	52	47	39.4	57.7
Na ⁺	21	20	14.9	20.0
K ⁺	19	19	11.2	14.6

Effect of Substrate Temperature: To study the effect of substrate temperature on the electrochromic properties, three different substrate temperature grown WO₃ thin films are used and the H⁺ ions is inserted in all thin films. EC properties of the thin films can be related to the diffusion properties of the intercalated ions in oxides. The diffusion coefficient of the ions in the thin film was calculated using C-V measurement in the range of -1.5 to +1.5 V. Figure 4.12 shows the cyclic-voltammogram recorded for WO₃ thin films for intercalated H⁺ ions at two different scan rates viz. 50 mV/s and 100 mV/s. The cyclic-voltammogram shows the cathodic spike in current density (i_{pc}) during negative potential

scans and anodic peak in current density (i_{pa}) during positive potential scans of the working electrode.



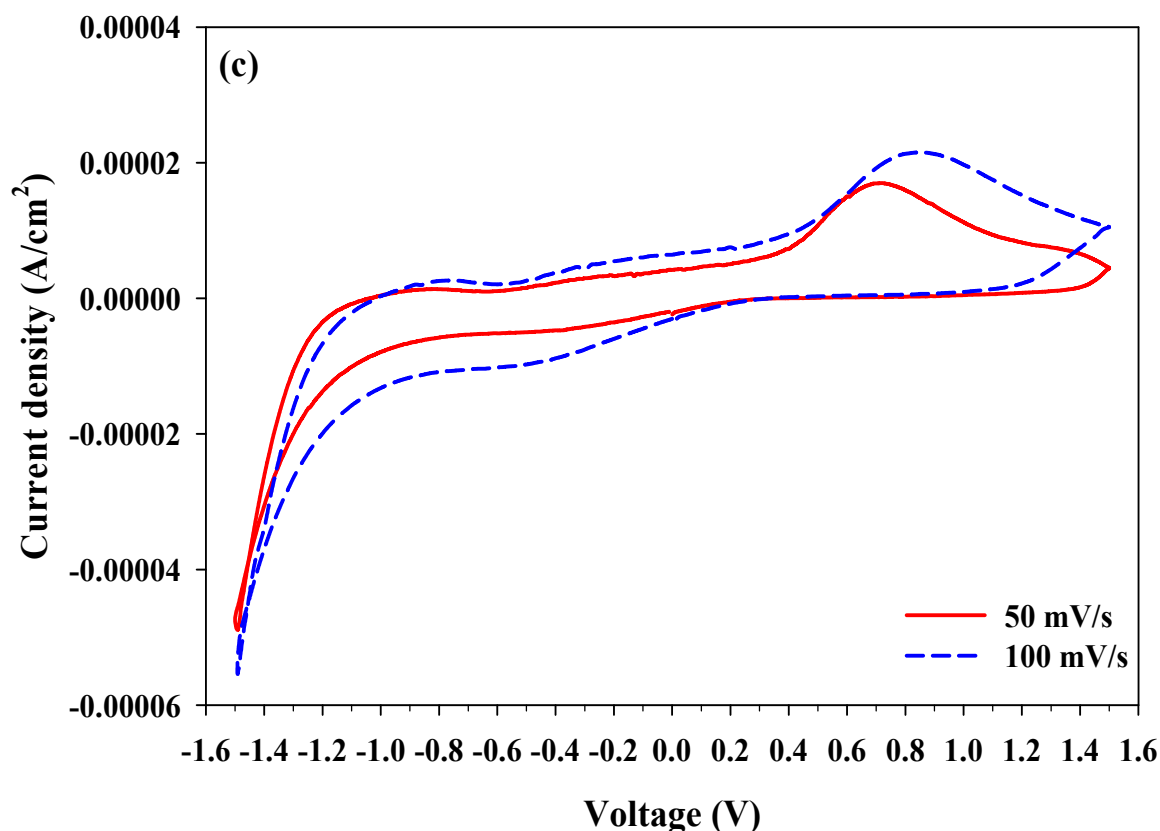


Figure 4.12: The cyclic-voltammogram of WO_3 thin films grown at (a) RT (b) $300\text{ }^\circ\text{C}$ and (c) $500\text{ }^\circ\text{C}$ substrate temperature and intercalated with H^+ ions at two different scan rates 50 mV/s and 100 mV/s.

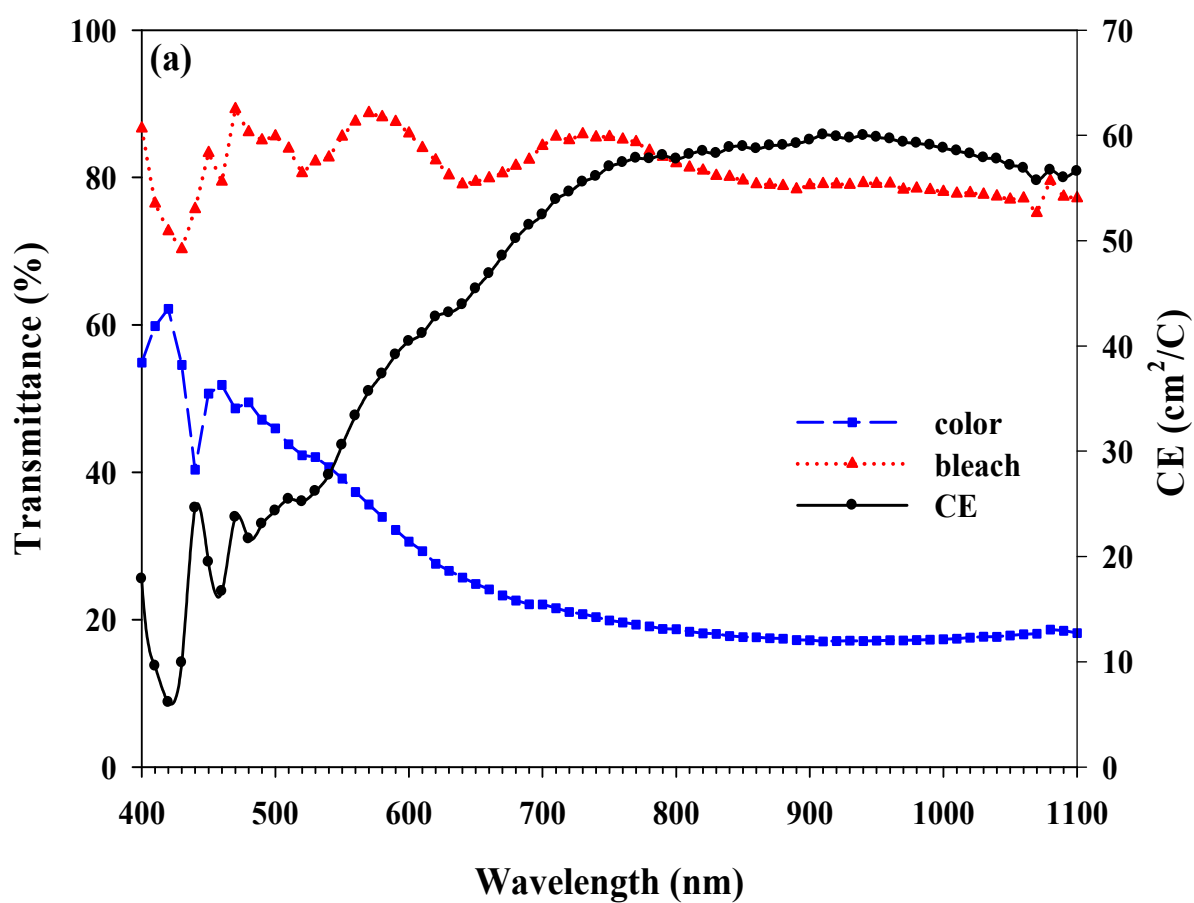
The values of both the i_{pc} and i_{pa} for H^+ ions are used to calculate the diffusion coefficient of the ions for different substrate temperature grown WO_3 thin films using the Randle-Servcik equation. The peak current density decreases as the substrate temperature increases from RT to $500\text{ }^\circ\text{C}$. The electrochemical parameters i_{pc} , i_{pa} , and diffusion coefficient (D) are shown in Table 4.4.

From the C-V measurement, the diffusion coefficient of the RT to $300\text{ }^\circ\text{C}$ films is three to four orders of magnitude greater than the $500\text{ }^\circ\text{C}$ films for H^+ ions, which is due to the crystallization of films at higher substrate temperature. A crystallized structure is less favorable for ions to diffuse through because of the densely packed atomic structure.

The electrochromic behavior of WO_3 thin films grown at different substrate temperatures is tested for H^+ ions and the same amount of charge is inserted in all the thin films. Coloration and bleaching processes were carried out at constant current density of $0.4\text{ mA}/\text{cm}^2$ applied for 25 s. Figure 4.13 shows the transmittance spectra in both the colored and bleached state, and the CE, of WO_3 thin films grown at different substrate temperatures viz. RT, $300\text{ }^\circ\text{C}$, and $500\text{ }^\circ\text{C}$.

Table 4.4: Electrochemical parameters i_{pc} , i_{pa} , and D of WO_3 thin films grown at different substrate temperature and intercalated with H^+ ions at 50 mV/s and 100 mV/s scan rates.

Substrate Temperature (°C)	Scan rate ν (mV/s)	Current density (i) (A/cm ²)		Diffusion coefficient D (cm ² /s)	
		Cathodic spike i_{pc}	Anodic peak i_{pa}	for i_{pc}	for i_{pa}
RT	50	2.87×10^{-3}	2.43×10^{-3}	5.71×10^{-8}	4.10×10^{-8}
	100	3.62×10^{-3}	2.96×10^{-3}	4.55×10^{-8}	3.04×10^{-8}
300	50	1.86×10^{-3}	1.47×10^{-3}	2.40×10^{-8}	1.50×10^{-8}
	100	2.48×10^{-3}	2.00×10^{-3}	2.13×10^{-8}	1.38×10^{-8}
500	50	4.99×10^{-5}	1.70×10^{-5}	1.66×10^{-11}	2.00×10^{-12}
	100	5.54×10^{-5}	2.15×10^{-5}	1.06×10^{-11}	1.60×10^{-12}



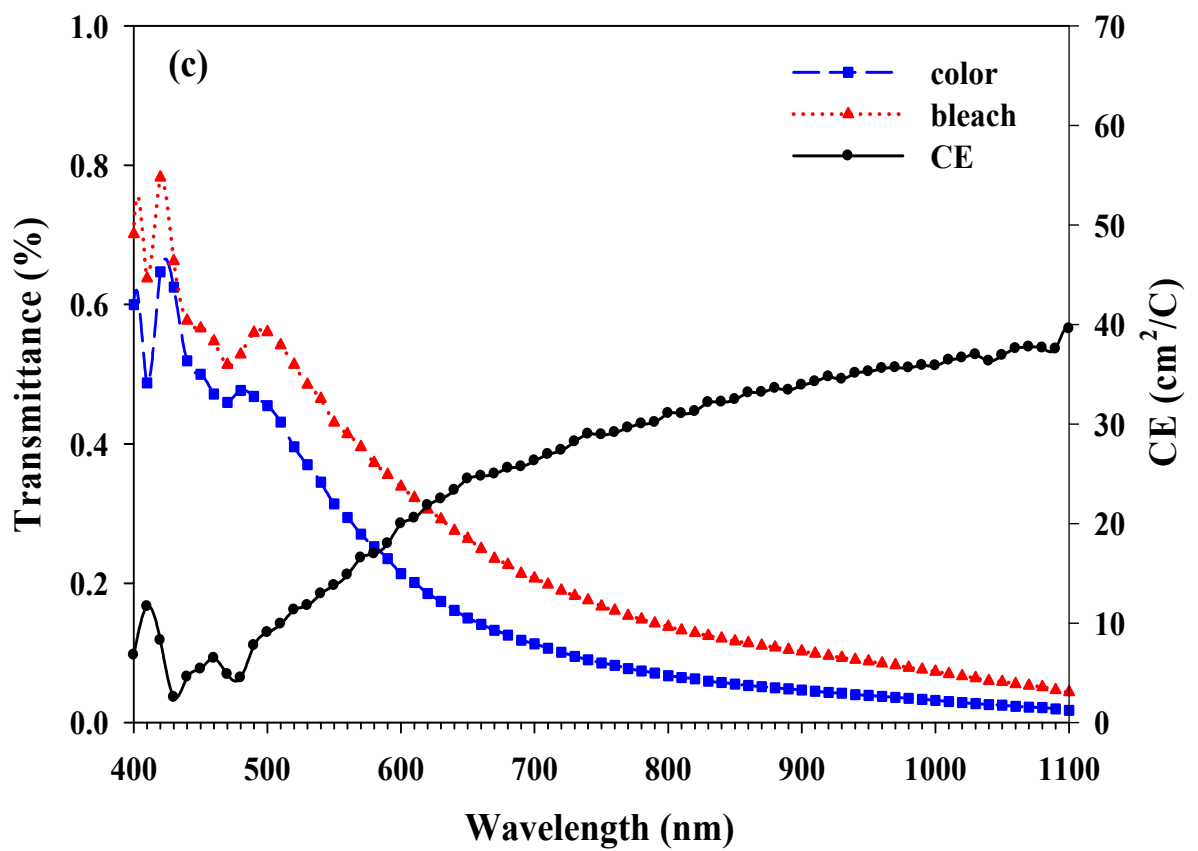
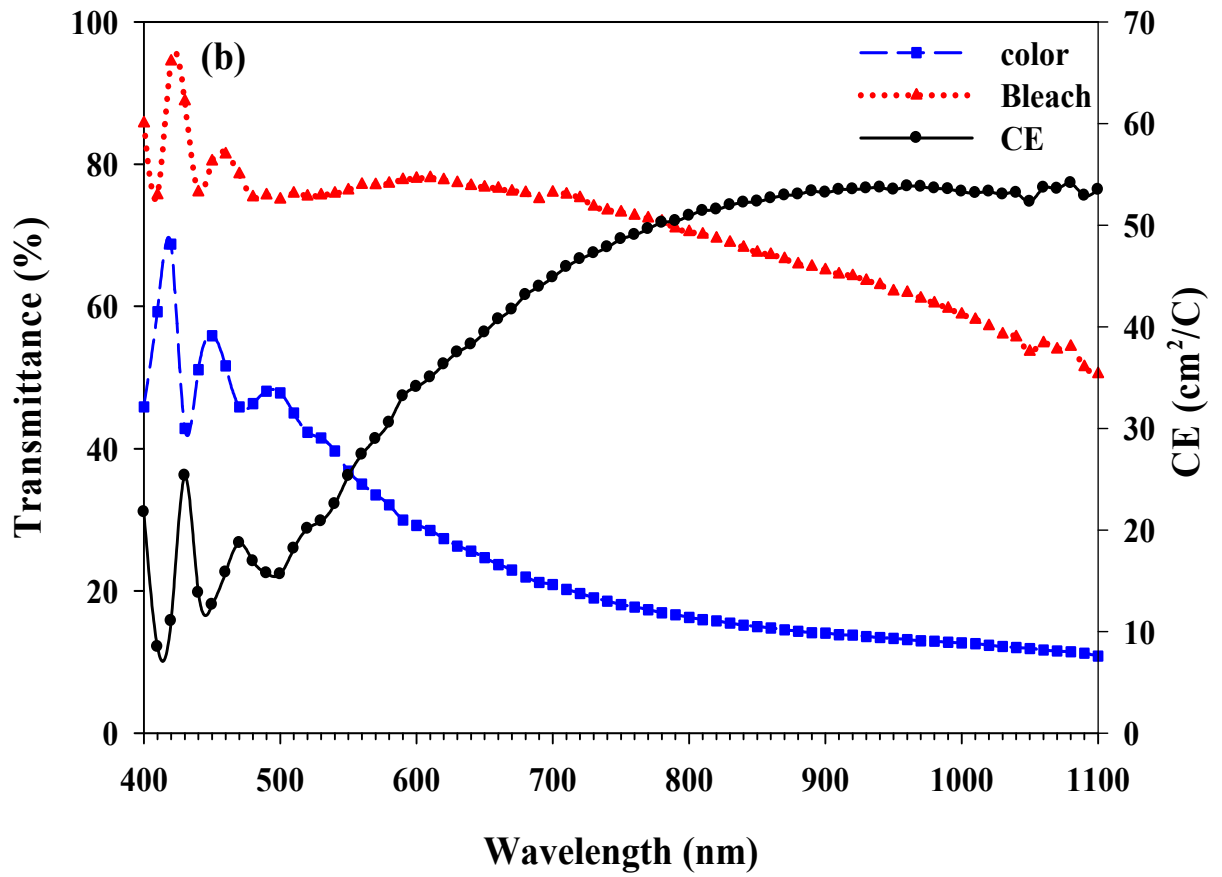


Figure 4.13: The transmittance spectra in the color and bleach state and the CE of WO_3 thin films grown at different substrate temperature viz. (a) RT (b) $300\text{ }^\circ\text{C}$ (c) $500\text{ }^\circ\text{C}$.

Table 4.5: The transmittance modulation and CE for WO₃ thin films grown at different substrate temperature.

Substrate Temperature, T _s (°C)	Transmittance Modulation, ΔT (%)		Coloration Efficiency, CE (cm ² /C)	
	λ = 650 nm	λ = 1000 nm	λ = 650 nm	λ = 1000 nm
RT	55	61	45.4	58.8
300	52	47	39.4	57.7
500	11	4	24.5	35.8

Table 4.5 shows the transmittance modulation and CE of WO₃ thin films, at wavelengths 650 nm and 1000 nm, grown at different substrate temperatures viz. RT, 300 °C, and 500 °C. The RT grown film shows a larger transmittance modulation and CE as compared to the higher substrate temperature grown thin films. The 300 °C substrate temperature grown WO₃ thin film shows only a slightly lower transmittance modulation and CE than that of the RT, whereas the transmittance modulation and CE for the 500 °C substrate temperature grown thin films are significantly low. As the substrate temperature increases the transmittance modulation as well as the CE decreases due to the improvement in the crystallinity: a crystallized structure is less favorable for ions to diffuse through because of the densely packed atomic structure [112].

The transmittance spectra for different levels of intercalation for insertion of H⁺ ions in the RT grown WO₃ thin film a constant current density of 0.2 mA/cm² applying for the insertion of H⁺ ions and concomitantly, recording the transmittance spectra are shown in Fig. 4.14 (a). The transmittance decreases with the increase in insertion of H⁺ ions and electrons. This is due to the increased absorption by creation of W⁵⁺ state in the films [114]. A nearly linear relationship is observed between change in optical density (ΔOD) and the inserted charge density, as shown in Fig. 4.14 (b). The slope of the linear part of the optical density (OD) and the inserted charge density graph directly give the CE value. The photographs of WO₃ thin films grown at RT and intercalated using H⁺ ions in bleached and colored state are shown in Fig. 4.15.

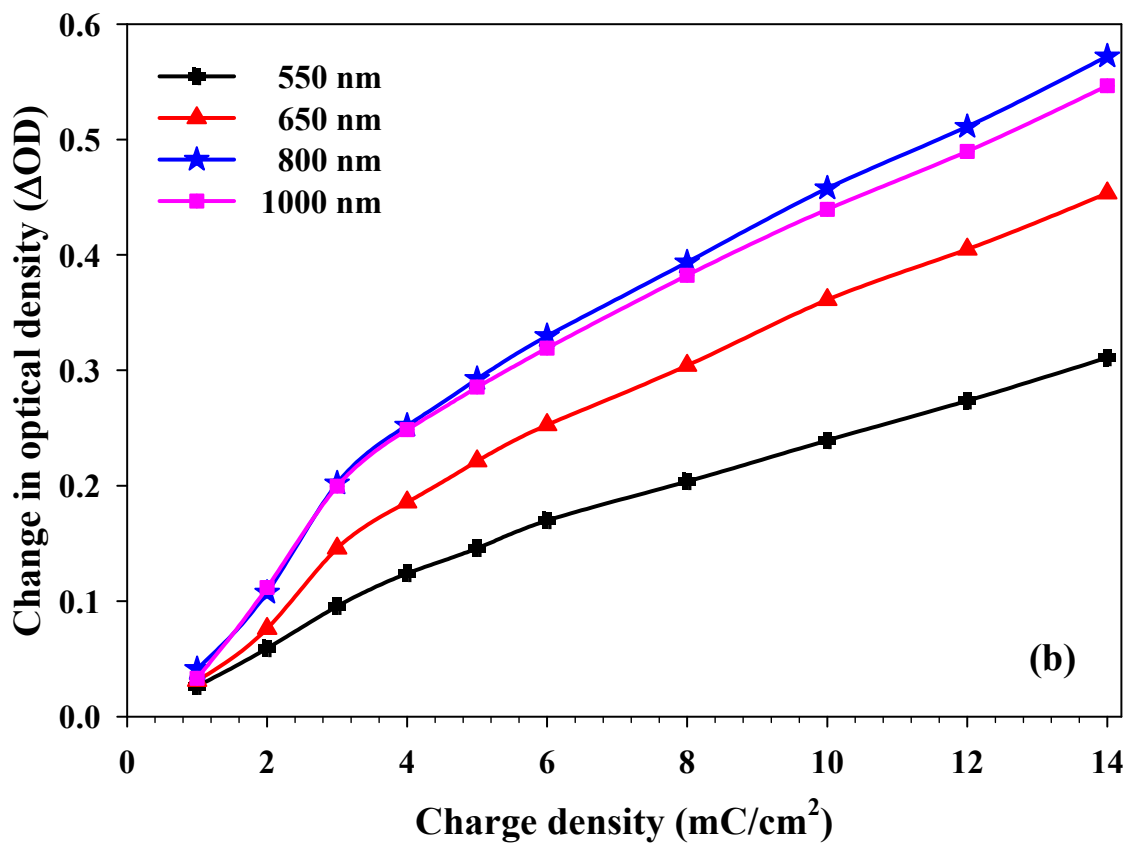
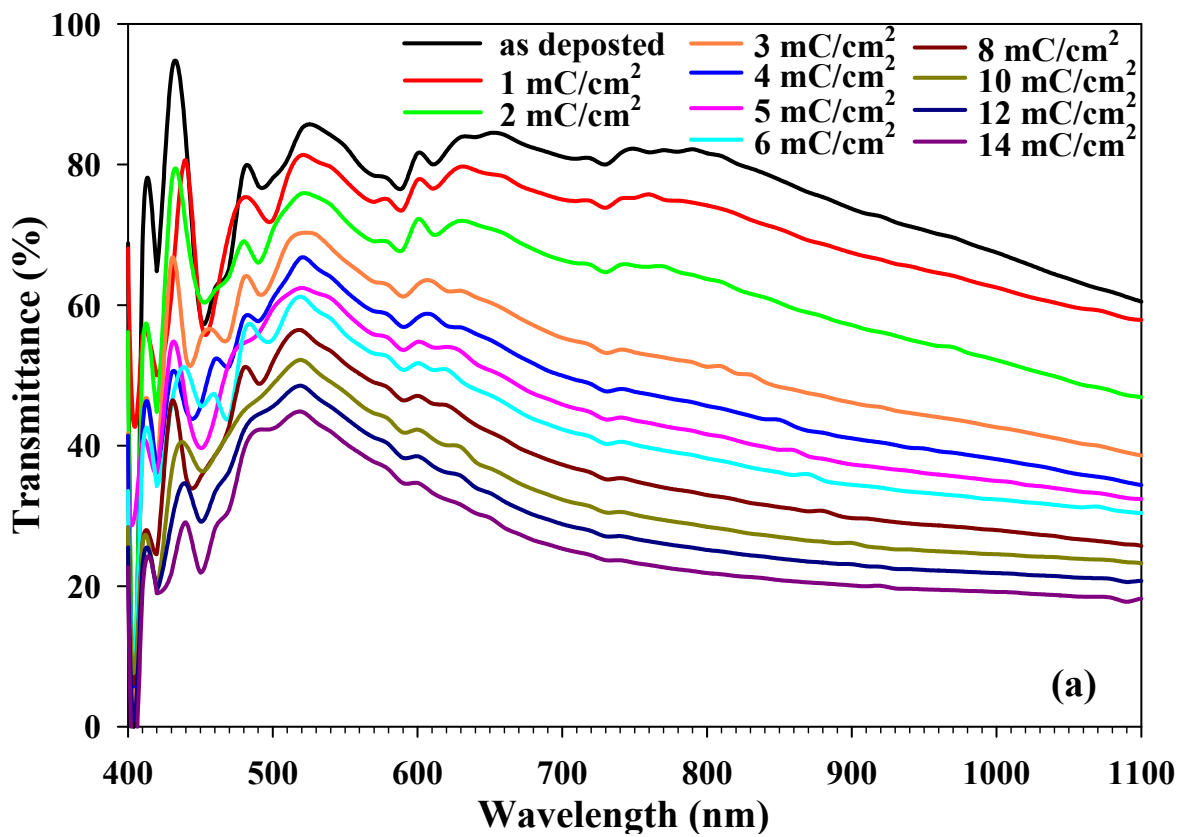


Figure 4.14: (a) The transmittance spectra for different levels of intercalation (b) relation between change in optical density (ΔOD) and the inserted charge density for insertion of H^+ ions in the RT grown WO_3 thin film.

Using the chronoamperometry technique, the switching time of the different substrate temperatures grown WO_3 thin films is measured by applying a square-wave potential of ± 1.5 V, at a frequency of 0.05 Hz, between the electrochromic electrode and the auxiliary electrode, both in 0.1M H_2SO_4 electrolyte solutions. In addition, concurrently, both the current and the variation in the optical transmittance with time are recorded. Figure 4.16 shows the current density and transmittance versus time, at 650 nm wavelengths, for a square-wave potential of ± 1.5 V.

The lower transmittance for the thin films in their coloration and bleach process for the film deposited at a higher temperature than at the RT is due to the absorption of light from some of the W^{5+} states already present in the thin films. The switching time, at 650 nm wavelength, is estimated from Fig. 4.16 (a) and (b) for the thermally evaporated WO_3 thin films grown at different substrate temperatures, as shown in Table 4.6.

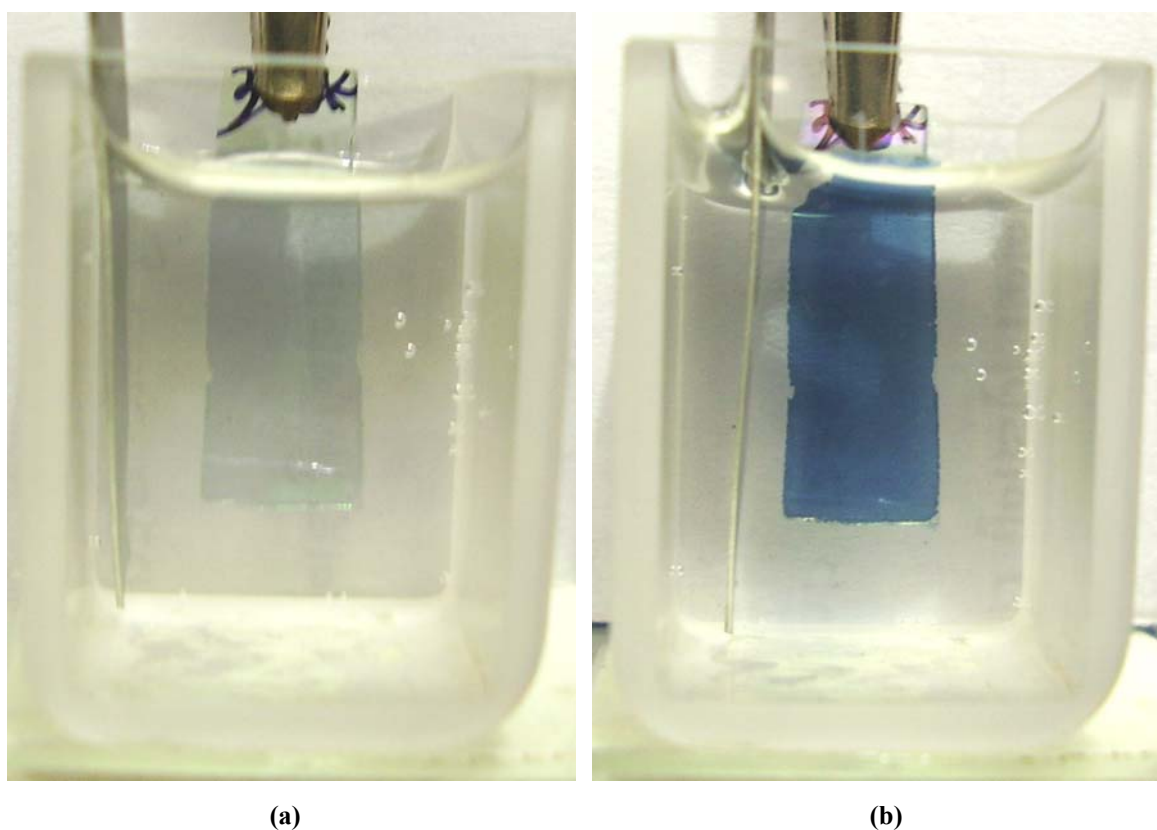


Figure 4.15: The photographs of WO_3 thin films grown at RT and intercalated using H^+ ions in (a) bleached and (b) colored state.

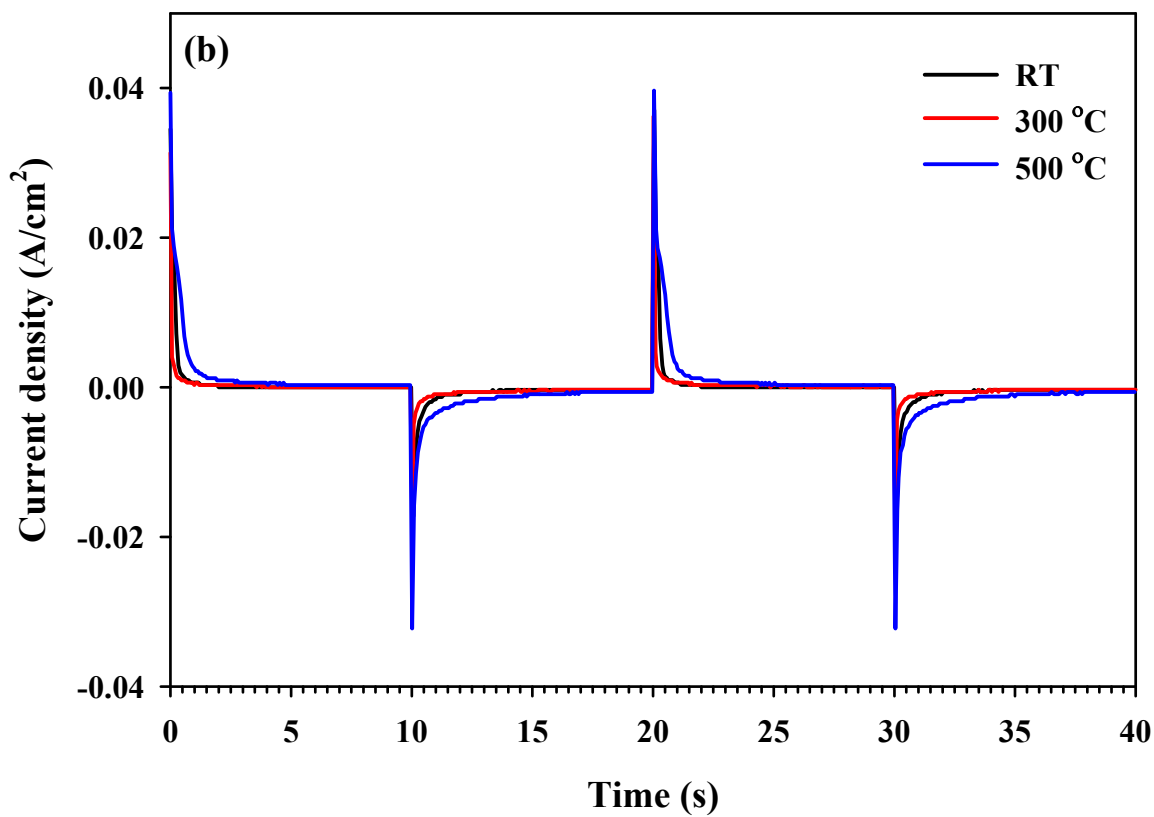
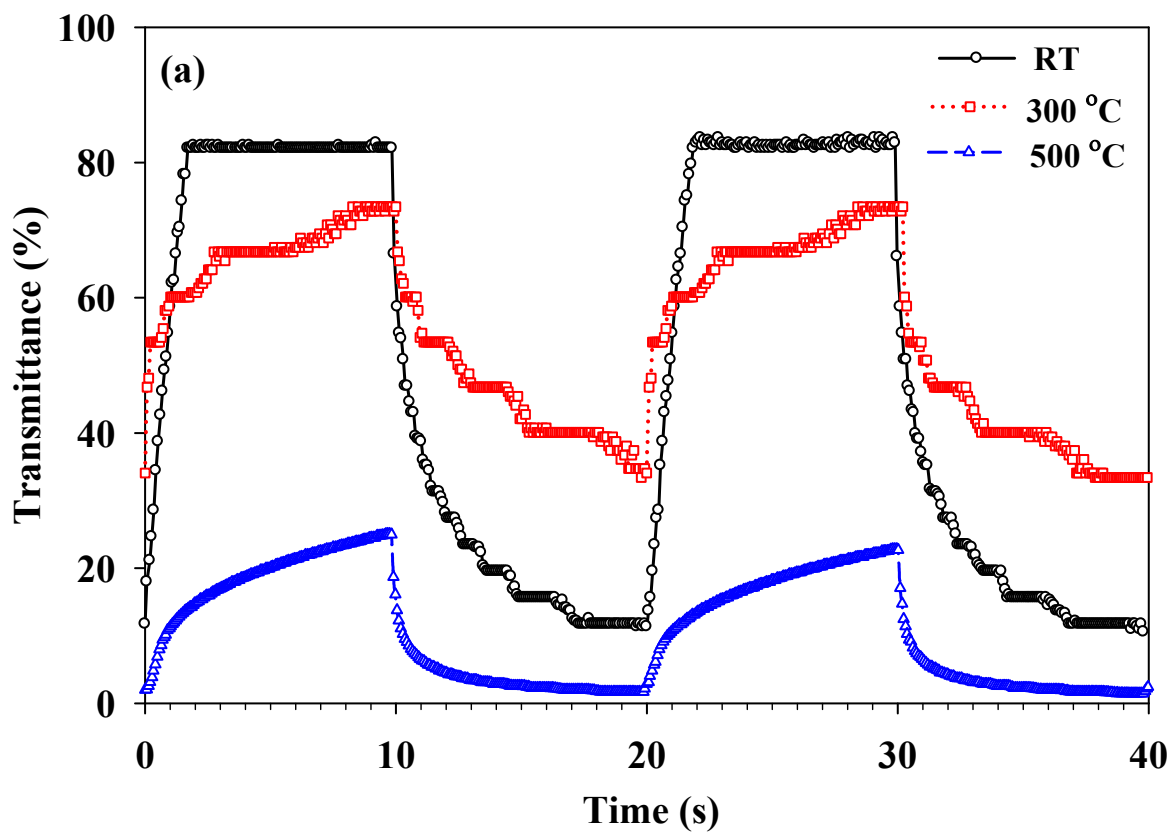


Figure 4.16: (a) The variation in the optical transmittance at 650 nm and, (b) the current density for WO₃ the thin films, grown at different substrate temperature, when the electrochemical cell is subjected to a square-wave potential of ± 1.5 V and frequency 0.05 Hz is applied.

Table 4.6: Switching time of thermally evaporated WO₃ thin films for different substrate temperature at 650 nm.

Substrate temperature, T_s (°C)	Bleaching time, t_b (s)	Coloration time, t_c (s)
RT	2	7.5
300	4	10
500	10	10

The differing rates of ion intercalation/de-intercalation during the coloration and bleaching processes involve an intricate interplay of various factors like the oxygen deficiency, amorphous or crystalline nature of the film, the substrate temperature, the development of back emf, the formation of the depletion layer, etc. The oxygen deficiency of the substrate temperature 300 °C thin films is more than that of the RT film. This leads to, initially, more intercalation and generation of back emf compared with the RT film. Thus a faster rise and decay in current density but subsequently, however, the partial crystallinity of the substrate temperature 300 °C film leads to a slower decay compared with the RT film, which is amorphous. In the case of the substrate temperature 500 °C, the crystalline nature provides a more dense structure than the partially crystalline substrate temperature 300 °C, and thus the differences in the rates, in spite of the former having more oxygen deficiency than the latter.

The change in transmittance of the WO₃ thin films occurring during the coloration and bleaching processes also depends on the number of ions intercalation/de-intercalation. The lower transmittance for the thin films in the coloration and bleaching processes for the film deposited at a higher temperature than at the RT is due to the absorption of light from some of the W⁵⁺ states already present in the thin films. For the coloration process, in all cases, the WO₃ thin films take nearly the same coloration time except that the RT grown films shows a little less time. From the current versus time transients, in the coloration process, the current decreases slowly to zero, and shows that more time is needed for coloration than bleaching [115].

4.4 CONCLUSIONS

The structural, electrical, optical and electrochromic properties of the WO₃ thin films grown by thermal evaporation depends strongly on the substrate temperature. Crystalline films are obtained at the substrate temperature above 450 °C. The optical energy band-gap also

decreases from 3.38 eV to 3.05 eV as the substrate temperature increases from RT to 500 °C, respectively. The WO₃ thin film, intercalated using H⁺ ions, shows greater CE compared to bigger ions Na⁺ and K⁺, because of the high diffusion coefficient of H⁺ ion in the WO₃ thin films. The transmittance modulation and CE are observed to be high for lower substrate temperature grown films. The electrochromic characterization shows that the amorphous nature of the films is desirable for high CE and low switching time.

Chapter - 5

Electrolyte

Zirconium Oxide (ZrO_2)

Thin Film Layer

5. ELECTROLYTE ZIRCONIUM OXIDE (ZrO₂) THIN FILM LAYER

In solid-state electrochromic devices the ion conducting electrolyte is the most important layer for ion transport between electrochromic layer and ion-storage layer. The device performance includes switching-time and cyclic-life, which is affected by the electrolyte used in the devices. In the present chapter, the ZrO₂ thin films are optimized and are used as a solid electrolyte. The physical properties, structure, and ion conduction mechanism are briefly discussed in this chapter. The ZrO₂ thin film preparation and characterizations are also discussed over here. The effect of substrate temperature on the growth, structural, compositional, optical, and dielectric properties is investigated.

5.1 INTRODUCTION

In the multilayered solid-state devices viz. electrochromic (EC), fuel cell, rechargeable batteries, one of the important elements of the device is electrolyte layer. Electrolyte is a material containing a large number of free ions and vacancies, which makes it ionically conductive. The activation energy is also low so that the ion can easily jump to nearby site. Small ions such as Hydrogen (H⁺), Lithium (Li⁺) are preferred because they can be moved easily through the electrolyte. Some factors of electrolyte like ionic conductivity, ion transport through the bulk and interface, and thermal stability can affect the performance of the devices. The electrolyte can be a liquid, a gel, or a solid, which also affects the device performance. Among them, a liquid or a gel electrolyte shows a high ionic conductivity compared to solid electrolyte. But solid electrolytes have attracted attention because their use improves the leakage problems often observed within liquid or gel electrolyte and their simple preparation.

In solid-state electrochromic devices (ECD), electrolyte is the ion containing layer between EC and ion-storage layer, which gives path to the ions for movement. Depending upon the polarity of applied voltage the ions are able to move between the EC layer and the ion-storage layer. The ionic conductivity, transparency, and stability of solid electrolyte are important for the ECD application. The number of defects present in the material plays an important role in ionic conductivity. In order for an ion to move through a crystal it must 'jump' from an occupied site to a vacant site. Schematic representation of ion-movement in a solid electrolyte is shown in Fig. 5.1.

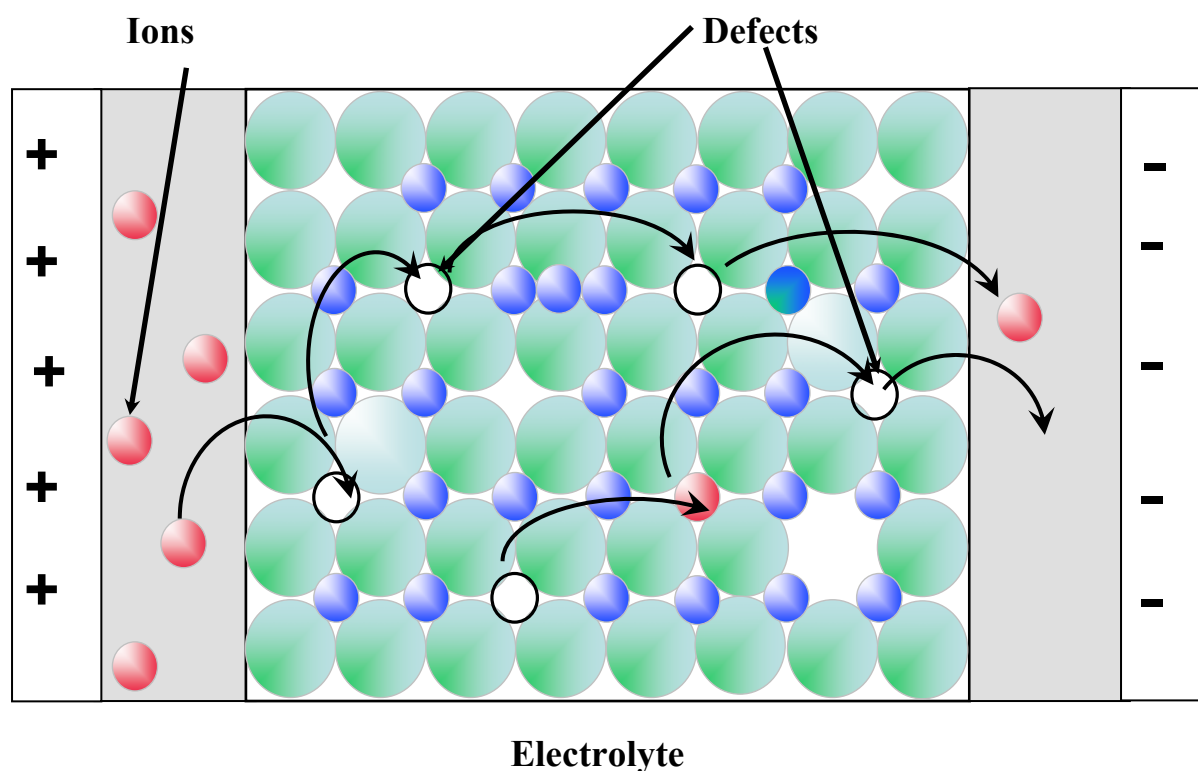


Figure 5.1: A schematic representation of ion-movement in a solid electrolyte.

The main advantage of the solid-state multilayered ECD is its memory effect, which is directly related to the electrolyte properties. The thickness of the electrolyte must be optimized. If the thickness is less then it will result in short circuiting between the two electrochromic layers and the device will fail or damaged and if the thickness is high then the coloration and bleaching time goes high which is not beneficial, and hence it should be properly optimized.

Mino Green in 1974 reported a solid-state electrochromic cell with $\text{RbAg}_4\text{I}_5/\text{WO}_3$ system in which Rubidium silver pentaiodide (RbAg_4I_5) was used as solid electrolyte [116]. In 1977, John H. Kennedy gave a review of thin film solid electrolyte including silver compounds, metal fluorides, metal chlorides, and metal oxides [117]. There are a large number of oxides which are used as solid electrolyte viz. Zirconium oxide (ZrO_2), β -alumina, Yttrium oxide (Y_2O_3), Tantalum pentoxide (Ta_2O_5), and exhibit high ionic conductivity and negligible electronic conductivity [117,118]. Among them today ZrO_2 is widely used as solid electrolyte due to its high ionic conductivity ($10^{-3} < \sigma_i < 10^{-8}$ S/cm) with ideally zero electrical conductivity and good mechanical and adhesive properties. ZrO_2 is an inorganic transition metal oxide having high dielectric constant (~ 25) and high thermal stability. The ZrO_2 powder appears white in colour with density 5.68 g/cm^3 and melting point of $2715 \text{ }^\circ\text{C}$.

Pure ZrO_2 exists in three crystal phases at different temperatures: For very high temperature ranges (> 2370 °C) it has a cubic structure, whereas at intermediate temperature ranges (1170 to 2370 °C) it has a tetragonal structure, and for low temperature ranges (below 1170 °C) the material has a monoclinic structure [119]. The high temperature phases can be stabilized down to room temperature (RT) by an addition of Al_2O_3 , Sc_2O_3 , and Y_2O_3 [120].

Zirconium dioxide is being investigated for its future potential applications as an insulator in transistors in nano-electronic devices [121]. It is also used to replace SiO_2 as the gate dielectric material in metal-oxide-semiconductor devices because of its high dielectric constant, good thermal stability on silicon, and large band-gap [122]. Zirconia-based ceramics are often used as thermal insulators because of their low thermal conductivity (2.2 W/mK) over temperatures ranging from cryogenic to >1200 °C, e.g., for thermal barrier coating (TBC) [123]. Zirconium dioxide is the most popular electrolyte material for solid oxide fuel cells and electrochromic devices due to its high ionic conductivity [124]. Zirconium dioxide is used as a thin film coating on the facets of high-power laser diode in order to protect the laser facets from degradation and to ensure long-term reliable operation [125]. As a semi-conducting oxide, zirconium dioxide is also used as a gas sensor to detect oxygen (O_2), carbon monoxide (CO), etc. [126,127].

Zirconium dioxide thin films can be prepared by a wide variety of techniques including e-beam evaporation [128,129], sputtering [130], chemical vapor deposition [131], and sol-gel process [132]. Each method has its advantages and disadvantages, but whichever technique is used it must be optimized first. In any deposition technique, the growth condition strongly affects the microstructure and the chemical compositions of the thin films, which directly affects the ion movement in electrolyte. In this chapter, the preparation of ZrO_2 thin film and the influence of the deposition conditions on the microstructure and the properties of thin films are discussed which can be used as the ionic conducting layer in solid-state EC devices.

5.2 FILM PREPARATION

Thin films of ZrO_2 were deposited on organically cleaned glass, sapphire, and indium tin oxide (ITO) coated substrate using an e-beam evaporation technique. The zirconium dioxide powder (Sigma Aldrich, 99 %) placed in a graphite crucible is used as the source material. The films were grown, at a base pressure of 10^{-5} mbar, at different substrate temperatures

ranging from room temperature (RT) to 400 °C. The substrate is heated using infrared (IR) heater, and its temperature is measured by a Chromel-Alumel thermocouple. Zirconium dioxide thin films of thickness 3000 Å at 5 Å/s rate are grown. The thickness measurement involves piezoelectric quartz crystal placed inside the vacuum chamber. The rate of deposition is controlled and monitored with the help of quartz crystal based thin film deposition controller (Sigma Instruments, SQC-122c). The small silver paste dot (2 mm) is placed on the ZrO₂ thin film prepared on an ITO coated glass substrate for the impedance spectroscopy measurement.

5.3 FILM CHARACTERIZATIONS

The microstructure of the ZrO₂ thin films is characterized by glancing incident X-ray diffraction (GIXRD) using Cu K α radiation at incident angle 0.5° (Bruker D8). The surface morphology of the films is carried out using AFM (Nanosurf easyScan 2) and the root mean square (rms) surface roughness is calculated using the instrument's software. The surface composition of these thin films is determined using X-ray photo-emission spectroscopy (XPS). The XPS measurement is carried out using VSW ESCA instrument, with Al-K α (1486.6 eV) X-ray source at a base vacuum of 8.0 x 10⁻¹⁰ Torr. The optical measurement, transmittance, in the range of 150 – 900 nm is measured using ultraviolet visible (UV-Vis) spectrophotometer. The impedance spectroscopy is performed using (Solartron SI 1260) impedance/gain phase analyzer in the frequency range of 10 Hz to 1 MHz at RT.

5.3.1 Structural and Compositional Characterizations

XRD Measurement: X-ray diffraction measurement is carried out in order to examine the crystallization behavior of ZrO₂ thin films deposited on glass substrate as a function of deposition temperature. Figure 5.2 shows the XRD patterns of ZrO₂ thin films prepared at different deposition temperatures ranging from RT to 400 °C. From the XRD patterns as shown in Fig. 5.2, it is observed that the films grown at RT to 100 °C show the amorphous nature with hump at the 2 θ range of 30 to 32°. While films grown at 200 °C show small peaks, which appear at 24.6°, 28.25°, 31.55°, 34.5°, and 50.4° corresponding to (110), ($\bar{1}11$), (111), (002), and (220), respectively. As the substrate temperature increases up to 400 °C the intensity of ($\bar{1}11$) and (111) increases and the other peaks almost disappear, which indicates the monoclinic structure [JCPDS-83 0940]. The average crystallite size, determined using Scherrer equation for ($\bar{1}11$) is found to be 8.55 nm and 15.0 nm for 300 °C and 400 °C

substrate temperatures, respectively. At higher substrate temperatures, the mobility of the condensing particles on the substrate surface is more, which favors the crystallization and the growth of large crystallites.

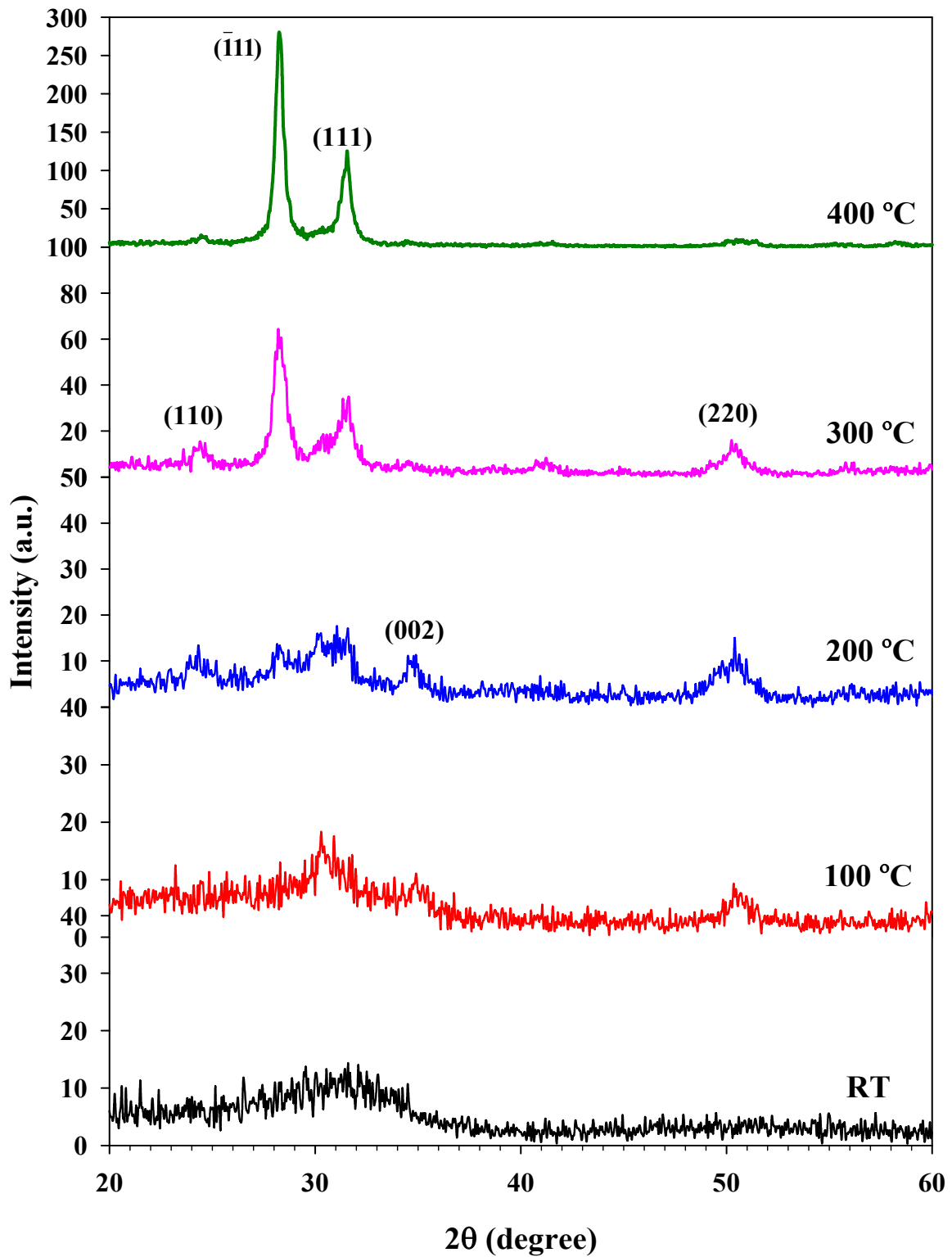


Figure 5.2: XRD spectra for ZrO₂ thin film deposited at different substrate temperatures.

AFM Measurement: Figure 5.3 shows the surface morphology of the ZrO_2 thin films deposited at different substrate temperatures as determined from the AFM with a scan area of $1 \mu m \times 1 \mu m$. The rms surface roughness of the films is determined using Nanosurf easyScan software.

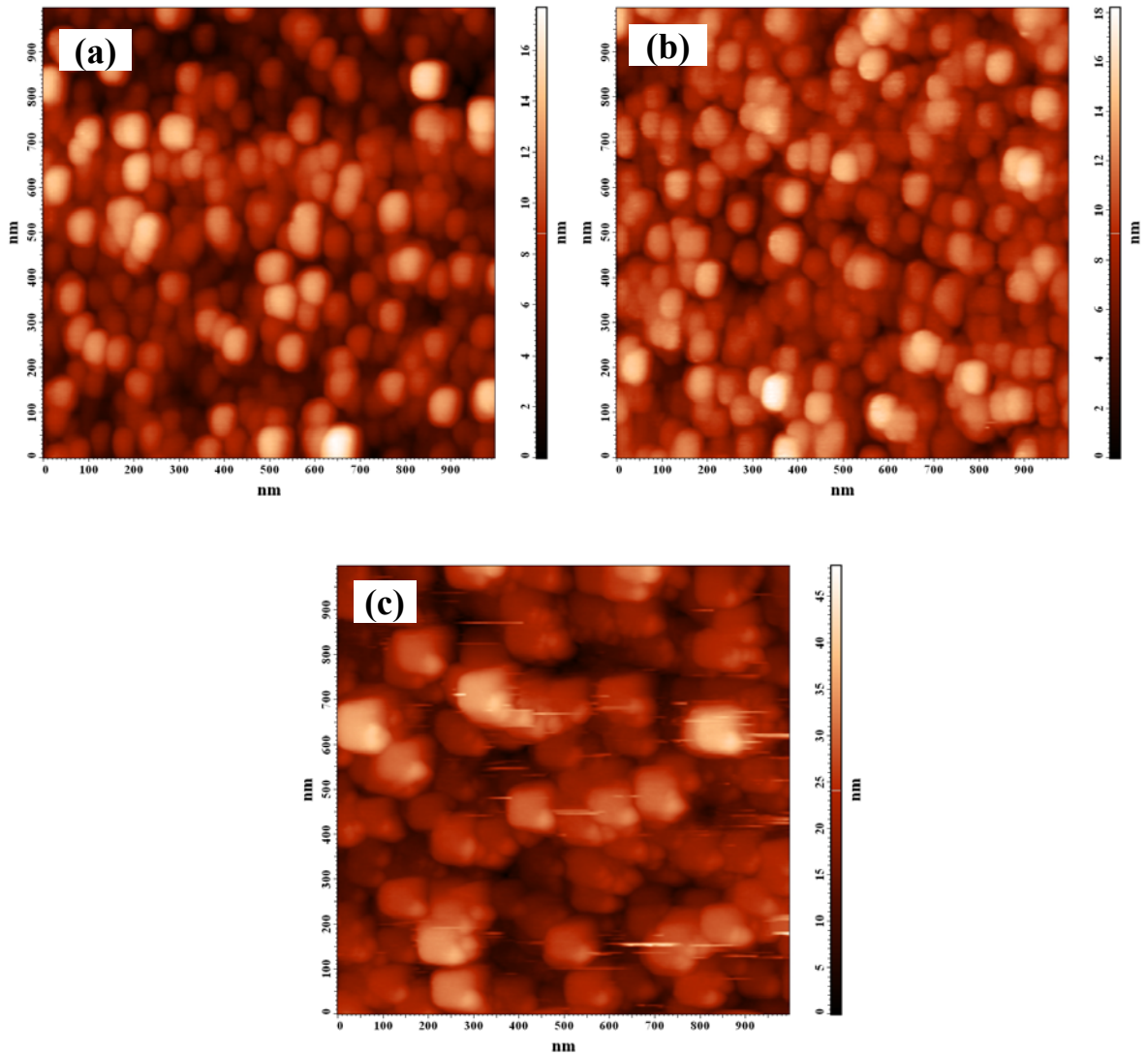


Figure 5.3: AFM image of ZrO_2 thin film deposited on at (a) RT, (b) 200, and (c) 400 °C substrate temperatures.

Room temperature deposited films have well-defined grains with a surface roughness rms value of 2.92 nm, while at 200 °C, the surface becomes smoother, with rms value of about 2.43 nm. Furthermore, with the increase of the substrate temperature to 400 °C the surfaces get much rougher again with the rms roughness of 5.46 nm. At the RT, the grain growth is observed but due to the porous structure of the film, the roughness is high compared with that at 200 °C. At 200 °C, substrate temperature the density of the grain increases due to uniform distribution and thereby the rms roughness slightly decreases.

Furthermore, with the increase in the substrate temperature to 400 °C some of the grains diffuse and clusters are formed, which results in the increase of the rms roughness of the film's surface.

XPS Measurement: The chemical composition of the surface of the ZrO₂ thin film is investigated using XPS measurement. Figure 5.4 shows the survey scan XPS spectra of zirconium oxide thin films on glass substrate in the binding energy range of 0 - 1000 eV.

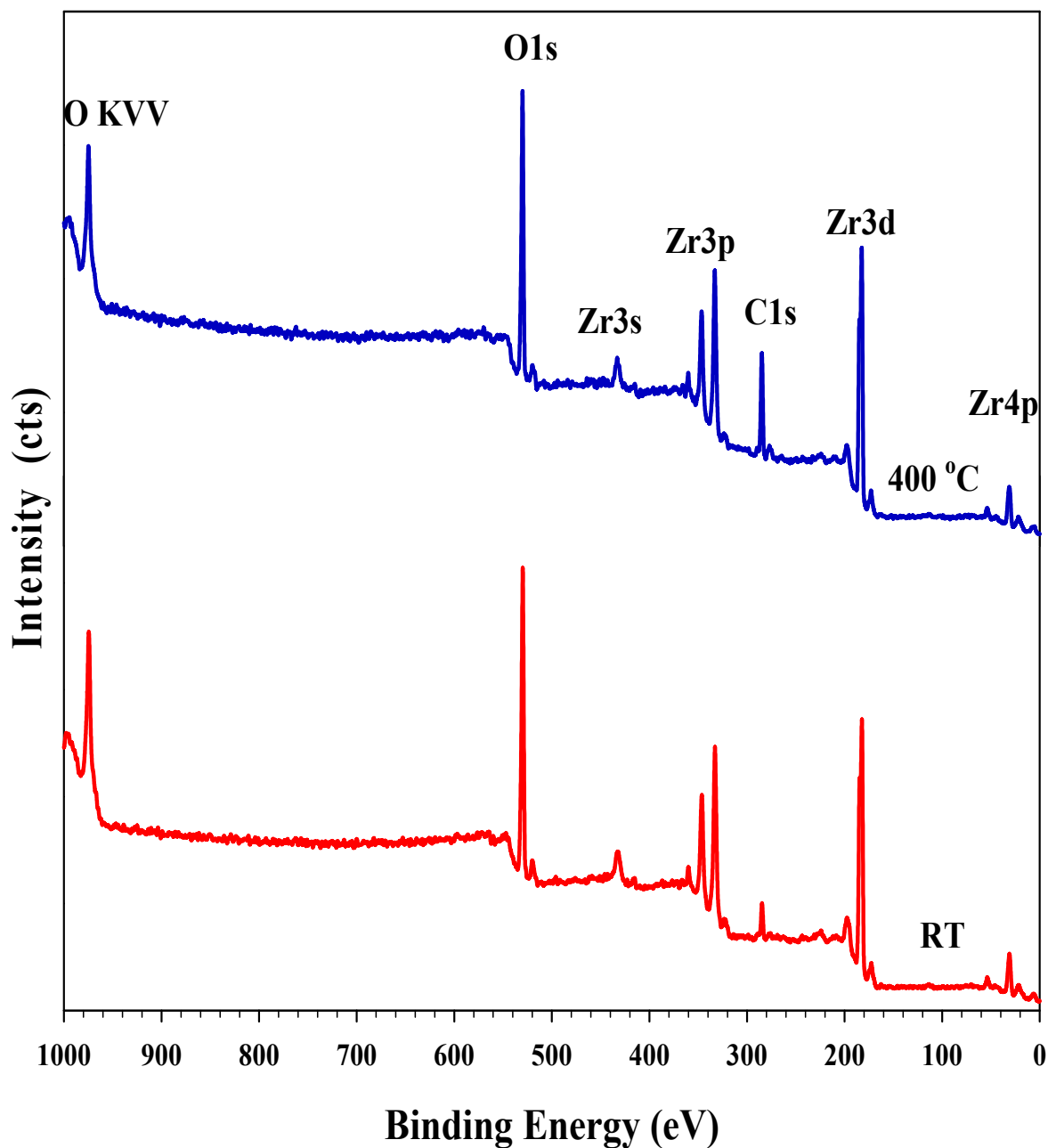
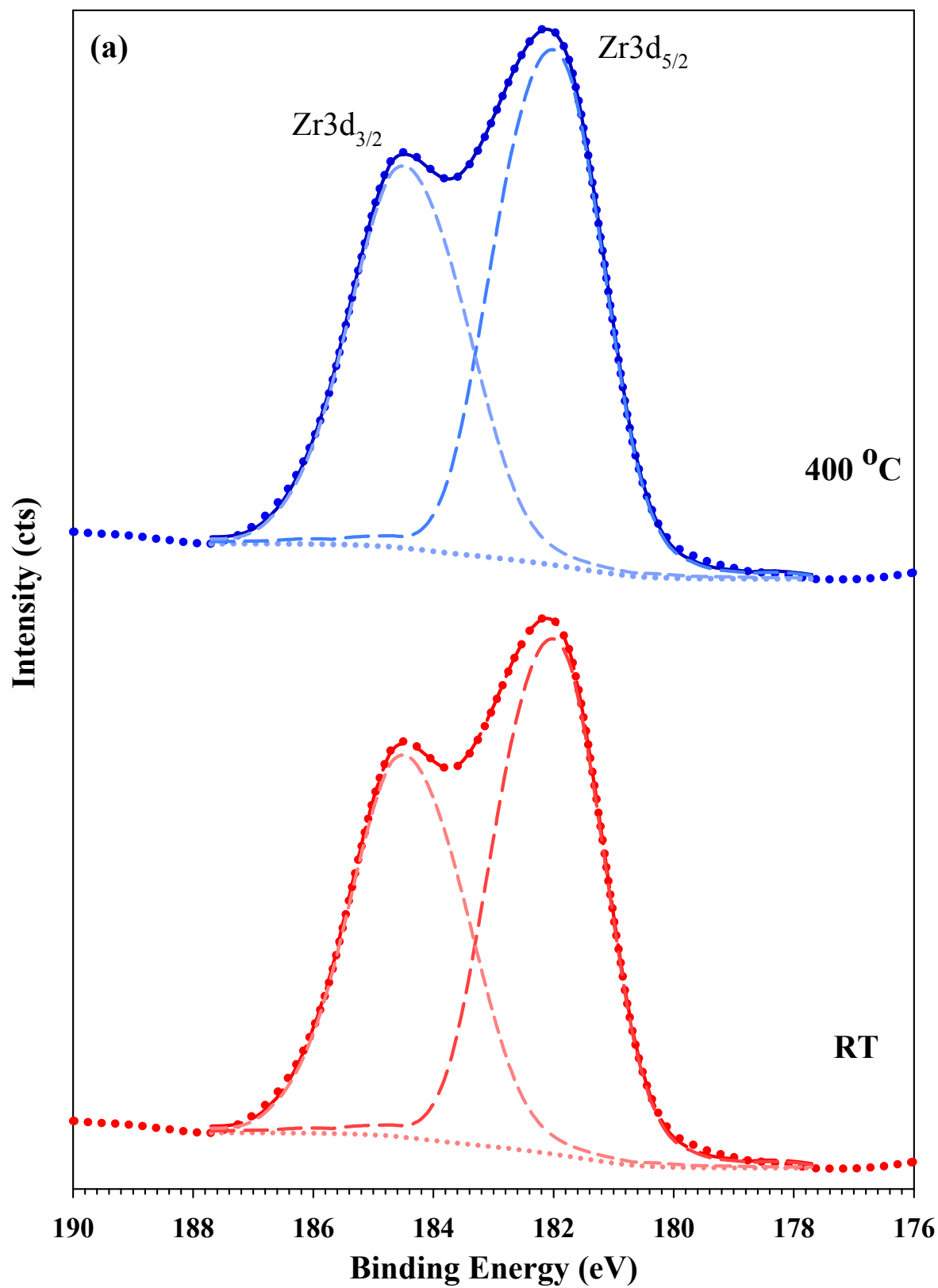


Figure 5.4: The XPS survey scan spectra of the ZrO₂ thin films grown at RT and 400°C substrate temperatures.

From Fig. 5.4, one can reckon the presence of zirconium (Zr), oxygen (O) and carbon (C) atoms on the surface of the films. Figure 5.5 (a) and (b) shows XPS core level spectra for zirconium Zr3d, and oxygen O1s at the surface of the ZrO₂ thin film, respectively.



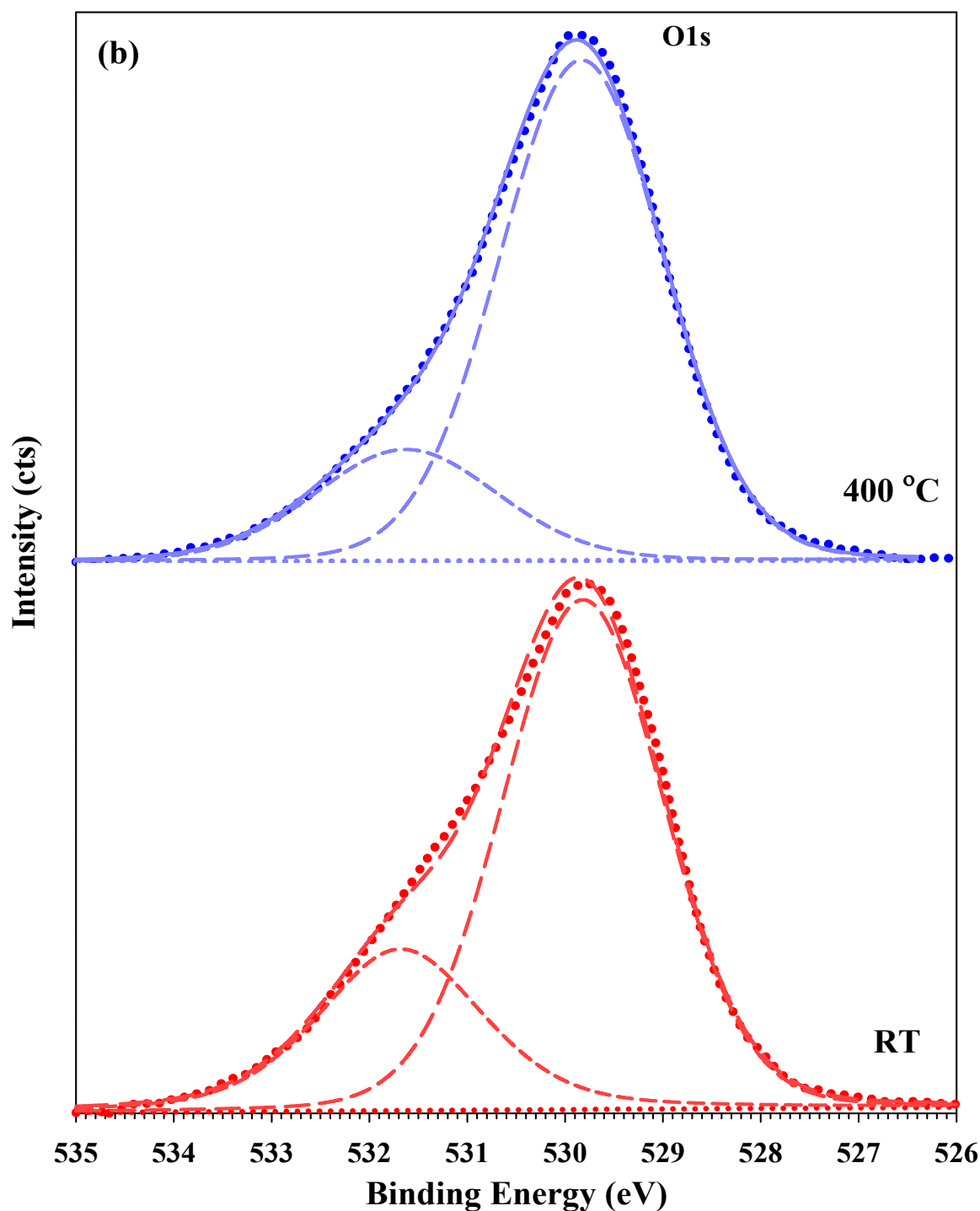


Figure 5.5: The XPS spectra of the (a) Zr3d and (b) O1s for ZrO₂ thin films grown at RT and 400 °C substrate temperature

In Fig. 5.5 (a), the doublet peaks centered at 182.1 eV and 184.5 eV, correspond to Zr3d_{5/2} and Zr3d_{3/2}, respectively. The binding energy of Zr3d_{5/2} is expected to be observed at 179 eV, and in our case, the Zr3d_{5/2} peak is located at 182.1 eV, which shows the formation of zirconium oxide in its +4 state [133]. The XPS spectra of the ZrO₂ thin film reveal that the binding energy of the O1s peak is 529.8 eV. The higher energy shoulder observed at 531.6

eV is perhaps due to the surface oxidation. The peak intensity is nearly the same for both the cases except for a slight higher intensity observed at 529.8 eV O1s peak, which indicates that there is an improvement in the chemical composition with increase in the substrate temperature.

5.3.2 Optical Characterization

The optical transmittance of the ZrO_2 thin films is measured in the range of 200 – 900 nm using UV-Vis spectrophotometer. The sapphire substrate is used for the optical measurement, which is nearly transparent from 200 – 900 nm wavelengths. The transmittance spectra of the sapphire substrate and the ZrO_2 thin film grown on sapphire substrate at different substrate temperatures are shown in Fig. 5.6.

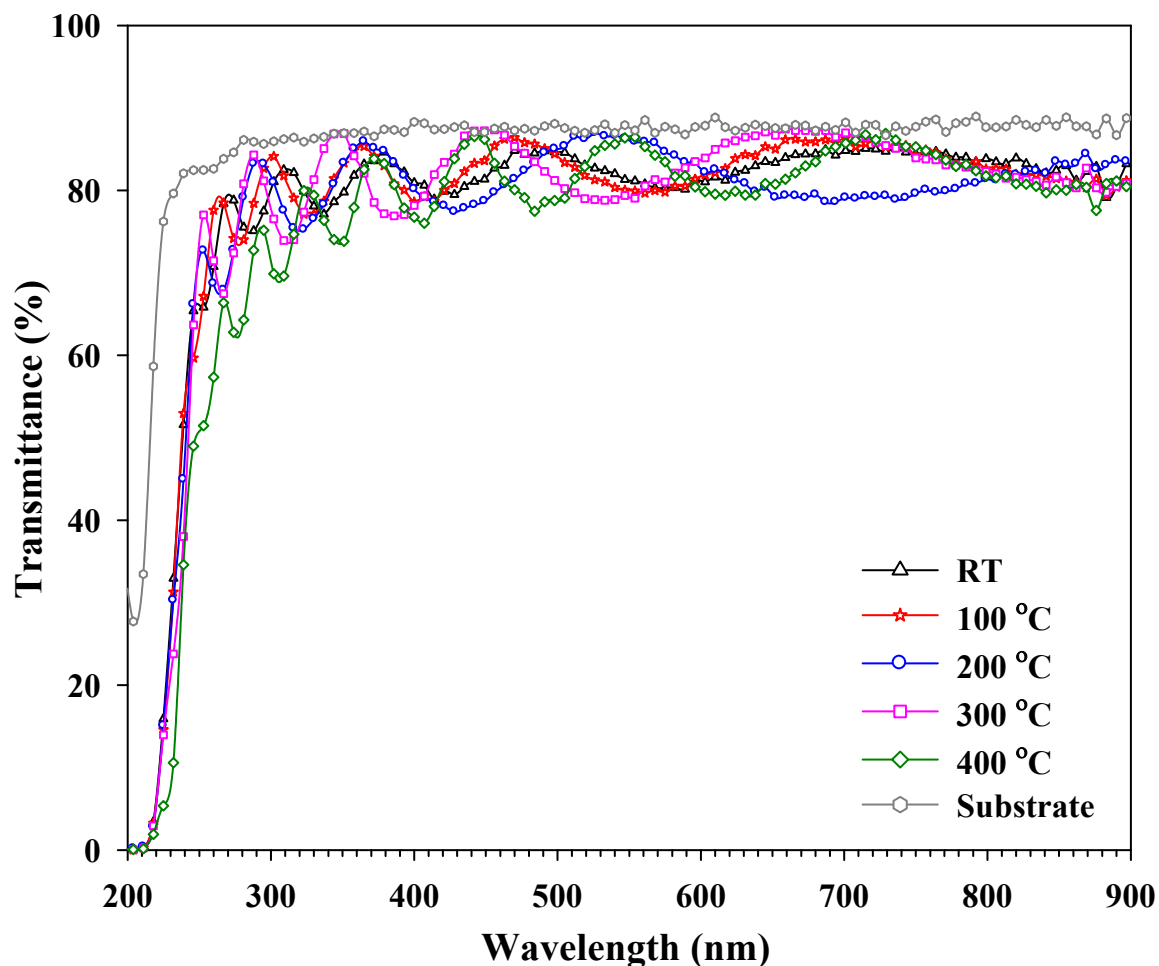


Figure 5.6: Transmission spectra of ZrO_2 thin films deposited at different substrate temperatures with the sapphire substrate.

From the optical transmittance spectra of the ZrO₂ thin films, all thin films show an average 80 % transmittance in the visible region of light. The thin film deposited from RT to 400 °C substrate temperature does not show any major change in the absorption edge. The band-gap is calculated using the Tauc's relation [49], (Eq. 2.4 in Chapter 2)

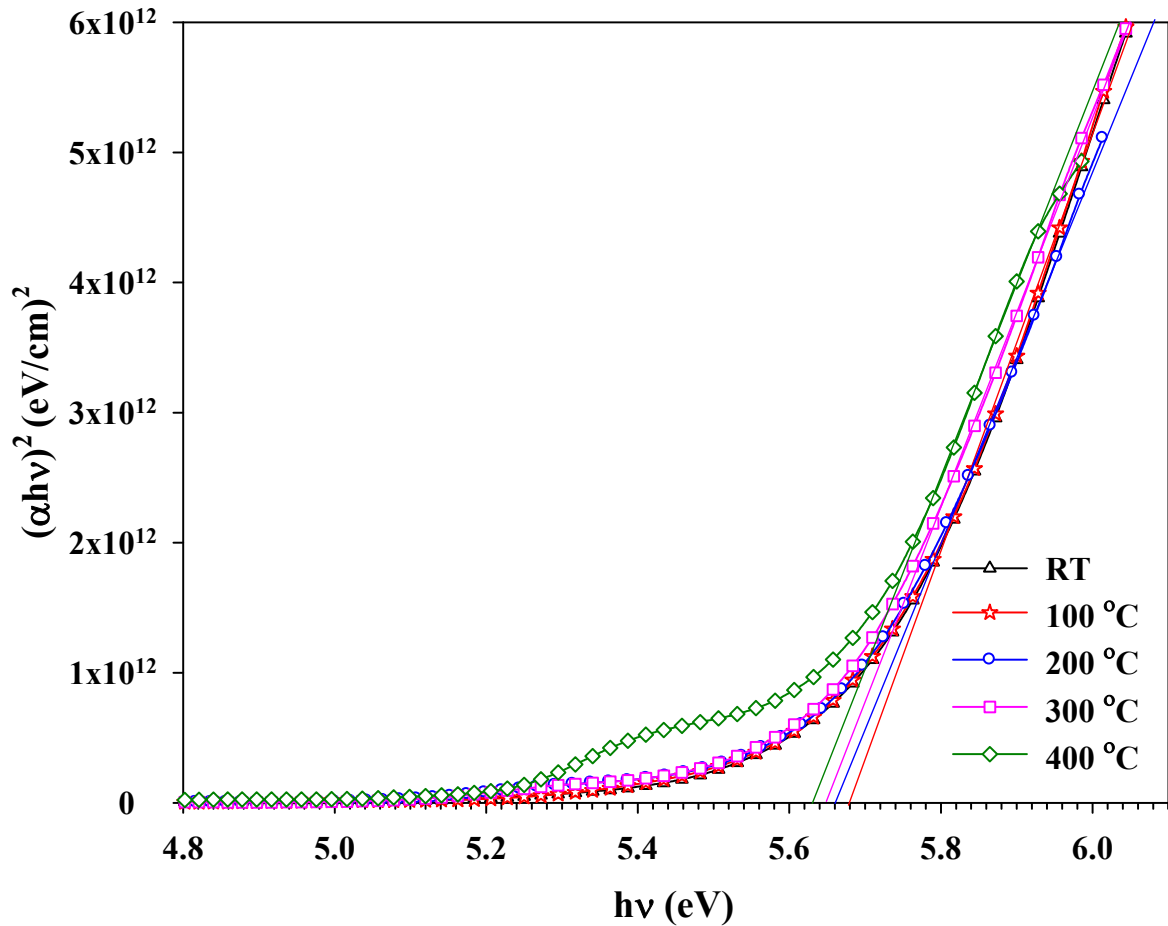


Figure 5.7: The plot of $(\alpha hv)^2$ vs. (hv) for the optical energy band-gap of ZrO₂ thin films.

From the Fig. 5.7 the optical energy band-gap of thin film is determined by plotting $(\alpha hv)^2$ versus the incident photon energy (hv) and linearly extrapolating the intercept of hv axis. This gives the energy band gap value which is presented in Table 5.1.

Table 5.1: The energy band-gap value and the corresponding substrate temperature for ZrO₂ thin films.

Substrate temperature (°C)	RT	100	200	300	400
Energy band-gap (eV)	5.68	5.68	5.66	5.65	5.63

There is a very small change observed in the energy band-gap with substrate temperature from RT to 400 °C because the substrate temperature is low compared to the high melting point (2715 °C) of ZrO₂. Furthermore, the small variation in the band-gap from 5.68 to 5.63 eV with increases in substrate temperature from RT to 400 °C is due to the improvement in the crystallization of the film. The optical energy band-gap is almost same as obtained by other methods as reported by H. Nohira et al. [134].

5.3.3 Impedance Spectroscopy

For Impedance measurement, the ZrO₂ samples are deposited on ITO coated glass are used. The measurements are performed in the frequency range 10 Hz to 1 MHz at RT using frequency analyzer. The impedance spectroscopy measurement gives the magnitude $|Z|$ and phase angle (ϕ) of impedance, which were further used to calculate the real and imaginary parts Z' , Z'' , of the impedance using $|Z|\cos\phi$ and $|Z|\sin\phi$, respectively, Fig. 5.8 show the frequency dependence of the real and imaginary parts Z' , Z'' , of the complex impedance at different substrate temperatures. It is observed that the magnitude of Z' and Z'' both decrease with increase in frequencies, which indicates an increase in the AC conductivity. The values of Z' merge at higher frequency, which indicates that the contribution from the grain dominates due to the absence of the space charge effect [135]. Complex impedance (Nyquist) plot i.e., the real vs the imaginary part of impedance ZrO₂ thin films are shown in Fig. 5.9.

The bulk resistance (R_b) of the ZrO₂ thin film is determined from the complex impedance representation by the intercept of the semi-circle with the real impedance axis. The bulk resistance of the ZrO₂ thin film is found to be $7.98 \times 10^7 \Omega$ for RT deposited film and the value increases up to $2.23 \times 10^8 \Omega$ for 400 °C deposited film. The bulk conductivity is calculated using $\sigma_b = (t/A) \times (1/R_b)$, where t , A and R_b are the thickness, electrode area, and the bulk resistance of the film, respectively. The bulk conductivity has been found to be 1.88×10^{-12} , 0.94×10^{-12} and 0.67×10^{-12} S/cm for RT, 200 °C and 400 °C substrate temperature respectively for ZrO₂ thin film. At 400 °C substrate temperature the film is crystalline in nature, however at lower substrate temperature (RT) the film is amorphous in nature, and some oxygen vacancies are also present in the film, which dominates the increased conductivity.

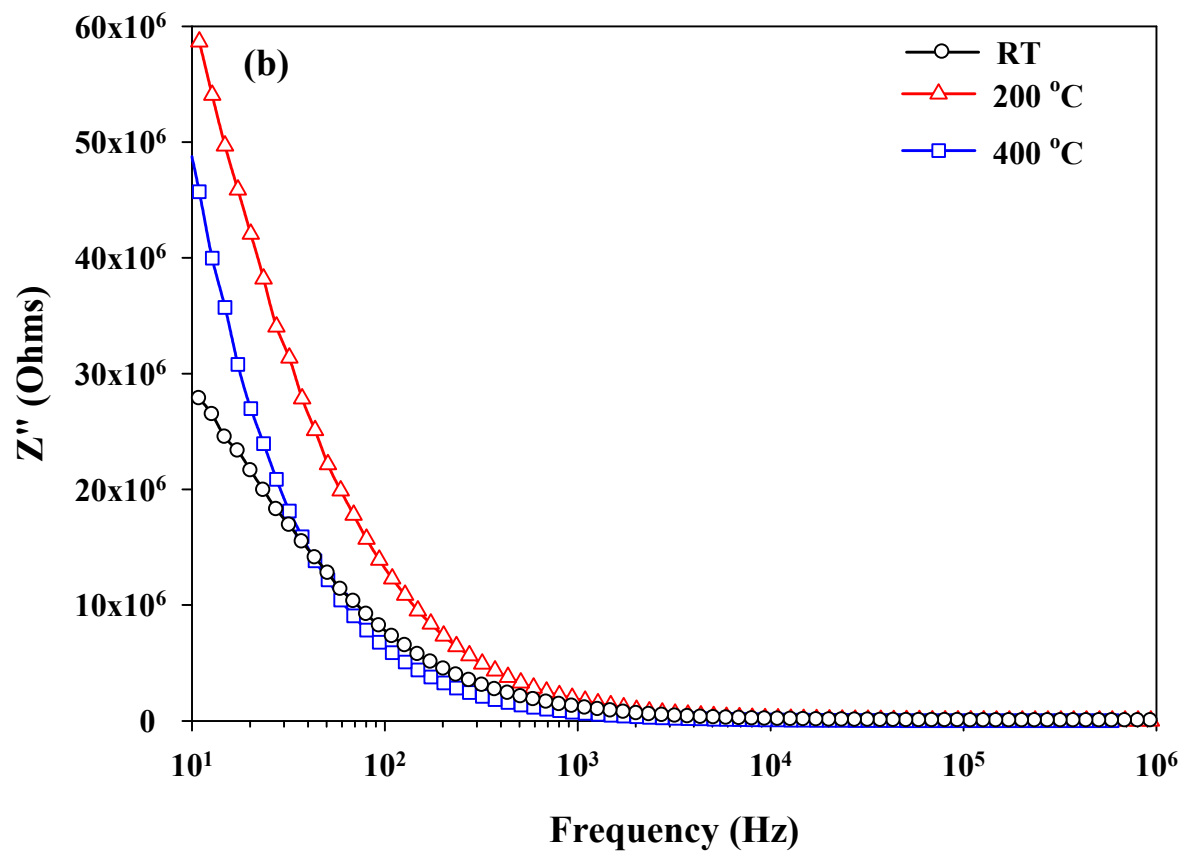
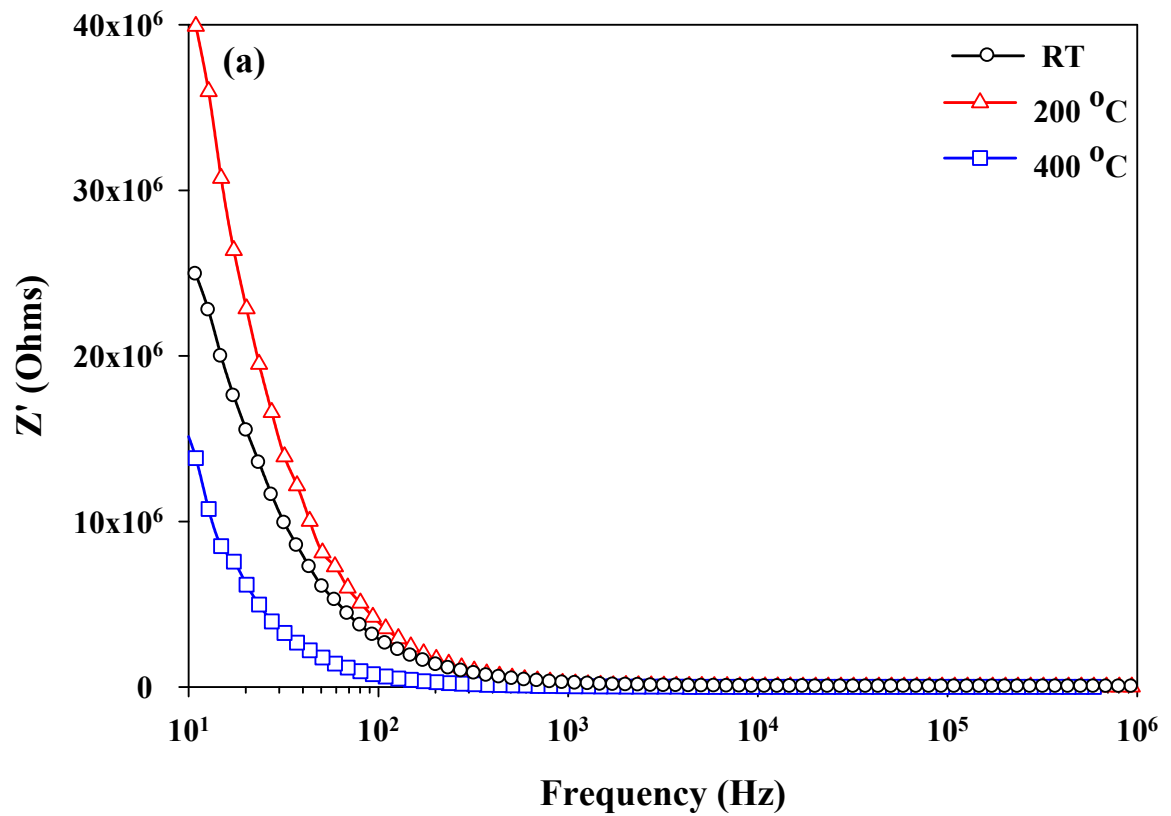


Figure 5.8: (a) real part of impedance (Z') and (b) imaginary part of impedance (Z'') as a function of frequency for the ZrO_2 thin films deposited at different substrate temperature.

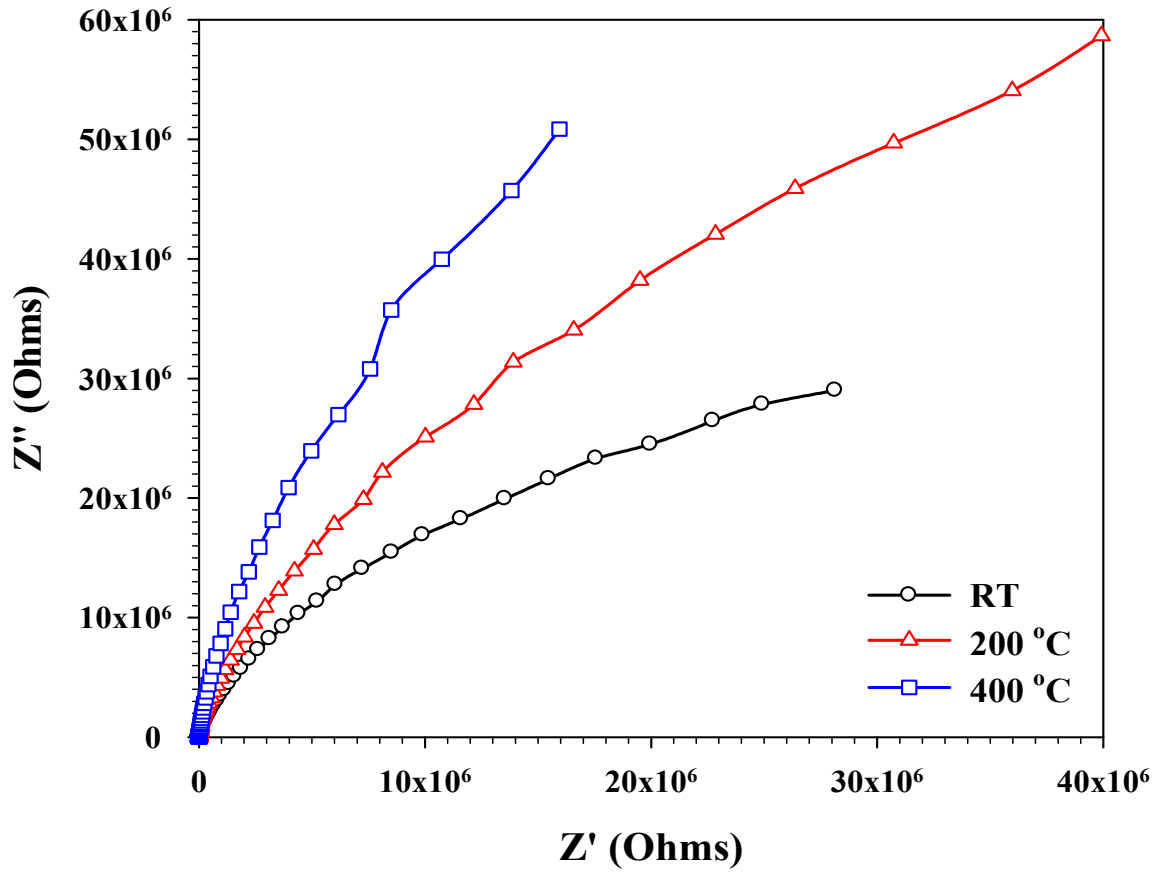


Figure 5.9: Complex impedance (Nyquist) plot for the ZrO₂ thin films deposited at RT, 200 °C, and 400 °C substrate temperature.

The frequency-dependence real part of the conductivity (σ') for different substrate temperatures grown ZrO₂ film is shown in Fig. 5.10. The frequency dependent AC conductivity is given by, $\sigma_{AC} = \sigma_0 + \sigma_{AC}(\omega)$ [136], where σ_0 is related to drift electric charge carriers. It is frequency independent and represents DC electrical conductivity. $\sigma_{AC}(\omega)$ is a frequency-dependent component of the conductivity. The frequency-dependent conductivity can be described in a form of power law $\sigma_{AC}(\omega) = A_{\sigma}\omega^s$ [137] where ω is the angular frequency, A_{σ} is the constant, and s is a frequency-dependent parameter having values less than unity. The increasing conductivity with increasing frequency may be interpreted by Maxwell-Wagner-type and by hopping conduction take place in ZrO₂ thin films. The Maxwell-Wagner dispersion is caused by interfacial polarization set up from in-homogeneity of the material. The hopping conduction is a mechanism in which carriers' transit from one localized state to another under the assistance of phonons. As the frequency of the applied field increases, the hopping of the charge carriers also increases thereby increasing the conductivity. The RT deposited film has oxygen vacancy, which is favorable for the conduction mechanism and shows slightly high conductivity.

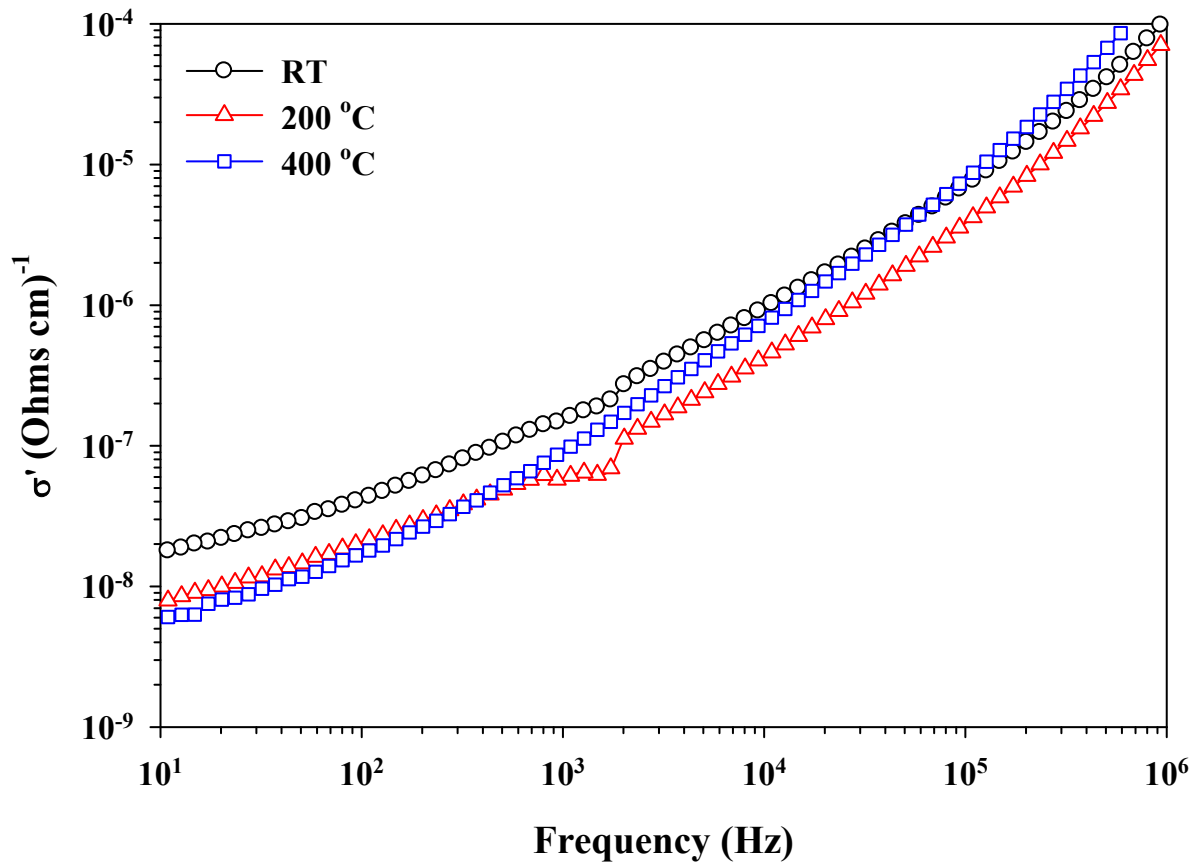


Figure 5.10: Frequency dependence real part of the conductivity (σ') for ZrO_2 thin films deposited at RT, 200 °C, and 400 °C substrate temperature.

5.4 CONCLUSIONS

Zirconium dioxide (ZrO_2) thin films were deposited on different substrates and at different temperatures using the e-beam evaporation method. The XRD measurement shows that the crystallization improves with increase in the substrate temperature and also the surface roughness increases as observed by AFM measurement. The optical properties of the thin films show that there is a small variation in the transmittance observed and the band gap varies from 5.68 to 5.63 eV with increase in substrate temperature from RT to 400 °C, respectively, due to the improvement in the crystallization of the film. The impedance measurement data shows that the conductivity decreases with increase in the substrate temperature, which is due to the crystallization as well as compositional changes. The RT deposited film shows 1.88×10^{-12} S/cm bulk conductivity slightly higher compared to 0.67×10^{-12} S/cm value at 400 °C substrate temperature. Thus, an amorphous ZrO_2 thin film can be used as an electrolyte layer in solid ECD.

Chapter - 6

Ion-Storage

Nickel Oxide (NiO)

Thin Film Layer

6. ION-STORAGE NICKEL OXIDE (NiO) THIN FILM LAYER

In the present chapter, we discuss about an ion-storage layer, which can supply ions, but remain colorless or have a complementary color in the electrochromic (EC) process. Nickel Oxide (NiO), an anodic coloring material, is used as ion-storage layer in EC devices in combination with WO₃ as an EC layer. Here, the electrochromic mechanism in NiO is discussed. The NiO thin film is grown by the electron beam evaporation method. The EC properties affected by the different structure and composition of the NiO thin films are investigated. Finally, optimization of NiO thin film as an ion-storage layer in electrochromic device is discussed.

6.1 INTRODUCTION

The electrochromic devices (ECD) work on the principle of ion exchange between two electrochromic (EC) layers. Therefore, ion will reside in one of the EC layers which can supply the ions during coloration process, but remain colorless or have a complementary color i.e., the primary EC film gets colored cathodically while the other EC layer, the ion-storage thin film layer gets colored anodically. The complementary coloring effect will enhance the optical modulation by simultaneously changing the color of both EC layers. Ion-storage layer is also used to protect the TCO coating from ion insertion process. In most of the thin film ECD, WO₃ thin film have been used as a primary EC layer due to its high coloration efficiency and good durability [138]. On the other hand, a number of inorganic materials like NiO, V₂O₅, IrO₂, CeO₂, TiO₂ are used as counter electrodes in ECD. But when certain factors viz., economical, toxicity, and durability are taken into consideration then it will result in the limitation of the use of certain materials as ion-storage layer. These problems broaden the possibility of NiO thin films as an ion-storage layer with WO₃ as an EC layer [139].

NiO is a transition metal oxide and the most common oxidation state of nickel is 2. The bulk powder of NiO is a green colored substance with a density of 6.67 (g/cm³) and melting point 1984 °C. Heating of NiO powder in oxygen or atmosphere leads to black NiO powder, which indicates non-stoichiometric nature of it. NiO has a simple structure, commonly known as the rock salt structure, as shown in Fig. 6.1.

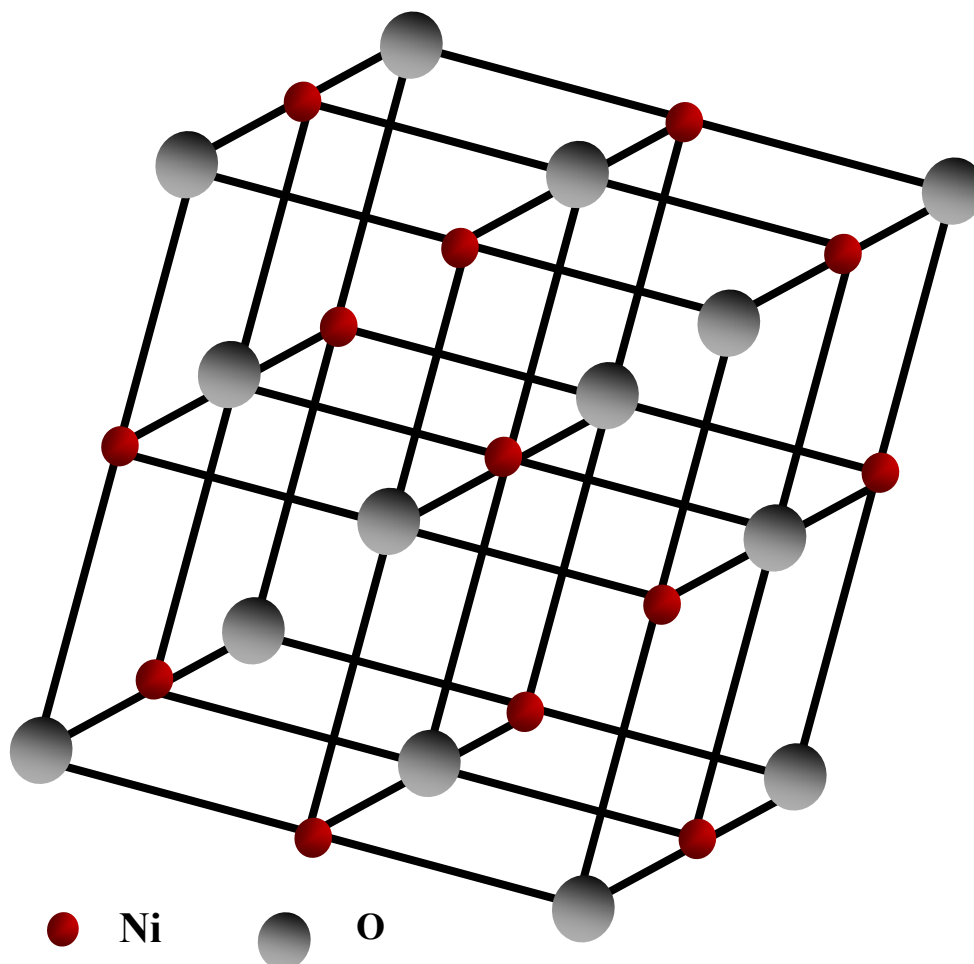
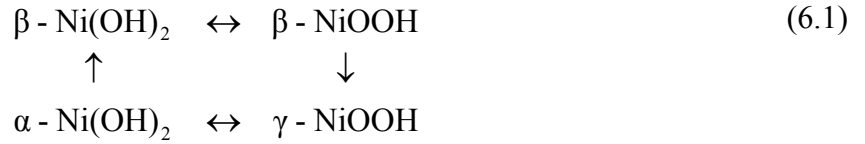


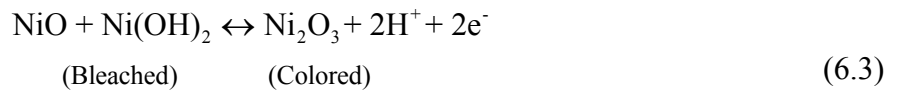
Figure 6.1: Rock salt crystal structure of NiO.

The color change from green to light black in NiO is due to the excess of oxygen in it produces Ni vacancies in NiO. For the charge neutrality, some of the Ni^{2+} converted to Ni^{3+} , which are responsible for the color. It has also been found that NiO thin film is nearly transparent, wide band-gap semiconductor, and nonstoichiometry which shows p-type semi-conducting behavior [140], which is used in many opto-electronic applications [141].

In NiO, the coloration, transition from a bleached to a colored (brown) state, is related to a charge-transfer process between Ni^{3+} and Ni^{2+} associated with the de-intercalation/intercalation of OH^- ions or H^+ ions and electron [1]. The stoichiometric NiO contains only Ni^{2+} ions and are transparent in the visible light, while the higher oxidation states are absorbing with Ni_2O_3 and NiOOH compounds. Electrochemical properties of nickel oxide based thin films have been mainly investigated in alkaline electrolyte, mostly aqueous KOH electrolyte. Electrochromism in NiO thin films is complicated. The transformation of nickel oxide, hydroxides, and oxyhydroxides into one another upon H^+ or OH^- exchange is explained by the Bode reaction scheme [142].

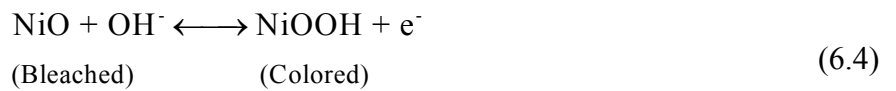


According to the Bode reaction scheme NiO reacts with hydroxyl ions and produces α and β -phases Nickel hydroxides (Ni(OH)_2). The difference between α and β phase Ni(OH)_2 is only the quantity of water needed for stabilization; the α phase occurs at a low content of water while the β phase occur at a higher content. These both phases can be further oxidized to the γ and β oxy-hydroxides, respectively. Bode reaction scheme restricts the information of the change of valency from 2+ to 3+ upon coloration in the case of NiO phase, thus an extension of this model is put forward to study the changes from NiO to Ni_2O_3 as shown below [143, 144].

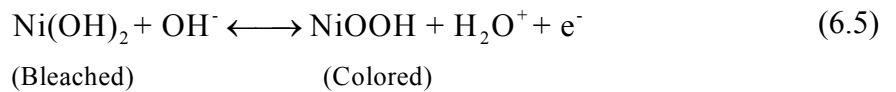


According to these reactions, the extraction of H^+ ion causes a transformation from Ni(OH)_2 to NiOOH , and the extraction of another H^+ is compensated by the creation of a hole on the Ni^{2+} in the NiO and created Ni_2O_3 .

Alternately, OH^- groups may contribute some reaction mechanisms for charge extraction/insertion as given in Eq. 6.4 [145] or 6.5 [146].



OR



The EC properties of the films show that NiO exhibit coloration associated with the extraction of H^+ or intercalation of OH^- for the formation of Ni^{3+} color centers. From the theoretical point of view, in NiO, the top of the valance band consists of nickel 3d states and it is assumed that the electrochromism in NiO is related to the reversibly extraction and insertion of Ni 3d electron. Equation (6.3) and (6.4) are the generally accepted model for the coloration in NiO materials. Furthermore, during the bleaching process certain oxides (viz. WO_3 , Nb_2O_5) have high transparency in the bleached state, whereas NiO has a residual brown color in the bleached state, which can be reduced using additives such as Mg, Al, Si, Zr, Nb or Ta in the NiO thin films [147].

Electrochromic NiO thin films have been grown by various physical and chemical thin film preparation methods viz. sputtering [148], pulsed laser deposition, Electron beam evaporation [149], sol-gel [150], spray pyrolysis [151]. The stoichiometry, structure, crystalline size, etc. change with different deposition methods and growth conditions; as a result the EC properties and CE vary once a wide range. The variation in the EC properties with different growth and annealing condition in the e-beam evaporation of NiO thin film was discussed by Y.G. Wu et al. [152]. In the present chapter, optical and EC properties of e-beam deposited nickel oxide thin films have been studied. The EC behavior was investigated in 1M KOH electrolyte by electrochemical characterization. In addition, the effect of the operating voltage on the transmittance modulation and the response-time was also measured.

6.2 FILM PREPARATION

NiO thin films were deposited on organically cleaned soda-lime and ITO coated glass substrate by e-beam evaporation system (Hindhivac, Model-15F6). NiO powder (Sigma Aldrich, 99.9 %) was used as a source material. The substrate temperature was varied from room temperature (RT) to 400 °C using radiant substrate heater and the temperature was monitored using Cr-Al thermocouple. The thickness of the film, 2500 Å, at the rate of deposition, 4 Å/s, was monitored and controlled by quartz crystal based thin film deposition controller (Sigma Instruments, SQC-122c). The ITO coated glass substrate has a sheet-resistance of 5-10 Ω/□.

6.3 FILM CHARACTERIZATIONS

The crystal structure of the thin film was investigated by Bruker D8 glancing incident X-ray diffractometer (GIXRD) using monochromatic high-intensity Cu α radiation ($\lambda = 0.15406$ nm) with angle of incidence 0.5° in a 2θ range from $20 - 65^\circ$. The surface morphology of the thin film was investigated by atomic force microscope (AFM) (Nanosurf easyScan 2). The surface composition of these thin films is determined using X-ray photo-emission spectroscopy (XPS). The XPS measurement is carried out using VSW ESCA instrument, with Al-K α (1486.6 eV) X-ray source at a base vacuum of 8.0×10^{-10} Torr. The optical transmittance was recorded with UV-Visible spectrophotometer (Shimadzu UV-2450) in the wavelength range 300 - 900 nm in order to find the energy band-gap. The EC properties of NiO thin films were investigated in an aqueous alkaline electrolyte (1M KOH) with the help

of two-electrode electrochemical cell, in which the NiO/ITO on glass substrate, acts as the working electrode and a stainless steel plate was used as a counter electrode. Concomitantly, the transmittance spectrum for electrochromic measurement was recorded in the range of 400 - 1200 nm using the transmittance measurement setup.

6.3.1 Structural and Compositional Characterizations

XRD Measurement: The XRD spectra of NiO thin films deposited on glass substrates held at different temperatures are shown in Fig. 6.2.

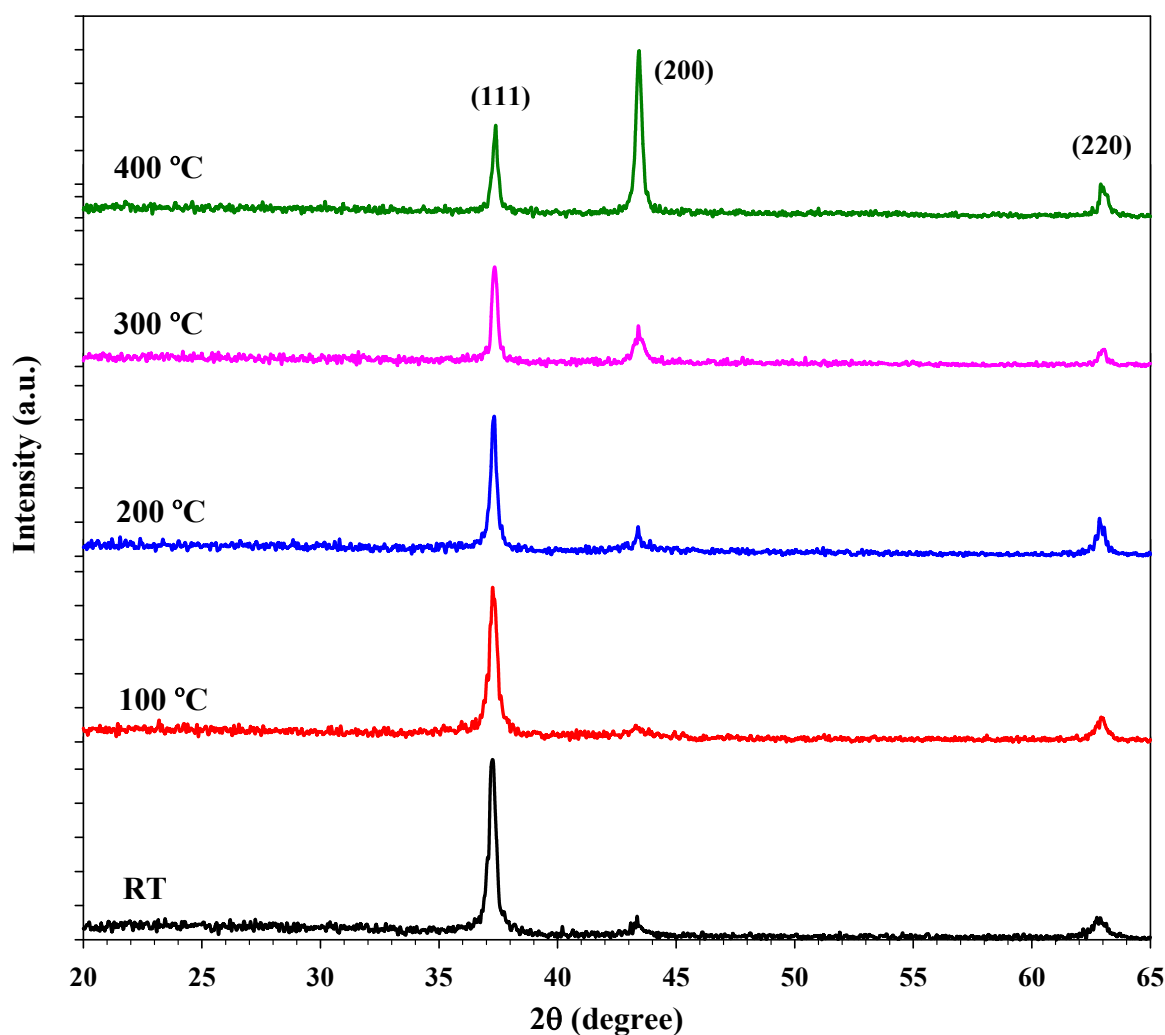


Figure 6.2: XRD spectra of NiO thin films at different substrate temperatures.

From the Fig. 6.2 it is observed that the film deposited from RT to 400 °C are polycrystalline in nature with a cubic structure. The films deposited at RT to 300 °C shows the (111) preferred orientation with (200) and (220) minor orientations. The intensity of the (111) peak decreases while the intensity of the (200) peak increases with the substrate

temperature i.e. the (200) preferred orientation improves with the substrate temperature. The intensity of (220) peak increases up to 200 °C and then a slight decrease in intensity is observed with further increase in substrate temperature. At 400 °C the preferred orientation changed from (111) to (200) directions. At the higher substrate temperature (400 °C) in NiO thin films the non-stoichiometry decreases and thus the films orientation changes from (111) direction into (200) directions [153]. The inter-plane spacing (d-value) can be calculated using $d = \lambda / 2\sin\theta$, and is presented in Table 1, where λ is the X-ray wavelength and θ is the Bragg's angle. The d-value decreases with substrate temperature due to the change in the composition and the crystal structure of the films with respect to the substrate temperature. The crystalline size was determined from the full width half maxima (FWHM) of major XRD peaks using the Scherrer's equation [45]. The d-value of the peak, the FWHM, and the crystalline size of the NiO thin films with different substrate temperatures, which were estimated from the XRD spectra, are presented in Table 1. The FWHM of the (200) and (220) decreases at the higher substrate temperature induces an increase in crystalline size. At the higher substrate temperature the deposited atoms or molecules have enough kinetic energy to produce better crystalline film.

Table 6.1: The d-value, the FWHM, and the crystalline size of the NiO thin films in (111), (200) and (220) orientations for different substrate temperatures.

Substrate temperature (°C)	d-value (Å)			FWHM (degree)			Crystalline size (nm)		
	(111)	(200)	(220)	(111)	(200)	(220)	(111)	(200)	(220)
RT	2.4141	-	1.4791	0.439	-	1.148	20	-	8
100	2.4116	-	1.4773	0.544	-	0.770	16	-	13
200	2.4109	-	1.4775	0.402	-	0.596	22	-	17
300	2.4079	2.0834	1.4760	0.328	0.772	0.545	27	12	18
400	2.4073	2.0838	1.4692	0.380	0.361	0.544	23	25	18

AFM Measurement: The surface morphology of the NiO thin film deposited at different substrate temperature was observed using AFM. Figure 6.3 shows the AFM images with the area of $1 \mu\text{m} \times 1 \mu\text{m}$ of the NiO thin films on the glass substrates deposited at RT to 400 °C substrate temperatures.

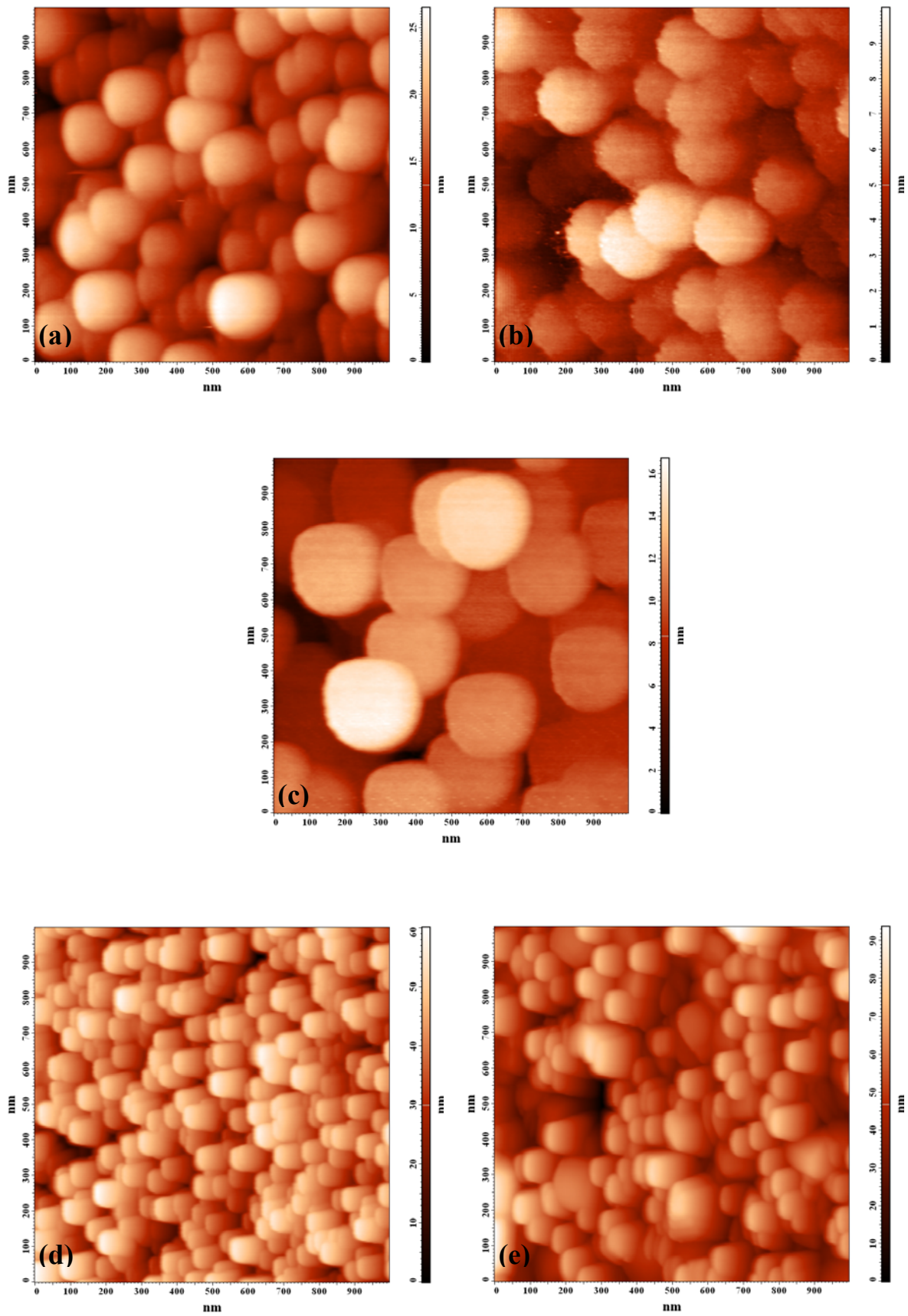


Figure 6.3: AFM image of NiO thin films at (a) RT, (b) 100 °C, (c) 200 °C, (d) 300 °C and (f) 400 °C substrate temperatures.

The AFM observation shows that the grain size of the films increases up to 200 °C and then it starts decreasing as the substrate temperature is increases due to change in the preferred orientation and the columnar grain growth [154]. The root mean square (rms) surface roughness of the thin films was measured from the AFM images, which is shown in Fig. 6.4. The film deposited at RT to 200 °C shows less surface roughness compared to other higher substrate temperature deposited films. Further increase in the substrate temperature (> 200 °C) the surface roughness of the film increases due to the columnar grain growth.

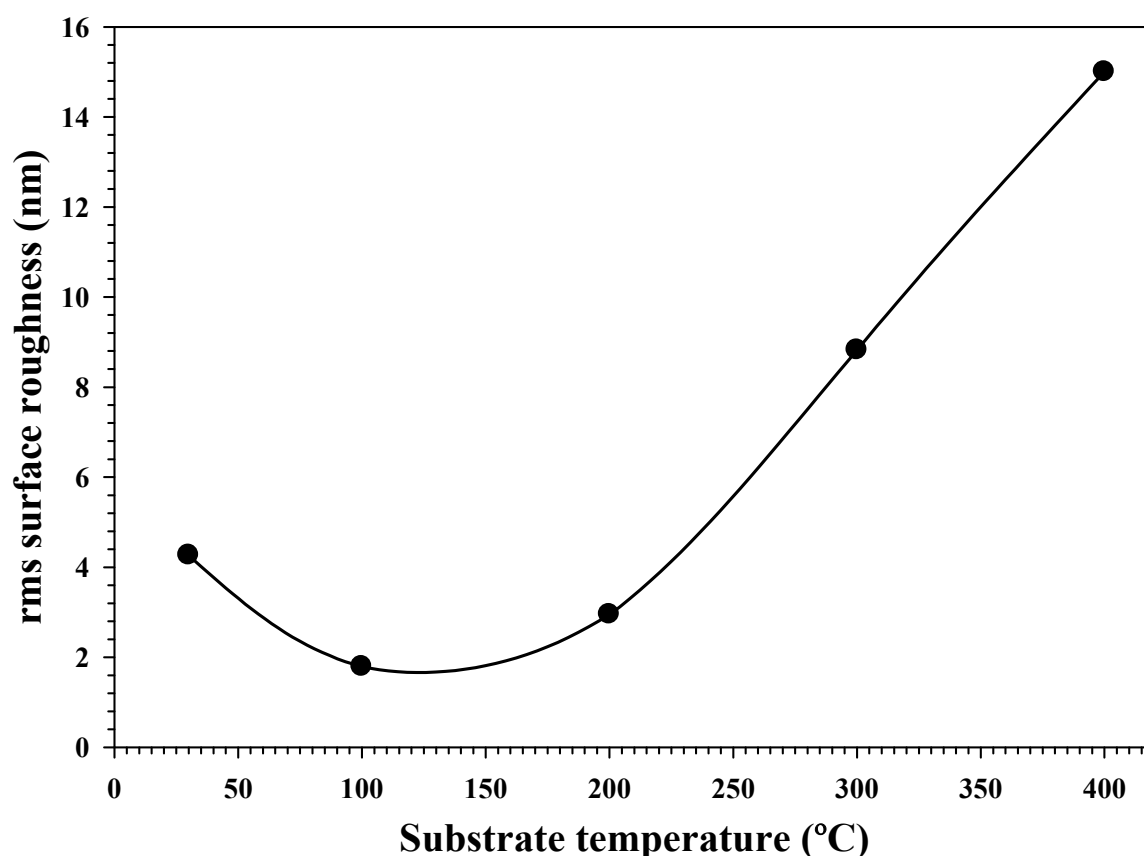


Figure 6.4: The rms surface roughness of the NiO thin films deposited at different substrate temperatures.

XPS Measurement: The compositional characterization of NiO thin films deposited on the glass substrates is determined using the XPS spectra measurements. Figure 6.5 shows the XPS survey scan spectra, in the 0 - 1000 eV binding energy range, of NiO thin films deposited at different substrate temperatures.

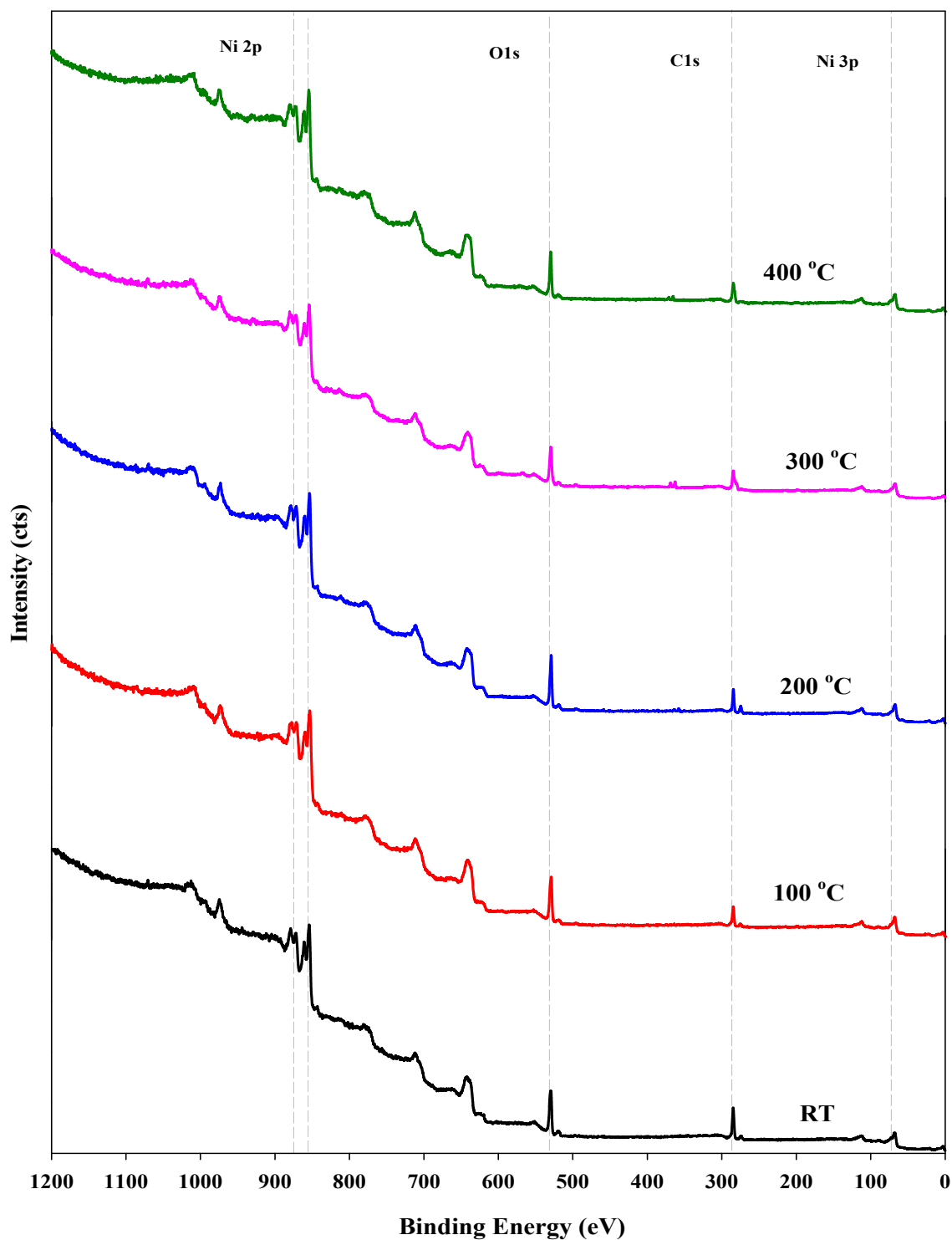
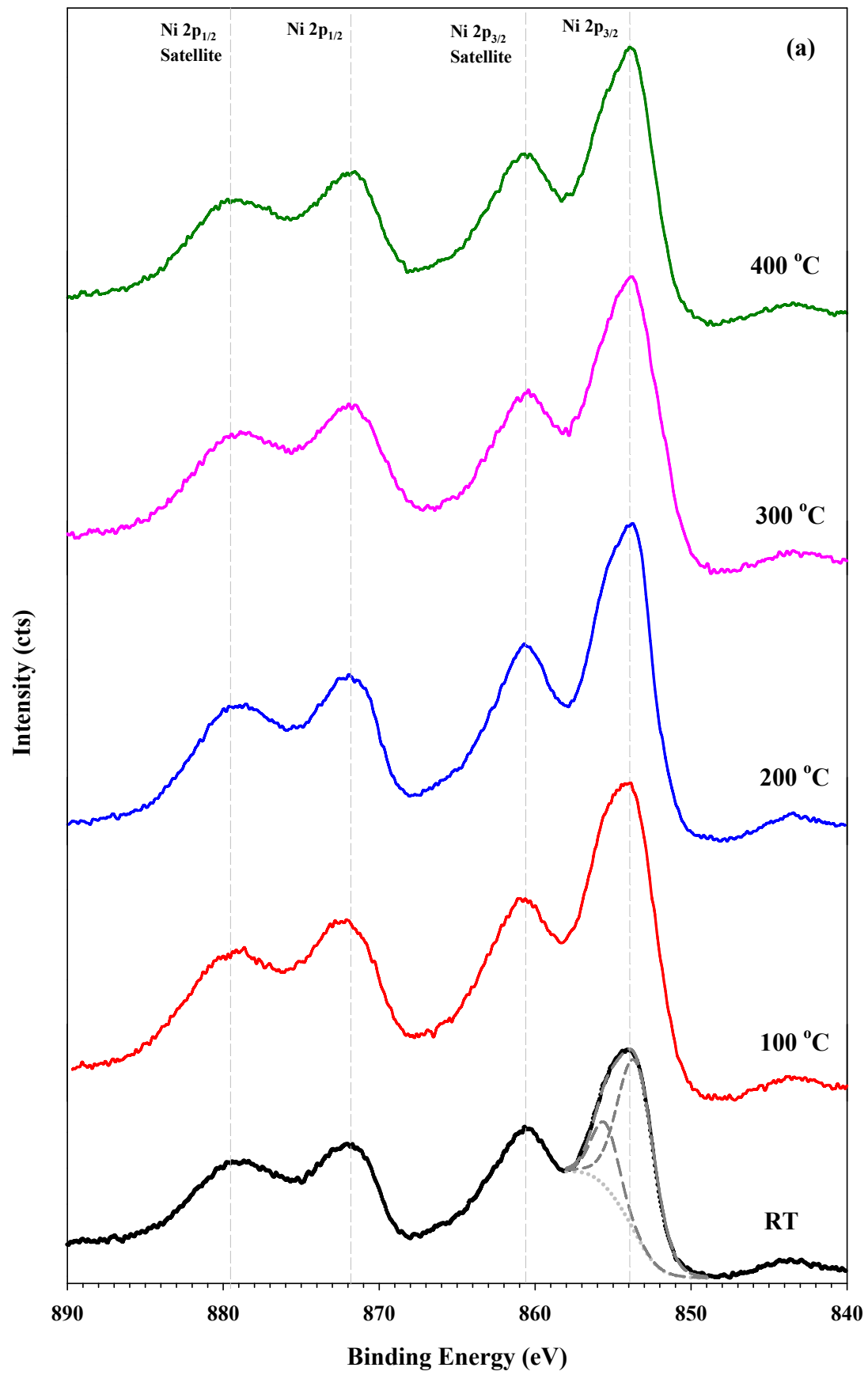


Figure 6.5: The XPS survey scan spectra of the NiO thin films for different substrate temperatures.

The XPS survey scan spectrum of the films shows the presence of Nickel, Oxygen, and carbon (reference) in the films. The Ni 2p_{3/2} and 2p_{5/2} peaks were located at 854 eV and 872 eV, respectively, and the O1s peak was detected at 529.2 eV, so the detailed scan spectra were recorded in the range of 840 to 890 eV for Ni 2p and 524 to 536 eV for O1s peak as shown in Fig 6.6.



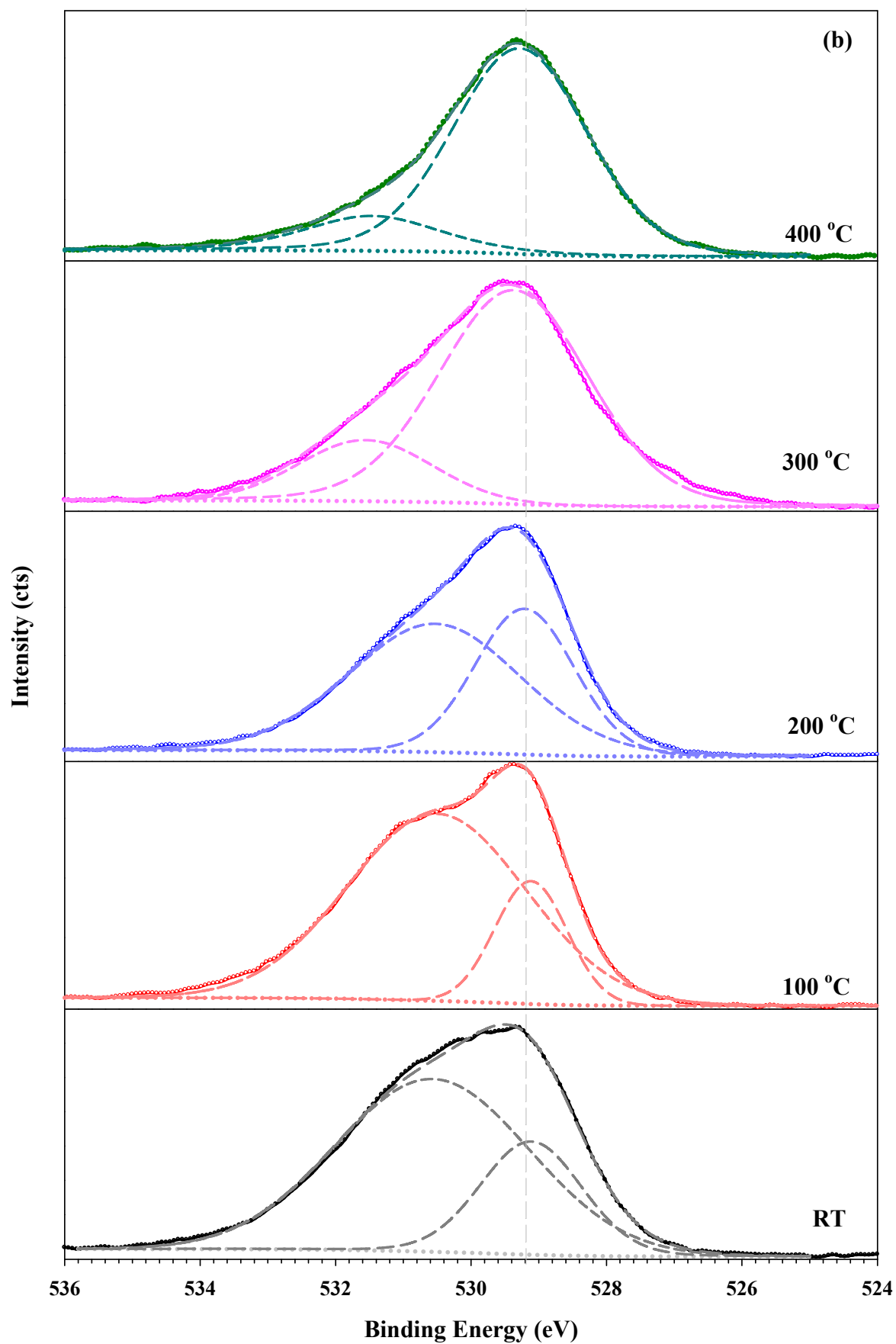


Figure 6.6: The XPS spectra of the (a) Ni 2p and (b) O1s for different substrate temperatures.

Figure 6.6 (a) shows the Ni 2p_{3/2} and 2p_{5/2} peaks, which were located at 854 eV and 872 eV, respectively; with their respective satellite peaks located at 861 eV and 879.5 eV. The satellite peak in NiO is caused due to various reasons: the multi-electron excitations, multiple splitting or surface plasmon loss [155]. As-deposited NiO contained not only Ni²⁺ but also some amount of Ni³⁺ ions so the Ni 2p_{3/2} peak fitted two peaks located at nearly 853.5 eV and 855.5 eV for Ni²⁺ and Ni³⁺, respectively. Although the fitted peaks do not give exactly the peak values but analyze which part of the spectra having larger influence. The fraction of Ni²⁺ state increases with respect to Ni³⁺ as the deposition temperature increases. This was also supported by the O 1s XPS spectra of the NiO thin film deposited at different substrate temperatures as shown in Fig. 6.6 (b). The O 1s spectra also got fitted in two peaks, higher binding energy peak nearly 529.2 eV is due to the Ni²⁺ and the lower binding energy peak are due to the Ni³⁺. As the substrate temperature increases the content of Ni³⁺ ions decreases and the content of Ni²⁺ ions increases in the films. The excess O in the NiO produces the Ni²⁺ vacancies and some of Ni²⁺ ions oxidized to Ni³⁺ ions to keep the charge neutral [156].

6.3.2 Optical Characterization

The optical transmittance spectra of NiO thin films deposited on glass substrates at different substrate temperatures are presented in Fig. 6.7 (a). It can be seen that the film prepared at RT exhibit light brown in color with ~50 % transmittance. The increase in substrate temperature of the films causes an increase in the transmittance. The lower transmittance is associated with an excess of oxygen in the lattice which creates Ni³⁺ ions and this appears as the color centers. This is also supported by our XPS data. Increase in transmittance with substrate temperature is due to the less defect-scattering (Ni³⁺) and improvement of crystalline microstructure of the films.

A strong absorption in the UV region is observed at wavelength ~325 nm which results in the fundamental band edge of NiO. The optical absorption coefficient α of the NiO thin films as a function of transmittance was given by $\alpha = 1/d \ln(1/T)$. The optical energy band-gap of the NiO thin films can be determined from the dependence of absorption coefficient on the photon energy using the Tauc's relation $\alpha h\nu = B (h\nu - E_g)^n$ [49], where n depends on the nature of transition taking place in the materials. NiO allows the direct transition so the energy band-gap could be obtained by plotting $(\alpha h\nu)^2$ vs. $(h\nu)$ plot and extrapolating the linear portion to $(\alpha h\nu)^2 = 0$ as shown in Fig. 6 (b). The value of E_g varies in the range 3.76 to 3.80 eV as the substrate temperature increases from RT to 400 °C. The change in the optical band-gap is due to the change in stoichiometry and crystallinity in the film.

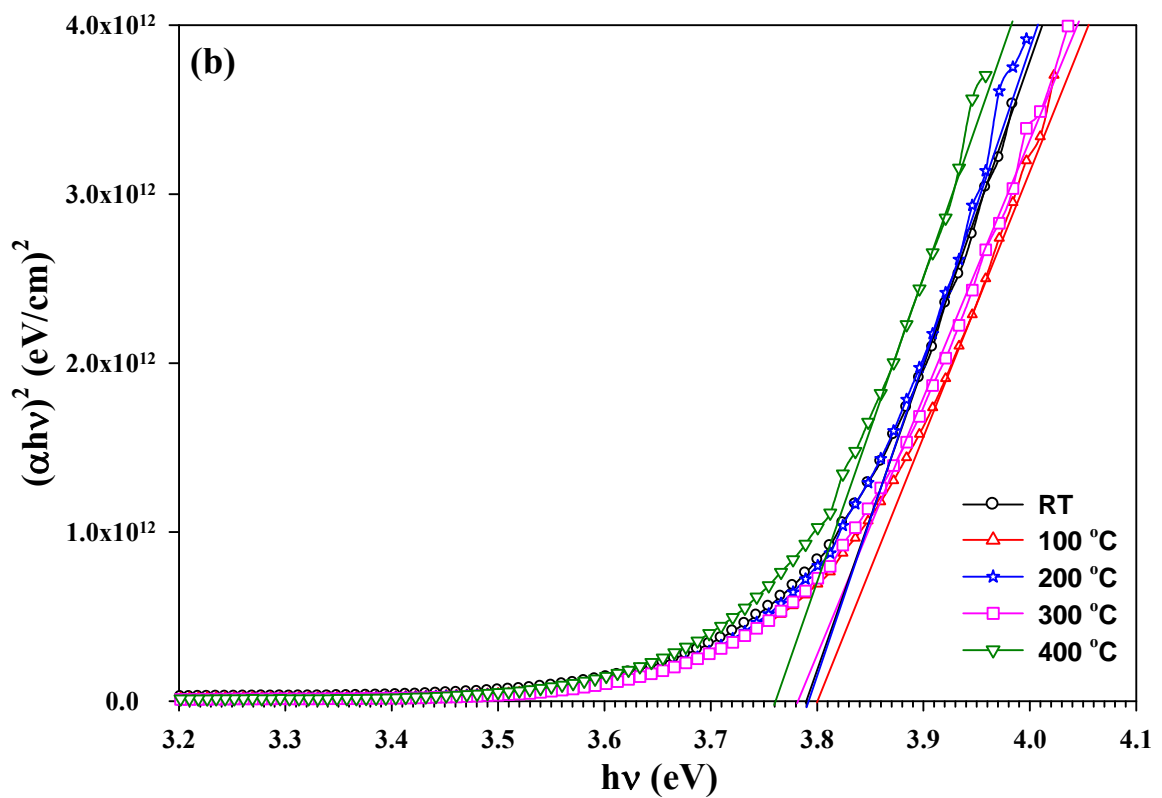
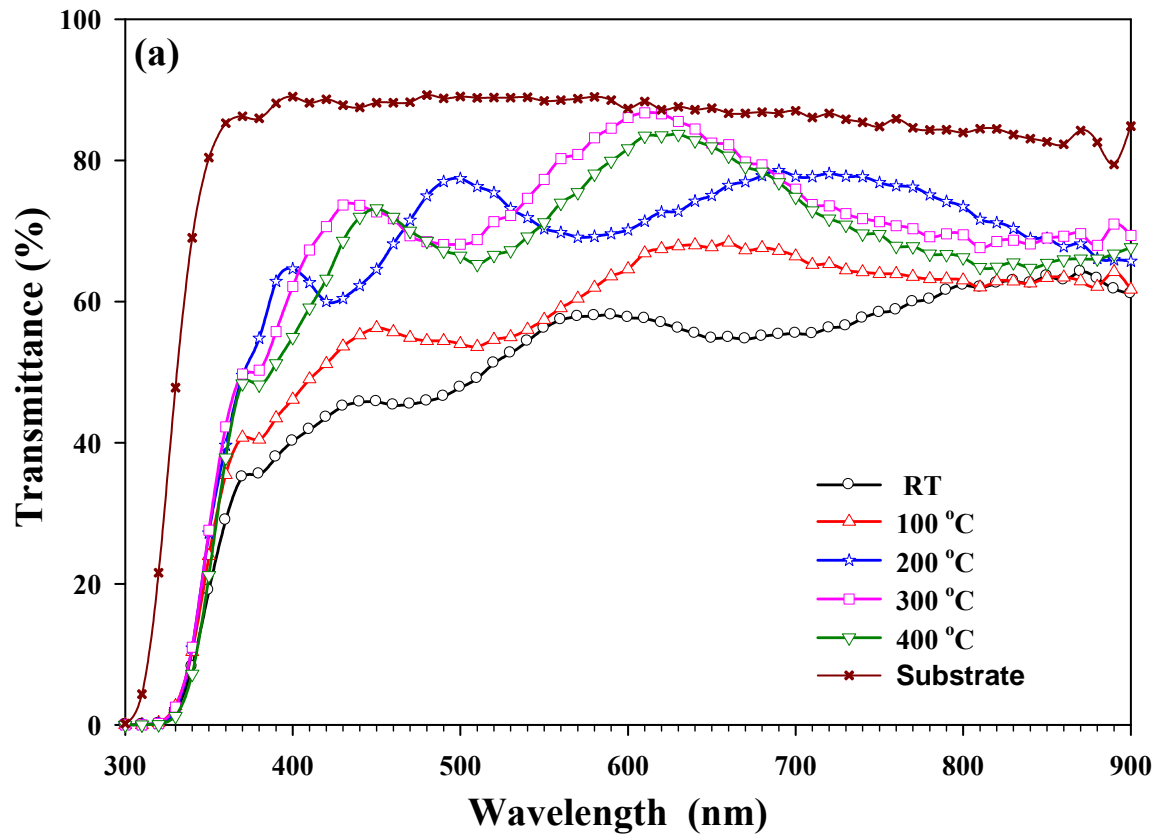
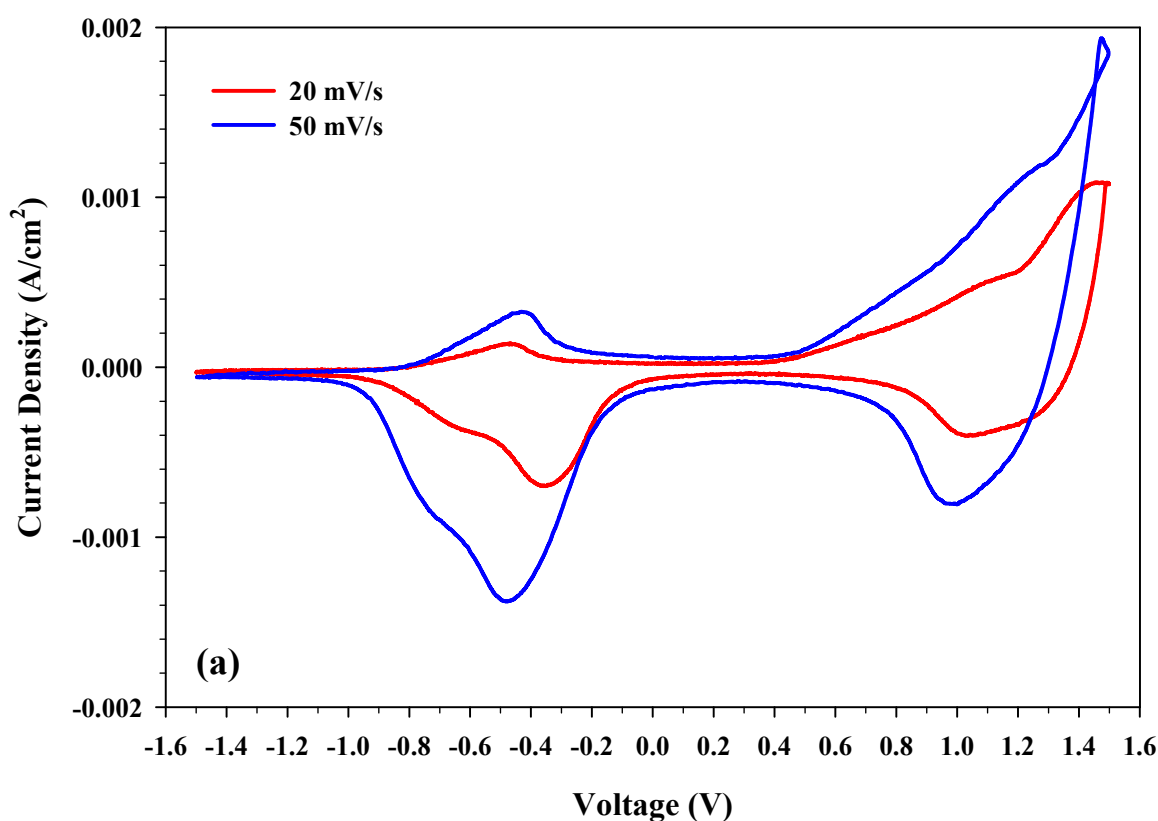


Figure 6.7: (a) Transmittance spectra and (b) $(\alpha h\nu)^2$ vs. $(h\nu)$ plot for NiO thin films deposited at different substrate temperatures.

6.3.3 Electrochromic Characterizations

The electrochromic properties of the NiO thin film were investigated using two-electrode electrochemical cell in 1 M KOH electrolyte. The cyclic-voltammetry (C-V) was performed to exhibit the electrochemical behavior of the film. Transmittance modulation (ΔT), was determined for the NiO thin film in the wavelength range of 400 - 1200 nm by constant current measurement technique. The switching time (t) measurement was done by chrono-amperometry with concurrently measuring the transmittance at ~ 650 nm wavelength.

Cyclic-Voltammetry Measurement: The coloration and bleaching in NiO thin film is due to the transition between Ni^{2+} and Ni^{3+} , which in turn is associated with insertion and de-insertion of OH^- ions and electrons in the film. Cyclic-voltammetry measurement of the NiO thin films, recorded in 1M KOH electrolyte at different scan rate, in the voltage range, -1.5 V to +1.5 V, to evaluate the electrochromic behavior of films, are shown in Fig. 6.8. During the anodic potential scan the current increases resulting in oxidation of NiO causing brown coloration of the film. Two different peaks appear in C-V, due to couple of redox processes taking place in NiO thin film [151]. Usually the redox processes are caused by the transition between NiO, $\text{Ni}(\text{OH})_2$, NiOOH or Ni_2O_3 .



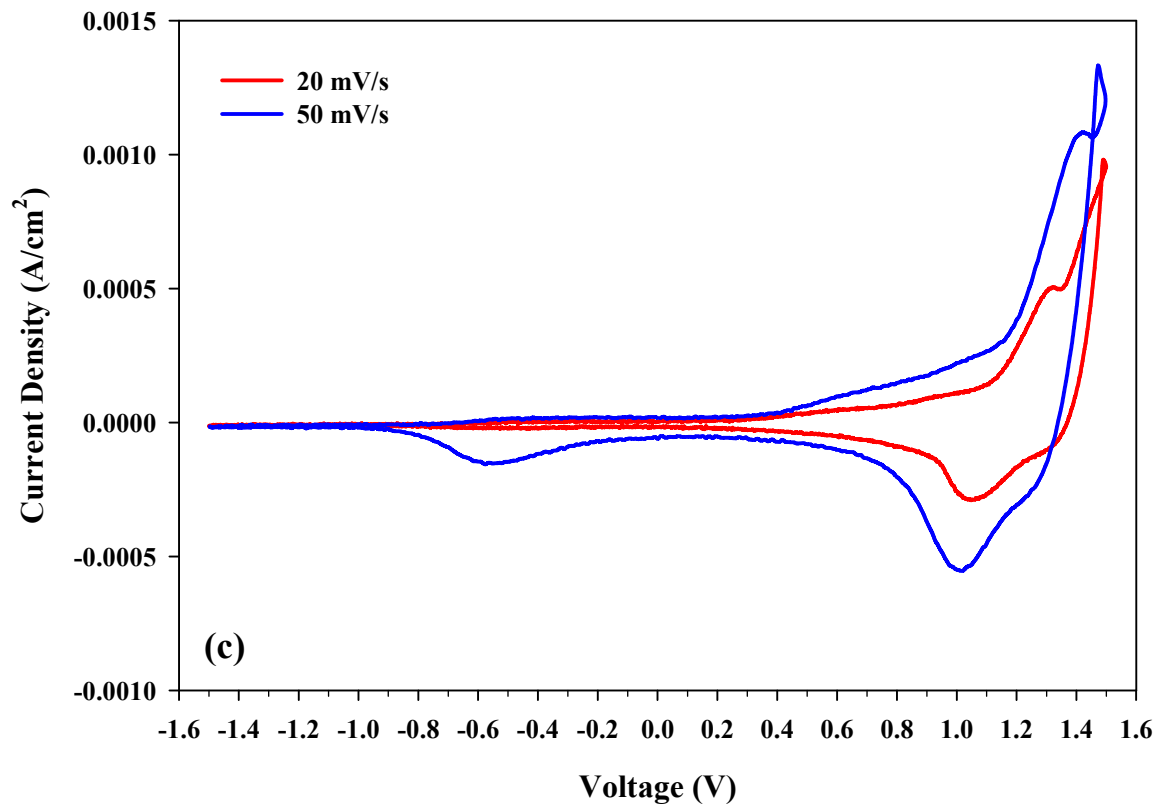
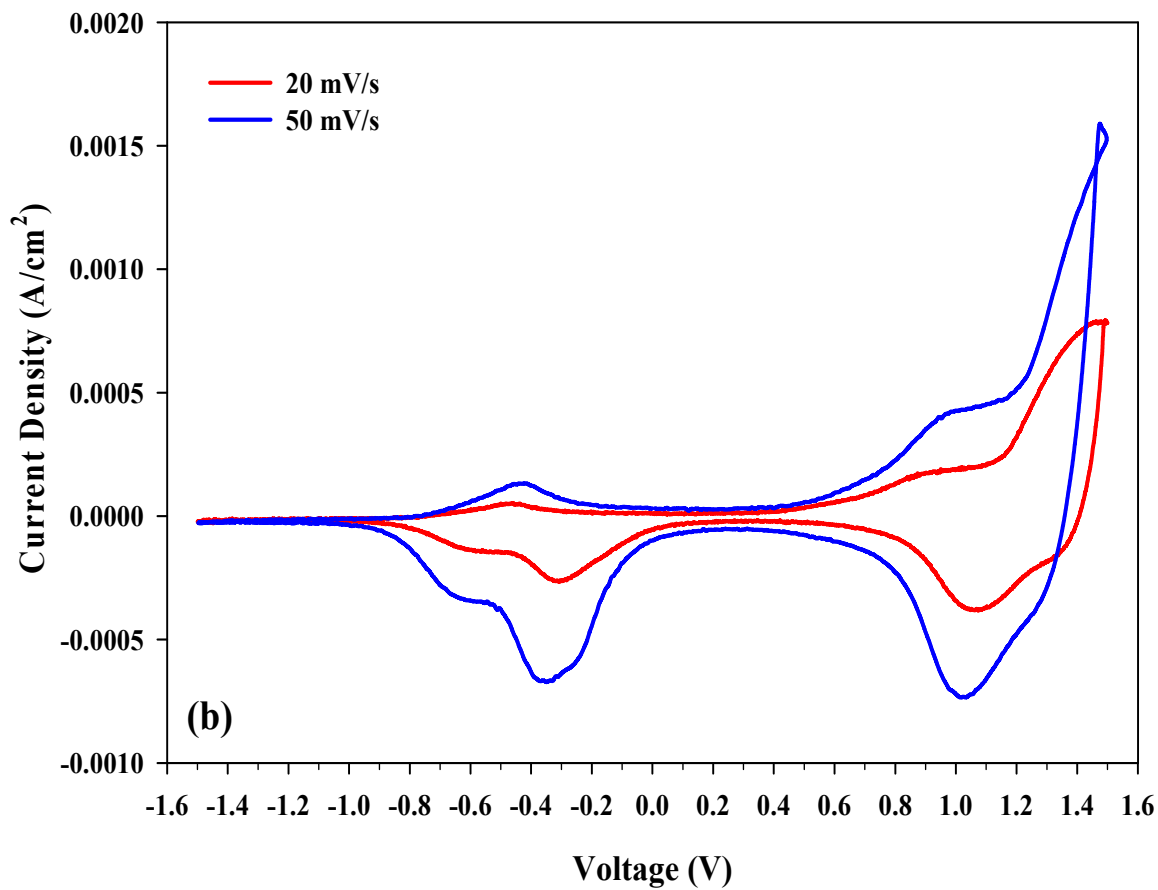


Figure 6.8: Cyclic-voltammogram for NiO thin film grown on (a) RT (b) 200 °C and (c) 400 °C substrate temperature recorded at 20 mV/s and 50 mV/s scan rates.

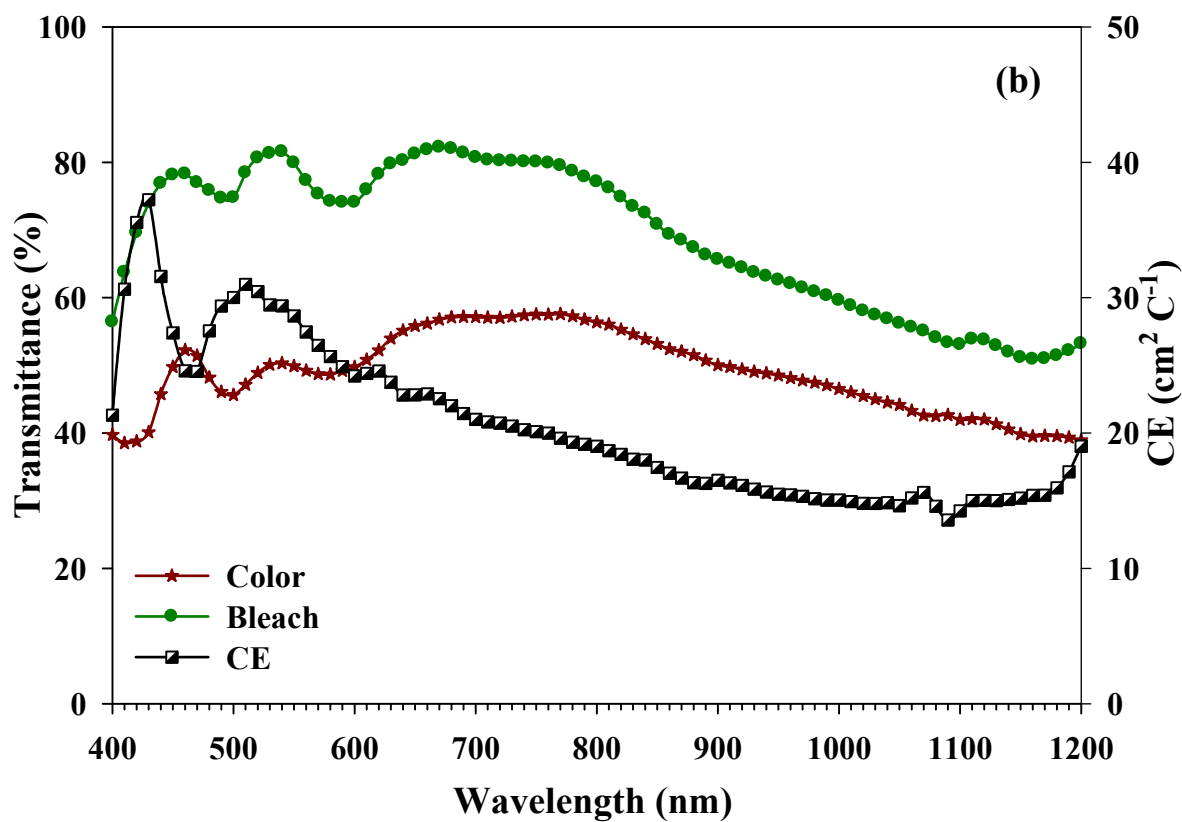
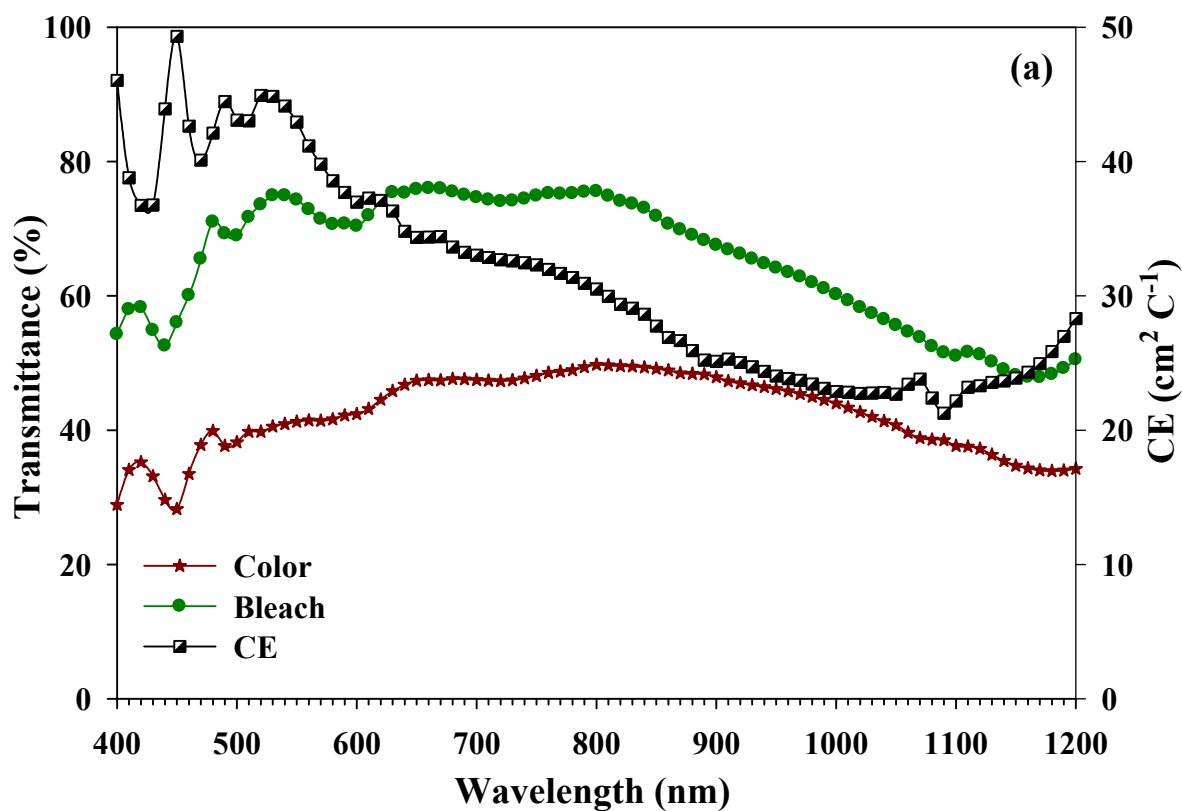
From Fig. 6.8 the anodic peak current density (j_{pa}) and the cathodic peak current density (j_{pc}) increases with the scan rate according to Randles–Servcik equation, which is further used to estimate the diffusion coefficient of ions in the NiO films. The peak current density and the diffusion coefficient at different substrate temperatures for 20 mV/s and 50 mV/s scan rate are shown in Table 6.2

Table 6.2: Electrochemical parameters i_{pc} , i_{pa} , and D of NiO thin films grown at different substrate temperatures in 1M KOH electrolyte at the scan rate 20 mV/s and 50 mV/s.

Substrate Temperature (°C)	Scan rate v (mV/s)	Current density I (A/cm ²)		Diffusion coefficient D (cm ² /s)	
		Anodic j_{pa}	Cathodic j_{pc}	for j_{pc}	for j_{pa}
RT	20	7.68×10^{-4}	5.69×10^{-4}	4.09×10^{-10}	2.24×10^{-10}
	50	1.53×10^{-3}	1.07×10^{-3}	6.49×10^{-10}	3.18×10^{-10}
200	20	1.05×10^{-3}	5.42×10^{-4}	7.59×10^{-10}	2.04×10^{-10}
	50	2.10×10^{-3}	1.17×10^{-3}	12.21×10^{-10}	3.82×10^{-10}
400	20	9.01×10^{-4}	3.88×10^{-4}	5.62×10^{-10}	1.04×10^{-10}
	50	1.37×10^{-3}	7.58×10^{-4}	5.21×10^{-10}	1.59×10^{-10}

The current densities of the anodic and cathodic peaks density decreases with increase in substrate temperature, i.e., the diffusion of ions in the film decreases. At the higher substrate temperature the crystallinity of the NiO thin film increases and thus the space between crystallites decrease, which make it difficult for the ion intercalation or de-intercalation and the diffusion coefficient also decreases.

Constant Current Measurement: In the measurement of transmittance modulation (ΔT) and coloration efficiency, the transmittance spectra of the samples for both colored and bleached states were recorded in the wavelength range of 400 - 1200 nm at RT. Coloration and bleaching processes were carried out at constant current density of 0.2 mA/cm² applied for 25 s. Figure 6.9 shows the spectral transmittance of the NiO thin films deposited at different substrate temperature in the colored and bleached states. It is seen that the variation in the colored and the bleached state decreases with increase in substrate temperature. The films deposited at RT shows the highest variation in the colored and the bleached state. The transmittance modulation and CE at 650 and 1000 nm wavelengths for NiO thin films grown at different substrate temperatures are summarized in Table 6.3 for comparison.



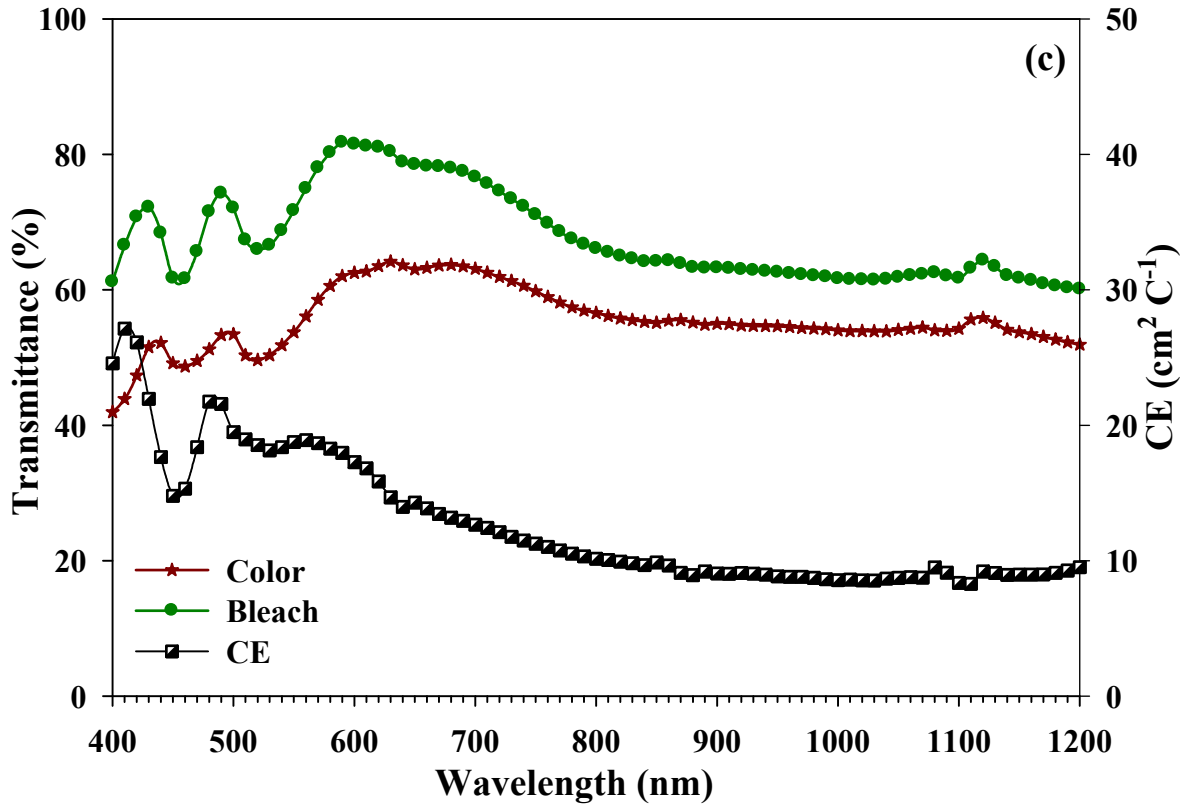


Figure 6.9: The transmittance spectra in the color and bleach state and the CE of NiO thin films grown at different (a) RT, (b) 200 °C, and (c) 400 °C substrate temperatures.

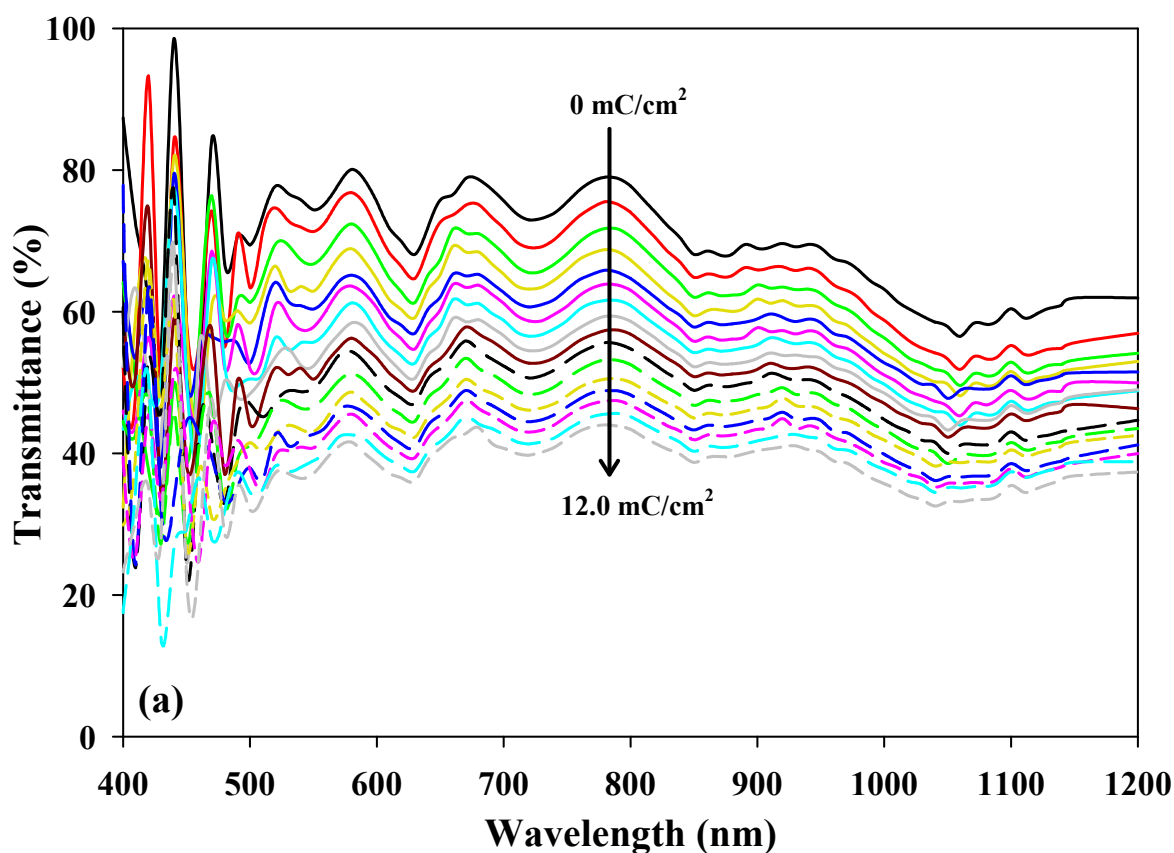
The CE and ΔT decreases with increase in substrate temperature for a given wavelength. It is believed that the higher substrate temperature is favorable to the formation of compact crystalline nickel oxide films. The EC process is associated with the double injection (extraction) of ions and electrons to (from) the film. At the lower substrate temperature the crystalline size are small and the space between the crystals are large enough for ion intercalation. However, with the increase in the substrate temperature the crystalline structure of the sample improves and thus the space between crystallites decreases which unfavorable for the ion intercalation or de-intercalation.

Table 6.3: The transmittance modulation and CE for NiO thin films grown at different substrate temperatures.

Substrate temperature, T_s (°C)	Transmittance modulation, ΔT (%)		Coloration efficiency, CE ($\text{cm}^2 \text{C}^{-1}$)	
	$\lambda = 650 \text{ nm}$	$\lambda = 1000 \text{ nm}$	$\lambda = 650 \text{ nm}$	$\lambda = 1000 \text{ nm}$
RT	29	16	34.5	22.8
200	25	13	22.8	15.1
400	15	8	14.3	8.6

To study the change in transmittance at the different levels of charge intercalation a constant current density of 0.2 mA/cm^2 is applied for the insertion of OH^- ions in the NiO thin film. Concomitantly, the transmittance spectrum for different levels of charge exchange, up to 12 mC/cm^2 , were recorded in the range of $400 - 1200 \text{ nm}$, as shown in Fig. 6.10. The change in the optical density (ΔOD) with the inserted charge density is shown in Fig. 6.10 (b). A linear relationship was observed between ΔOD and the inserted charge density. The photographs of NiO thin films grown at RT in bleached and colored state are shown in Fig. 6.11.

Chronoamperometry Measurement: The rate at which an ECD can be switched from one state to another state is importance for some potential application. The electrochromic switching time of NiO thin film was determined by chronoamperometry measurement at a potential of $\pm 1.5 \text{ V}$ and frequency 0.05 Hz . Figure 6.12 shows the response of optical power and current density with time during application of pulse potential for the NiO thin films deposited at different substrate temperatures.



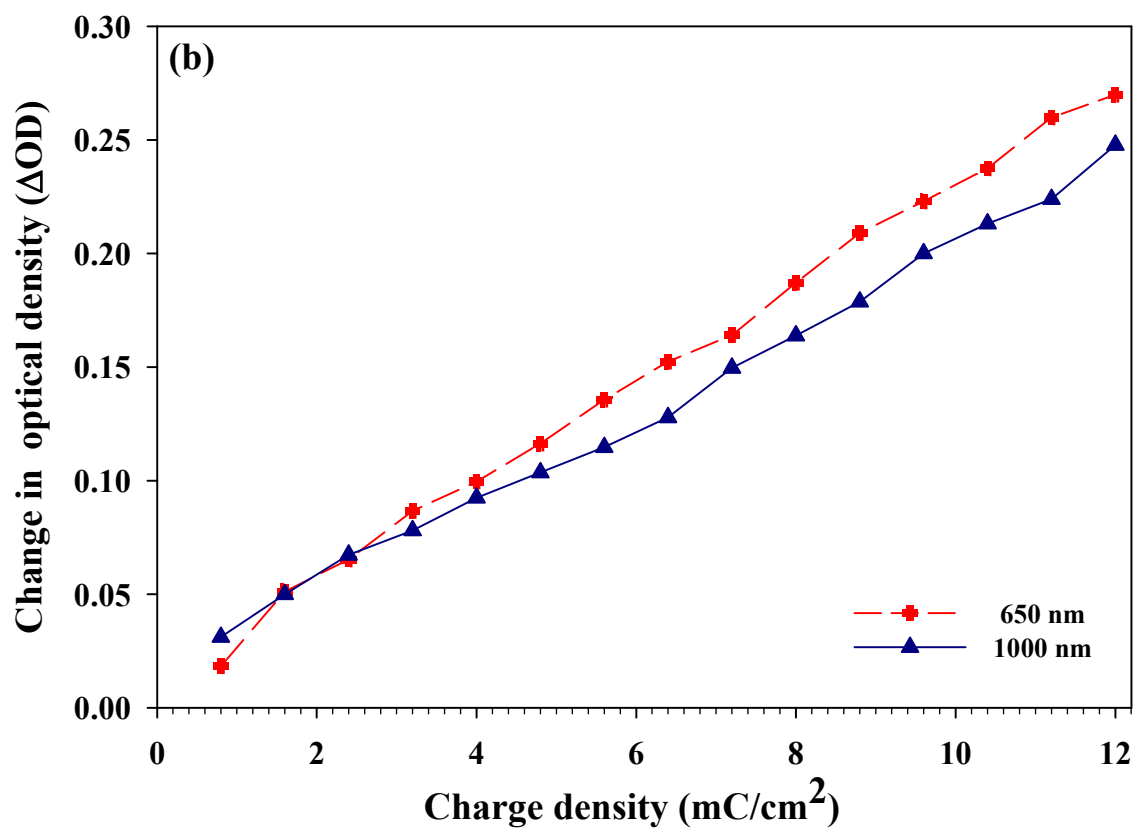


Figure 6.10: (a) Transmittance spectra for different intercalation level in step of 0.8 mC/cm² (b) The change in the optical density with inserted charge density and CE at different wavelengths of NiO thin films.

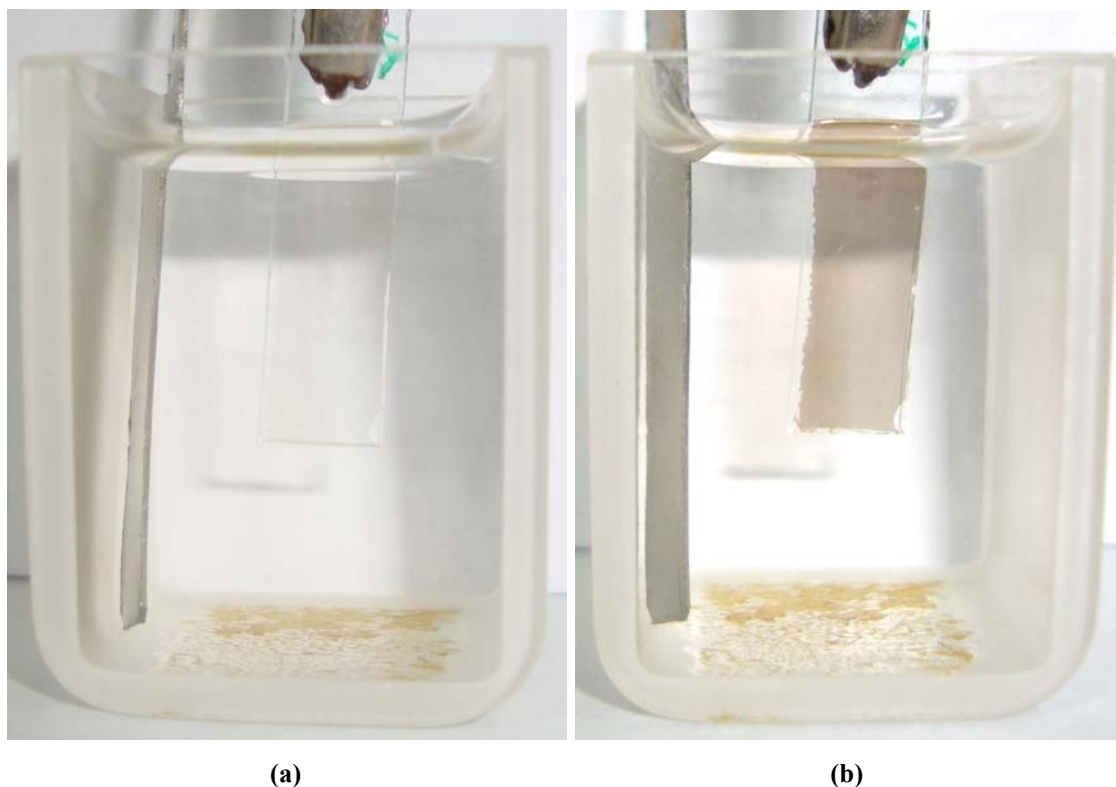


Figure 6.11: shows the photographs of NiO thin films grown at RT in (a) bleached and (b) colored state.

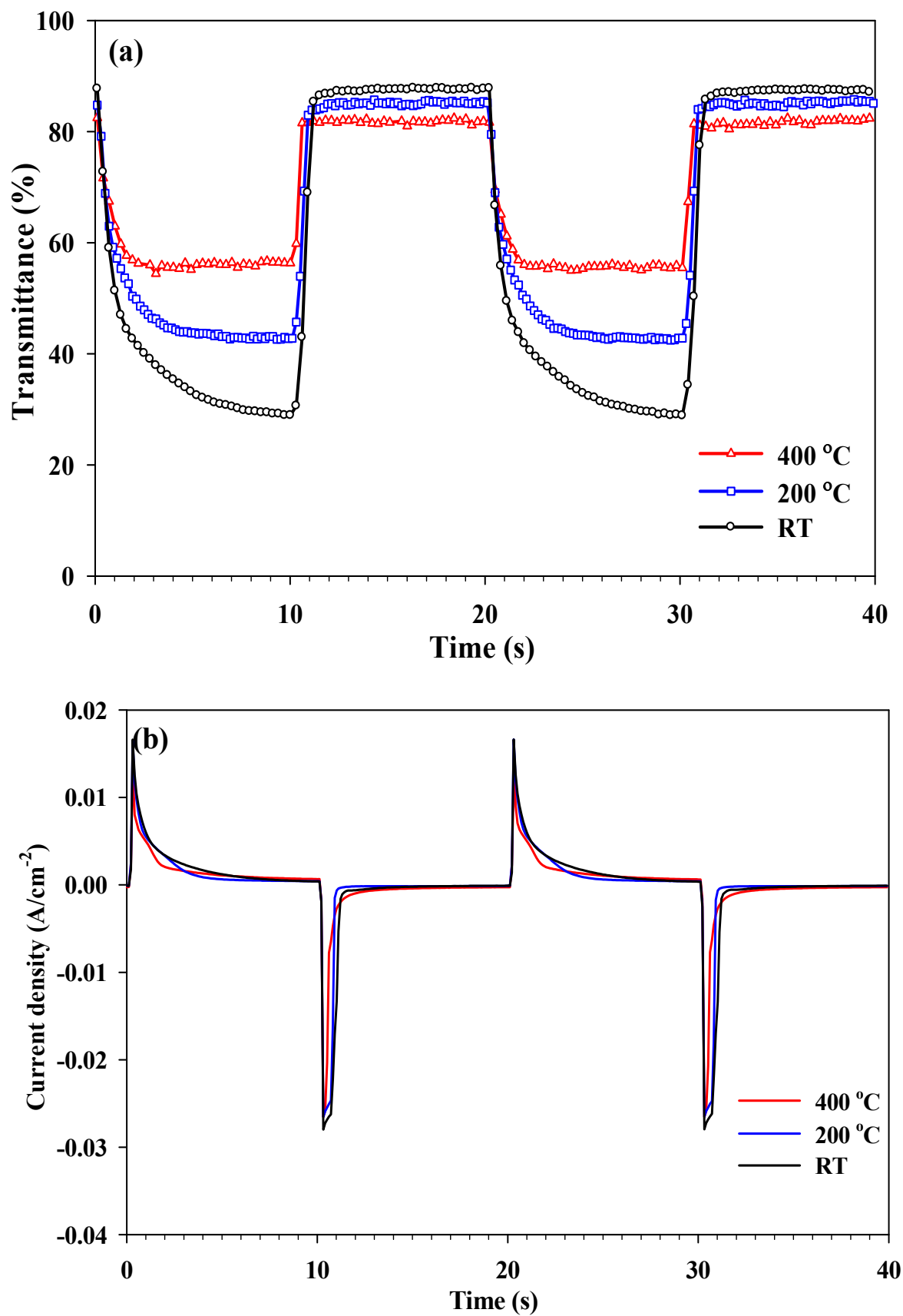


Figure 6.12: (a) The variation in the optical transmittance at 650 nm wavelength and, (b) the current density for NiO the thin films, grown at different substrate temperature, when the electrochemical cell is subjected to a square-wave potential of ± 1.5 V and frequency 0.05 Hz is applied.

The decrease in current with time is due to the increase in the chemical potential of the injected anions (OH^-) or cations (H^+), as intercalation proceeds. The switching time, at 650 nm wavelength, is estimated from Fig. 6.12, for the NiO thin films grown at different substrate temperatures and presented in Table 6.4.

Table 6.4: Switching time data of NiO thin films for different substrate temperature at 650 nm.

Substrate temperature (T_s) °C	Bleaching time (t_b) s	Coloration time (t_c) s
RT	2	10
200	1.5	10
400	3	10

The coloration and bleaching process is associated by the ion intercalation/de-intercalation and thus the switching time is directly affected by several factors such as applied potential, crystal structural, or the composition of the films. The film grown at 200 °C substrate temperature show ‘low’ bleaching time, 1.5 s, and as the substrate temperature increases the bleaching time increases up to 3 s for 400 °C temperature. The increase in bleaching time may be due to crystallization or improvement in composition. The coloration time for all the samples is same as ~ 10 s. The response time during the coloring process was higher than that during the bleaching process, due to differences in conductivity between $\text{Ni}(\text{OH})_2$ and NiOOH . The conductivity of $\text{Ni}(\text{OH})_2$ was lower than that of the NiOOH . Therefore, it would be expected that the coloring process, which involves the transition of $\text{Ni}(\text{OH})_2$ to NiOOH , is slower than the bleaching process, which results in the transition of NiOOH to $\text{Ni}(\text{OH})_2$.

6.4 CONCLUSIONS

NiO anodic EC thin films are prepared by the e-beam evaporation technique at different substrate temperatures. From the GIXRD measurement, the preferred orientation changes from (111) to (200) direction with increase in substrate temperature. At the higher substrate temperature say 300 - 400 °C, there is a columnar grain growth, which results in the increase of the surface roughness. The XPS spectra results show improvement in the composition, which was also confirmed by the optical data i.e. the transmittance of NiO thin film increases with substrate temperature. The EC result shows that the film prepared at RT gives the good electrochromic performance i.e. the good transmittance modulation with $34.5 \text{ cm}^2\text{C}^{-1}$ coloration efficiency, compared to film grown at higher substrate temperature.

Chapter - 7

Electrochromic Device Fabrication and Characterizations

7. ELECTROCHROMIC DEVICE FABRICATION AND CHARACTERIZATIONS

Electrochromic devices (ECD) are of considerable interest in many commercial applications due to their controllable transmission, absorption, and/or reflectance. In this chapter, we discuss a few ECD structures reported in earlier days and present a study of a solid-state ECD structure prepared in our laboratory consisting of layers ITO / NiO / ZrO₂ / WO₃ / ITO on a glass substrate. The aim of this chapter is to illustrate the construction and working of an ECD. To improve the performance of an ECD, the thickness of the ion-conducting, ZrO₂ thin film layer need to be optimized. The indigenously developed devices' characteristic like optical modulation, memory effect, switching time, and cycle-life are presented in this chapter.

7.1 INTRODUCTION

Today, electrochromic devices (ECD) are extensively studied due to its widespread use in many applications. The ECD operated in the transmittance modulation mode is used in smart windows and optical displays, while reflectance modulation is used for automobile rear-view mirrors and thermal control. In the past, many authors have proposed different types of device structures. The first ECD having a sandwich structure of WO₃ thin film on transparent conducting oxide (TCO), followed by a thin film (~ 100 Å) of Au was reported by S.K. Deb in 1969 [13]. However, in this device when the polarity of the applied field was reversed then the bleached state was not observed due to the symmetrical structure. This was soon followed by the completely reversible structure achieved by introducing an asymmetry in the device structure, viz. by introducing an insulating layer of SiO at one of the oxide electrode interfaces. Thus the device structure consisting of multilayered thin films of Au-SiO-WO₃-SnO₂ was deposited on a single substrate, which shows the reversible coloration [157,158].

Over the past few decades many articles have been published which are related to electrochromic (EC) effect. There are many possible device structures reported in the literature [1,159,160,161]. The ECD structure may have five layers (transparent conducting oxide (TCO) layer / ion storage layer (IS) / solid electrolyte / EC layer / TCO layer) superimposed on one substrate or may be positioned between two substrates in the laminate configuration (see Fig. 1.1). The central layer is a pure ionic conducting layer for small ions

such as H^+ , Li^+ , and Na^+ . The EC layer is located on one side of the ion-conducting layer, and an ion-storage layer serves as a counter electrode on the other side of the ion-conducting layer. Furthermore, TCO layers, one on the outer side of the EC layer, and the other on the outer side of the counter electrode layer are used to induce the EC effect by an applied electrical field. In laminated EC devices, liquid or gel is used as an electrolyte as it is easy to construct but it has a problem related to its tendency to dissolve the EC thin film layers and thus leads to leakage of liquid electrolytes. So, in solid thin film ECD, solid inorganic or organic material is used as an electrolyte.

C. G. Granqvist et al. have reviewed a brief discussion of ECD, which was investigated between 1998 to 2001, and in 2003 [162]. In the year 2003, A. Azens et al. also reported a six-layered device, which was made by reactive dc magnetron sputtering, in which WO_3 and NiO are EC layers and ion-storage layers, respectively and the WO_3 film between the acidic ZrO_2 and the NiO_xH_y film was used to serve as an optically passive protective layer [163]. They have also reported the EC device structure like ITO / WO_3 / electrolyte / ZrO_2 / NiO_x / ITO configuration using Polymer electrolytes [164]. Recently, Yanchun He et al. reported a solid-state ITO / WO_3 / Ta_2O_5 / NiO / Ag / Glass ECD structure for thermal control [165].

Over the years, people have shown more interest in EC technology for commercial applications. The EC devices fabricated in commercial and university labs are reviewed by C. Lampert in 1998 [166]. The review article by R. Baetens et al. gives the survey of smart windows that are currently available in the market [167]. Large-area commercial EC windows for buildings are produced by SAGE Electrochromics [<http://www.sage-ec.com/>], EControl-Glas [www.econtrol-glas.de] and Gesimat [www.gesimat.de] companies. Some other companies like Saint Gobain Sekurit (France), ChromoGenics (Sweden), and Gentex (MI, USA) produce EC glass on small scale, mainly for automotive applications.

In the present chapter, we study a solid ECD consisting of layers ITO / NiO / ZrO_2 / WO_3 / ITO on a single glass substrate fabricated in our laboratory. In our proposed ECD structure, cathodically colored WO_3 is the EC film responsible for the optical modulation. The ZrO_2 thin film acts as an ion-conducting layer that passes the hydrogen ions when a voltage is applied to the electrodes. The NiO thin film acts as an ion-storage layer, which provides the ions during the coloration of the device. The ITO thin films acts as a transparent conducting electrode. The fundamental properties of ITO, WO_3 , ZrO_2 , and NiO films were

previously examined in the earlier chapters of this thesis and therefore in this chapter we focus on the fabrication of the solid-state ECD and investigate its EC properties.

7.2 ELECTROCHROMIC DEVICE FABRICATION

The different layers of solid ECD are deposited by different physical vapor deposition techniques in a vacuum chamber. Organically cleaned glass slides are used as the substrate material. The ITO thin films are deposited by RF magnetron sputtering onto the externally unheated soda-lime glass substrates having an area of $2 \times 2 \text{ cm}^2$. The ITO coated glass substrate has a sheet resistance of 5-10 Ω/\square . Subsequently, NiO and ZrO₂ are deposited by e-beam evaporation method on the ITO coated glass substrate. H⁺ ions are injected into the NiO film, via ZrO₂ / NiO / ITO film structure by electrochemically cycling it in 0.1 M KOH electrolyte. After removing the film structure from the KOH electrolyte it is washed with distilled water to get rid of KOH and dried using dry air. Now the WO₃ thin film is deposited by thermal evaporation method on the above structure. Finally, the ITO thin film is deposited on the top of the above device structure using RF magnetron sputtering. The film preparation method, the rate of deposition, thickness of the film, and the substrate temperature are listed in Table 7.1.

Table 7.1: Thin film deposition method and deposition parameters for the fabrication of the ECD.

Thin film	Film preparation method	Substrate temperature (°C)*	Thickness of the film (Å)	Rate of deposition (Å/s)
ITO	RF magnetron sputtering	RT	4000	3.5
NiO	e-beam evaporation	200	2500	2.5
ZrO ₂	e-beam evaporation	RT	2000-5000	2
WO ₃	Thermal evaporation	200	2500	4
ITO	RF magnetron sputtering	RT	4000	3.5

* Deposition temperature is the temperature at which the substrate is held, the temperature increases during deposition is not considered

As discussed in earlier chapters that the NiO and WO₃ thin film deposited at lower substrate temperature (RT - 100 °C) shows good EC properties. Nevertheless, in device's fabrication, NiO and WO₃ thin films are deposited at 200 °C substrate temperature to provide better adhesion and to protect it from being damaged while ZrO₂ and ITO thin films are deposited on it via high kinetic energies. A frame-shaped shadow mask having an area 2×2

cm² is used to avoid short-circuiting between the different layers from the edge. During the deposition of the different layers of the solid-state EC device, the structure is taken out from the vacuum chamber to change the source material and the shifting mask. The active area of the device is ~1.6 cm². The final configuration of the multilayered EC structure is shown in Fig. 7.1.

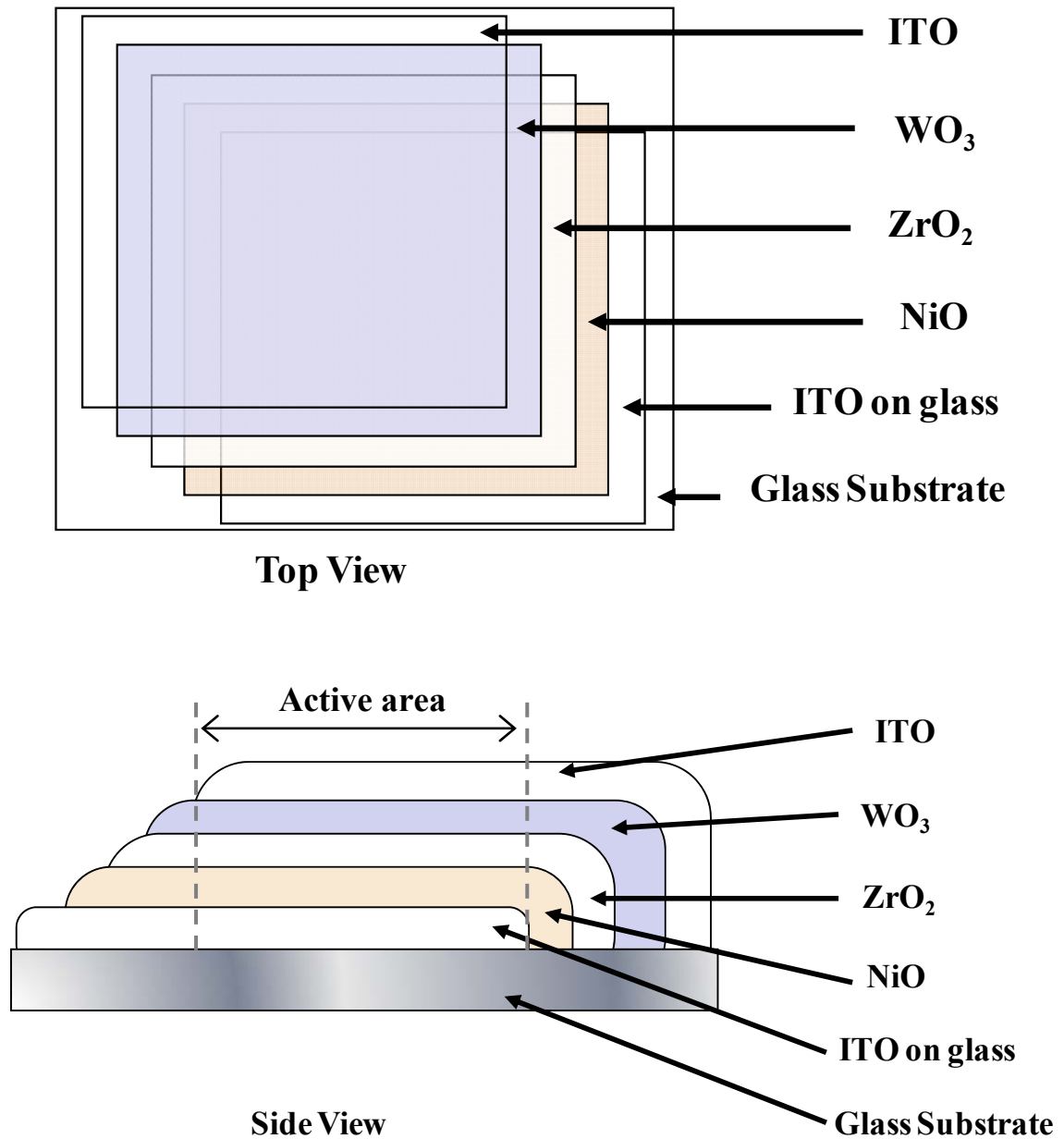


Figure 7.1: A schematic diagram of the ECD's structure with a frame-shaped shadow mask (2.0×2.0 cm²).

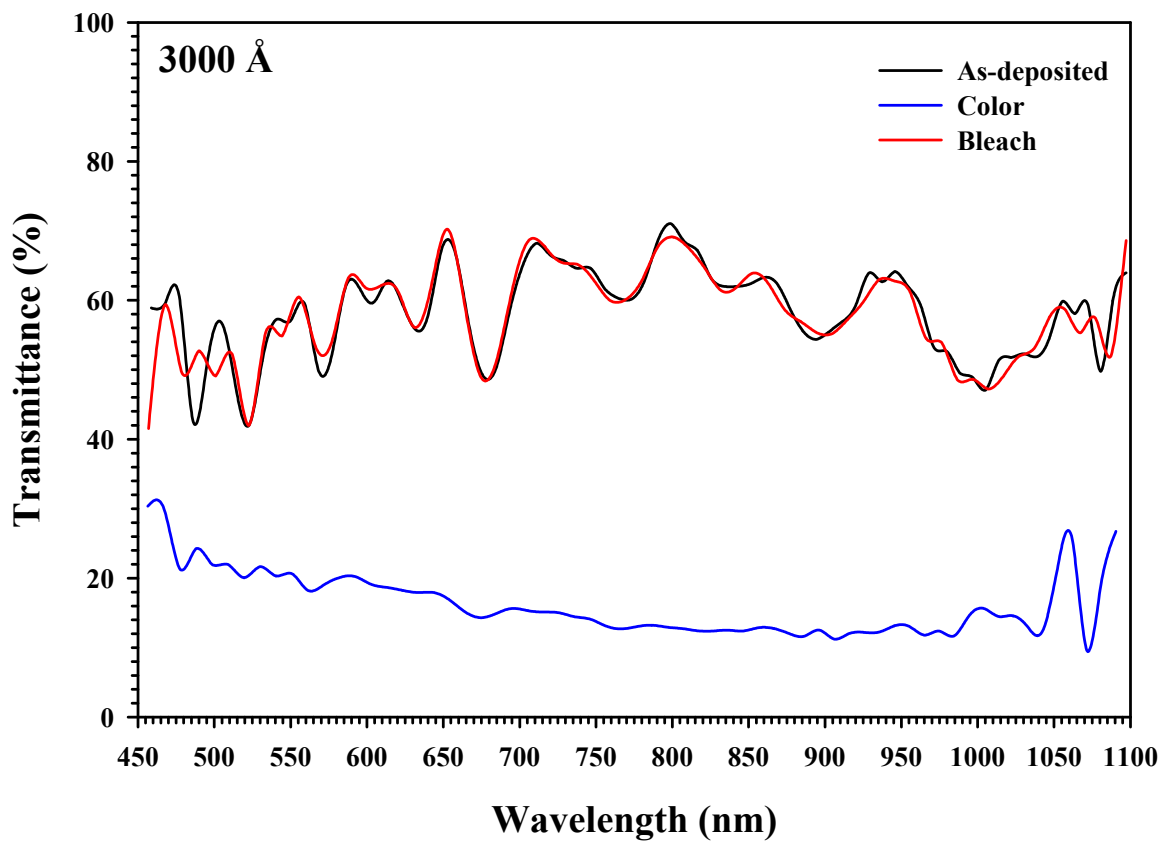
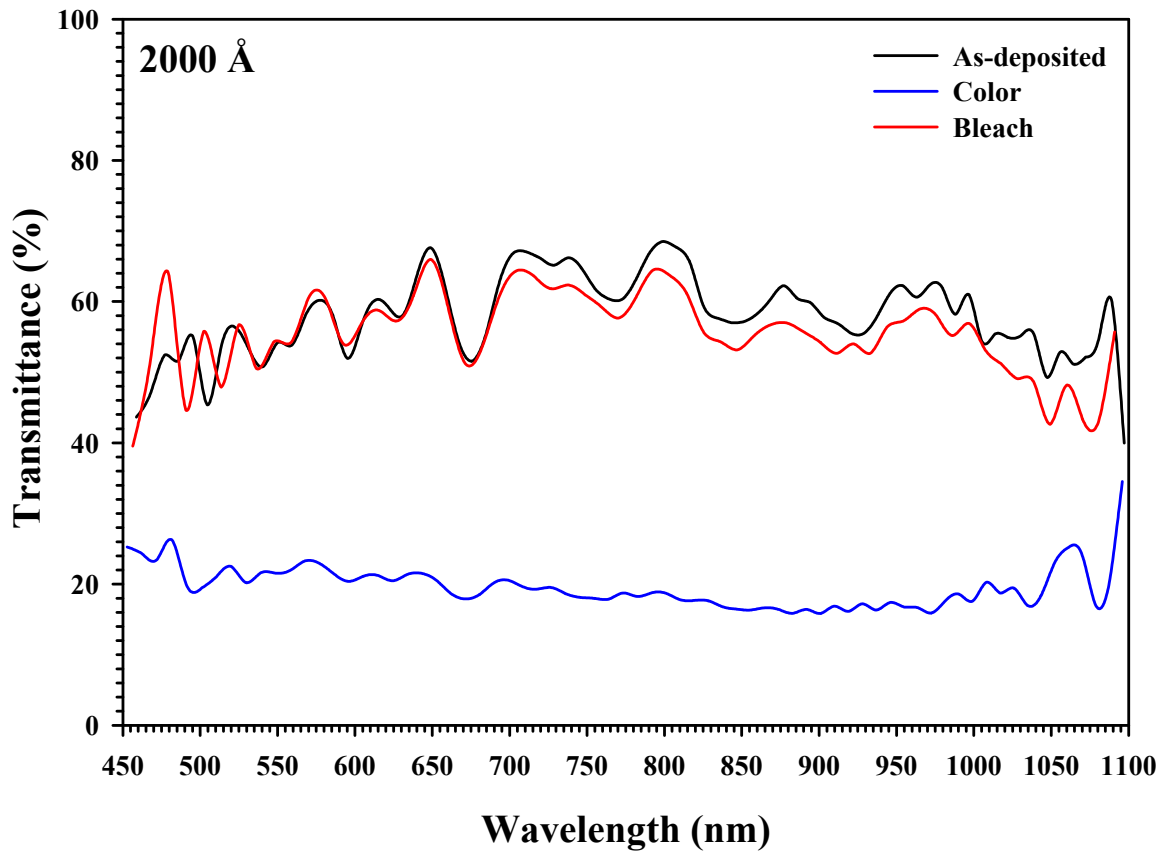
7.3 ECD CHARACTERIZATIONS

The ECD can be characterized by the following: transmittance modulation, open-circuit memory effect, switching time, and cycle-life. The transmittance modulation of the ECD is measured by applying a constant voltage difference between both ITO electrodes to color and to bleach the device and concomitantly measuring the transmission spectra for both the fully color and the bleach states. For the open-circuit memory effect measurement, voltage pulse was applied for the coloration of the device and the optical behavior in an open-circuit condition with time was measured. A square wave pulse voltage was applied to the device for evaluating the switching time of the ECD and concurrently the optical measurements were performed using a Laser diode (650 nm) and a Si photo-detector. For the cycle-life time measurement of the device, it was subjected to continually color-bleach cycling in the same way as for the switching time measurement.

7.3.1 Transmittance Modulation

The ZrO₂ electrolyte gives pathway for the ions to be injected into or ejected from the EC layers. Thus, the effect of ZrO₂ thin film's thickness on transmittance modulation was investigated. The transmittance modulation (i.e., change in the transmittance of bleached (T_b) and the colored (T_c) state of the ECD) is measured by applying a constant voltage ($\pm 5V$) for color and bleach states of the device. When a positive potential is applied to the bottom ITO film, the color changes to dark from transparent and when a negative potential is applied, the color changes to transparent reversibly. During coloration, H⁺ ions are intercalated electrochemically into the WO₃ film from NiO film via ZrO₂ electrolyte, while during the bleaching process H⁺ ions are de-intercalated from the WO₃ thin film. The optical transmittances for the as-deposited, colored, and bleached states of devices with varying ZrO₂ thickness are presented in Fig. 7.2.

The ZrO₂ thin film has more than 90 % transmittance so it does not affect the overall transmittance of the device and thus all the devices have ~59 % transmission in the as-deposited state. The transmittance modulations of the device are calculated from Fig. 7.2 and are presented in Table 7.2.



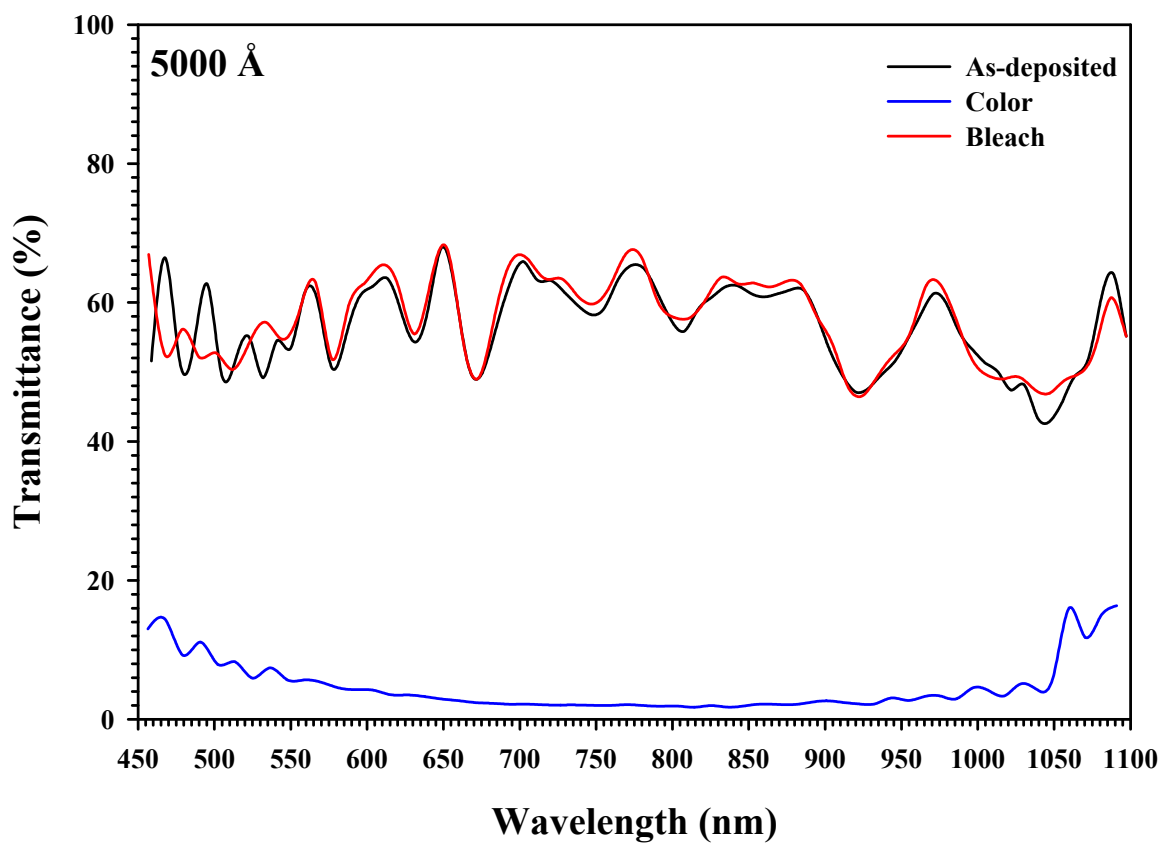
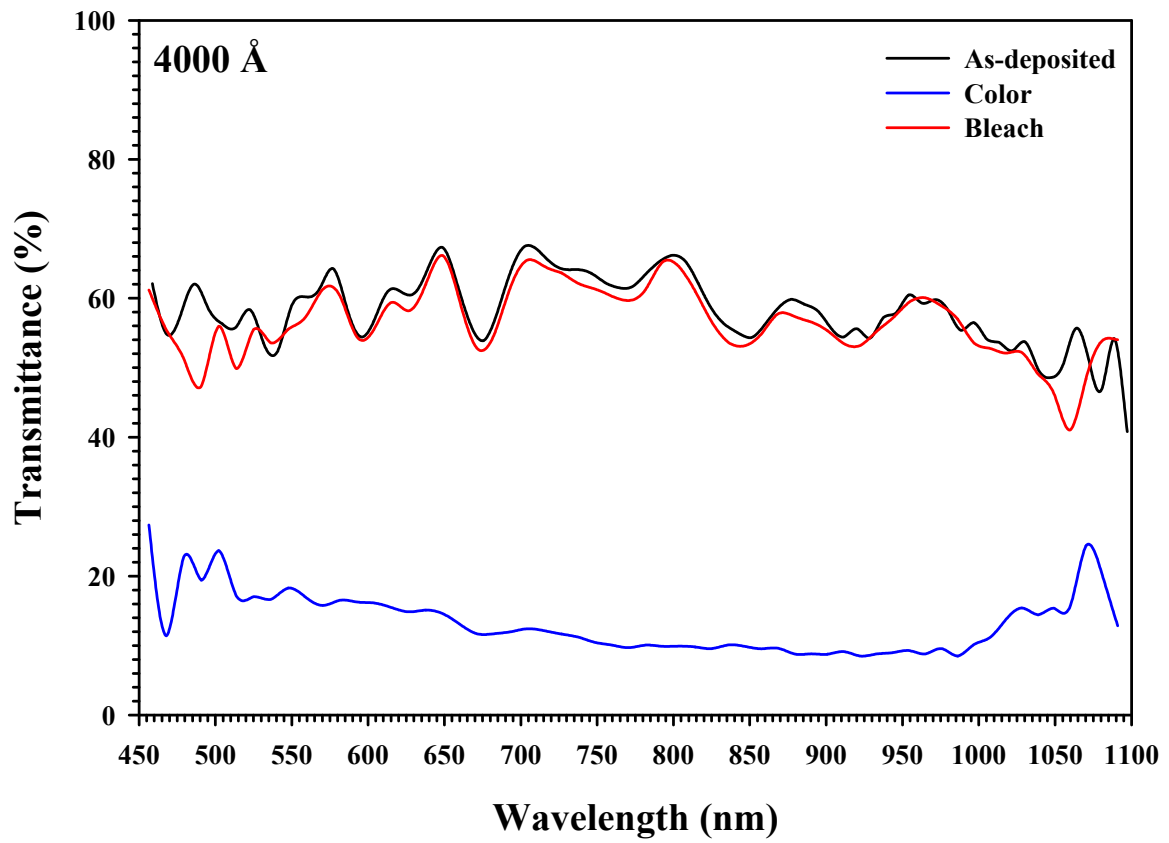


Figure 7.2: The transmittance spectra in the as-deposited, color, and bleach state of ECD with different ZrO_2 thickness.

Table 7.2: The transmittance modulation of ECD for different ZrO₂ thicknesses.

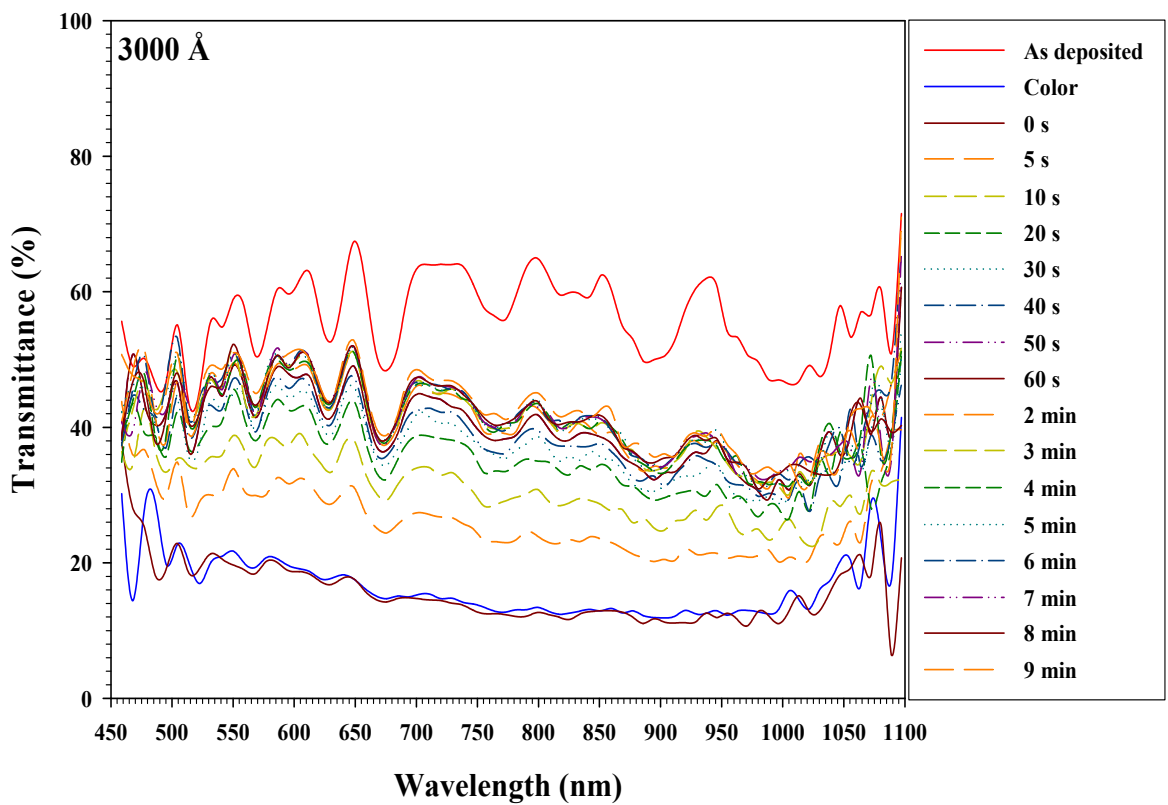
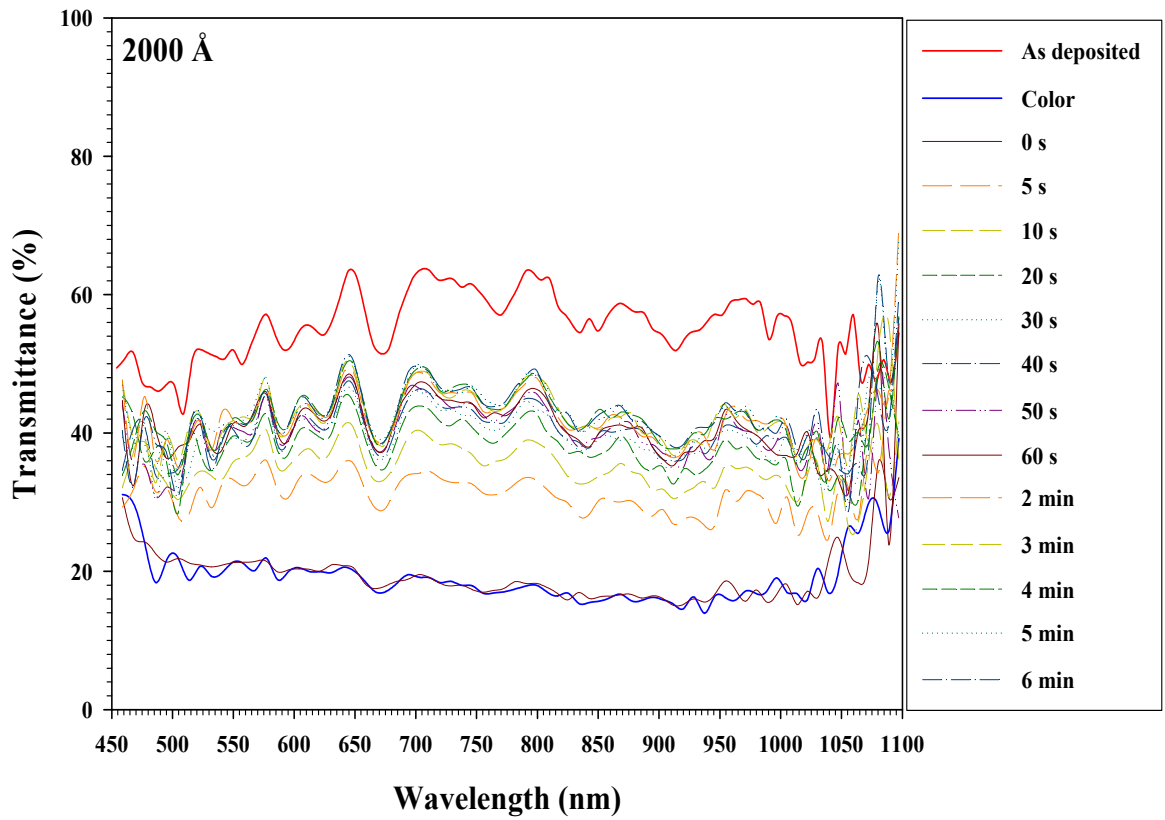
ZrO₂ thickness (Å)	Transmittance T_(avg) (%)		Transmittance Modulation ΔT (%)
	Bleach	Color	
2000	59	19	40
3000	59	16	43
4000	59	12	47
5000	59	3	56

The transmittance modulation of the ECD increases with increase in ZrO₂ film's thickness and the maximum transmittance modulation was 56 % for the device having 5000 Å ZrO₂ film thickness. Optimization of the electrolyte thickness layer is also important for the memory effect in ECD. Thus, we have also monitored the open-circuit memory effect behavior for different ZrO₂ film's thicknesses.

7.3.2 Memory Effect

The memory effect is one of the excellent benefits of ECD. As discussed in Chapter 1, open-circuit memory effect is defined as the time duration in which the material remains in steady state even after switching off the applied voltage. In the bleached state, the WO₃ and NiO thin film layers are thermodynamically stable and thus no change was observed if ECD was initially in the bleached state. In this experiment, we applied a voltage of +5 V for the coloration of the device and then measured the optical behavior in an open-circuit condition. The transmittance of the device was monitored after various open-circuit times and is presented in Fig. 7.3.

As shown in the Fig. 7.3, if the ECD is initially in the color state, the transmittance of the device increases with time and reaches the bleach state. The self-bleaching rate decreases monotonically with increasing ZrO₂ electrolyte thickness. For the 2000 Å ZrO₂ thickness the transmittance in colored state was 19 %, and as the open-circuit time increased the transmittance increased slowly and reached ~55 % after 6 min. In contrast, 5000 Å ZrO₂ device showed excellent long-term memory, with transmittance in colored state below 3%, and the colored state remained constant up to 20 % after 170 min.



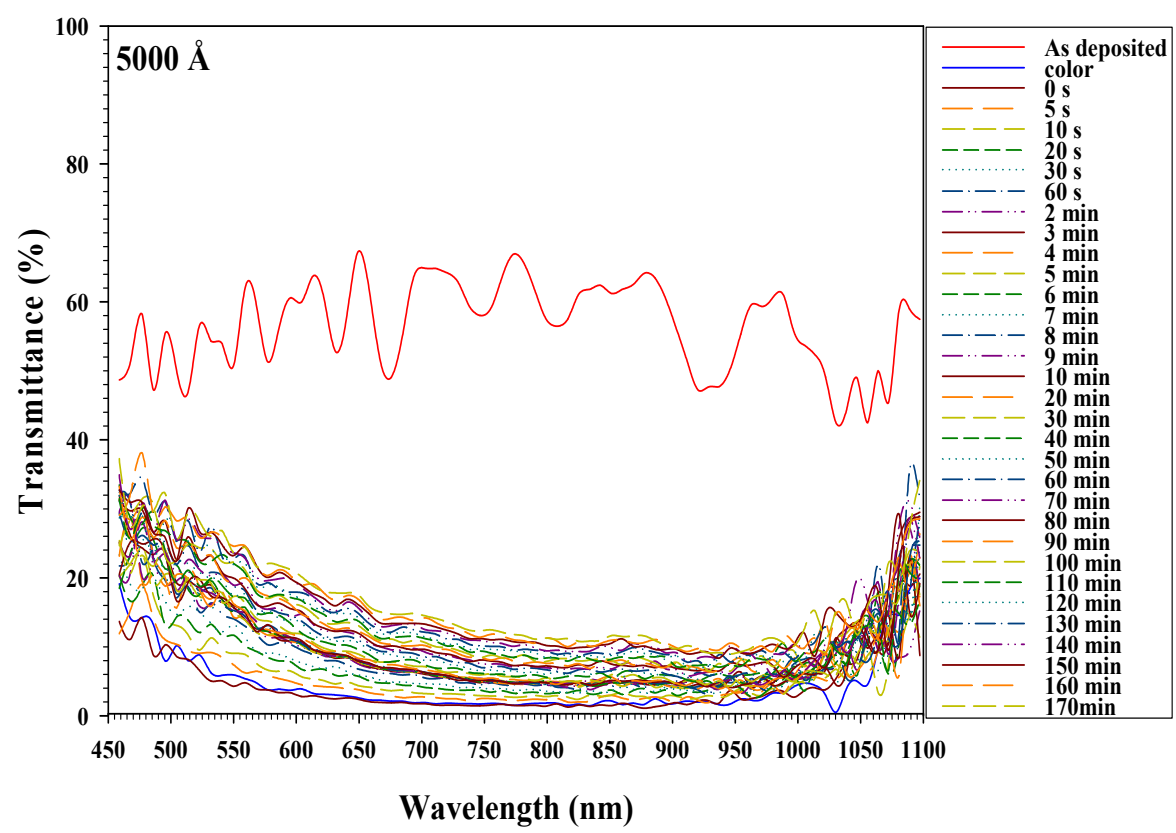
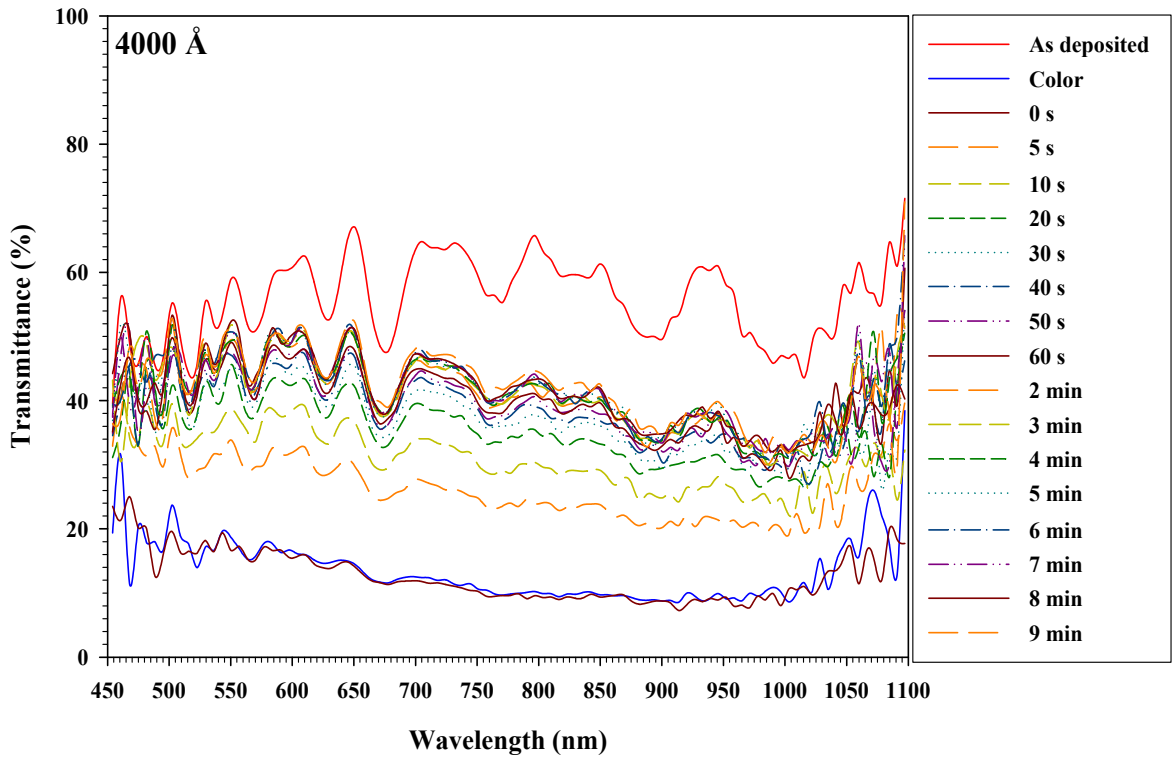


Figure 7.3: The change in the optical density with time in open circuit conditions of ECD having different ZrO₂ thickness.

This self-bleaching of the ECD was observed due to the short-circuiting between WO_3 and NiO layer originating from “pin-holes” during ZrO_2 film depositions, producing oxidation and reduction (de-intercalation and intercalation) of WO_3 and NiO, respectively. In case of lesser thickness of ZrO_2 film, there is a large possibility for the short-circuiting between WO_3 and NiO and thus less transmittance modulation and memory effect were observed. Another reason for the self-bleaching is due to the chemical reaction at the edge or the film surface with oxygen from the atmosphere. However, a new voltage pulse easily regains the optical loss. The ECD having 5000 Å ZrO_2 thickness shows the high transmittance modulation and open-circuit memory effect, so this ECD was used for further EC measurement i.e. switching time and cycle-life.

7.3.3 Switching Time

The switching and stability of the devices were measured by applying a square wave voltage to the device. In addition, concurrently, the variation in the optical transmittance with time was recorded. Figure 7.4 shows the transmittance versus time, at 650 nm wavelengths, subjected to different square-wave potential for the ECD having 5000 Å ZrO_2 thickness.

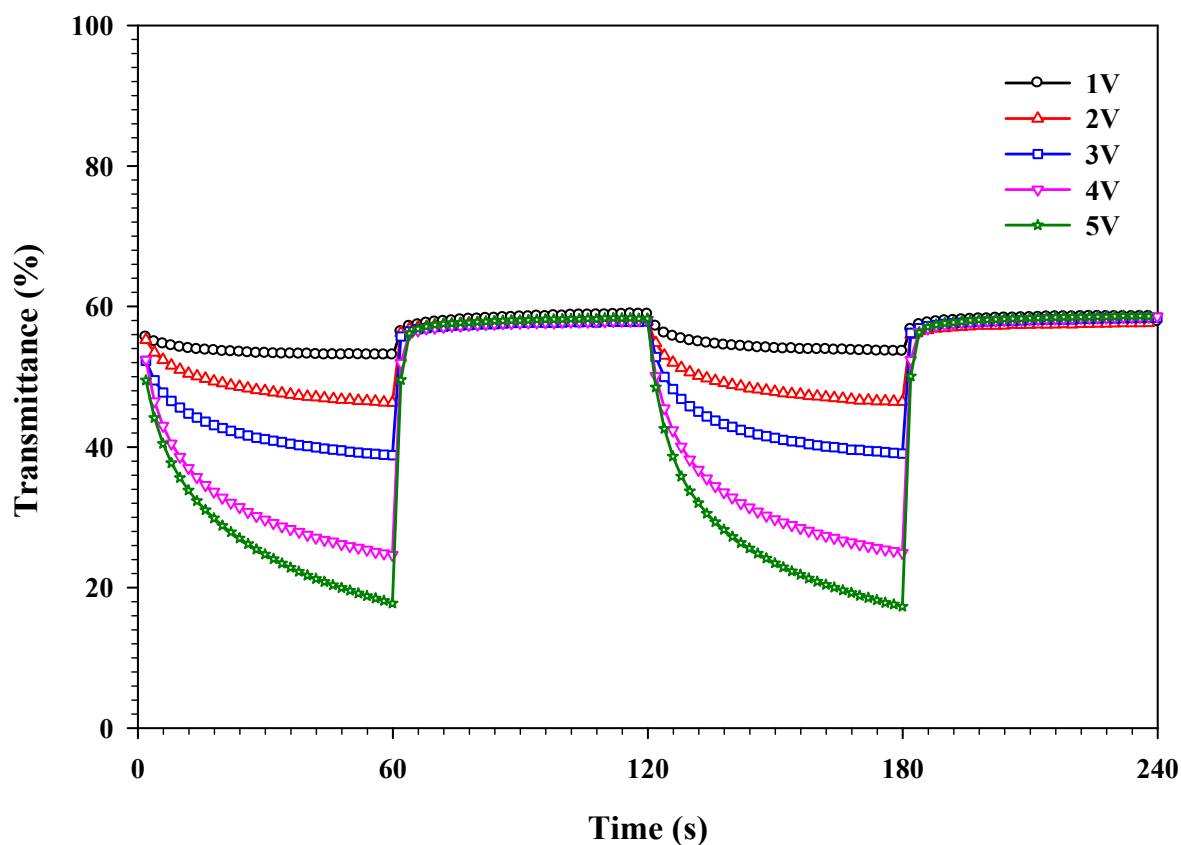


Figure 7.4: The variation in the optical transmittance at 650 nm wavelength for ECD having 5000 Å ZrO_2 thickness.

The switching time, at 650 nm wavelength, is estimated from Fig. 7.4 for ECD under various applied voltages. The changes in transmittance take place within a few tens of a second after application of the voltage pulse but coloration does not reach saturation even after several minutes. The change in optical density increases with increase in applied voltage. The maximum transmittance change was observed for an applied voltage of ± 5 V with coloration and bleaching time of 120 and 2 s, respectively. The photographs of the corresponding colored and bleached state are presented in Fig. 7.5. The application of high voltage leads to fast coloration but also increases the possibility of side reaction, and thereby reducing the devices performance and the life. Low voltage make switching safer, thereby increasing the life of the devices but the switching time increases and the optical modulation is also less compared to that at a higher voltage. Thus, it is important to optimize the device's operating voltage to achieve a reasonable switching time and an optical modulation with a better lifetime.

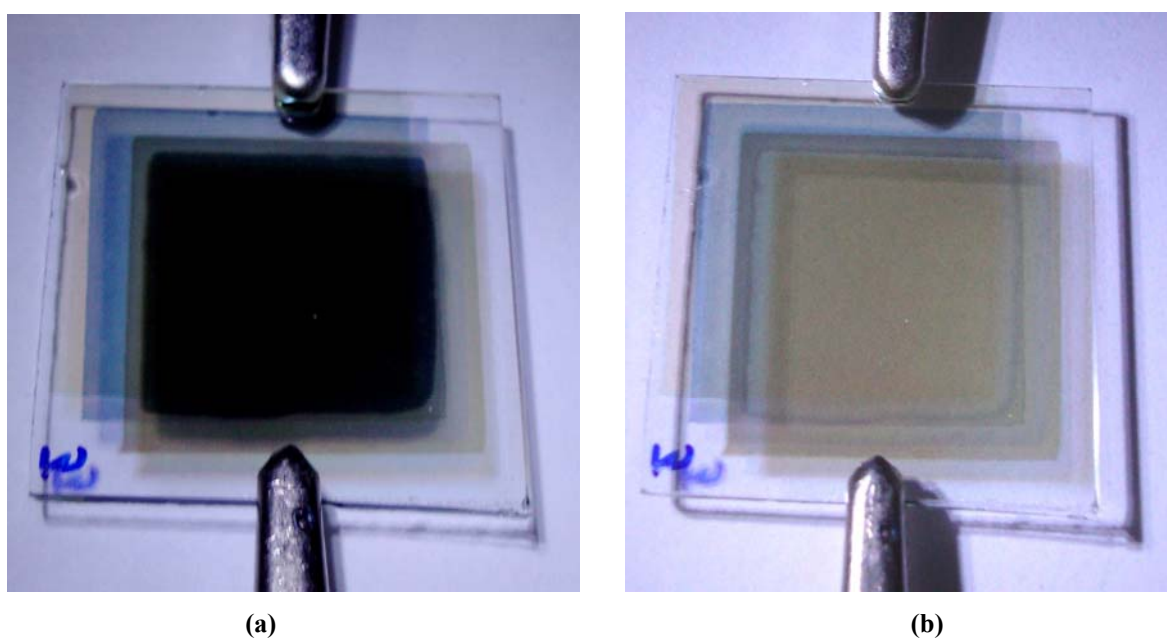


Figure 7.5: The photographs of the (a) colored and (b) bleached state of ECD.

7.3.4 Cycle-Life

Cycle-life represents the number of color-bleach cycles that can be performed by the ECD before any significant extent of degradation has occurred. For the cycle-life measurement of the device, the device was continually subjected to color-bleach cycles by application of ± 5 V. Figure 7.6 shows the initial color bleach cycle of transmittance modulation of ECD with time.

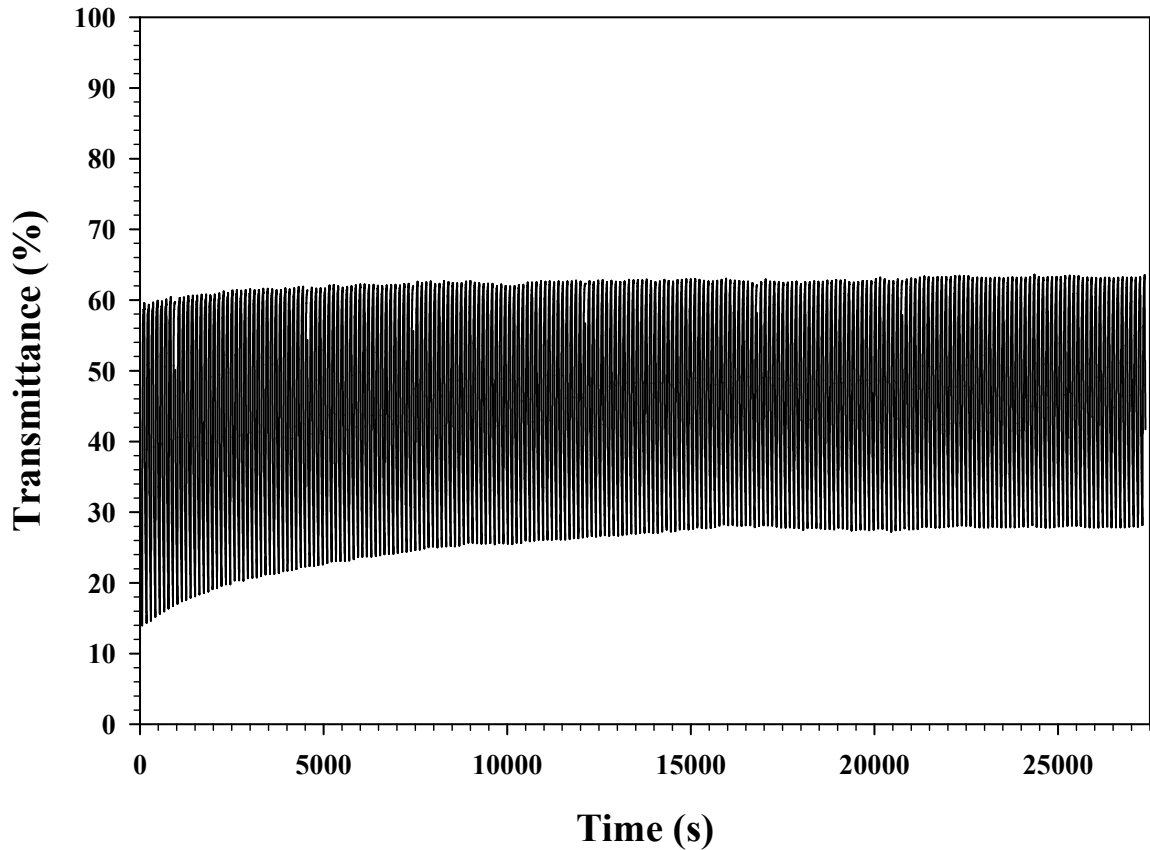


Figure 7.6: The transmittance modulation of ECD with number of cycles.

From Fig. 7.6, one can see that there was no obvious decrease in transmittance modulation (60 % - 20 %) even after 225 cycles, which indicates that this ECD has a good stability. Furthermore, this is not the maximum number of cycles performed by ECD, also the degradation of the device could not be observed until after a long time operation.

7.4 CONCLUSIONS

We have made an effort to fabricate thin film ECD having structure of ITO / NiO / ZrO₂ / WO₃ / ITO on a glass substrate. The transmittance modulation and memory effect was improved with increases of ZrO₂ electrolyte thickness. The device having optimum ZrO₂ thickness shows good transmittance modulation (56 %) in wavelength range of 450 - 1000 nm with good open-circuit memory effect of 170 min. The fabricated ECD shows the coloration and bleaching time of 120 s and 2 s, respectively with desirable cycle-life.

Chapter - 8

W₃O₃ Based Thin Film Gas Sensor

8. WO₃ BASED THIN FILM GAS SENSOR

Many gases in the environment are injurious to our health if they are in higher concentration. Thus, the detection of various gases in the environment is necessary for the pollution control. The electrical properties of some metal-oxide-semiconductor (MOS) have been found to be sensitive to the gas composition of the surrounding atmosphere. So in the present chapter we discuss about the MOS gas-sensing mechanism and device's fabrication. Tin (Sn) modified WO₃ thin film gas sensor was prepared on Aluminum interdigitated electrodes by thermal evaporation for detecting Ammonia (NH₃) gas. Gas sensing measurement set up is briefly discussed here. We have also made an effort to fabricate a sensor that shows the response at RT towards NH₃.

8.1 INTRODUCTION

Gas sensor is used to detect various explosive, flammable, and toxic gases, which are widely used in the industrial and commercial application for pollution control and safety purposes. Compared to the organic and elemental semiconductors, metal-oxide-semiconductor (MOS) is a more suitable material for the fabrication of gas sensors due to long-term cyclic stability in air atmosphere, simplicity, low-cost, and compact size [168]. The MOS gas sensor is conductometric type gas sensor i.e., the MOS material changes its conductivity when the gas atoms or molecules interact with the semiconductor surface. W. H. Bardeen and J. Brattain in 1953 demonstrated that the gas molecules interacting with semiconductor surfaces can change the electrical conductivity [169]. In the same year, S. R. Morrison also reported the change in conductivity and the contact potential in germanium as a function of the ambient atmosphere [170]. Subsequently, in 1962 T. Seiyama et al. [39] reported ZnO thin film layer for detecting inflammable gases and R. Taguchi [171] fabricated a gas sensing alarm system using resistive type gas sensing devices.

Semiconductors of n- and p-type have opposite 'direction' of conductivity change when they interact with the same gas. It is known [172] that p-type oxides are relatively unstable because of the tendency to exchange lattice oxygen easily with air. Consequently, in recent years MOS gas sensor based on n-type semiconductor metal oxide such as In₂O₃, WO₃, TiO₂, ZnO, SnO₂ have been widely studied for detect various gases [173]. In n-type semiconductor gas sensors when exposed to oxidizing gas atmosphere the overall conductance reduces while exposed to a reducing gas the conductance of the sensors

increases. The most important parameter of the gas sensor is the response and selectivity towards the particular gas. Usually, response can be calculated as R_a/R_g for reducing gases or R_g/R_a for oxidizing gases, where R_a is the resistance of gas sensors in the air and R_g is the resistance in the gas atmosphere. The gas sensing properties is related to gas adsorption on the surface of the thin films, so in practice, enhanced response and selectivity is achieved by surface modification and bulk doping. The surface modification will increase the active area of the sensor with the gas and the doping of materials promoting chemical reactions with the surface. The most of MOS gas sensor gives the response towards the gas at high operating temperature from 200 to 400 °C. The working temperature varies depending on the gas and on the sensing material. The design of the sensor operated at a high operating temperature is complicated due to the need for integration of heater and temperature sensor, which, in turn increases the power consumption and reduces the life of the sensor. But the doping of metal in the oxide film surface will reduce the operating temperature as well as enhance the sensor response. Doping of some material modifies the surface and hence affects the gas sensor response [42]. Surface dopant also acts as a catalyst and increases the chemical reaction at the surface as well as the sensitivity. The surface metal doping can lead to two different sensitization mechanisms: chemical sensitization, and electronic sensitization. In the chemical sensitization, generally the noble metal platinum, palladium, and gold are used, which promote the gas sensing by enhancing the 'spill-over effect' on surface. In the electronic sensitization, doping of fine particles of some metals to n-type metal oxides, the electron transfer from the metal oxide to the metal loaded onto its surface and which corresponds to an increase of the width of space-charge, results in a rise of the base resistance in air. When the metal oxide surface is exposed to reducing gas, consumption of oxygen adsorbed on the metal react with gases and enhances the sensitivity. Surface doping can also modify the microstructure of the base material, and control the grain growth mechanism. One of the major drawbacks of MOS gas sensors is that it is not selective to one particular gas.

Among n-type semiconductor metal oxides, WO_3 thin films are particularly attractive material as gas sensors because they have high catalytic behaviors both in oxidation and reduction reactions [174], which is widely useful for the detection of various toxic and flammable gases. First work on WO_3 thin films as gas sensor was reported by P. J. Shaver, who showed that the conductivity and physical properties of Pt-activated WO_3 thin films changed in the ambient concentration of hydrogen [175]. A number of experiments has demonstrated that WO_3 thin film is particularly interesting for their sensing properties towards the various gases CO, CO_2 , NH_3 , NO etc [176,177]. The WO_3 layer is highly

resistive, therefore, interdigitated electrodes are used in order to reduce the resistance to be measured. There are many deposition techniques like thermal evaporation, e-beam evaporation, sputtering, etc, used for the deposition of active layers of the gas sensor. In the present study we have investigate the gas sensing properties of WO_3 thin film, deposited by thermal evaporation technique, towards the NH_3 gas. Nowadays, ammonia (NH_3) is widely used as a food preservative, fertilizer, and a refrigerant. It is also used in pharmaceutical and chemical industries. Owing to its widespread use and the fact that it is hazardous for life, its detection is extremely important [178]. Different authors have already reported the sensing of NH_3 using WO_3 thin films but in most of the cases the operating temperature of the device is high, usually varying from 200 to 400 °C [177,179]. In the present study, our attempt is to fabricate WO_3 gas sensor operated at nearly room temperature by modifying it with Tin (Sn) metal. The bare WO_3 and Sn modified WO_3 thin films are prepared by the thermal evaporation method. The films annealed in air at 200 °C do not show measurable sensing properties towards the NH_3 gas. Thus, in the present study, we discuss the different Sn amount in WO_3 thin film annealed at 300 °C in air. The fundamental of gas sensing mechanism at RT of WO_3 towards the NH_3 is briefly explained.

8.2 GAS SENSING MECHANISM

In nonstoichiometric n-type semiconductor oxide, conduction is due to the oxygen vacancy present in it. When n-type semiconductor oxide interacts with air or oxygen, the oxygen molecules are adsorbed on the surface of the metal oxide and the adsorbed oxygen extracts electron from the conduction band, which leads to the formation of a surface depletion region that results in the reduction of the overall conductance. However, a reducing gas (such as hydrogen, carbon monoxide, ammonia, and hydrocarbon) will react with chemi-adsorbed oxygen on the film surface, which will re-inject the carriers and, hence, decrease the width of the depletion region thereby resulting in the increase of the sensor's conductance. The dissociation of oxygen on the film surface is responsible for the gas sensing at high temperature and the principle of WO_3 ammonia gas detection at high operation temperature is well-known.

At room temperature, there would be no oxygen adsorption taking place and also for the oxygen to dissociate into oxygen ions for its reaction with the gas need some kind of energy (i.e. temperature). Therefore, the oxygen adsorption-desorption mechanism is not adequate to explain the sensing of the NH_3 gas at room temperature. There are some reports, which show evidence of NH_3 sensing at room temperature but at present the room

temperature NH₃ sensing mechanism is still unclear [180,181,182]. At low temperature, near to room temperature, there is always a thin layer of moisture (H₂O) adsorbed on the film's surface and the sensor's response may be due to the NH₃ gas reaction with the water molecules [183]. As a result, the response is measured in terms of the ratio of the resistance of the gas sensor in air R_a, and the resistance of the gas sensor in the presence of a reducing gas R_g, i.e., R_a/R_g.

8.3 GAS SENSOR FABRICATION AND CHARACTERIZATIONS

8.3.1 Sensor Fabrication

The Sn-modified WO₃ gas sensor was fabricated on a glass substrate having aluminum (Al) interdigitated electrode. Interdigitated electrode, of thickness 1000 Å, was grown by thermal evaporation of Al on organically cleaned soda-lime glass substrate with a copper mask. The interdigitated electrode's width as well as the inter-electrode spacing is 0.25 mm. The active layer of WO₃ thin films were grown by thermal evaporation of WO₃ powder (Sigma Aldrich, 99.9 %). The active area of the WO₃ thin film sensor is 5 mm × 5 mm with 2000 Å thickness at the deposition rate 4 Å/s. The thickness and the average rate of deposition were monitored by the quartz crystal based thin film deposition monitor. The substrate temperature during the film's deposition was kept constant at 200 °C. To modify the WO₃ thin films, Sn metal films was deposited on WO₃ layer by the thermal evaporation method. The Sn thickness was varied from 25 Å to 150 Å at a deposition rate of 1 Å/s. The sensing device was annealed at 300 °C temperature in air for 4 hr. Figure 8.1 shows a step-by-step process involved in the fabrication of MOS gas sensor.

8.3.2 Sensor Characterization

The composition and the surface morphology of Sn modified WO₃ thin film was investigated using energy dispersive X-ray spectroscopy (EDX) and scanning electron microscopy (SEM) measurement, respectively. The gas-sensing measurements were carried out by resistance measurement using two-point probe method with the Keithley 2420C source meter. A brief introduction about gas sensing measurement setup are discussed below.

Gas Sensing Measurements: The NH₃ gas-sensing measurements were carried out by placing the sensor in a chamber and the liquor ammonia (25 % NH₃), as NH₃ gas, was exposed to the sample surface by operating a mechanical valve.

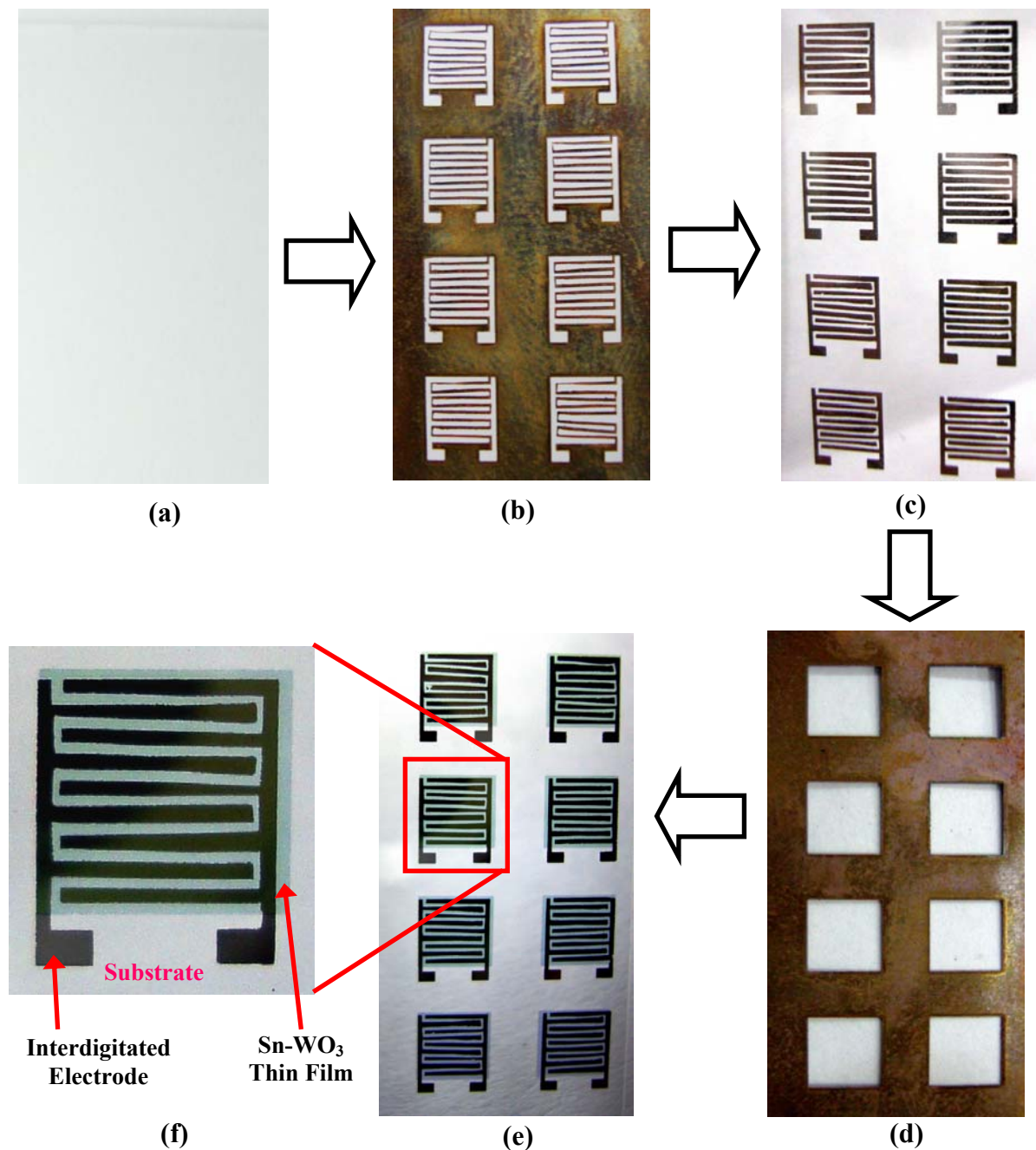


Figure 8.1: Schematic representation of the steps involved in the fabrication of MOS gas sensor devices: (a) Glass substrate, (b) Mask for interdigitated electrode, (c) Interdigitated electrode on glass substrate, (d) Mask for WO₃ thin film and Sn metal, (e) Complete device structure, and (f) Sensor consisting of the electrode and the sensing layer on the substrate.

The resistance of the sample was measured by direct current (DC) two-point probe method using Keithley 2420C source meter. Mechanical shutter and the exhaust pump were operated one at a time for exposing the gas to the sensor and removing the gas from the chamber, respectively. All gas-sensing measurements were performed in air atmosphere at RT ($\sim 25 \pm 1$ °C). The measurement setup was interfaced with computer and automated with the help of LabVIEW (ver. 8.2) program. The block diagram of the experimental setup for NH₃ gas sensing and the LabVIEW VI front panel are shown in Fig. 8.2 (a) and (b), respectively.

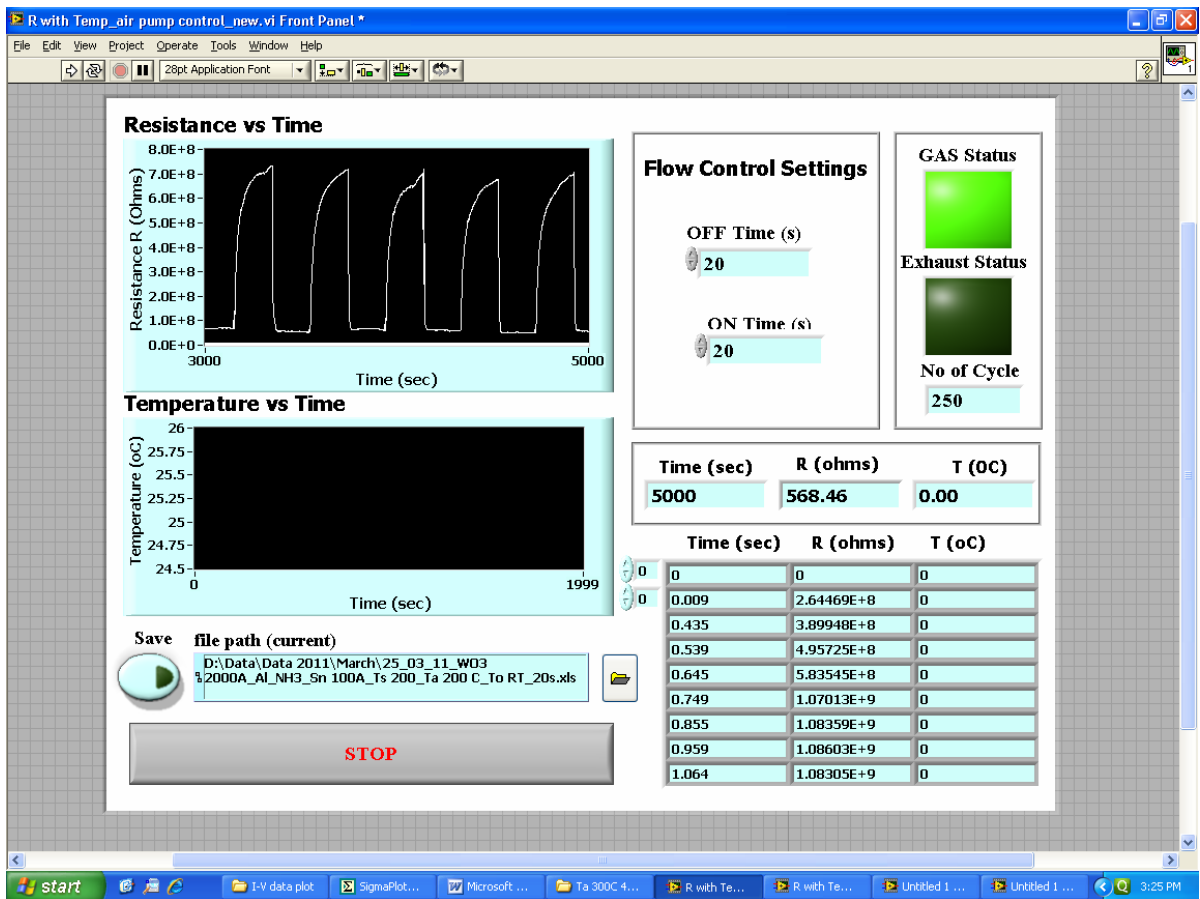
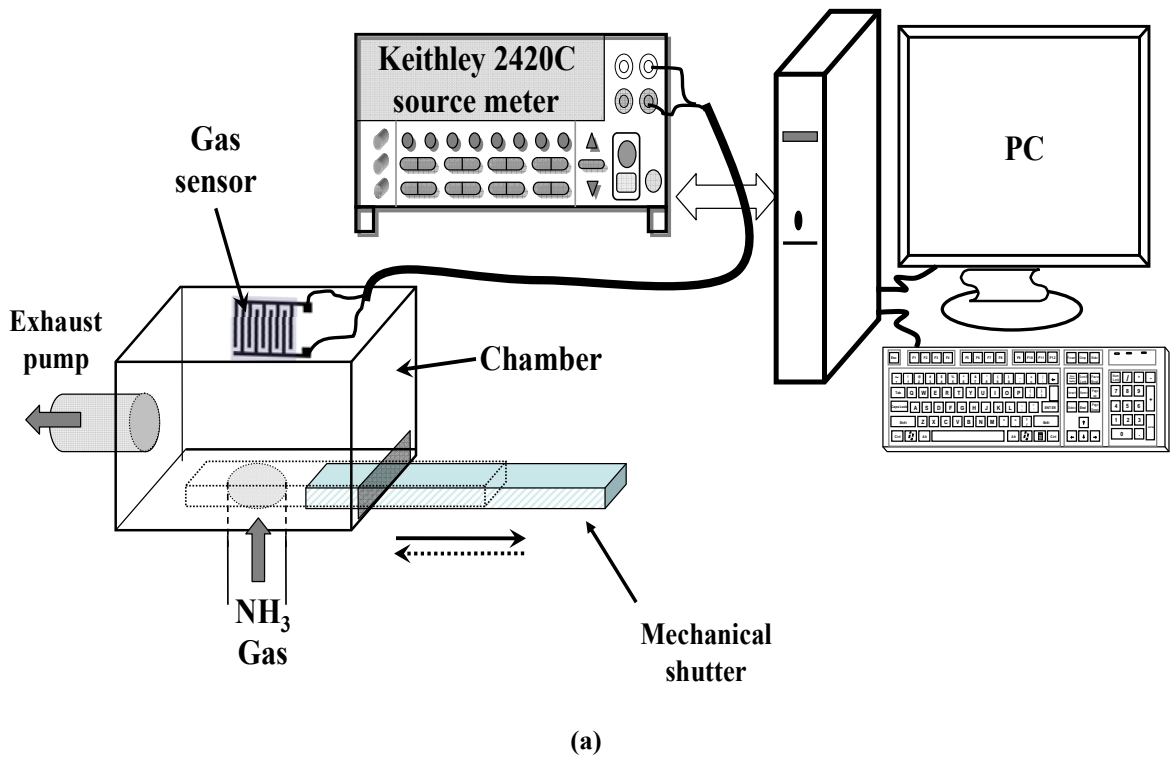


Figure 8.2: (a) The block diagram of the experimental setup for gas sensing measurement and (b) the front panel of LabVIEW program VI.

With the help of the LabVIEW program we can control the mechanical shutter and the exhaust pump operation time. The data are continually measured with time and stored in specified location, which were further used for the calculation of gas sensor response and response and recovery time.

8.4 RESULTS AND DISCUSSIONS

8.4.1 EDX and SEM Analyses

The Sn concentration in WO₃ thin films grown on Al interdigitated electrode were analyzed using an energy dispersive spectrometer. Figure 8.3 shows the EDX spectra of the 25 and 150 Å thicknesses of the Sn on the WO₃ thin film surface. The peaks in the spectra occur due to tungsten (W), Tin (Sn), and Aluminum (Al); the detector cannot measurably detect oxygen due to the presence of the sodium (Na) window in front of it, which absorbs the low-energy X-rays. The variations in the concentration of Sn with different deposition thicknesses are analyzed from the EDX spectra and presented in Fig. 8.4. It can be observed from Fig. 8.4 that the concentration of Sn increases from 2.13 to 6.85 (at %) as the thickness varies from 25 to 150 Å, respectively. The effect of Sn concentration on the surface morphology of WO₃ thin films is observed by SEM and the results are presented in Fig. 8.5.

From the SEM images, we observed that the WO₃ thin film having 25 to 75 Å Sn thicknesses has uniform flat surface. As the Sn thickness increases irregular shaped particles form on the surface and the highest particle size is observed at 125 Å Sn thickness. On further increasing the Sn thickness, up to 150 Å, a drastic change is observed in the surface morphology, the surface becomes flat again. This shows that there must be an optimum amount of Sn concentration required for surface modification.

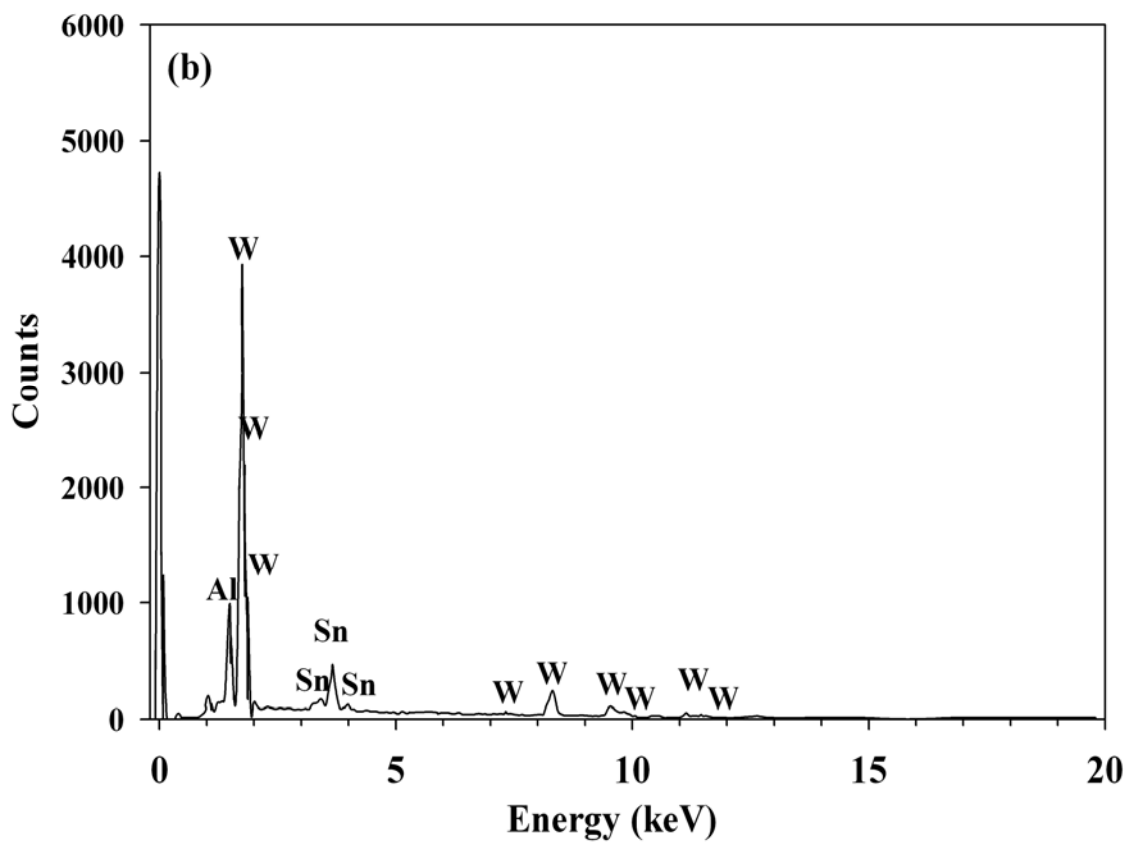
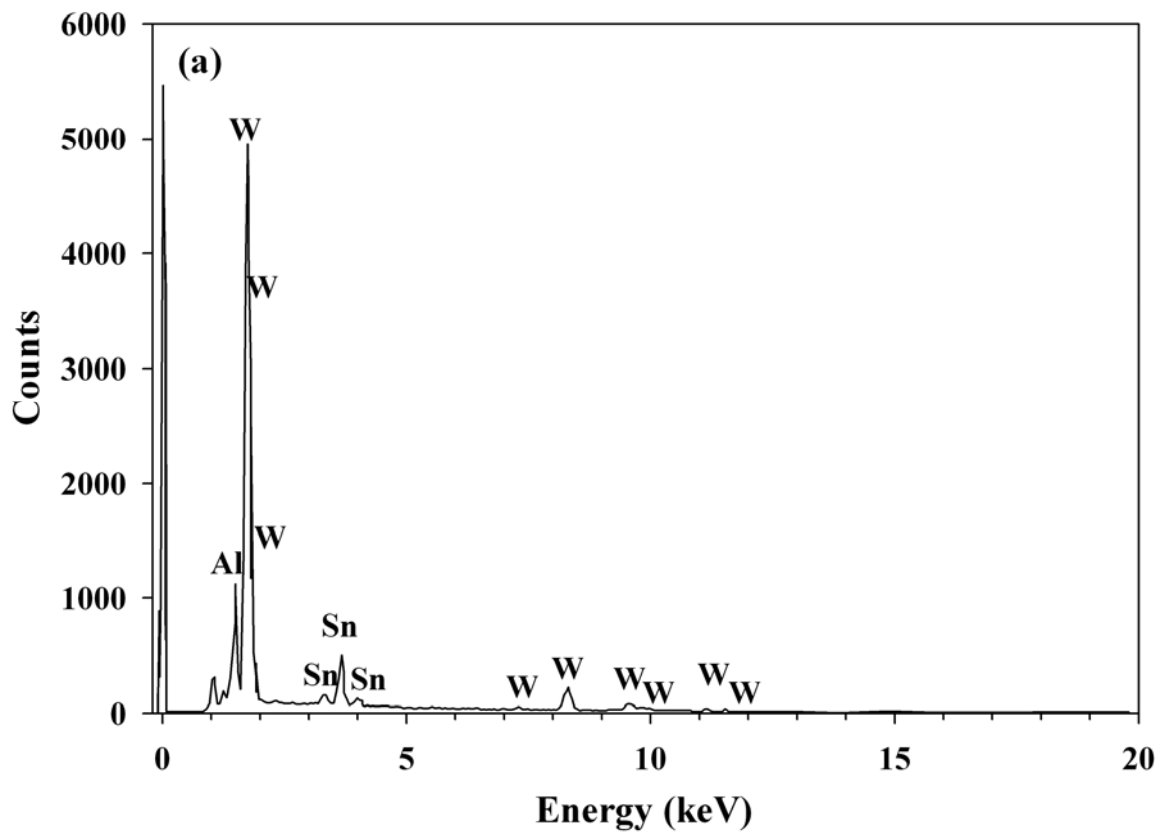


Figure 8.3: EDX spectra of 25 and 150 Å Sn thicknesses on WO₃ thin films annealed at 300 °C in air.

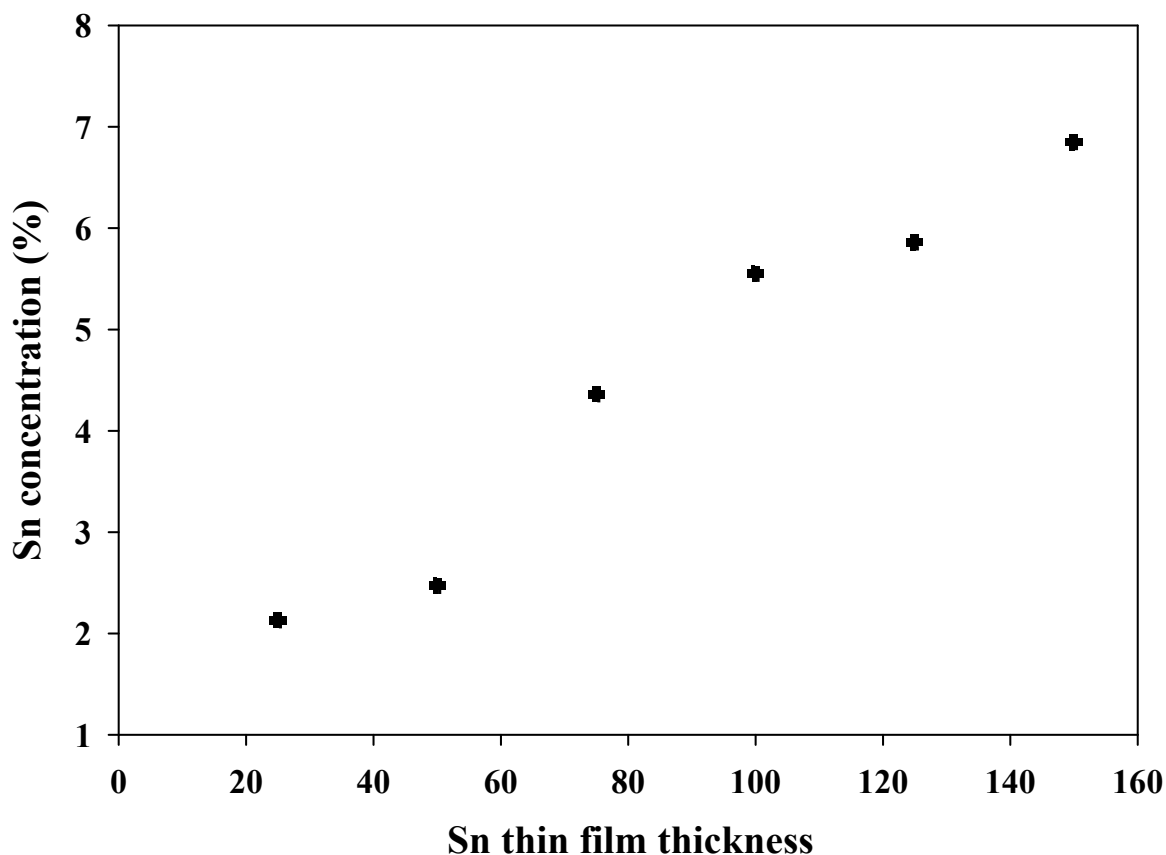
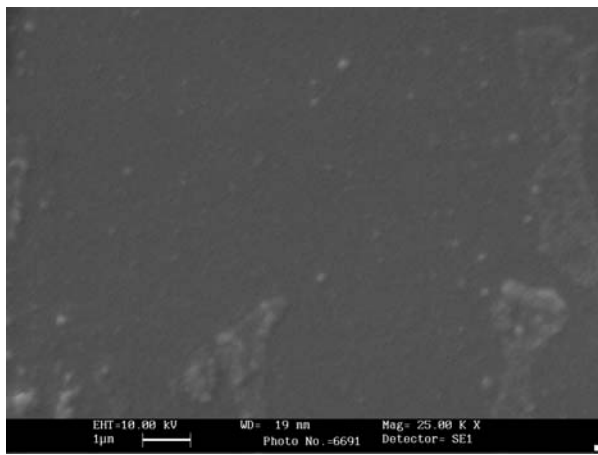


Figure 8.4: Concentration of Sn with different deposition thickness on WO₃ thin films annealed at 300 °C in air.

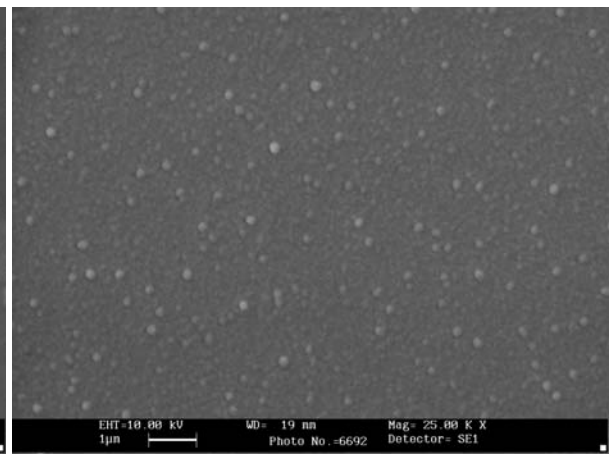
8.4.2 Gas Sensing Properties

To investigate the effect of Sn concentration on the gas-sensing properties, different thicknesses of Sn film varying from 25 to 150 Å, was deposited on 2000 Å WO₃ thin film and then the sensor was annealed in atmospheric air at 300 °C for 4 hr. The sensor was exposed to NH₃ gas for 20 s and, subsequently, for removing the gas from the chamber, the exhaust pump is operated for 20 s. Resistance of all the sensing films decreases drastically when NH₃ was exposed to the sensor, the transient response characteristics, (R_a/R_g), of different concentrations of Sn on WO₃ thin films is presented in Fig. 8.6 (a). The variation in the response with different Sn thickness is shown in Fig. 8.6 (b).

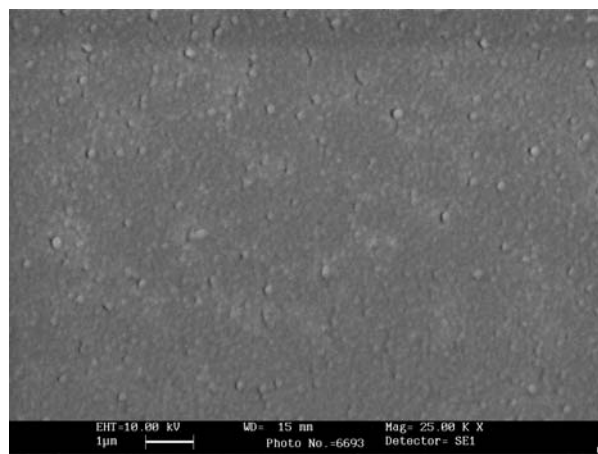
As shown in the Fig. 8.6, when the Sn amount increases, the response also increases up to 125 Å Sn thickness and thereafter the response decreases drastically. The maximum response ($R_a/R_g = 19$) was attained for the sensor modified with 125 Å of Sn thickness.



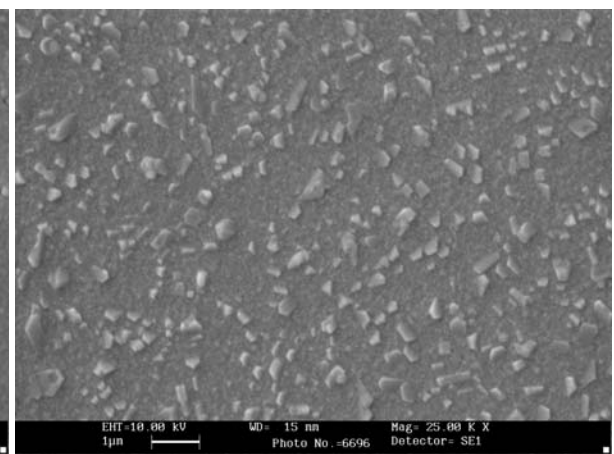
(a)



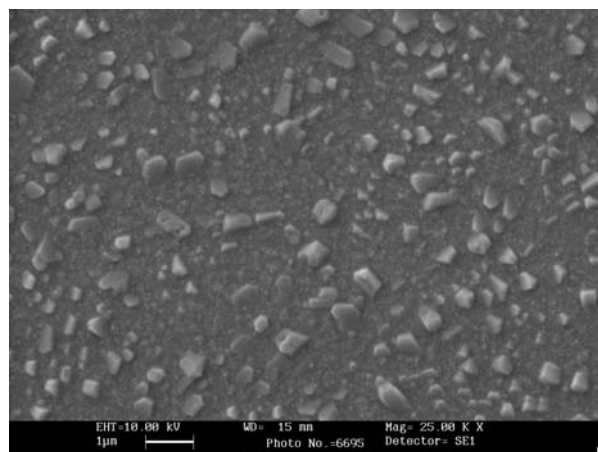
(b)



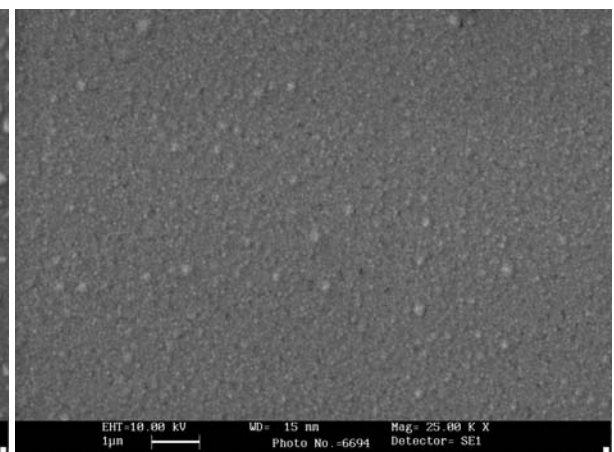
(c)



(d)



(e)



(f)

Figure 8.5: The SEM images of (a) 25 Å (b) 50 Å (c) 75 Å (d) 100 Å (e) 125 Å and (f) 150 Å Sn thickness on WO₃ thin film annealed at 300 °C in air.

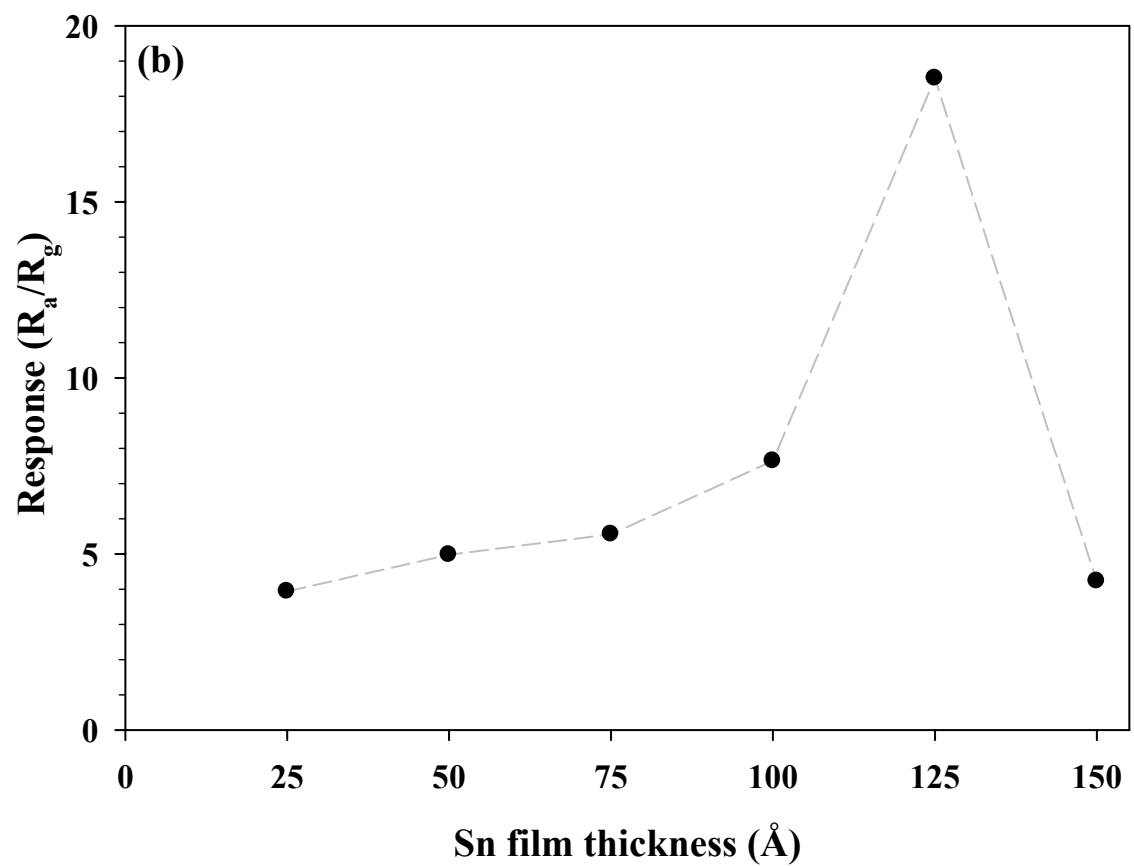
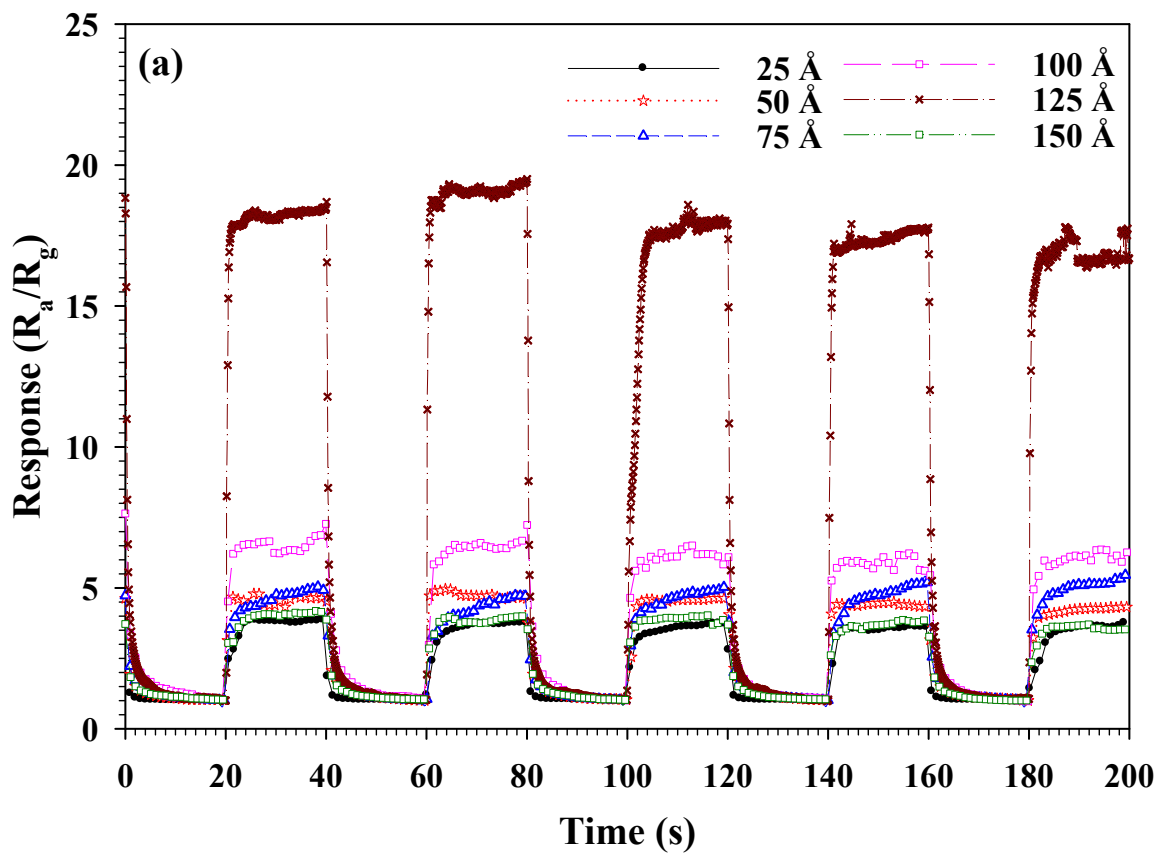


Figure 8.6. (a) The transient response characteristics and (b) response towards NH_3 gas of WO_3 thin film modified with different Sn thickness on 2000 Å WO_3 thin films annealed at 300 °C in air.

Response and Recovery Time: The sensor's response-time and recovery-time is defined as the time for the sensor's resistance to reach 90 % of its steady state value after exposure to or removal of the target gas, respectively. In fact, the voids and islands of particle formulation play a crucial role in gas sensing response and recovery time. It is found that the 125 Å Sn thickness film show a large active surface area (Fig. 8.5) on the WO₃ film surface. Figure 8.7 shows the response and recovery towards the NH₃ gas for the WO₃ thin film modified with 125 Å Sn and annealed at 300 °C in air.

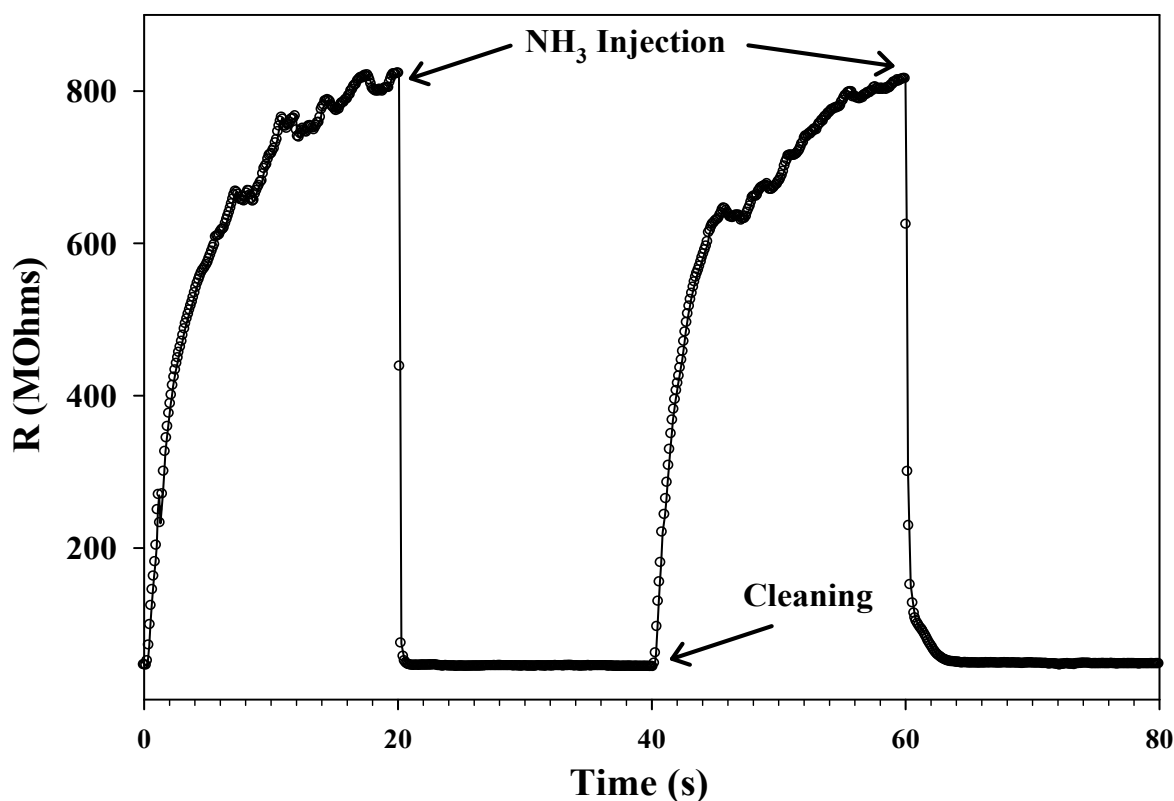


Figure 8.7: Response and recovery towards the NH₃ gas of WO₃ thin film modified with 125 Å Sn thicknesses annealed at 300 °C in air.

From Fig. 8.7, we see that when NH₃ was injected into the chamber the resistance decreased and reached the steady state value in 1 s. On the other hand, on removal of NH₃ from the chamber, the resistance rose slowly and reached its initial value after 20 s. Therefore, it is apparent that an optimum amount of additive concentrations will increase the response as well improve the response time of the thin film sensor. Although the above result may not be undermined, nevertheless, the precise role of WO₃ and Sn, at RT remain inexplicable.

8.5 CONCLUSIONS

The sensing properties towards the NH_3 gas was investigated using Sn modified WO_3 thin film gas sensor. The sensor was prepared on an Al interdigitated electrode by thermal evaporation method and subsequently annealed at $300\text{ }^\circ\text{C}$. At RT the optimum amount of Sn sensing layer of 125 \AA on 2000 \AA WO_3 thin film, shows the highest response of $R_a/R_g = 19$ with the fastest response and recovery time of 1 and 20 s, respectively. The results warrant a satisfactory explanation in terms of the role of WO_3 and Sn at RT.

Chapter - 9

Summary and
Future Outline

9. SUMMARY AND FUTURE OUTLINE

9.1 SUMMARY

Electrochromic device (ECD) modulates the light transmission, which decreases energy consumption, when it use as windows in buildings, in automotive vehicles or display. We have made an effort to fabricate solid-state thin film multilayered ECD structure, grown one by one on a single glass substrate using physical vapor deposition (PVD) technique. ECD having a layer of ITO / NiO / ZrO₂ / WO₃ / ITO on a glass substrate were prepared. The overall performance of the ECD depends on the properties of the individual thin film layers. Thus, it is necessary and useful to optimize each individual thin film layer of material as it plays an important role in ECD. We have optimized the different growth parameters for improvement of the device's performance.

The ITO thin film, prepared by RF magnetron sputtering, is used as a transparent conducting electrode for ECD, having a high transparency of above average 80 % and a low-sheet resistance of 4.7 Ω/\square . In the next step, the WO₃ thin film was optimized as electrochromic (EC) layer using thermal evaporation method. The WO₃ thin film deposited at lower substrate temperature (RT) and intercalated using H⁺ ions show greater EC performance i.e., ~55 % transmittance modulation with lower switching time of 7.5 s for coloration and 2 s for bleaching at 650 nm wavelength. Further, we have optimized ZrO₂ thin film deposited using the e-beam evaporation method. The ZrO₂ thin film deposited at lower substrate temperature having amorphous nature shows high ionic conductivity, which is used as a solid electrolyte for ECD fabrication. Finally, the NiO thin film layer was optimized as an ion-storage layer using e-beam evaporation method. The NiO film deposited at lower substrate temperature gives ~29 % transmittance modulation with the fastest switching time of 10 s and 2 s for coloration and bleaching, respectively, at 650 nm wavelength.

We have prepared solid-state ECD in our laboratory by varying ZrO₂ electrolyte thickness. The transmittance modulation and open-circuit memory effect of the ECD increases with increase in ZrO₂ film thickness. The ECD having 5000 Å ZrO₂ film thickness shows the maximum transmittance modulation of 56 % with good open-circuit memory effect up to 170 mins. The fabricated ECD also shows the coloration and bleaching time of 120 s and 2 s, respectively, with a desirable cycle-life.

As a spin-off, we have also attempted to fabricate Sn modified WO₃ thin film gas sensor for NH₃ gas detection at room temperature. Optimum amount of Sn (125 Å) modified WO₃ (2000 Å) thin film gas sensor shows the highest response (R_a/R_g) of 19 with the fastest response and recovery time of 1 and 20 s, respectively.

9.2 FUTURE OUTLINE

In the present case, the ECD has ~60 % transmittance in bleach state. The residual brown color in the bleached state of NiO thin film is responsible for that. To overcome this, one can introduce additives such as Mg, Al, Si, Zr, Nb, or Ta in the NiO thin films. The major issues in all-solid-thin film ECD are to reduce the coloration time and to get a long-term stability. One of the reasons for all-solid-thin film ECD failure is short-circuiting between EC and ion-storage layer, which originates due to the pinhole formed in the electrolyte. One can divide the ECD into individual sub devices, so that the major part of the device works if one of the sub-devices fails due to pinhole formation.

Integration of EC technology with photovoltaic (PV) for the self-power ECD operation is a new direction [184]. Photovoltaic electrochromic (PV-EC) device can show color change in EC layers without additional power source. This results in enormous energy saving which is perhaps a major application on the part of ECD. At present, people have also tried to develop ECD, which show high optical modulation with different colors. Due to the complex fabrication of multilayered structure, the cost of the device is high. Thus, this area is still open for new and innovative solutions in developing high efficient low price ECD.

REFERENCES

- [1] C. G. Granqvist, *Handbook of Inorganic Electrochromic Materials*, Elsevier, Amsterdam, (1995)
- [2] D. A. Hinckley, P. G. Seybold, D. P. Borris, *Spectrochimica Acta*, **24A** (1986) 747
- [3] A. I. Gavriluk, *Electrochimica Acta*, **44** (1999) 3027
- [4] J. Burgess, S. Maguire, A. McGranaghan, S. A. Parsons, B. Nowicka, A. Samotus, *Transition Met. Chem.*, **23** (1998) 615
- [5] A. Marini, A. Munoz-Losa, A. Biancardi, B. Mennucci, *J. Phys. Chem. B*, **114** (2010) 17128
- [6] G. B. Kaufman, *Inorganic Coordination Compounds: Nobel Prize Topics in Chemistry*, Heyden, Philadelphia, (1981)
- [7] J. J. Berzelius, *Afh. Fys. Kemi Miner.*, **4** (1815) 293, as cited in ref. [1]
- [8] F. H. Smith, *British Patent*, **328** (1929) 017, as cited in ref. [1]
- [9] N. Kobosew, N. I. Z. Nekrassow, *Electrochem.*, **36** (1930) 529, as cited in ref. [1]
- [10] E. O. Brimm, J. C. Brantley, J. H. Lorenz, M. H. Jellinek, *J. Am. Chem. Soc.*, **73** (1951) 5427
- [11] T. Kraus, Labor-Bericht, Balzers AG, unpublished (1953), as cited in ref. [1]
- [12] J. R. Platt, *J. Chem. Phys.*, **34** (1961) 862
- [13] S. K. Deb, *Appl. Opt.*, **8(S1)** (1969) 192
- [14] S. K. Deb, *Philos. Mag.*, **27** (1973) 801
- [15] P. M. S. Monk, R. J. Mortimer, D. R. Rosseinsky, *Electrochromism: Fundamentals and Applications*, VCH, Weinheim, (1995)
- [16] A. J. C. Da Silva, F.A. Ribeiro Nogueira, J. Tonholo, A.S. Ribeiro, *Sol. Energ. Mater. Sol. Cell*, **95** (2011) 2255
- [17] S. Papaefthimiou, G. Leftheriotis, P. Yianoulis, *Ionics*, **4** (1998) 321
- [18] A. Azens, L. Kullman, *Sol. Energ. Mater. Sol. Cell*, **56** (1999) 193
- [19] Q. Zhang, G. Wu, B. Zhou, J. Shen, J. Wang, *J. Mater. Sci. Technol.*, **17** (2001) 417
- [20] F. G. K. Baucke, *Mater. Sci. Engg. B*, **10** (1991) 285
- [21] P. Pennarun, S. Papaefthimiou, P. Yianoulis, P. Jannasch, *Sol. Energ. Mater. Sol. Cell*, **91** (2007) 330
- [22] C. G. Granqvist, *Sol. Energ. Mater. Sol. Cell*, **91** (2007) 1529
- [23] T. Minami, *Semicond. Sci. Technol.*, **20** (2005) S35
- [24] C. G. Granqvist, A. Hultaker, *Thin Solid Films*, **411** (2002) 1
- [25] M. Scholten, J. E. A. M. van den Meerakker, *J. Electrochem. Soc.*, **140** (1993) 471
- [26] J. M. Bell, I. L. Skryabin, *Sol. Energ. Mater. Sol. Cell*, **56** (1999) 437

- [27] H. Huang, J. Tian, W. K. Zhang, Y. P. Gan, X. Y. Tao, X. H. Xia, J. P. Tu, *Electrochim. Acta*, **56** (2011) 4281
- [28] J. S. E. M. Svensson, C. G. Granqvist, *Sol. Energ. Mater.*, **11** (1984) 29
- [29] E. S. Lee, E.S. Claybaugh, M. LaFrance, *Energy and Buildings*, **47** (2012) 267
- [30] C. G. Granqvist, *Smart Mater. Bull.*, **2002** (2002) 9
- [31] A. Azens, C. G. Granqvist, *J. Solid State Electrochem.*, **7** (2003) 64
- [32] K. Tajima, Y. Yamada, S. Bao, M. Okada, K. Yoshimura, *Surf. Coating Tech.*, **202** (2008) 5633
- [33] M. Green, K. Kang, *Displays*, **9** (1988) 166
- [34] P. M. S. Monk, C. Turner, S. P. Akhtar, *Electrochim. Acta*, **44** (1999) 4817
- [35] C. Ma, J. Zheng, S. Yang, D. Zhu, Y. Bin, C. Xu, *Organic Electronics*, **12** (2011) 980
- [36] M. Buyan, P. A. Bruhwiler, A. Azens, G. Gustavsson, R. Karmhag, C. G. Granqvist, *Int. J. Ind. Ergon.*, **36** (2006) 11
- [37] P. M. S. Monk, F. Delage, S. M. C. Vieira, *Electrochim. Acta*, **46** (2001) 2195
- [38] P. T. Moseley, *Meas. Sci. Technol.*, **8** (1997) 223
- [39] T. Seiyama, A. Kato, K. Fujishi, M. Nagatani, *Anal. Chem.*, **34** (1962) 1502
- [40] G. N. Chaudhari, A. M. Bende, A. B. Bodade, S. S. Patil, S. V. Manorama, *Talanta*, **69** (2006) 187
- [41] M. Penza, C. Martucci, G. Cassano, *Sens. Actuators B*, **50** (1998) 52
- [42] X. Wang, N. Miura, N. Yamazoe, *Sens. Actuators B*, **66** (2000) 74
- [43] D. M. Mattox, *Handbook of Physical Vapor Deposition (PVD) Processing*, Noyes, New Jersey (1998)
- [44] M. Ohring, *Materials science of thin films: Deposition and Structure*, Academic Press, California, (2006)
- [45] B. D. Cullity, *Elements of X-ray diffraction*, Addison-Wesley, Massachusetts (1956)
- [46] C. S. Barrett, Structure of Metals, *Crystallographic methods, Principles and Data*, McGraw-Hill, New -York, (1952)
- [47] S. H. Cohen, M. L. Lightbody, *Atomic Force Microscopy/Scanning Tunneling Microscopy*, Kluwer Academic, New York, (2002)
- [48] J. F. Moulder, W. F. Stickle, P. E. Sobol, and K. D. Bomben, *Handbook of X-ray Photoelectron Spectroscopy*, Perkin-Elmer Corp., Eden Prairie, (1992)
- [49] J. Tauc, in: J. Tauc (Ed.), *Amorphous and Liquid Semiconductors*, Plenum, London, (1974)
- [50] D. K. Schroder, *Semiconductor material and device characterization*, John Wiley and sons, New Jersey, (2006)

- [51] J. R. Macdonald, *Ann. Biomed. Eng.*, **20** (1992) 289
- [52] M. A. Habib, D. Glueck, *Sol. Energ. Mater.*, **18** (1989) 127
- [53] K. Badeker, *Ann. Phys. (Leipzig)*, **327** (1907) 749
- [54] A. Thelen, H. Konig, *Naturwissenschaften*, **43** (1956) 297
- [55] R. Groth, E. Kauer, *Philips Tech. Rev.*, **26** (1965) 105
- [56] R. Groth, *Phys. Stat. Sol. B.*, **14** (1966) 69
- [57] K. L. Chopra, S. Major, D. K. Pandya, *Thin Solid Films*, **102** (1983) 1
- [58] G. B. Gonzalez, T. O. Mason, J. P. Quintana, O. Warschkow, D. E. Ellis, J. H. Hwang, J. P. Hodges, J. D. Jorgensen, *J. Appl. Phys.*, **96** (2004) 3912
- [59] W. F. Wu, B. S. Chiou, S. T. Hsieh, *Semicond. Sci. Technol.*, **9** (1994) 1242
- [60] J. B. Chu, S. M. Huang, H. B. Zhu, X. B. Xu, Z. Sun, Y. W. Chen, F. Q. Huang, *J. Non-Crystalline Solids*, **354** (2008) 5480
- [61] Y. H. Tak, K. B. Kim, H. G. Park, K. H. Lee, J. R. Lee, *Thin Solid Films*, **411** (2002) 12
- [62] L. Ai, G. Fang, L. Yuan, N. Liu, M. Wang, C. Li, Q. Zhang, J. Li, X. Zhao, *Appl. Surf. Sci.*, **254** (2008) 2401
- [63] L. Meng, M. P. dos Santos, *Thin Solid Films*, **303** (1997) 151
- [64] A. Salehi, *Thin Solid Films*, **324** (1998) 214
- [65] H. R. Fallah, M. G. Varnamkhasti, M. J. Vahid, *Renewable Energy*, **35** (2010) 1527
- [66] H. Kim, J. S. Horwitz, A. Pique, C. M. Gilmore, D. B. Chrisey, *Appl. Phys. A*, **69** (1999) S447
- [67] Y. Hu, X. Diao, C. Wang, W. Hao, T. Wang, *Vacuum*, **75** (2004) 183
- [68] I. Baia, M. Quintela, L. Mendes, P. Nunes, R. Martins, *Thin Solid Films*, **337** (1999) 171
- [69] G. Brauer, *Surf. Coatings Tech.*, **112** (1999) 358
- [70] M. A. Martinez, J. Herrero, M. T. Gutierrez, *Sol. Energ. Mater. Sol. Cell*, **26** (1992) 309
- [71] C. V. R. Vasant kumar, Abhai Mansingh, *J. Appl. Phys.*, **65** (1989) 1270
- [72] Y. S. Kim, Y. C. Park, S. G. Ansari, J. Young, B. S. Lee, H. S. Shin, *Surf. Coatings Tech.*, **173** (2003) 299
- [73] A. M. Gheidari, F. Behafarid, G. Kavei, M. Kazemzad, *Mater. Sci. Engg. B*, **136** (2007) 37
- [74] F. Kurdesau, G. Khripunov, A. F. da Cunha, M. Kaelin, A.N. Tiwari, *J. Non-Crystalline Solids*, **352** (2006) 1466
- [75] K. J. Patel, M. S. Desai, C. J. Panchal, *J. Mater. Sci: Mater. Electron*, **22** (2011) 959

- [76] A. Antony, M. Nisha, R. Manoj, M. K. Jayaraj, *Appl. Surf. Sci.*, **225** (2004) 294
- [77] E. Burstein, *Phys. Rev.*, **93** (1954) 632
- [78] T. S. Moss, *Proc. Phys. Soc. B*, **67** (1954) 775
- [79] R. B. H. Tahar, T. Ban, Y. Ohya, Y. Takahashi, *J. Appl. Phys.*, **83** (1998) 2631
- [80] G. Haacke, *J. Appl. Phys.*, **47** (1976) 4086
- [81] M. Carl Lampert, *Sol. Energy Mater.*, **11** (1984) 1
- [82] S. K. Deb, *Sol. Energ. mater. Sol. Cell*, **92** (2008) 245
- [83] R. Cerc korosec, P. Bukovec, *Acta Chim. Slov.*, **53** (2006) 136
- [84] R. Hurditch, *Electrocomponent Sci. Technol.*, **3** (1977) 247
- [85] H. Kamal, A. A. Akl, K. Abdel-hady, *Physica B*, **349** (2004) 192
- [86] M. G. Hutchins, N. S. Butt, A. J. Topping, J. Gallego, P. Milne, D. Jeffrey, I. Brotherston, *Electrochimica Acta*, **46** (2001) 1983
- [87] C. Trimble, M. Devries, J. S. Hale, D. W. Thompson, T. E. Tiwald, J. A. Woollam, *Thin Solid Films*, **355-356** (1999) 26
- [88] B. W. Faughnan, R. S. Crandall, P. M. Heyman, *RCA Review*, **36** (1975) 177
- [89] O. F. Schirmer, V. Wittwer, G. Baur, G. Brandt, *J. Electrochemical Soc.*, **124** (1977) 749
- [90] L. D. Landau, *Phys. Z. Sowjetunion*, **3** (1933) 664, as cited in *Physica Scripta*, **T25** (1989) 309
- [91] A. Deneuve, P. Gerard, *J. Electron. Mater.*, **7** (1978) 559
- [92] S. -S. Sun, P. H. Holloway, *J. Vac. Sci. Technol. A*, **2** (1984) 336
- [93] T. Yoshimura, *J. Appl. Phys.*, **57** (1985) 911
- [94] J. -G. Zhang, D. K. Benson, C. E. Tracy, S. K. Deb, A. W. Czanderna, C. Bechinger, *J. Electrochem. Soc.*, **144** (1997) 2022
- [95] F. Wooten, *Optical properties of solid*, Academic, New York, (1972)
- [96] J. S. E. M. Svensson, C. G. Granqvist, *Appl. Phys. Lett.*, **45** (1984) 828
- [97] E. Gerlach, *J. Phys. C:Solid state phys.*, **19** (1986) 4584
- [98] R. Sivakumar, R. Gopalakrishnan, M. Jayachandran, C. Sanjeeviraja, *Smart Mater. Struct.*, **15** (2006) 877
- [99] C. -C. Liao, F. -R. Chen, J. -J. Kai, *Sol. Energy Mater. Sol. Cell*, **91** (2007) 1258
- [100] P. Losier, P. V. Ashrit, *J. Mater. Sci. Lett.*, **22** (2003) 1095
- [101] A. A. Joraid, *Curr. Appl. Phys.*, **9** (2009) 73
- [102] G. Fang, Z. Liu, K. L. Yao, *J. Phys. D: Appl. Phys.*, **34** (2001) 2260
- [103] Y. -M. Lu, C. P. Hu, *J. Alloys Compd.*, **449** (2008) 389
- [104] R. Solarska, B. D. Alexander, J. Augustynski, *C. R. Chim.*, **9** (2006) 301

- [105] Y. Yamada, K. Tabata, T. Yashima, *Sol. Energy Mater. Sol. Cell*, **91** (2007) 29
- [106] G. Leftheriotis, S. Papaefthimiou, P. Yianoulis, A. Siokou, *Thin Solid Films*, **384** (2001) 298
- [107] H. Zheng, J. Z. Ou, M. S. Strano, R. B. Kaner, A. Mitchell, K. Kalantar-Zadeh, *Adv. Funct. Mater.*, **21** (2011) 2175
- [108] K. J. Patel, C. J. Panchal, V. A. Kheraj, M. S. Desai, *Mater. Chem. Phys.*, **114** (2009) 475
- [109] J. Y. W. Seto, *J. Appl. Phys.*, **46** (1975) 5247
- [110] M. G. Hutchins, O. Abu-Alkhair, M. M. El-Nahass, K. Abd el-Hady, *Mater. Chem. Phys.*, **98** (2006) 401
- [111] <http://www.webelements.com/>
- [112] K. J. Patel, C. J. Panchal, M. S. Desai, P. K. Mehta, *Mater. Chem. Phys.*, **124** (2010) 884
- [113] K. D. Lee, *Thin Solid Films*, **302** (1997) 84
- [114] K. J. Patel, M. S. Desai, C. J. Panchal, *Proceedings of the 54th DAE Solid State Physics Symposium*, **54** (2009) 449
- [115] M. Deepa, D. P. Singh, S. M. Shivaprasad, S. A. Agnihotry, *Curr. Appl. Phys.*, **7** (2007) 220
- [116] M. Green, D. Richman, *Thin Solid Films*, **24** (1974) S45
- [117] J. H. Kennedy, *Thin Solid Films*, **43** (1977) 41
- [118] Y. Hajimoto, M. Matsushima, S. Ogura, *J. Electron. Mater.*, **8** (1979) 301
- [119] R. H. French, S. J. Glass, F.S. Ohuchi, *Physical Review B*, **49** (1994) 5133
- [120] S. B. Qadri, E. S. Skelton, M. Harford, P. Lubitz, L. Aprigliano, *J. Appl. Phys.*, **67** (1990) 2655
- [121] M. J. Biercuk, D. J. Monsma, C. M. Marcus, *Appl. Phys. Lett.*, **83** (2003) 2405
- [122] J. P. Chang, Y. S. Lin, K. Chu, *J. Vac. Sci. Technol. B*, **19** (2001) 1782
- [123] H. Guo, S. Gong, K. A. Khor, H. Xu, *Surf. Coating Tech.*, **168** (2003) 23
- [124] B. Zhu, *Solid State Ionics*, **119** (1999) 305
- [125] W. H. Lowdermilk, D. Milam, F. Rainer, *Thin Solid Films*, **73** (1980) 155
- [126] T. Nguyen, E. Djurado, *Solid State Ionics*, **138** (2001) 191
- [127] H. Okamoto, H. Obayashi, T. Kudo, *Solid State Ionics*, **1** (1980) 319
- [128] I. M. Ochando, M. Vila, C. Prieto, *Vacuum*, **81** (2007) 1484
- [129] M. Levichkova, V. Mankov, N. Starbov, D. Karashanova, B. Mednikarov, K. Starbova, *Surf. Coating Tech.*, **141** (2001) 70
- [130] L. Q. Zhu, Q. Fang, G. He, M. Liu, L. D. Zhang, *Nanotechnology*, **16** (2005) 2865

- [131] L. Ben-Dor, A. Elshtein, S. Halabi, L. Pinsky, J. Shappir, *J. Electron. Mater.*, **13** (1984) 263
- [132] Wen-Chao Liu, Di Wu, Ai-Dong Li, Hui-Qing Ling, Yue-Feng Tang, Nai-Ben Ming, *Appl. Surf. Sci.*, **191** (2002) 181
- [133] A. Ortiz, J. C. Alonso, E. Haro-poniatowski, *J. Electron Mater.*, **34** (2005) 150
- [134] H. Nohira, W. Tsai, W. Besling, E. Young, J. Petry, T. Conard, W. Vandervorst, S. De Gendt, M. Heyns, J. Maes, M. Tuominen, *J. Non-Cryst. Solids*, **303** (2002) 83
- [135] S. Mahboob, G. Prasad, G. S. Kumar, *Bull. Mater. Sci.*, **29** (2006) 347
- [136] A. A. Dakhel, *Thin Solid Films*, **476** (2005) 366
- [137] A. Ghosh, *Phys. Rev. B*, **41** (1990) 1479
- [138] K. Bange, *Sol. Energ. Mat. Sol. Cell*, **58** (1999) 1
- [139] Z. Xuping, Z. Haokang, L. Qing, L. Hongli, *IEEE Electron Device Lett.*, **21** (2000) 215
- [140] K. J. Patel, C. J. Panchal, M. S. Desai, Bharati rehani, *J. Nano- electron. Phys.*, **3** (2011) 376
- [141] Hung-Lu Chang, T. C. Lu, h. C. Kuo, S. C. Wang, *J. Appl. Phys.*, **100** (2006) 124503
- [142] H. Bode, K. Dehmelt, J. Witte, *Electrochim. Acta*, **11** (1966) 1079
- [143] C. M. Lampert, T. R. Omstead, P. C. Yu, *Sol. Energ. Mater.*, **14** (1986) 161
- [144] E. Avendano, H. Rensmo, A. Azens, A. Sandell, G. de M. Azevedo, H. Siegbahn, G. A. Niklasson, C. G. Granqvist, *J. Electrochem. Soc.*, **156** (2009) P132
- [145] L. Ottaviano, A. Pennisi, F. Simone, *Surf. Interface Anal.*, **36** (2004) 1335
- [146] I. Serebrennikova, V. I. Birss, *J. Electrochem. Soc.*, **144** (1997) 566
- [147] E. Avendano, A. Azens, G. A. Niklasson, C. G. Granqvist, *Sol. Energ. Mat. Sol. Cell*, **84** (2004) 337
- [148] Kwang-Soon Ahn, Yoon-Chae Nah, Yung-Eun Sung, *Solid State Ionics*, **156** (2003) 433
- [149] K. J. Patel, C. J. Panchal, M. S. desai, P. K. Mehta, *J. Nano- electron. Phys.* **3** (2011) 362
- [150] K. K. Purushothaman, G. Muralidharan, *Sol. Energ. Mat. Sol. Cell*, **93** (2009) 1195
- [151] L. D. Kadam, P. S. Patil, *Sol. Energ. Mat. Sol. Cell*, **69** (2001) 361
- [152] Y. G. Wu, G. M. Wu, X. Y. Ni, X. Wu, *Sol. Energ. Mat. Sol. Cell*, **63** (2000) 217
- [153] W. L. Jang, Y. M. Lu, W. S. Hwang, T. L. Hsiung, H. P. Wang, *Surf. Coat. Tech.*, **202** (2008) 5444
- [154] H. L. Chen, Y. M. Lu, W. S. Hwang, *Thin Solid Films*, **514** (2006) 361
- [155] J. M. Sanz, G. T. Tyuliev, *Surf. Sci.*, **367** (1996) 196

- [156] S. R. Jiang, P. X. Yan, B. X. Feng, X. M. Cai, J. Wang, *Mater. Chem. Phys.*, **77** (2002) 384
- [157] S. K. Deb, US Patent, 3829196 (1976)
- [158] S. K. Deb, R. F. Shaw, US Patent, 3521961 (1970)
- [159] C. G. Granqvist, *Electrochromic tungsten-oxide based thin films: physics, chemistry, and technology*, In *Physics of Thin Films*, Vol. 17, Francombe M. H. and Vossen J. L. (Eds), (1993a) Academic, San Diego
- [160] J. P. Cronin, T. J. Gudgel, S. R. Kennedy, A. Agrawal, D. R. Uhlmann, *Materials Research*, **2** (1999) 1.
- [161] J. Nagai, T. Seike, U.S. Patent, 5721633, 1998
- [162] C. G. Granqvist, E. Avendano, A. Azens, *Thin Solid Films*, **442** (2003) 201
- [163] A. Azens, G. Vaivars, M. Veszelei, L. Kullman, C. G. Granqvist, *Proceeding of 4th International Meeting on Electrochromism (IME-4)*, Uppsala, Sweden, 21-23, Aug., 2000
- [164] G. Vaivars, A. Azens, C. G. Granqvist, *Proceeding of 4th International Meeting on Electrochromism (IME-4)*, Uppsala, Sweden, 21-23, Aug., 2000.
- [165] Y. He, Y. Xiong, J. Qiu, M. Xu, J. Wang, C. Wu, Y. Zhao, *Physics Procedia*, **18** (2011) 61
- [166] C. M. Lampert, *Sol. Energ. Mat. Sol. Cell*, **52** (1998) 207
- [167] R. Baetens, B. P. Jelle, A. Gustavsen, *Sol. Energ. Mat. Sol. Cell*, **94** (2010) 87
- [168] G. Korotcenkov, *Materials Science and Engineering B*, **139** (2007) 1
- [169] W. H. Brattain, J. Bardeen, *Bell System Tech. J.*, **32** (1953) 1
- [170] S. R. Morrison, *J. Phys. Chem.*, **57** (1953) 860
- [171] R. Taguchi, Japanese Patent No. 4538200 (1962)
- [172] M. J. Madou, S. R. Morrison, *Chemical Sensing with Solid State Devices*, Academic Press, Inc./Harcourt Brace Jovanovich Publ., Boston, NY, (1987)
- [173] N. Yamazoe, G. Sakai, K. Shimano, *Catal. Surveys Asia*, **7** (2003) 63
- [174] H. H. Kung, *Transition metal Oxides: Surface Chemistry and Catalysis*, Elsevier, NY, (1989)
- [175] P. J. Shaver, *Appl. Phys. Lett.*, **11** (1967) 255
- [176] A. Ponzoni, E. Comini, M. Ferroni, G. Sberveglieri, *Thin Solid Films*, **490** (2005) 81
- [177] V. Khatko, G. Gorokh, A. Mozalev, D. Solovei, E. Liobet, X. Vilanova, X. Correig, *Sens. Actuators B*, **118** (2006) 255
- [178] B. Timmer, W. Olthuis, Albert van den Berg, *Sens. Actuators B*, **107** (2005) 666

- [179] C. N. Xu, N. Miura, Y. Ishida, K. Matuda, N. Yamazoe, *Sens. Actuators B*, **65** (2000) 163
- [180] G. S. T. Rao, D. Tarakarama, *Sens. Actuators B*, **55** (1999) 166
- [181] L. A. Patil, L. S. Sonawane, D. G. Patil, *Journal of Modern Physics*, **2** (2011) 1215
- [182] D. R. Patil, L. A. Patil, *Talanta*, **77** (2009) 1409
- [183] A. Helwing, G. Muller, G. Sberveglieri, M. Eickhoff, *Journal of sensors* (2009) Artical ID 620720
- [184] L. M. Huang, C. W. Hu, H. C. Liu, C. Y. Hsu, C. H. Chen, K. C. Ho, *Sol. Energ. Mater. Sol. Cells*, **99** (2012) 154

LIST OF SYMBOLS

Ω/\square	Ohm/square	L	Crystallite size
$^{\circ}\text{C}$	Degree Celsius	m^*	Electron effective mass
μm	Micrometer	mm	Millimeter
A	Ampere	min	minute
A	Area	mV	Millivolt
\AA	Angstrom	ν	X-ray frequency
at%	Atomic Percent	n	Carrier concentration, Number of electrons
B	Magnetic field	nm	Nanometer
b	Spacing between diffracting planes	P	Pressure
C	Coulomb	Q	Charge density
C_0	Concentration of active ions	q	Charge
cm	Centimeter	r	Molecular diameter
D	Diffusion coefficient	ρ	Resistivity
d	Thickness	R	Resistance
ΔOD	Change in the optical density	R_a	Resistance in air
ΔT	Transmittance modulation	R_b	Bulk resistance
E_b	Binding energy	R_g	Resistance in gas
E_g	Energy band-gap	R_H	Hall coefficient
E_k	Kinetic energy	R_s	Sheet resistance
eV	Electron volt	S	Gas sensitivity
ϕ	Phase angle	s	Second
ϕ_{TC}	Figure of merit	S/cm	Siemen/cm
h	Planck's constant	σ_b	Bulk conductivity
hr	Hour	σ_e	Electron conductivity
h ν	Photons of energy	σ_i	Ionic conductivity
Hz	Hertz	t	Time
I	Current	T	Transmittance
i	Current density	T_a	Absolute temperature
j	Imaginary coefficient	T_{avg}	Average transmittance
k	Shape factor	T_b	Transmittance in bleached state
k_B	Boltzmann constant	t_b	Bleaching time
		T_c	Transmittance in colored state

t_c	Coloration time	Z''	Imaginary part of Impedance
T_s	Substrate temperature	Z'	Real part of Impedance
V	Voltage	α	Absorption coefficient
v	Scan-rate	ΔE_g	Shifting of the band gap
V_H	Hall voltage	θ	Incident angle
w	Width	λ	Wavelength
W	Watt	μ	Hall mobility
wt. %	Weight percent	σ'	Real part of the conductivity
ω	Angular frequency	σ_{AC}	AC conductivity
Z	Impedance	ℓ	Mean free path

ABBREVIATIONS

2D	Two dimensional	IR	Infrared
3D	Three dimensional	IS	Impedance spectroscopy
AC	Alternating current	ITO	Indium-doped tin oxide
AFM	Atomic force microscopy	IVCT	Inter-valence charge transition
Al-ZnO	Aluminum doped Zinc oxide	LabVIEW	Laboratory Virtual Instrumentation Engineering Workbench
B-M effect	Burstein–Moss effect	LED	Light emitting diode
CA	Chronoamperometry	MOS	Metal-oxide semiconductor
CE	Coloration Efficiency	OD	Optical density
COM	Communication	PVD	Physical vapor deposition
CV	Cyclic-voltammetry	RF	Radio frequency
CVD	Chemical vapor deposition	rms	Root mean square
DC	Direct current	rpm	Revolutions per minute
DI	De-ionized	RT	Room temperature
EC	Electrochromic	SEM	Scanning electron microscopy
ECD	Electrochromic devices	TBC	Thermal barrier coating
EDX	Energy dispersive X- ray spectroscopy	TCE	Trichloroethylene
emf	Electromotive force	TCO	Transparent conducting oxide
ESCA	Electron spectroscopy for Chemical analysis	UV	Ultraviolet
FPD	Flat panel displays	UV-Vis	Ultraviolet Visible
FTO	Fluorine-doped tin dioxide	VI	Virtual instrument
FWHM	Full width half maxima	XPS	X-ray photoelectron spectroscopy
GIXRD	Grazing Incidence X-ray Diffraction	XRD	X-ray diffraction
GPIB	General purpose interface bus		
ICDD	International center for diffraction data		

LIST OF PUBLICATIONS

➤ International Journals

- 1. Growth, structural, electrical and optical properties of the thermally evaporated tungsten trioxide (WO₃) thin films**
K. J. Patel, C. J. Panchal, V. A. Kheraj, M. S. Desai
Materials Chemistry and Physics, **114** (2009) 475
- 2. An investigation of the insertion of the cations H⁺, Na⁺, K⁺ in WO₃ thin films grown at different substrate temperatures by thermal evaporation of WO₃ powder**
K. J. Patel, C. J. Panchal, M. S. Desai, P. K. Mehta
Materials Chemistry and Physics, **124** (2010) 884
- 3. Properties of RF magnetron sputtered indium tin oxide (ITO) thin films on externally unheated glass substrate**
K. J. Patel, C. J. Panchal, M. S. Desai
Journal of Material Science: Material in Electronics, **22** (2011) 959
- 4. Optical and electrochromic properties of e-beam evaporated nickel oxide thin film**
K. J. Patel, C. J. Panchal, M. S. Desai, P. K. Mehta
J. Nano- Electron. Phys., **3** (2011) 362
- 5. p-type transparent NiO thin films by e-beam evaporation techniques**
K. J. Patel, C. J. Panchal, M. S. Desai, Bharati Rehani
J. Nano- Electron. Phys., **3** (2011) 376
- 6. The influence of substrate temperature on the structure, morphology, and optical properties of ZrO₂ thin films prepared by e-beam evaporation**
K. J. Patel, M. S. Desai, C. J. Panchal
American Journal of Materials Science, (Communicated)
- 7. Tin modified Tungsten oxide thin film for Ammonia gas sensing at room temperature**
K. J. Patel, M. S. Desai, C. J. Panchal
Sensors & Transducers Journal, (Communicated)

➤ **Conference Proceedings**

1. Electrochromic behavior of the a-WO₃ thin films grown by thermal evaporation

K. J. Patel, M. S. Desai, and C. J. Panchal

Proceedings of 54th DAE solid state physics symposium - 2009

The M. S. University of Baroda, Vadodara, 14- 18 December, 2009

➤ **Conference Presentations**

1. Tungsten trioxide (WO₃) thin films for electrochromic device

National Conference on Semiconductor Materials and Technology (NC-SMT 2008)

Gurukul Kangri University, Haridwar, 16-18 October, 2008

2. Optimization of thermally evaporated tungsten trioxide (WO₃) thin films for electrochromic device applications

Condensed Matter Days 2009 (CMDAYS 09)

Department of Physics, Jadavpur University, Kolkata, 26-28 August, 2009

3. Effect of film thickness on electrochromic properties of thermally evaporated tungsten trioxide (WO₃) thin films

National Symposium on Vacuum Technology and Its Applications to Electronic Devices and Systems (IVSNS - 2009),

Central Electronics Engineering Research Institute (CEERI), Pilani, Rajasthan, 11-13 November, 2009